Interaction between optically trapped particles due to optomechanical coupling

DISSERTATION

zur Erlagerung des akademischen Grades
Doktor der Naturwissenschaften
an der
Fakultät für Mathematik, Informatik und Physik
der
Leopold–Franzens-Universität Innsbruck
vorgelegt von

János K. Asbóth

Februar 2007

Abstract

Whenever optically trapped particles modify substantially the propagation of the trapping light field, the field will mediate an interaction between them. In this Thesis we explore the dynamical effects of this interaction for atoms trapped in high-Q cavities and for large optical lattices.

We start with a study of the simplest setup where this interaction can occur: two atoms trapped in a single-mode high-Q standing wave cavity which is fed by laser light, with the atoms constrained to move along the cavity axis. We simulate the motion of the atoms by stochastic differential equations using a model previously developed in the group of Helmut Ritsch. We find that whenever cavity cooling is expected to be effective, the motion of deeply trapped atoms develops correlations: the two particles oscillate in their potential wells with a 90° relative phase shift. This mode of motion is very weakly coupled to the cavity and thus these correlations seriously limit the efficiency of cavity cooling. The final temperature in these cases corresponds to the Doppler limit.

We also investigate a cavity cooling setup where the field-mediated interaction plays a constructive role: the dynamics of many atoms in a standing-wave cavity, where instead of feeding the cavity directly, the pumping laser is directed at the atoms. As previously predicted and experimentally observed, above a laser power threshold the atoms form one of two stable lattice-like patterns that produce superradiant scattering into the cavity. We present here a detailed study of this self-organization phenomenon. A simple mean-field model is used to derive analytical formulas for the threshold and the details of this phase transition. We also perform numerical simulations of the dynamics revealing that, on a laboratory timescale, a hysteresis masks the mean-field behaviour. Simple physical arguments are used to explain this phenomenon and to derive expressions for the observable threshold. Above a certain density of the atoms a limited number of "defects" appear in the organized phase and influence the statistical properties of the system. We also study the scaling of the cavity cooling mechanism and the achievable phase-space density with the atom number. We then apply the mean-field model to a ring cavity, and map out the phase diagram of thermodynamic states of (i) uniform distribution, (ii) self-organized Bragg lattice, (iii) lattice with defects, and (iv) instability.

We address the question of how to model the dynamics if the collective back-action of the trapped particles is so large that they not only influence the occupation of the cavity mode, but the very shape of the mode function itself. The dependence of the mode function on the atomic positions has to be calculated by solving the Helmholtz equation, in the simplest 1-dimensional model systems this is straightforward with the transfer matrix method. We comment on recent attempts to derive the steady state of a regular distribution of atoms inside a pumped standing-wave cavity. We point out that the approach based on the minimization of the dipole Hamiltonian leads to nonphysical conclusions. Deriving the optical forces via the Maxwell Stress Tensor, we find that the steady state of the atoms corresponds to a regular lattice, and that no bistability of the kind predicted in the literature should occur.

We explore the dynamics of a 1-dimensional optical lattice due to optomechanical coupling. We derive the force on a disk-shaped cloud of trapped particles including the back-action on the trapping light, and analyze its relation to the standard perturbative approach giving the "dipole force" and "radiation pressure". Unexpectedly, we find that the pump asymmetry, i.e., the ratio of power in the two beams used to trap the atoms, plays a key role in the dynamics of this system. We calculate the self-consistent lattice constant for both red and blue detuned lattices and find that it decreases – by the same amount in the two cases – as the pump asymmetry is increased. We find that the vibrations of the trapped atoms are coupled by the field-mediated interaction, and in the presence of asymmetry, this results in traveling wavelike collective oscillations. By increasing the size of the lattice or the pump asymmetry, these can destabilize the lattice even in the overdamped limit. We present a detailed derivation of the lattice vibration eigenmodes using the transfer matrix method, which reveals that the instability is enhanced resonantly at certain settings of the asymmetry.

Finally, in this Thesis we include some of the research work done during the PhD years which is not related to optomechanical coupling. We propose the entanglement potential (EP) as a measure of nonclassicality for quantum states of a single-mode electromagnetic field. It is the amount of two-mode entanglement that can be generated from the field using linear optics, auxiliary classical states, and ideal photodetectors. The EP detects nonclassicality, has a direct physical interpretation, and can be computed efficiently. These three properties together make it stand out from previously proposed nonclassicality measures. We derive closed expressions for the EP of important classes of states and analyze as an example of the degradation of nonclassicality in lossy channels.

Zusammenfassung

Wenn immer mit Licht gefangene Teilchen die Ausbreitung des Fangenlichtes im wesentlichen verändern, dann wird das Lichtfeld zwischen ihnen eine Wechselwirkung vermitteln. In der vorliegenden Dissertation betrachten wir die dynamische Effekte dieser Wechselwirkung für Atome in optische Hohlraumresonatoren und für grosse optische Gitter.

Wir beginnen mit einer Studie der einfachste Konfiguration, wo diese Wechselwirkung auftreten kann: zwei Atome, die in das Lichtfeld eines single-mode Hohlraumresonators mit hohem Gütefaktor gefangen sind, und die sich nur entlang die Achse des Resonators bewegen können. Wir simulieren die Bewegung der Atome durch stochastische Differentialgleichungen. Wir stellen fest, dass wann immer eine wirksame Hohlraumkühlung erwartet ist, die Bewegung der tief gefangenen Atome wird korreliert sein: die zwei Teilchen oszillieren in ihren Potenzialtöpfen mit einer relativen Phasenverschiebung von 90°. Diese Art von Bewegung ist nur sehr schwach gekoppelt an der Resonator und folglich begrenzt diese Wechselwirkung ernsthaft die Leistungsfähigkeit des Resonatorkühlungs. In diesen Fällen entspricht die endgültige Temperatur der Doppelschen Grenze.

Wir untersuchen auch eine Konfiguration, wo die vom Lichtfeld vermittelte Wechselwirkung eine konstruktive Rolle spielt: die Dinamik vielen Atomen in eine Stehwelle-Resonator, wo anstatt die Hohlraum direkt zu pumpen, ist die Laser an den Atomen anrichtet. Wie bereits vorhergesagt und experimentell beobachtet, oberhalb einer Schwelle der Laserleistung bilden die Atome eine der zwei stabile Gitter-Muster, die superradiante Streuung in den Hohlraum ergiebt. Wir stellen hier eine detaillierte Studie über diese Selbstorganisation. Mit einem einfachen mittelfeld Modell können wir analytische Formeln für die Schwelle und die Einzelheiten dieser Phasenübergangs ableiten. Wir fhren auch numerische Simulationen der Dynamik durch, und finden, dass auf die Zeitskala des Experiments verdeckt ein Hysteresis das mittelfeld Verhalten. Mit einfachen physikalischen Argumente können wir dieses Phenomän erklären und Ausdrücke für die wahrnehmbare Schwelle ableiten. Ab einer bestimmten Dichte der Atome erscheint eine begrenzte Anzahl von “ Fehler” der selbstorganisierten Gitter und beeinflussen die statistischen Eigenschaften des Systems. Wir studieren auch die Skalierung des Hohlraum-Khl-Mechanismus und die erreichbare Phasenraumdichte mit dem Anzahl der Atome. Dann wenden wir die mittelfeld Modell zu einem Ring-resonator an, erstellen die Phasendiagramm der thermodynamischen Zustnde von (i) die gleichmige Verteilung, (ii) selbstorganisierte Bragg-Gitter, (iii) Gitter mit Mngeln, und (iv) die Instabilitt.

Wir gehen auch der Frage nach, wie der Dynamik modelliert wird, wenn das kollektive rck-Aktion der gefangenen Teilchen so gro ist, dass sie nicht nur Einfluss auf die Besetzung der Modusfunktion, aber auf die Form selbst der Funktion haben. Die Abhngigkeit der Modusfunktion von der atomaren Positionen soll mit der Lsung der Helmholtz-Gleichung berechnet werden, in 1-dimensionalen Modell-Systemen ist das einfach durch dem Transfer-Matrix-Methode. Wir kommentieren neue Versuche zur Ermittlung der Steady-State einer regelmässigen Verteilung von Atomen in einem gepumpten stehende-Welle Hohlraum. Wir weisen darauf hin, dass die Minimierung der Dipol Hamiltonian zu nichtphysikalische Schlussfolgerungen fhrt. Nach Ableitung der optischen Krfte durch die Maxwell-Stress-Tensor, stellen wir fest, dass die Steady-State der Atome einem regelmäigen Gitter entspricht, und dass es keine bistabilität der Art, der in der Literatur vorausgesagt wird, auftreten sollte.

Wir erforschen die Dynamik einer 1-dimensionalen optischen Gitter wegen der optomechanische Kopplung. Wir leiten die Kraft auf einen scheibenfrmigen Wolke gefangenen Partikeln, und analysieren seine Beziehung zu den perturbativen Standardannäherung von “ Dipol-Kraft”und “Strahlungsdruck”. Unerwartet stellen wir fest, dass die Asymmetrie der Pumpe — das Verhltnis der Energie in den zwei Lichtstrahlen die die Falle erzeugen — spielt eine zentrale Rolle in der Dynamik des Systems. Wir berechnen die Gitterkonstante fr beide rot und blau verstimmte Gitter und finden, dass es sich verringert — um den gleichen Betrag in den beiden Fllen — als die Asymmetrie erhht wird. Wir stellen fest, dass die Schwingungen der gefangenen Atome durch dem Feld-vermittelte Interaktion gekoppelt sind, und in Anwesenheit von Asymmetrie, ergeben sich reisenden wellenartigen kollektive Schwingungen. Durch die Erhöhung der Gröe des Gitters oder die Asymmetrie der Falle, knnen diese Schwingungen zur Destabilisierung des Gitters führen, auch in den oberdämpften Grenzfall. Wir präsentieren eine detaillierte Ableitung der Gitter-Vibrations-Moden mit Hilfe der Transfer-Matrix-Methode, die zeigt, dass die Instabilitt resonant zu bestimmten Einstellungen der Asymmetrie erhht wird.

Schlielich sind in dieser Dissertation auch einige unserer Ergebnisse erhalten, die keine direkte Zusammenhange mit Optomechanische Kopplung haben. Wir schlagen die Verschränkungspotential (EP) als Mass für die nichtklassizität Quanten-Zustnde eines Modes des elektromagnetischen Felds vor. Es ist die Menge der zwei-Modus Verschränkung, dass aus dem Zustand mit linearer Optik, klassischen “ancilla” Zuständen, und idealen Photodetektoren generiert werden kann. Das EP erkennt nichtklassizität, hat eine direkte physikalische Deutung, und kann effizient ausrechnet werden. Diese drei Eigenschaften zusammen machen die EP einzigartig zwischen den bisher vorgeschlagenen Massen der nichtklassizität. Wir leiten analytische Ausdrcke fr die EP wichtige Klassen von Zustände ab, und als Beispiel fr dessen Anwendung analysieren wir die Verminderung der nichtklassizität in verlustbehaftete Kanle.

Contents

Acknowledgements

These four years of PhD studies were for me marked by a sort of double existence. I started working on issues related to cavity cooling with Peter Domokos, who was a postdoc in the group of Helmut Ritsch, and then, as Peter moved back to Budapest, divided my time between the Institute of Theoretical Physics in Innsbruck and the Department of Nonlinear and Quantum Optics at the Research Institute for Solid State Physics (SZFKI) in Budapest, with excursions to the University of Pecs, where I gave courses during the time spent in Hungary.

I would like to thank Helmut Ritsch for being enthusiastic, available for discussion, supportive, and inspiring to work with. I have often enjoyed the hospitality of his family in Mieders, staying at their "guest residence" with the unparalleled view on Serles and the Stubai Glacier. In a large part, I could enjoy the stimulating work atmosphere in Innsbruck because of the open and interesting people I met there and who became my friends. The ever-ironic Jean-Noël Fuchs, the great cook Stefano Cerrito, the very positive John Calsamiglia, the thoughtful Walter Rantner, the radiant Barbara Mroz, Alessio Recati, Thomas Salzburger, Caroline Kruszynski, Christian Roos, Regis Danielian, Elisa Vianello, and Andrew Daley. They made this time far from home and friends in Budapest become not only a work experience, but also one of personal growth, and have provided support when I needed it badly. Most of them took part in, or helped me organize, the weekly "CineClub" sessions at the Institute. Although they are now living in different cities, I am happy to have more or less managed to keep these contacts. I have also enjoyed discussions with other members of the Ritsch group, in particular Igor Mekhov, Hashem Zoubi, and Christoph Maschler.

I am grateful to Peter Domokos for the interesting physics, the very active cooperation, and the help with organizing this often chaotic work schedule. More than being an advisor, he is a friend, an important member of my sports team "Ötballáb", and I enjoy immensely the time I spend with his family. I have been working together with András Vukics on and off for nine years now (both in Budapest and Innsbruck), and have profited from the great many discussions about physics and life as well as games of go and chess. The group at the SZFKI in Budapest was fun and very helpful: Zoltán Kurucz, Aurél Gábris, Dávid Nagy, Tamás Kiss, Zsolt Kis, Peter Adam, Mátyás Koniorczyk, Attila Kárpáti, Géza Tóth, and József Janszky have provided a relaxed but productive work environment.

I am grateful to my family, my parents Margit and Bence, my sisters Zsófi and Cili, and my brother Lőrinc, for their support throughout these years. They have been a stable point and it is always reassuring to feel their acceptance and love.

I thank my wife Anna for the wonders of love. Through her sensitivity I have learnt to know life as never before.

Introduction

0.1 Optical manipulation of matter

The interaction of light and matter is one of the central topics of physics. Since the earliest days of science, matter has been used in a variety of ways to tailor the motional state of light. The associated theoretical and experimental techniques, which form the subject of optics, have been at the heart of physical research as well as numerous technological achievements ever since. Clearly, this interaction is reciprocal, and light also changes the kinematical state of material particles. However, it is only in the last three decades, following the development of the laser, that the use of light as a tool to manipulate the motional state of material particles has revolutionarized atomic physics and biophysics.

Although “radiation pressure” has been thought by many to play a role in directing the coma of comets opposite to the Sun, its existence has only been experimentally verified at the turn of the 19th-20th century by Lebedev, Nichols and Hull [1, 2, 3]. The development of the laser, an intensive and coherent source of light, has enabled physicists to explore the forces due to light in more detail. In 1970, Ashkin has used a focused Gaussian beam to trap transparent latex spheres in water [4]. Apart from the expected “push” of the laser photons bouncing off the spheres, he has also found that the beads were “pulled” by light to the center of the beam, which he could explain with geometric optics and momentum conservation. Further experiments and theoretical work have led to the characterization of these two types of radiation pressure acting on sub-wavelength particles: the “scattering force” pointing in the direction of net photon flux, and the “dipole force” pointing along the intensity gradient. The possibility to trap, hold, and stretch microscopic objects without direct physical contact has invigorated biological research as well as physics. Since 1987, when Ashkin et al. [5] used “optical tweezers” to trap tobacco viruses and living bacteria, optical forces have been applied to, e.g., the manipulation of chromosomes, mechanical characterization of molecular motors and cell organelles, and to test the cancerousness of cells [6].

The fact that atoms can be deflected or accelerated by the “scattering force”, the resonance radiation pressure due to absorption and subsequent spontaneous emission of photons, has already been shown as early as 1933 [7]. As realized in 1975 by Hänsch and Shawlow [8], because of the Doppler effect this force can be used to cool the motion of atoms. For this so-called Doppler cooling, atoms are irradiated from all sides by lasers whose frequency is slightly red-detuned with respect to the atomic resonance. Atoms are then always more likely to absorb photons from the lasers they are moving towards, as those are blue-shifted by the Doppler effect. Due to momentum conservation, each such absorption event decreases the kinetic energy of the atom. The precise description of this and other optical manipulations schemes, accounting for the vacuum fluctuations, required the extension of the theory of light-induced forces to the motion of single atoms. This work was initiated in 1980 by Gordon and Ashkin [9], with crucial insights provided by Cohen-Tannoudji, Dalibard, and coworkers [10]. In the 1985, the groups of Phillips and Metcalf have used the scattering force to “stop” a beam of atoms emanating from an oven, which could then be trapped by inhomogeneous magnetic fields and cooled by Doppler cooling in what is known as a

Magneto-Optical Trap [11]. In 1997, Chu [12], Cohen-Tannoudji [13] and Phillips [14] have been given the Nobel prize for the “development of methods to cool and trap atoms with laser light” (for a review, see [15]).

Optical manipulation of the motion of atoms has led to the realization of degenerate quantum gases, and predictions dating from the early days of quantum mechanics could be checked. The creation of Bose-Einstein Condensates (BEC) [16, 17] has been awarded with a Nobel prize (Ketterle, Cornell and Wieman, 2001) and has stimulated a great amount of interest. More recently, ultracold Fermi gases have also been realized, and are used to study the BEC-BCS (Bardeen-Cooper-Schrieffer pairing) transition. Using the standing-wave interference pattern of several laser beams to trap (ultra-) cold atoms, “optical lattices”, artificial crystals can be created and used to model important theories of solid-state physics [18].

0.2 Opto-mechanical coupling, cavities

Note the two complementary ways in which light and matter act on each other. In optics, matter is an inert tool that is used to manipulate the direction of propagation or wavelength of photons. Passing through an optical setup, a photon encounters many atoms, each of which only influence the motion of the photon slightly. The overall effect, however, can be very large. In “atom optics”, light is a tool that is used to deflect, accelerate, decelerate, or cool material particles. The intensive laser fields contain many photons, each of interacts with the atom at most once, giving it a slight momentum kick. What happens when both aspects of the kinematics of light-matter interaction are present, if light is deflected by *and* deflects matter considerably at the same time? In this regime, commonly referred to as “opto-mechanical coupling”, light conveys a mechanical interaction between the material particles. The effects of this interaction form the subject of this Thesis.

The central idea to access the regime of “opto-mechanical coupling” for atoms is to recycle the photons, so that each photon is very likely to meet the same atom several times over. This can be achieved by enclosing the system between highly reflective mirrors that form an optical cavity. Inside such a high-Q optical cavity photons can bounce as many as 10^8 times before exiting the system. This enhances the sensitivity of cavities to the presence of atoms, and permits their use as “microscopes” [19]. On the other hand, even a single photon can trap and hold an atom between the cavity mirrors [20, 21]. If both of these effects are present, in the so-called strong-coupling regime, single atoms can be cooled efficiently with the use of cavities.[1].

The dynamics of atoms trapped in a high-Q cavity can be treated with simple and robust mathematical techniques [25]. These rest on two pillars: the quantum description of the light-induced forces for the atoms [10], and the quantum optics techniques (Master equation, Wigner function) treatment of the single quasi-resonant mode (or, in some cases, more modes) of the cavity central to cavity quantum electrodynamics [26]. This fruitful approach has given many insights into the ways cavities can be used to control atomic motion, and can be used to describe the light-mediated interaction between trapped atoms. In some schemes, this interaction has been predicted to be detrimental to cooling efficiency. In other setups, however, it has been predicted [27] and oberved [28] to lead to a “crystallization” of the trapped atoms giving a spectacular advantage for both trapping and cooling.

If the number of atoms in the cavity is so large that they distort the mode functions themselves, the above mentioned approach breaks down. Apart from being of theoretical interest, this so-called “Super-strong coupling” regime is now approached by experiments where BEC’s are loaded into

---

[1] A closely related idea is to use the cavity field to cool the motion of a vibrational mode of one of the mirrors themselves [22, 23, 24]

cavities [29]. In this case, the light-induced forces cannot be easily described in terms of exchange of excitations between some fixed cavity modes, since such fixed modes are inappropriate. Thus new ways of describing the dynamics are called for. One can turn to the description of light-induced forces on microscopic particles. Here, the influence of the particles on the light field is much more complicated than that of the essentially pointlike atoms, the Maxwell equations have to be solved including high-order multiple scattering events. Some attempts have been made to define "potentials" for the particles, but in the general case the forces have to be calculated via the Maxwell stress tensor. The phenomenon of "optical binding" of microspheres [30] has shown that optomechanical coupling can play a decisive role in the dynamics. Recently, this effect is explored in more depth in the complicated 2-dimensional motion of trapped microspheres or of rods.

0.3 Outline of the Thesis

In the first part of the Thesis we investigate atoms trapped in optical cavities with the theoretical tools reviewed in [25].

In Chapter 2 of this Thesis, published in Phys. Rev. A, **70**, 013414 (2004) [31], we discuss the motion of two atoms trapped in the same high-Q Fabry-Perot cavity. Using one of the standard approaches described in [25] for the description of the dynamics we ask what correlations build up between the motion of the atoms and how these affect the cooling efficiency. Simulating the atomic motion with classical noisy dynamics based on the Heisenberg-Langevin equations we map the parameter space to find the amount of correlations and the achievable final temperatures.

In Chapter 3 of this Thesis, published in Phys. Rev. A **72**, 053417 (2005) [32], we present a detailed study of the self-organized buildup of an optical lattice predicted in [27]. Here we use the other approach of [25] leading to classical ordinary differential equations where the field is kept explicitly as a dynamical variable. Using simple theoretical arguments we derive thresholds on the laser power necessary for the "crystallization" to occur. We then perform extensive simulations and find that the simple mean field picture needs to be modified: on laboratory timescales a hysteresis occurs, and at high intensities atoms trapped at minority sites also modify the results.

In Chapter 4, published in Europhys. Lett. **74** (2), 254-260 (2006) [33], we apply the mean-field model of light-mediated interaction to a gas of cold atoms trapped in a ring cavity and pumped directly by laser light. Instead of two distinct superradiant patterns, there is here a continuous manifold of "crystallized" phases. We map the occurence of various thermodynamic phases as functions of the control parameters.

The second part of the Thesis contains our contribution to the physics of the "super-strong coupling" regime.

In Chapter 6 we reproduce our critique of the analysis of a model system for the "super-strong coupling" regime by Meiser and Meystre, published in Phys. Rev. A **76**, 057801 (2007) [34]. We show that modeling the atomic dynamics based on optical *potentials* is flawed. We calculate the optical *forces* in this simple setup in two ways, and obtain simple formula. We show that these lead to results that contradict those based on the minimization of the optical potential in a cavity as well as in free space.

In Chapter 7 we analyze the dynamics of a one-dimensional optical lattice due to optomechanical coupling. This Chapter has been submitted to Phys. Rev. A, and the essence of the results was published in Phys. Rev. Lett. **98**, 203008 (2007) [35]. We supplement the model of [36], where the optical lattice is a stack of 2-dimensional disk-shaped clouds of atoms, by the formulas for the forces on these clouds. We detail the connection of these forces to the "dipole force" and "radiation pressure" forces which act on single atoms. We find that the "asymmetry", or the relative power of the two trap beams creating the lattice, is a control parameter having an important influence on the dynamics of the lattice. We show that the reduction of the lattice constant predicted in [36] and observed in [37] can be enhanced by orders of magnitude by switching to asymmetric pumping. Even more interestingly, the asymmetry alters the field-mediated interaction between the atom clouds. As a spectacular consequence, we show that asymmetrically pumped optical lattices become dynamically unstable above a certain size, even if viscous friction forces are applied to stabilize the lattice. We find that asymmetry alters both the equilibrium and the dynamics of blue detuned lattices in the same way as red detuned lattices.

In the third part of the Thesis we report on some of the research done during the years of the doctoral studies which does not concern the dynamics of atoms, published in Phys. Rev. Lett. **94**, 173602 (2005) [38]. We define the Entanglement Potential (EP), a quantitative measure of "nonclassicality" of the quantum state of a single mode of a bosonic field (e.g., light in a cavity). We show that it has advantegeous properties, and as an application, we use it to study how nonclassicality is lost during dissipation into vacuum.

Part I

Optomechanical coupling in a high-Q cavity

Chapter 1

Background

In this Chapter we introduce some key concepts forming the background of the work summarized in the first Part of the Thesis. Although the later Chapters discussing our results are self-contained, and start with their own introductory Sections, we here sketch the concepts behind our work, as well as provide some useful references.

1.1 Interaction of atoms with light

1.1.1 Two-level atoms

Atoms are characterized by *external* (position $\hat{\mathbf{x}}$ and momentum $\hat{\mathbf{p}}$) and *internal* (electronic, nuclear, etc.) degrees of freedom. We assume the simplest case, where the internal variables can be reduced to two stationary energy levels separated by $\hbar\omega_A$. At the beginning of the experiment the atoms are prepared in the "ground state" $|g\rangle$. Laser photons can induce real or virtual electronic transitions to an "excited state" $|e\rangle$. It is supposed that the only allowed transition from $|e\rangle$ is back to $|g\rangle$ (either stimulated by the laser photons, or via spontaneous emission). If this cannot be ensured, e.g. for molecules, which can decay into other rovibrational states, we require that there be only virtual transitions to the upper state $|e\rangle$, whose occupation should be small throughout the experiment. Furthermore, the state $|g\rangle$ is assumed to be stable: there are no allowed transitions for its spontaneous decay. Using standard notation, the fermionic deexcitation and excitation operators are

$$\hat{\sigma} = |g\rangle\langle e|\,; \quad \hat{\sigma}^\dagger = |e\rangle\langle g| \tag{1.1}$$

Since neither of the stationary states $|g\rangle$ and $|e\rangle$ have a dipole moment, the 2×2 matrix of the dipole moment operator can have no diagonal elements. With a suitable choice of 3D coordinate system, this operator is given by $\hat{\mathbf{d}} = \mathbf{d}\left(\hat{\sigma} + \hat{\sigma}^\dagger\right)$.

1.1.2 Light modes

To discuss the interaction of the atom with the light, one needs a good choice of coordinates for the (optical frequency) electromagnetic field. In other words, a *modal decomposition* of the field is necessary, so that the (orthogonal) modes best fit the problem at hand. For the modes of the field orthogonal to the mode of the laser, the "vacuum modes", the choice of modes is a matter of taste. A popular choice is the set of plane waves:

$$\hat{\mathbf{E}}(\mathbf{x}) = i \sum_j \mathcal{E}_j \hat{a}_j \varepsilon_j e^{i\mathbf{k}_j\mathbf{x}} + h.c., \tag{1.2}$$

with $\hat{a}_j$ being the annihilation operator, $\mathbf{k}_j$ the wavevector, ε_j the polarization vector, $\mathcal{E}_j$ a normalization constant of the jth mode. The sum runs over a discrete set of modes in a finite, but large quantization volume L^3. Instead of following fully the dynamics of the vacuum operators $\hat{a}_j$, within the Markov approximation, their effect on the system of interest is included by the addition of Liouvillean terms [26].

Continuous wave lasers excite specific modes, which can often be approximated by plane waves [10]:

$$\mathbf{E}_L(\mathbf{r}, t) = \boldsymbol{\varepsilon}(\mathbf{r})\mathcal{E}(\mathbf{r})\cos[\omega_L t + \Phi(\mathbf{r})], \tag{1.3}$$

with $\boldsymbol{\varepsilon}(\mathbf{r})$ the polarization, $\mathcal{E}(\mathbf{r})$ the the amplitude, and $\Phi(\mathbf{r})$ the phase of the laser field in $\mathbf{r}$. In the usual *classical* approximation, $\mathbf{E}_L$ is not treated as an operator, but as a complex number-field, corresponding to the quantum state of the mode being an eigenstate of the photon annihilation operator, a *coherent state*. The intensive laser beam is perturbed only slightly by the atoms, and thus is not a dynamical variable.

If the atoms are inside high-Q optical resonators, the choice of the *mode* for the field is fixed by the geometry of the resonator. As a simple case, in standing-wave cavities, the electric field is given by

$$\hat{\mathbf{E}}(\mathbf{r}) = \mathcal{E}\varepsilon\hat{a}f(\mathbf{x}) + h.c., \quad \text{with} \quad f(x) = \cos(\mathbf{kx}). \tag{1.4}$$

Here the explicit form of the *mode function* $f(\mathbf{x})$ is largely simplified, many details, most notably, the transverse structure (e.g., TEM00) are dropped - for a full description, consult [39]. In many cases of interest (specifically, confocal or ring cavities), it is necessary to include more cavity modes, with a straightforward generalization of the above formula. Although the mode function of the cavity is fixed, the occupation of the mode is a dynamical variable: these modes occupations are to be quantized, and the corresponding "photon" annihiliation operators $\hat{a}$ are dynamical variables. The normalization constant is $\mathcal{E} = \sqrt{\hbar\omega_c}/2\epsilon_0 0\mathcal{V}$, with ω_c denoting the resonance frequency of the cavity and $\mathcal{V}$ the effective mode volume. Thus small cavity volumes give large electric fields per photon, which results in a strong atom-photon interaction.

1.1.3 Quantum Master Equation

To derive a tractable model of the two-level atom coupled to the light field, some standard approximations are done. The size of the atom is much smaller than a wavelength, and thus the light-matter interaction can be treated within the *dipole approximation*, a term to the Hamiltonian $\hat{\mathbf{d}}\hat{\mathbf{E}}(\hat{\mathbf{x}})$, with $\hat{\mathbf{E}}$ denoting the total electric field. The only modes that play important roles in the dynamics have frequencies much closer to ω_A then to 0 or $2\omega_A$, allowing the *rotating wave approximation*: a replacement of $(\hat{\sigma} + \hat{\sigma}^\dagger)(\hat{a} + \hat{a}^\dagger)$ by the Jaynes–Cummings term $(\hat{a}^\dagger\hat{\sigma} + \hat{\sigma}^\dagger\hat{a})$, with the mode and atom indices suppressed for convenience. Finally, as mentioned above, due to the large (infinite) size of the vacuum, information entering it does not come back to the system, this is the Markov approximation. This allows the separation of the *system* from the *environment*. The former consists of the atoms (their internal and external degrees of freedom) and the occupation of the cavity mode(s), the quantum state of the system given by a density operator ρ. The latter is constituted by the vacuum modes, whose effects on the system are included via the standard Liouvillean superoperator technique. In the appropriate interaction picture called the *rotating frame*, the dynamics of the system is then given by a quantum master equation

$$\dot{\rho} = -\frac{i}{\hbar}[\hat{H}, \rho] + \mathcal{L}\rho. \tag{1.5}$$

The dipole Hamiltonian for N atoms moving in a single-mode cavity reads

$$\begin{aligned}\hat{H} = \sum_{k=1}^{N}\left[\frac{\hat{\mathbf{p}}_k^2}{2m} - \hbar\Delta_A\hat{\sigma}_k^z - i\hbar\left(\eta_t(\hat{\mathbf{x}}_k)\hat{\sigma}_k^\dagger - \eta_t^*(\hat{\mathbf{x}}_k)\hat{\sigma}_k\right)\right] \quad - \hbar\Delta_c\hat{a}^\dagger\hat{a} - i\hbar\eta\left(\hat{a} - \hat{a}^\dagger\right) \\ - i\hbar\sum_{k=1}^{N}\left(g(\hat{\mathbf{x}}_k)\hat{\sigma}_k^\dagger\hat{a} - g^*(\hat{\mathbf{x}}_k)\hat{a}^\dagger\hat{\sigma}_k\right),\end{aligned} \tag{1.6}$$

and the Liovillean superoperator is given by

$$\begin{aligned}\mathcal{L}\hat{\varrho} = \kappa\left(2\hat{a}\hat{\varrho}\hat{a}^\dagger - \hat{a}^\dagger\hat{a}\hat{\varrho} - \hat{\varrho}\hat{a}^\dagger\hat{a}\right) \\ + \gamma\sum_{k=1}^{N}\Big(2\int d^2\mathbf{u}\, N(\mathbf{u})\hat{\sigma}_k e^{-ik_A\mathbf{u}\hat{\mathbf{x}}_k}\,\hat{\varrho}e^{ik_A\mathbf{u}\hat{\mathbf{x}}_k}\hat{\sigma}_k^\dagger \quad - \hat{\sigma}_k^\dagger\hat{\sigma}_k\hat{\varrho} - \hat{\varrho}\hat{\sigma}_k^\dagger\hat{\sigma}_k\Big).\end{aligned} \tag{1.7}$$

Here, $\Delta_A = \omega - \omega_A$ and $\Delta_C = \omega - \omega_C$ are the atomic and cavity detunings, respectively. Two classical lasers are included, with effective pump strengths (Rabi frequencies) η for the laser feeding the cavity, and η_t for the one irradiating the atoms directly. The two are assumed to have the same frequency and be phase stabilized with respect to each other, this determines the phase of the complex η_t. The coupling strength (single photon Rabi frequency) of the atoms to the cavity mode is given by the position-dependent $g(\hat{\mathbf{x}}) = (\mathbf{d}\cdot\varepsilon)\mathcal{E}f(\hat{\mathbf{x}})$. It is important to note that it is only through this coupling that the Hamiltonian depends on $\hat{\mathbf{x}}$ explicitly.

1.2 Adiabatic separation of the timescales. External dynamics of the atoms

For the *internal* dynamics (assuming that the atoms are fixed or flying through the cavity without noticeable mechanical effects of light), the above Hamiltonian and Liovillean constitute one of the most studied model systems of quantum optics, the Jaynes–Cummings model. A taste of the rich physics of this model: Rabi oscillations, atom–field entanglement, atom–atom entanglement, decoherence of Schrödinger-cat states [40, 41].

Here, however, we are interested in the *external* dynamics, i.e., in the motion of the atoms, that takes place on a timescale several orders of magnitude longer than that of the internal dynamics of the atom or of the cavity field. A straightforward approach is the *adiabatic separation of the timescales*. Note that the Markov approximation already involved such a separation of timescales, we assumed that the correlation time of the vacuum field, $\tau_v \approx 1/\omega_A$ [10], is much shorter than any other characteristic timescales of the system. Now we can expect that due to the dissipative coupling to the vacuum, the internal dynamics equilibrates on a timescale of $1/\gamma$ or $1/\kappa$, whichever is larger. If the atoms are moving slowly such that the timescale of the atomic motion exceeds both of these by far, $\lambda/v \gg \gamma^{-1}, \kappa^{-1}$, then we can solve the internal dynamics (Heisenberg–Langevin equations) and obtain the values of $\hat{a}$ and $\hat{\sigma}_k$ assuming fixed atomic positions $\hat{\mathbf{x}}_k$. This amounts to slaving the internal variables to the external variables in a manner similar to the Born-Oppenheimer approximation of molecular physics. Although one might be tempted to construct an “effective Hamiltonian” for the atomic motion by substituting the $\hat{\mathbf{x}}_k$-dependent steady-state values of $\hat{a}$ and $\hat{\sigma}_k$ into Eq. (1.6), as we discuss in Chapter 6, this leads to nonphysical results. Instead, for the external variables, the operators $\hat{\mathbf{p}}_k$ and $\hat{\mathbf{x}}_k$, we take the Heisenberg equations of motion directly from the dipole Hamiltonian (1.6):

$$\frac{d}{dt}\hat{\mathbf{x}}_k = \frac{i}{\hbar}[\hat{\mathbf{x}}_k, \hat{H}] = \frac{1}{m}\hat{\mathbf{p}}_k; \tag{1.8}$$

$$\frac{d}{dt}\hat{\mathbf{p}}_k = \hat{\mathbf{F}}_k = \frac{i}{\hbar}[\hat{\mathbf{p}}_k, \hat{H}] = i\hbar\left[\nabla g(\hat{\mathbf{x}}_k)\,\hat{\sigma}_k^\dagger \hat{a} - \nabla g^*(\hat{\mathbf{x}}_k)\,\hat{a}^\dagger \hat{\sigma}_k\right] . \tag{1.9}$$

We assume that the atoms are well localized in position and momentum state, such that a *semiclassical approximation* can be applied, and we can treat the position and momentum of the atoms as classical variables. For a more detailed discussion of the precise requirements, see [10]. Thus we exclude situations such as Bose-Einstein Condensates trapped in cavities [42, 29], or atoms cooled to the ground state of harmonic potentials [43] where alternative approaches are called for (e.g., [44, 45]). Within the semiclassical limit we approximate $\hat{\mathbf{x}}_k$ by its expectation value $\mathbf{x}_k = \langle\hat{\mathbf{x}}_k\rangle$ and $\hat{\mathbf{p}}_k$ by $\mathbf{p}_k = \langle\hat{\mathbf{p}}_k\rangle$. We then wish to give the dynamical equations for $\mathbf{x}_k$ and $\mathbf{p}_k$ that follow from the Heisenberg equations of motion.

The adiabatic separation of the timescales provides us with the formulas for the expectation values of $\hat{a}$ and $\hat{\sigma}_k$, and thus, for the expectation value of $\hat{\mathbf{F}}_k$, the light-induced forces on the atoms. As with the optical forces on plastic beads, in the general case the (expectation value of the) force is a sum of two types of forces, but the usual terminology here is slightly different:

Radiation pressure arises from the absorption and subsequent spontaneous emission of photons, in the example of Eq. (1.3), it is proportional to the gradient of the phase $\Phi(\mathbf{x})$ [10].

Dipole force arises from the stimulated transfer of photons between laser modes, for Eq. (1.3), it is proportional to the gradient of the field amplitude $\mathcal{E}(\mathbf{x})$ [10].

However, taking just the expectation value of the force is not enough. Vacuum fluctuations induce noise in the polarization $\hat{\sigma}$ and the cavity field $\hat{a}$, and these fluctuations thus enter the optical force as well. On the other hand, the separation of the timescales between internal and external variables is not perfect: the state of the atom, and that of the cavity, follow the atomic position with some small, but finite, time delay. This effect, which for fast atoms in a high-Q cavity can be quite substantial, can lead to heating, but also to cooling, and is thus very important from the point of view of optical trapping.

In this Thesis, we take two different approaches to consistently derive the classical stochastic differential equations for the dynamics of the atoms. Both approaches are discussed in [25], and are introduced in the corresponding Chapters, but we here give a brief overview and compare them.

The first approach (detailed in [10] for atoms in free space) is to retain only the $\mathbf{x}_k$ and $\mathbf{p}_k$ as dynamical variables, but modify the equations of motion, adding Langevin white noise terms and viscous friction terms to the expectation value of the Heisenberg equation, $\dot{\mathbf{p}}_k = \left\langle \hat{F}_k \right\rangle$. The Langevin terms are chosen so that the the noise in the dynamics reproduces the quantum noise faithfully. The linear friction terms arise from perturbation in the atomic velocities $\mathbf{v}_k$, detailed in [25]. Briefly, we write $\langle\hat{\sigma}_k\rangle = s_k^{(0)} + \sum_l \mathbf{v}_l \mathbf{s}_{lm}^{(1)}$, and $\langle\hat{a}\rangle = a_k^{(0)} + \sum_l \mathbf{v}_l \mathbf{a}_{lm}^{(1)}$, and in the semiclassical approximation of the Heisenberg – Langevin equations for the internal variables, we replace d/dt by $\partial/\partial t + \sum_k \mathbf{v}_k \nabla_k$. Then we can solve for the steady state of the semiclassical approximation of the Heisenberg–Langevin equations to obtain the coefficients in the expansion of the force: $\left\langle \hat{\mathbf{F}}_k \right\rangle = \mathbf{f}_k^{(0)} + \sum_l \mathbf{f}_{lm}^{(1)} \mathbf{v}_l$.

The advantage of this approach is that it gives *explicit* expressions for the heating and cooling arising from the corrections to adiabaticity, allowing predictions to be made about expected final temperatures without actually performing the simulations. Its disadvantage is that because of its perturbative nature, it cannot be used to treat fast atoms in very high-Q cavities, where the equilibration time of the field is long.

An alternative approach [25] is to do away with the adiabatic approximation for the cavity field altogether. We treat the expectation value of the cavity field, $\alpha = \langle \hat{a} \rangle$, on the same footing as the classical variables $\mathbf{x}_k$ and $\mathbf{p}_k$. For simplicity, now the atomic polarizability is "slaved" to the atomic position and the cavity field, and this is done on the operator level, before making the semiclassical approximation, so that the noise is treated consistently. As above, Langevin terms are to be added to the equations of motion, but now their second-order correlations are derived in a different way. As in [46], the quantum master equation is used to derive a partial differential equation for the Wigner function representing the atomic motion and the state of the cavity light field. This partial differential equation is truncated to second-order derivatives giving a Fokker–Planck equation, which can then be exactly modeled by the ordinary stochastic differential equations for the dynamical variables $\alpha, \mathbf{x}_k, \mathbf{p}_k$.

This second approach has the advantage of reproducing the cavity–induced friction correctly even in the limit of fast atoms and very high-Q cavities. It can be used to show explicitly the time-lag of the cavity field responsible for the cooling. However, it does not take into account Doppler cooling, and it can only be used if the cavity field has a large number of photons.

Chapter 2

Publication: Correlated motion of two atoms trapped in a single-mode cavity field

2.1 Introduction

It is a well established fact, both theoretically and experimentally, that light forces on atoms are substantially modified within resonant optical cavities [25, 47, 48, 49, 50, 51, 52, 53]. Possible experimental realizations range from single atoms or ions [54, 55] in microscopic super cavities to several thousand [56, 57] or up to a million atoms [50, 58] in a high Q ring cavity. Applications of these systems include possible implementations of quantum information processing setups [59, 60], and controlled nonclassical light sources [61, 62] as well as new possibilities for trapping and cooling of atoms and molecules. The basic physical mechanism in these setups can be traced back to the backaction of the atoms on the field. They act as a moving refractive index and absorber, modifying the intensity and phase of the intracavity field, which in turn governs their motion. This coupled dynamics is at the heart of cavity enhanced trapping and cooling.

It is clear that if a single atom is able to change the field, it will influence other atoms in the same field irrespective of their distance. This introduces long range atom-atom interactions, which are widely tailorable by suitable choices of cavity geometries and operating conditions. On one hand these interactions are useful and can be used to implement bipartite quantum gates [59]. On the other hand they play a decisive role in the scaling properties of cavity enhanced cooling [63, 64]. For perfectly correlated atoms, the change of refractive index induced by one atom can be compensated by a second atom, so that the effective atom-field back reaction can be strongly reduced. For several atoms in a ring cavity this effect only allows a weak damping of relative motion, while the center of mass motion is strongly damped [65]. This model is closely related to the so-called CARL laser, where the kinetic energy of an atomic beam leads to gain into the counterpropagating mode of a single side pumped ring resonator [66]. New effects were also found in the study of the coupling of two Bose-condensates in a cavity [67].

Several limiting cases for N atoms commonly interacting with a cavity mode have already been studied. For the case of N strongly trapped atoms in a standing wave cavity mode, it is possible to derive a set of coupled equations for the total kinetic and potential energy as well as the field amplitude [68], which exhibit collective, damped oscillations ending in highly correlated steady states. This approach, however, does not give much insight into the details of the individual dynamics and correlations. In the opposite limit of N untrapped atoms moving in the cavity field, numerical simulations show little influence of atom-atom correlations and cooling proceeds independent of the atom number [63] for proper rescaling of the cavity parameters.

Recently an approach for several atoms in a single mode cavity has been developed, which concentrates on the effect of the $N-1$ other particles on the cooling properties of a single one [64]. This, in principle, makes it possible to study the combined optical potential and friction forces. It has been recently proposed theoretically [27] and confirmed experimentally [28], that if the atoms are pumped directly from the side (as opposed to pumping the cavity), the buildup of spatial correlations within a cloud of trapped atoms can lead to superradiant light scattering and enhanced cooling behavior. The theoretical results in this case are based on numerical simulations of the semiclassical equations of motion for a large number $N \gg 1$ of particles [27]. This clearly demonstrates collective effects, but does not give much quantitative insight in the buildup and role of atom-atom correlations.

The central goal of the present work is to study the basic physical mechanisms responsible for the motional correlations and to develop quantitative measures of the established steady state correlation. For this we restrict ourselves to the simplest nontrivial example, namely two atoms strongly coupled to a single standing wave field of a cavity. The energy loss is compensated by cavity pumping, and large detuning from the atomic transition is taken to ensure low atomic saturation. Moreover, the motion of the atoms is only followed along the cavity axis. As we will see, this contains most of the essential physics but still allows us to derive analytical expressions for many relevant quantities. Most of the analytical results are valid for the more general N-atom case.

The article is organized as follows: after presenting our model and the approximations used in section II, we analytically discuss the central physical mechanisms present in section III. In section IV we quantify the results using numerical simulations, which are then analyzed in more detail in section V.

2.2 The model

Let us start by outlining the system which is shown in Fig. 2.1. We consider $N = 2$ two-level atoms with transition frequency ω_A strongly coupled to a single mode of a high-finesse cavity with frequency ω_C. The system is driven by a coherent laser field of frequency ω and amplitude η injected into the cavity through one of the mirrors. The model and its theoretical treatment follow closely Ref. [25]. Coupling to the environment introduces a damping via two channels. First, the atoms spontaneously emit with a rate of 2γ into the vacuum outside the cavity. Second, the cavity photons decay with rate $2\,\kappa$ via the output coupler mirror of the cavity. The atoms can move freely in the cavity, however, for the sake of simplicity, their motion is restricted to the cavity axis (dashed line in Fig. 2.1).

Applying the standard Born-Markov approximation the dynamics are governed by a quantum master equation,

$$\dot{\rho} = -\frac{i}{\hbar}[\hat{H}, \rho] + \mathcal{L}\rho. \tag{2.1}$$

Using rotating-wave and dipole approximations the Hamiltonian and the Liouville operators

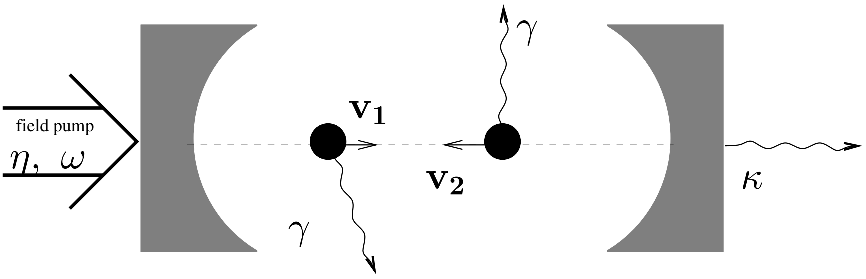

Figure 2.1: *The setup.* The motion of two two-level atoms in a far-detuned, high-Q optical cavity is studied. The cavity is pumped by a strong laser beam, almost on resonance with the cavity mode. Atomic motion is discussed along the cavity axis only.

in an interaction picture read [25]:

$$\begin{aligned}\hat{H} &= \sum_{k=1}^{N}\left[\frac{\hat{\mathbf{p}}_k^2}{2m} - \hbar\Delta_A\hat{\sigma}_k^z\right] - \hbar\Delta_c\hat{a}^\dagger\hat{a} - i\hbar\eta\left(\hat{a}-\hat{a}^\dagger\right)\\ &\quad - i\hbar\sum_{k=1}^{N}\left(g(\hat{\mathbf{x}}_k)\hat{\sigma}_k^\dagger\hat{a} - g^*(\hat{\mathbf{x}}_k)\hat{a}^\dagger\hat{\sigma}_k\right) \end{aligned}\tag{2.2a}$$

$$\begin{aligned}\mathcal{L}\hat{\varrho} &= \kappa\left(2\hat{a}\hat{\varrho}\hat{a}^\dagger - \hat{a}^\dagger\hat{a}\hat{\varrho} - \hat{\varrho}\hat{a}^\dagger\hat{a}\right)\\ &\quad + \gamma\sum_{k=1}^{N}\left(2\int d^2\mathbf{u}\; N(\mathbf{u})\hat{\sigma}_k e^{-ik_A\mathbf{u}\hat{\mathbf{x}}_k}\hat{\varrho}e^{ik_A\mathbf{u}\hat{\mathbf{x}}_k}\hat{\sigma}_k^\dagger - \hat{\sigma}_k^\dagger\hat{\sigma}_k\hat{\varrho} - \hat{\varrho}\hat{\sigma}_k^\dagger\hat{\sigma}_k\right). \end{aligned}\tag{2.2b}$$

The atomic and cavity field detunings are defined as $\Delta_A = \omega - \omega_A$ and $\Delta_C = \omega - \omega_C$, respectively. The annihilation and creation operators of the cavity field are $\hat{a}$ and $\hat{a}^\dagger$, while $\hat{\sigma}_k$ and $\hat{\sigma}_k^\dagger$ are the lowering and raising operators of the k-th atom. The Hamiltonian consists of the motional and internal energy of the atoms, the self-energy of the cavity field, the classical (laser) pump, and the Jaynes–Cummings-type interaction between the atoms and the field. The position dependence of the coupling constant is due to the spatial structure of the field mode: $g(\mathbf{x}_k) = g_0 f(\mathbf{x}_k)$, where in our standing-wave cavity $f(\mathbf{x}_k) = \cos(k_C x_k)$, with $k_C = 2\pi/\lambda$ being the cavity wavenumber. The Liouvillean operator includes the effect of cavity losses and of the spontaneous emissions on the combined atom-cavity field density operator $\hat{\varrho}$. This latter is given by the last term, where the integral goes over the directions of photons spontaneously emitted by the atomic dipole, having expected wavenumber $k_A = \omega_A/c$ and angular distribution $N(\mathbf{u})$.

We consider cold atoms but with a temperature well above the recoil limit $k_B T_{rec} = \hbar k_A^2/(2M)$, where M is the mass of one atom. In this limit the atomic coherence length is smaller than the optical wavelength and the position and momentum of the atoms can be replaced by their expectation values and treated as classical variables. We still keep the quantum nature of the internal variables $\hat{a}$ and $\hat{\sigma}_k$. Moreover, if the atoms move much less than a wavelength during the equilibration time of the internal variables

$$v \ll \lambda\kappa, \lambda\gamma, \tag{2.3}$$

we can adiabatically separate the ”fast” internal from the ”slow” external dynamics as in standard laser cooling models [69].

2.2.1 The internal dynamics

For given positions of the atoms $\mathbf{x}_k$ the internal atomic dynamics can be rewritten in the form of quantum Langevin equations. For low saturation, i.e. when $\langle\hat{\sigma}^\dagger\hat{\sigma}\rangle \ll 1$, we can approximate the operator $\hat{\sigma}_z$ by $-1/2$ (this is called bosonization of the atomic operators). The resulting Heisenberg–Langevin equations then reduce to the following set of coupled linear differential equations:

$$\frac{\mathrm{d}}{\mathrm{d}t}\hat{a} = (i\Delta_C - \kappa)a + \sum_k g^*(\mathbf{x}_k)\hat{\sigma}_k + \eta + \hat{\xi} \tag{2.4a}$$

$$\frac{\mathrm{d}}{\mathrm{d}t}\hat{\sigma}_k = (i\Delta_A - \gamma)\hat{\sigma}_k - g(\mathbf{x}_k)\hat{a} + \hat{\zeta}_k. \tag{2.4b}$$

The noise operators $\hat{\xi}$ and $\hat{\zeta}_k$ appear as a result of the coupling to the external vacuum through the cavity mirrors and through spontaneous emission. They contain the annihilation operators of the external vacuum modes, and therefore give 0 when acting on the environment's state. Their second-order correlation functions are as follows:

$$\langle\hat{\xi}(t_1)\hat{\xi}^+(t_2)\rangle = 2\kappa\,\delta(t_1 - t_2), \tag{2.5a}$$

$$\langle\hat{\zeta}_k(t_1)\hat{\zeta}_m^+(t_2)\rangle = 2\gamma\,\delta_{km}\delta(t_1 - t_2), \tag{2.5b}$$

while all other correlations vanish.

The steady state expectation values of the internal variables $\hat{a}$ and $\hat{\sigma}_k$ obtained from the Heisenberg–Langevin equations (2.4) then read:

$$\langle\hat{a}\rangle = \eta\frac{\gamma - i\Delta_A}{\mathcal{D}'} \tag{2.6a}$$

$$\langle\hat{\sigma}_l\rangle = -\eta\frac{g(\mathbf{x}_l)}{\mathcal{D}'}. \tag{2.6b}$$

Here $\mathcal{D}'$ is the reduced determinant of the Bloch matrix,

$$\mathcal{D}' = (i\Delta_C - \kappa)(i\Delta_A - \gamma) + \sum_l g(\mathbf{x}_l)^2. \tag{2.7}$$

Since the factor $1/\mathcal{D}'$ appears in both expectation values and in later formulae as well, it is worthwhile to rewrite it to reveal its resonance structure with respect to the cavity detuning:

$$\frac{1}{\mathcal{D}'} = \frac{1}{(i\Delta_A - \gamma)}\,\frac{1}{i(\Delta_C - U) - (\kappa + \Gamma)}, \tag{2.8}$$

$$\text{where} \qquad U = \frac{\Delta_A\sum_l g^2(\mathbf{x}_l)}{\Delta_A^2 + \gamma^2} = U_0\sum_l f^2(\mathbf{x}_l), \tag{2.9}$$

$$\text{and} \qquad \Gamma = \frac{\gamma\sum_l g^2(\mathbf{x}_l)}{\Delta_A^2 + \gamma^2} = \Gamma_0\sum_l f^2(\mathbf{x}_l), \tag{2.10}$$

and we used $g(x) = g_0 f(x)$. It is clearly seen that each atom broadens the resonance at most by Γ_0 and displaces it by U_0.

2.2.2 The external dynamics

The motion of the atoms is governed by the force operator,

$$\hat{\mathbf{F}}_k = \frac{i}{\hbar}[\hat{p}, \hat{H}] = i\hbar\left[\nabla g(\mathbf{x}_k)\,\hat{\sigma}_k^\dagger\hat{a} - \nabla g^*(\mathbf{x}_k)\,\hat{a}^\dagger\hat{\sigma}_k\right]\;. \tag{2.11}$$

Since $\hat{\mathbf{F}}_k$ is normally ordered, its expectation value is easily obtained upon insertion of the stationary solution (2.6) of the internal variables. For a moving atom this expression is only approximately valid: there will be a time lag in the internal dynamics with respect to the atom's current position, and hence we will include corrections to $\hat{\mathbf{F}}_k$ to first order in the atomic velocities.

The slow evolution of the centers of mass of the atoms, smoothed out on the timescale $\tau \approx \max\{1/\kappa, 1/\gamma\}$ is described by the coupled Langevin equations:

$$\dot{\mathbf{x}}_k = \mathbf{p}_k/M, \tag{2.12a}$$

$$\dot{\mathbf{p}}_k = \mathbf{f}_k + \sum_{m=1}^{N} \boldsymbol{\beta}_{km}\mathbf{p}_m/M + \Xi_k \, . \tag{2.12b}$$

In these equations $\mathbf{f}_k = \left\langle \hat{\mathbf{F}}_k \right\rangle$ are the vectors giving the steady state $v = 0$ contribution of the force, while $\boldsymbol{\beta}_{km}$ are the tensors describing the first order corrections to the force acting on atom k. Ξ_k denotes the Langevin noise forces due to photon recoil. They correspond to random kicks along the cavity axis with zero average and second moments given by $\langle \Xi_k \Xi_m \rangle = \mathcal{D}_{km}$. Note that the matrix $\mathcal{D}_{km}$, representing the strength of the Langevin noise, depends on the time-varying atomic positions. It represents the quantum fluctuations of the force due to the fact $\left\langle \hat{F}_k \circ \hat{F}_m \right\rangle \neq \left\langle \hat{F}_k \right\rangle \circ \left\langle \hat{F}_m \right\rangle$. It is by the addition of the noise terms Ξ_k that we tailor our classical force to give the same second-order expectation values as its quantum counterpart[25].

2.3 Interaction channels

The Hamiltonian (2.2) contains no direct coupling between the two atoms: these only arise indirectly due to coupling to the same field mode. Interestingly the atom-atom interaction appears in all the three types of forces present in classical equations of motion (2.12). First, the steady state force $\mathbf{f}_k$ depends on the positions of both atoms via the steady state intensity. Second, not only does the friction coefficient on one atom depend on the position of the other, but the friction matrix has off-diagonal terms as well. This means that apart from ordinary viscous friction ($\dot{\mathbf{p}}_k \propto \mathbf{v}_k$) a strange phenomenon, which we call cross-friction ($\dot{\mathbf{p}}_k \propto \mathbf{v}_l$, for $l \neq k$) is also present. Here the velocity of one atom influences the friction experienced by the other atom. Third, the Langevin noise term on one atom has an expected magnitude influenced by the position of the other, and the noise terms Ξ_k are directly correlated as well. Hence we get joint "kicks" on both atoms leading to correlated motion. In the following we will analyze these interaction channels in more detail.

2.3.1 Steady state force f

Formally the expectation value $\mathbf{f}_k$ of the force operator looks very similar to the case of free-space Doppler cooling:

$$\mathbf{f}_k = -\hbar \frac{\Delta_A}{\Delta_A^2 + \gamma^2} \left\langle \hat{a}^\dagger \hat{a} \right\rangle \nabla_k g^2(\mathbf{x}_k). \tag{2.13}$$

However it additionally depends on the positions of the other atoms via the cavity field intensity. This dipole force is conservative and can be derived from a potential. The potential looks more complicated than in free space as it contains the dynamical nature of the cavity field, but still can be given in closed form [64] :

$$V = \frac{\hbar \Delta_A |\eta|^2}{\Delta_A \kappa + \Delta_C \gamma} \mathrm{atan} \frac{\gamma\kappa - \Delta_A \Delta_C + \sum_l g^2(x_l)}{\Delta_A \kappa + \Delta_C \gamma}. \tag{2.14}$$

To show the effects of dynamic field adjustment, we plot this potential for two typical cases in Fig. 2.2. For the experimental parameters used in an experiment at MPQ in Garching [70] (Garching parameters), $\kappa = \gamma/2$, $g_0 = 5\gamma$, and for a detuning $\Delta_A = -50\gamma$ (upper graph) the effective interaction between the atoms is relatively weak and the potential resembles the familiar "egg-carton" surface proportional to $\sin^2(k_C x_1) + \sin^2(k_C x_2)$. For a somewhat stronger atom-field coupling $g_0 = 20\gamma$ (lower graph in Fig. 2.2) the atomic interaction is quite obvious and the shape of the potential of the second atom strongly depends on the position of the first atom and vice versa. Basically in this second case either both atoms are trapped, or both are free.

The peculiar g_0-dependence of the interaction and the trapping effects can be understood physically by looking at formula (2.13). The atoms see each other through the cavity field $\langle \hat{a}^\dagger \hat{a} \rangle$. As we saw in formulae (2.8,2.9,2.10), the field is in resonance when $U(\mathbf{x}_1, \mathbf{x}_2)$ is approximately $\Delta_C \pm (\Gamma + \kappa)$. Each atom can shift U in this far-detuned case by approximately $U_0 \approx g_0^2/\Delta_A$, whereas the cavity linewidth is approximately $\kappa + \gamma g_0^2/\Delta_A^2$. Using the MPQ parameters $U_0 < \kappa$, and therefore the back-action of the atoms on the cavity field is weak. In the large-g_0 case, $U_0 > \kappa$, but $\Gamma_0 < \kappa$, meaning that the atoms can shift the cavity resonance significantly more than a linewidth. Hence if one of the atoms leaves its trap it will shift the cavity out of resonance and cause the other atom to be released as well. Moreover, the amplitude of the force is proportional to the cavity field, which in the large-g_0 case decreases faster with the distance from the trapping point. This implies that less work needs to be done to free an atom: the potential is smaller, despite the same maximum light shift.

Let us now analyze the interaction in a more quantitative way. We start from the limiting case of neglecting the atomic back-action on the field (i.e. we assume a constant field intensity). This corresponds to the force (2.13)

$$\mathbf{f}_l \approx \frac{\hbar |\eta|^2}{2\Delta_A \kappa^2} \nabla_l g^2(\mathbf{x}_l) \tag{2.15}$$

one obtains in the limit of very large atom-field detuning. We can now find corrections from the cavity-mediated interaction to this force by expanding the potential (2.14) in a power series. Setting the driving field to resonance, $\Delta_C = U_0 - \kappa$, the potential Eq. (2.14) to second order in γ/Δ_A reads

$$\begin{aligned} V \approx \frac{\hbar |\eta|^2}{\kappa} \Bigg[& \frac{\pi}{4} - \left(\left(1 + \frac{\pi}{4}\right) + \frac{g_0^2}{2\kappa\gamma} \sum_{l=1}^{N} f^2(x_l) \right) \frac{\gamma}{\Delta_A} \\ & + \left\{ \left(1 + \frac{\pi}{4}\right) - \left(1 + \frac{\pi}{2}\right) N + \left(\frac{g_0^2}{2\kappa\gamma}\right)^2 \left(\sum_{l=1}^{N} f^2(x_l) \right)^2 \right\} \left(\frac{\gamma}{\Delta_A}\right)^2 \Bigg] . \end{aligned} \tag{2.16}$$

To first order in the small parameter we have a sum of single-atom potentials, giving the "egg-carton" shape. The corrections to this are given by terms of higher order in our expansion parameter, of which we give the first nontrivial term here. Note that since it is not simply the distance of the atoms upon which the potential depends, the interatomic force between them – as can be read out from the above formula – is not a "force" in the sense of Newton's third law.

2.3.2 Forces linear in velocity: friction and cross-friction

To lowest order in the adiabatic separation of the internal and external dynamics we used the steady state values of the internal variables for fixed positions of the atoms to calculate the above potentials. As a next step we can include corrections for $\hat{a}$ and the $\hat{\sigma}_k$ linear in the velocity $\mathbf{v}_m$ of each atom, which should be valid for low velocities. As described in [25] this leads to a friction matrix $\boldsymbol{\beta}_{km}$ as first order correction to $\mathbf{f}_k$.

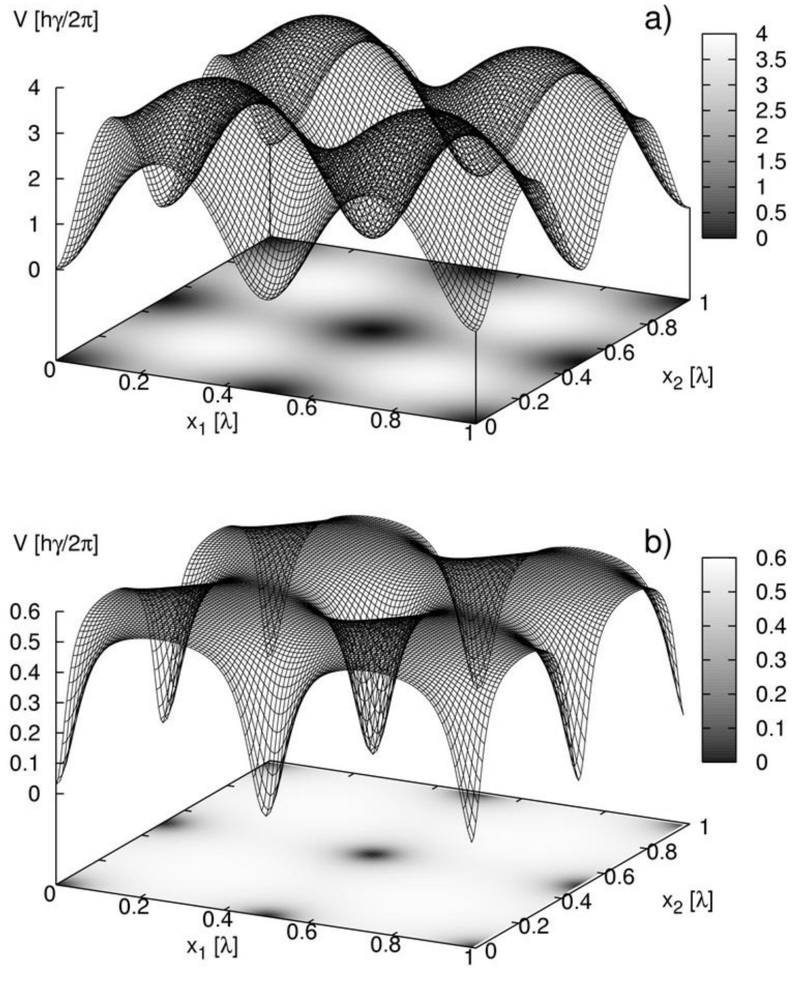

Figure 2.2: *Potential as a function of atomic positions* The potential (2.14) is plotted as a function of positions of the two atoms. In a) the Garching parameters ($\kappa = \gamma/2$,$g_0 = 5\gamma$) are used, in b) g_0 was increased fourfold. In the first case, the potential is well approximated by a sum of two single-particle potentials. In the second case, it is seen that either both atoms are trapped or both are free. The trap is deeper for smaller couplings.

We obtain the following explicit formula for the friction matrix,

$$\boldsymbol{\beta}_{km} = 2\hbar\nabla_k g(\mathbf{x}_k) \circ \nabla_m g(\mathbf{x}_m) \frac{\eta^2}{|\mathcal{D}'|^2}\gamma\frac{2\Delta_A}{\Delta_A^2+\gamma^2}\delta_{km} + \hbar\nabla_k g^2(\mathbf{x}_k) \circ \nabla_m g^2(\mathbf{x}_m)\frac{\eta^2}{2\,|\mathcal{D}'|^2}\cdot \\ \mathrm{Im}\left\{\frac{1}{\mathcal{D}'^2}\cdot\left(2(1+\chi)\left((i\Delta_A-\gamma)^2-\sum_l g(\mathbf{x}_l)^2\right)+(1+3\chi)\mathcal{D}'\right)\right\} \tag{2.17}$$

where $\chi = (i\Delta_A + \gamma)/(i\Delta_A - \gamma)$ is a complex factor of unit modulus, which for large atomic detuning, $\Delta_A \gg \gamma$, becomes approximately $\chi \approx 1$. This formula differs somewhat from that obtained by Fischer et al. [64] by a slightly different approach. The most important difference is that we find a matrix *symmetric* in the indices km. This is important because it is these off-diagonal terms that couple the velocities of the atoms, and have a decisive influence on the buildup of correlated motion. We defer detailed discussion of the formula (2.17) to Section 2.5.

2.3.3 Random forces due to quantum noise

Spontaneous emission and cavity decay introduce quantum noise into the atomic motion. These heat up the system and generally tend to decrease motional correlations of the atoms. Following the line of reasoning briefly mentioned at the end of section 2.2 and discussed in more detail in [25], we can calculate the influence of the noise operators $\hat{\xi}$ and $\hat{\zeta}$ of eq. (2.4) on the dynamics. For N atoms we arrive at the following simple formula:

$$\mathcal{D}_{km} = 2\hbar^2\nabla_k g(\mathbf{x}_k) \circ \nabla_m g(\mathbf{x}_m)\frac{\eta^2}{|\mathcal{D}'|^2}\gamma\delta_{km} \\ + 2\hbar^2\nabla_k g(\mathbf{x}_k)^2 \circ \nabla_m g(\mathbf{x}_m)^2\frac{\eta^2}{|\mathcal{D}'|^2}\Delta_A\frac{\kappa\Delta_A+\gamma\Delta_C}{|\mathcal{D}'|^2}. \tag{2.18}$$

This is a simple extension of the corresponding formula for one atom given in [25]. Let us remark here, that the diagonal part of this diffusion matrix $\mathcal{D}_{km}$ has been also found by Fischer et al. [64]. Surprisingly one also obtains off-diagonal terms, which have not been considered before. These terms lead to correlated kicks on the atoms, which can .add to the atom-atom correlations, rather than destroying them.

Spontaneous emission adds recoil noise, which gives an extra term to the noise correlation matrix of the form:

$$\mathcal{D}_{km}^{\mathrm{sp}} = \delta_{km}2\hbar^2k_A^2\overline{u^2}\frac{\eta^2 g(\mathbf{x})^2}{|\mathcal{D}'|^2}\gamma. \tag{2.19}$$

Here $k_A = \omega_A/c$ is the expected wavenumber of the emitted photons and $\overline{u^2}$ is the correction factor coming from the spatial distribution of the photons, in our case $\overline{u^2} = 2/5$. As expected, spontaneous emission, being a single-atom process, induces no correlations between the atoms.

2.4 Numerical simulations of the correlated atomic motion

Having discussed the qualitative nature of the combined atom field dynamics, we now turn to numerical simulations for some quantitative answers. We numerically integrate the Langevin equations (2.12), varying the ratio of the cavity loss rate to the linewidth of the atom κ/γ as well as the relative coupling strength g_0/γ. Note that the relative magnitude of radiation pressure and dipole force can be changed by varying the detuning between pump frequency and the atomic resonance. As we are interested in cooling and trapping the atoms we fix the cavity frequency at

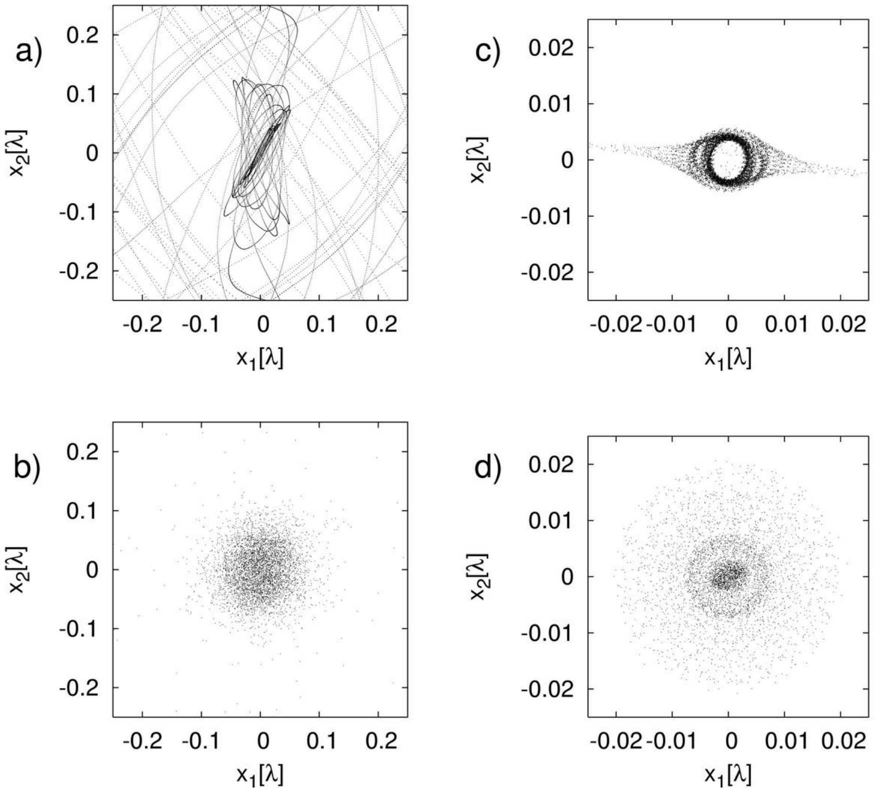

Figure 2.3: *Typical trajectories in coordinate space.* In the left column, in a) and b), the parameters of the Garching group are used, in the right column, in c) and d), we considered a better resonator ($\kappa = 0.1\gamma, g_0 = 10\gamma$) and larger detuning ($\Delta_A = -10000\gamma$). In both cases the first 50μs, in a) and c), and the first 3ms, in b) and d), are shown. The coordinate is the distance from the nearest trappping point.

$\Delta_C = NU_0 - \kappa$ to ensure efficient cooling [71, 25]. The pump power is always chosen to keep the atomic saturation low and approximately at ($\langle \hat{\sigma}_k^+ \hat{\sigma}_k \rangle < 0.1$) at all times.

Typical trajectories of atom pairs are shown in Figure 2.3. The atomic positions $\big(x_1(t_n), x_2(t_n)\big)$ are plotted at regular time intervals t_n. For better visibility the coordinate is always measured from the nearest trapping point. In the left column the detuning was chosen ($\Delta_A = -50\gamma$), with the cavity parameters of the MPQ group at Garching [70] ($\kappa = \gamma/2$, $g_0 = 5\gamma$). The first 50μs are displayed in the figure on the top, and the first 3ms in the one on the bottom. Both atoms localize during the first 50μs to within 1/4 of a wavelength around respective trapping centers, a sign of cooling and trapping by the cavity. In the right column, the detuning is chosen much larger ($\Delta_A = -10^4\gamma$) with stronger atom-field coupling ($\kappa = \gamma/10$, $g_0 = 10\gamma$). In this case the relative importance of spontaneous emission is strongly reduced. The cooling in the cavity is faster and both atoms reach a steady state rapidly.

The appearance of a circular structure is the striking feature of the right column. This indicates that the motion of the atoms is correlated. Both atoms move sinusoidally about their respective trapping points, with some noise but in such a way that the relative phase of the two oscillations is likely to be $+90°$ or $-90°$.

To quantify the correlation between the atomic oscillators we define their oscillator phases.

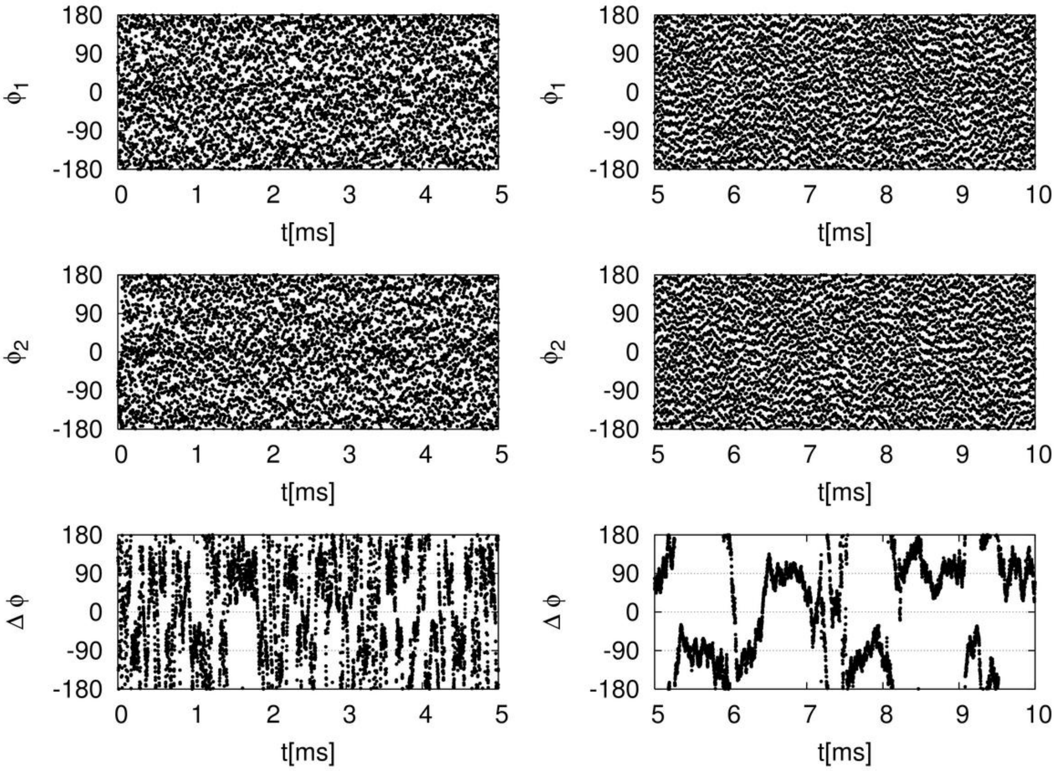

Figure 2.4: *The phases of the atomic oscillations and the relative phase.* The time evolution of the oscillator phases of the first (upper row) and second (middle row) atoms is shown, with the phase difference (bottom row). On the left the parameter set of the Garching experiments is used, on the right a better cavity is taken with larger atomic detuning, as in the text. The phases of the atoms evolve too fast on this timescale, only noise is seen. The phase difference is slower, with the "improved" parameter set it appears to stabilize at $+90°$ and $-90°$.

This is computed in the simulation using the trap frequency, which is:

$$\omega_{\text{trap}} = \sqrt{2\hbar \left|\Delta_A\right| \left\langle \hat{\sigma}^\dagger \hat{\sigma} \right\rangle k_C^2 / M}, \tag{2.20}$$

if both atoms are well trapped. Here k_C is the resonator mode wavenumber, and $\left\langle \hat{\sigma}^\dagger \hat{\sigma} \right\rangle$ is the saturation of either atom at the trapping point. This formula can be derived by expanding the potential (2.14), and substituting our particular choice of η and Δ_C.

The measured time evolution of the oscillator phases for the MPQ parameters (left column) and the "improved" parameters (right column) are shown in Fig. 2.4. For each parameter set, representative runs shown in Fig. 2.3 are used, and the oscillator phases of atom 1 (upper row), atom 2 (middle row) and the phase difference (lower row) are displayed. The rapid oscillation of the atoms (the period is 2.9 μs for the Garching parameters and 0.17 μs for the idealized ones) means that the time evolution of the phases is too fast to be followed on the timescale shown, in the upper and middle rows only "noise" is seen. The phase difference, however, evolves more slowly. This effect is more pronounced for the second parameter set, where the dipole force dominates. Moreover, in this second case, the phase difference clearly stabilizes around $+90°$ or $-90°$, with random jumps in between, as expected from the results shown in Fig. 2.3.

What is left is to define a single number that quantifies the strength of the time averaged

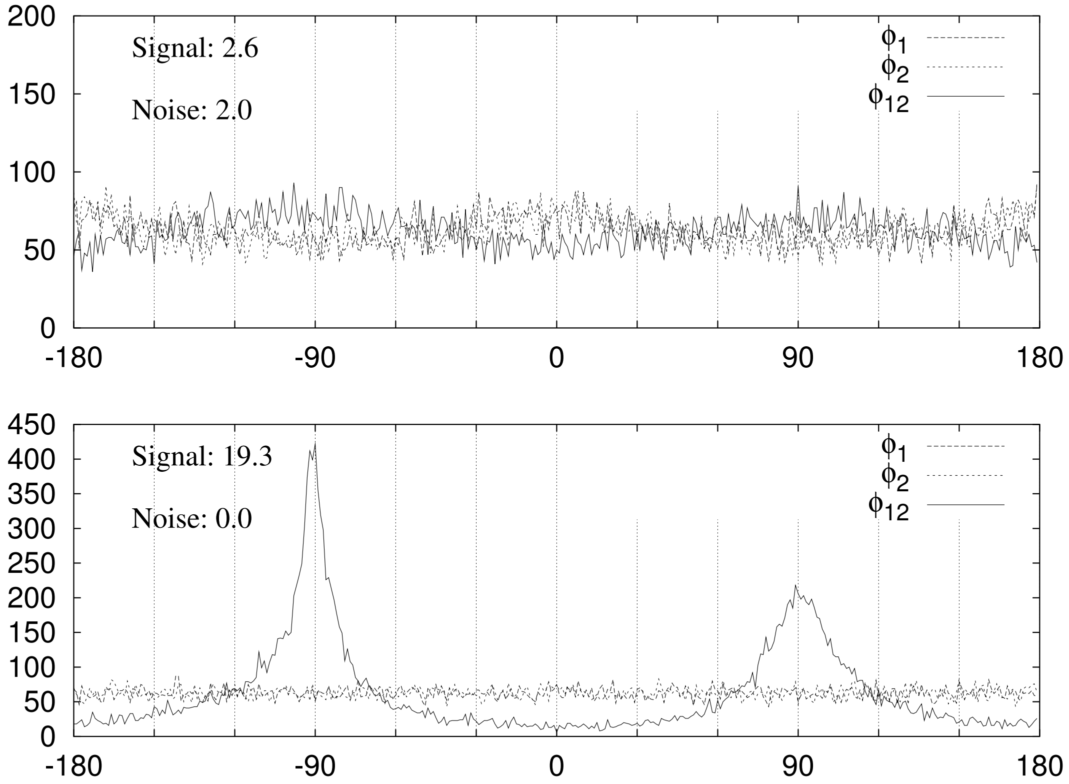

Figure 2.5: *The distribution of the phases (Φ_1, Φ_2) and the relative phase (phases (Φ_{12}).* For the Garching parameter set (upper figure) the distributions are flat. Slight peaks in Φ_1 and Φ_2 at 0° and $\pm 180^\circ$ signal fast and free atoms. With the improved parameters (lower figure) the trapping is better. Strong peaks at $\pm 90^\circ$ in Φ_{12} indicate correlation of atomic motion. The strength of these peaks is quantified by their width, both for the phase (Noise) and the phase difference (Signal).

correlations. For this we sample the distributions of the oscillation phases and the phase difference over time to create the histograms shown in Fig. 2.5. As we expect, the distribution of the phases is relatively flat for both parameters sets. However, there is a significant difference in the distribution of the relative phase: we find very pronounced peaks around $+90^\circ$ and -90° for the second parameter set.

The asymmetry in these peaks is a numerical artefact due to the finite sampling time. It is strongly diminished if we average over several different initial conditions. A parameter that measures the magnitude of the correlation is the width W of these peaks, defined through $W^2 = \overline{(|\Delta\phi| - 90^\circ)^2}$, where the overbar denotes averaging over time and over several trajectories with different initial conditions. Subtracting this width from the width of the flat distribution we get the signal strength $S = 51.96^\circ - W$, which can be obtained directly during the simulation.

Let us point out here, that this measure S of motional correlation is useful only if the atoms are well trapped. In fact, fast atoms freely moving along the lattice generate peaks in the single atom phase distributions of ϕ_1 or ϕ_2 around 0° or 180°. We therefore monitor the single atom distributions simultaneously and measure the widths of the peaks around 0° and 180° in the same way as we did for the signal S. If the "Noise strength" is too large, ($> 10^\circ$, an arbitrary value), we declare our correlation measure unusable.

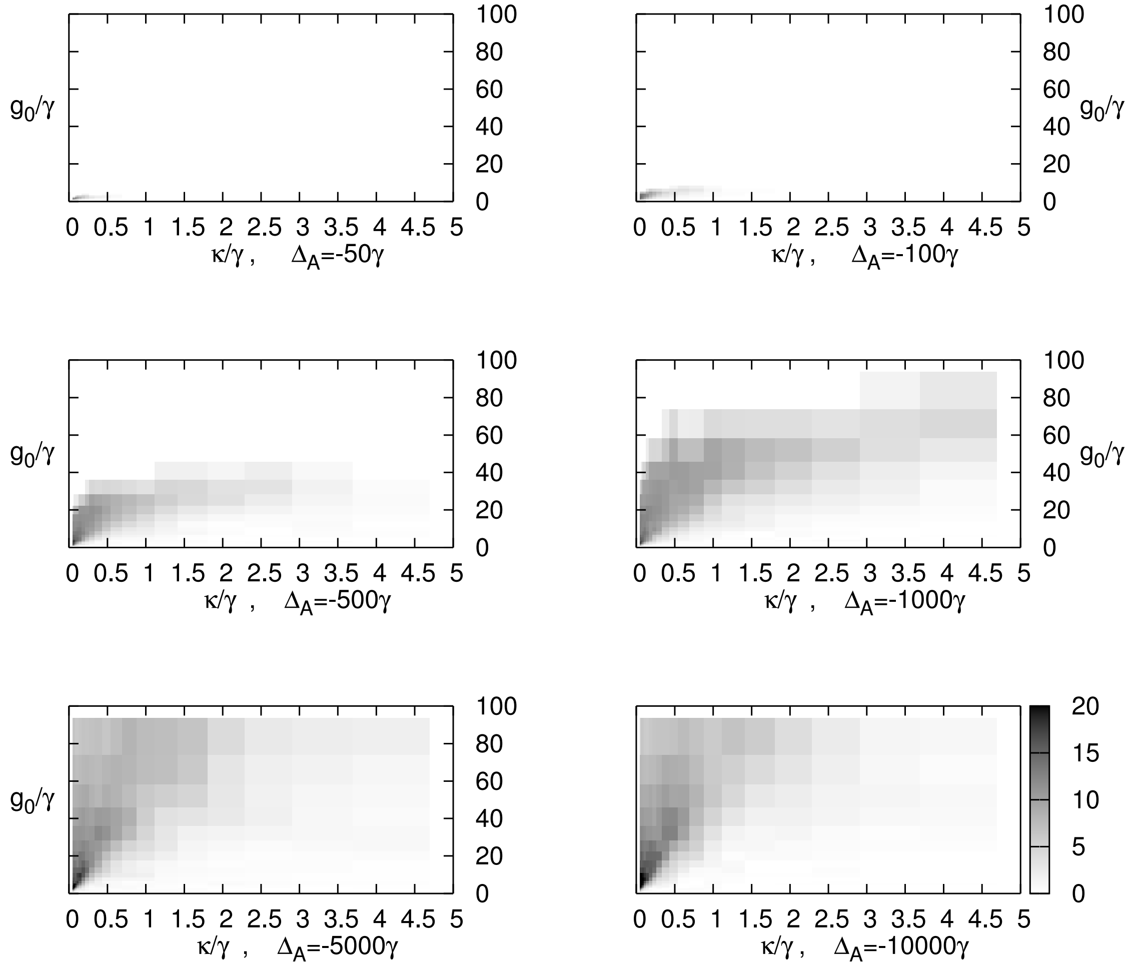

Figure 2.6: *Correlation vs κ and g_0 at various detunings.* At small detunings $|\Delta_A| < 100\gamma$ the atoms are cooled but not trapped, correlation cannot be measured. At higher detunings trapping is good enough, and the correlation strength measured as described in the article is shown in with shades of gray.

2.4.1 Scanning the parameter space

Having defined a suitable measure of correlation between the motion of two atoms in the same cavity, we are in the position to quantitatively investigate the parameter dependence of this phenomenon. To this end, we ran the simulation program for cavity decay rates of $1/50\,\gamma < \kappa < 5\gamma$ and coupling strengths $\gamma < g_0 < 100\gamma$, at atomic detunings of $-10^4\gamma < \Delta_A < -50\gamma$ (at detunings of higher magnitude the atoms move too rapidly and adiabaticity does not hold). The results are plotted in Fig. 2.6.

At atomic detunings of 100γ or less, the atoms are cooled but generally not trapped by the cavity, except for a small region of $g_0 < 5\gamma$ and $\kappa < \gamma$. In that case the motion of two atoms will not be correlated. For detunings as large as 5000γ, the cavity field traps and cools the atoms for any considered values of the parameters. The correlation becomes apparent for $g_0 > 40\kappa$, and grows weaker if g_0 is further increased.

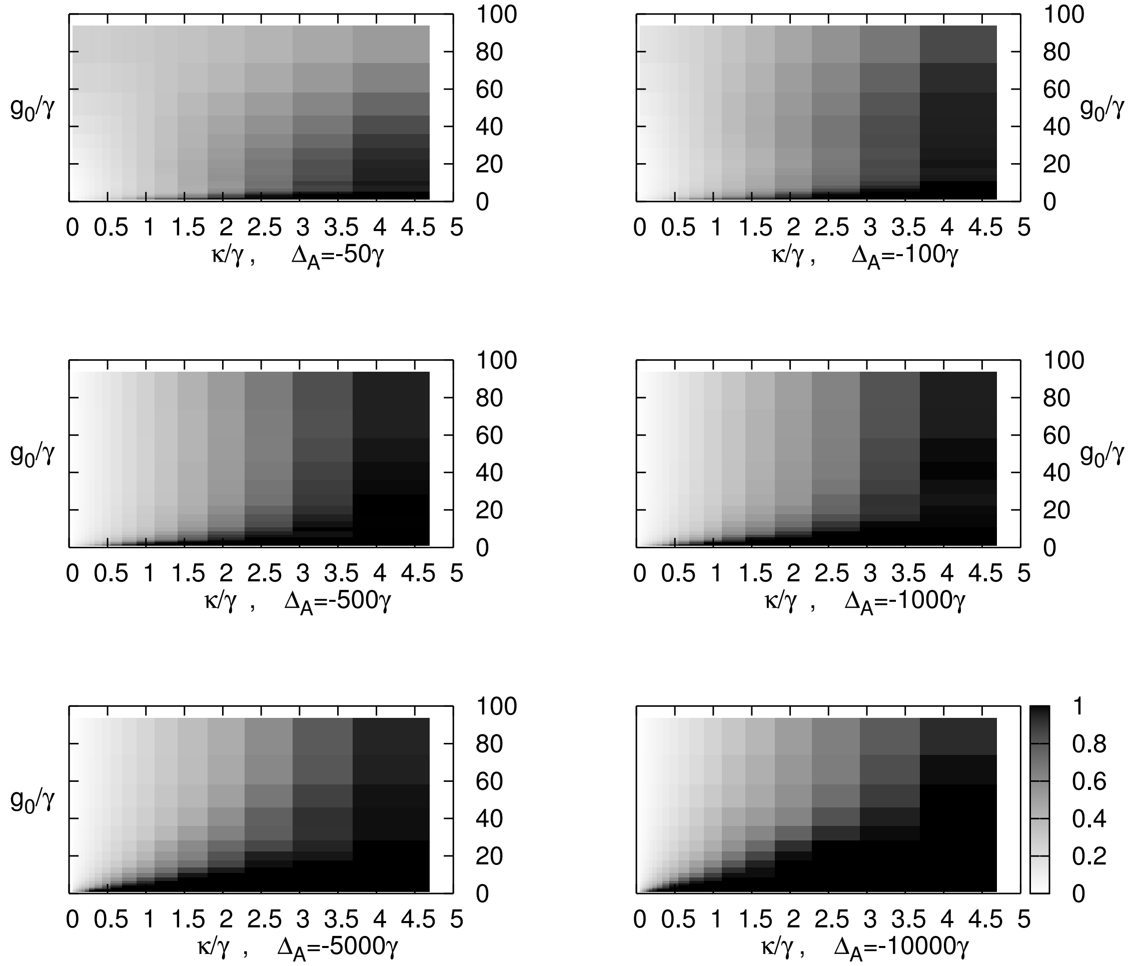

Figure 2.7: *One atom in the cavity: final temperature vs.* κ *and* g_0, *for different atomic detunings.* Temperature is shown in units of $\hbar\gamma$ with shades of gray. Black denotes temperature above the Doppler limit of $\hbar\gamma$.

2.4.2 Correlation and cooling

A decisive advantage of cavity cooling of an atom is the fact that it needs little spontaneous emission [71]. It has been argued that this is a single atom effect and correlations established between the atoms' motion will decrease efficiency or even turn off cooling [68] for a trapped thermal ensemble. On the other hand, in some simulations for very weakly bound atoms, this effect seemed not to play any role [63].

In our model we can now study the effect of correlations on cavity cooling in a very controlled way for a large range of parameters. We performed several runs of our simulation with different cavity parameters and at different detunings, comparing the equilibrium temperature for one and two atoms in the cavity. Our results are plotted in Figs. 2.7 (one atom) and 2.8 (two atoms). All shades of gray show temperatures below Doppler temperature $\hbar\gamma$, while black denotes temperatures above that value.

Putting one atom into the cavity (Fig. 2.7), we find that sub-Doppler cooling is achieved in the good-coupling regime $g_0 > \kappa, \gamma$. In that regime, the final temperature does not depend on g_0,

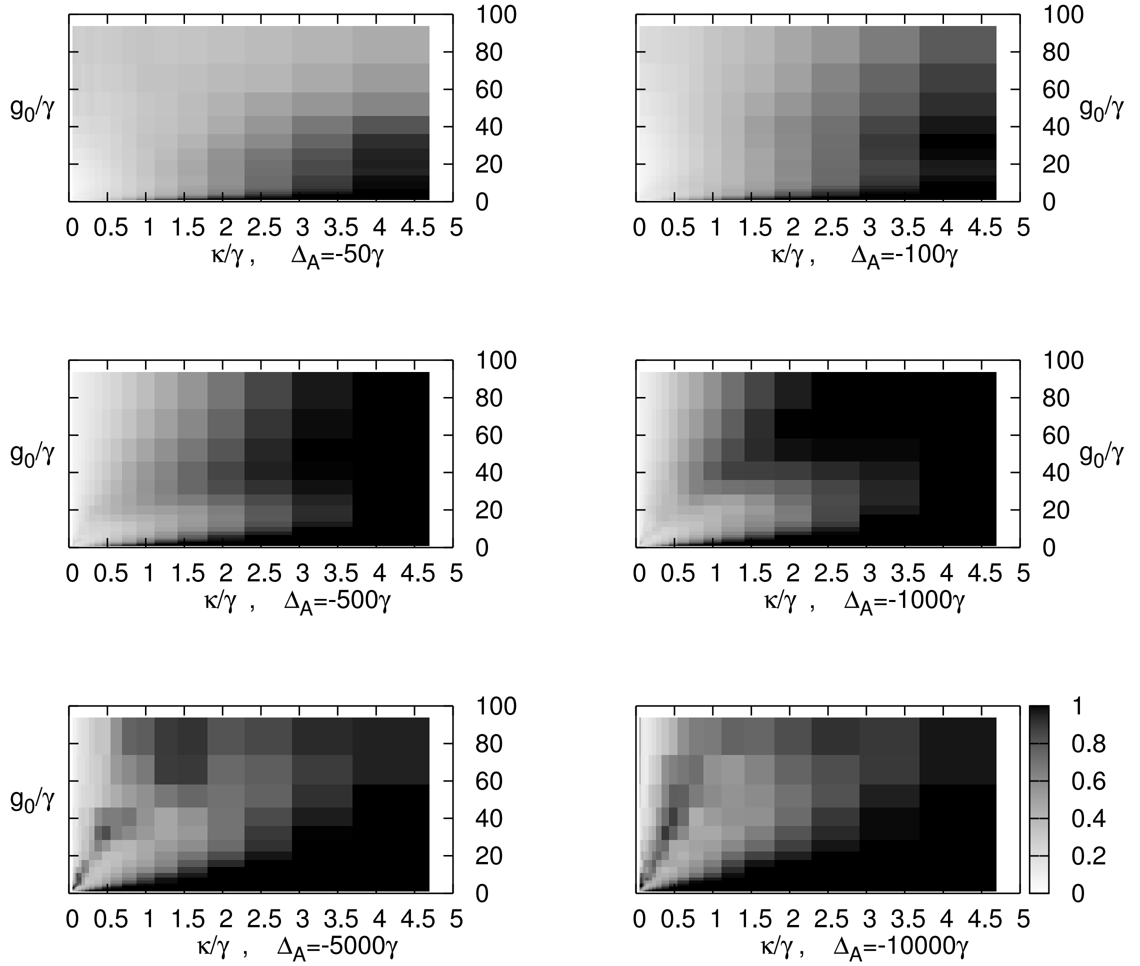

Figure 2.8: *Two atoms in the cavity: final temperature vs.* κ *and* g_0*, for different atomic detunings.* Temperature is shown in units of $\hbar\gamma$ with shades of gray, as in Figure 2.7. For low atomic detuning $|\Delta_A| < 100\gamma$ the temperature is the same as in the one-atom case. For large atomic detuning new structures appear in the plots.

but is approximately proportional to κ, as expected from previous work [72, 69]. Here one has to be cautious of the results, since if the atom's kinetic energy is only a few times the ground-state energy of the harmonic trap potential, the validity of the semiclassical approximation can be questioned.

Interestingly, the temperature plots look different if we load two atoms into the cavity (Fig. 2.8). At moderately large detunings, $\Delta_A = -50\gamma$ and $\Delta_A = -100\gamma$, temperatures are the same as in the single-atom case. In these cases the atoms are cooled, but not trapped, by the cavity field. At larger detunings, $\Delta_A = -500\gamma$ and larger, we see regions in the plot where "extra heating" compared to the single-atom case is observed. This effect is most prominent at extremely large detunings $\Delta_A = -5000\gamma$ and $\Delta_A = -10^4\gamma$, where for $\kappa < \gamma$ a new structure appears in the temperature plots. This points to the highly reduced efficiency of cavity cooling: whereas for a single atom a better resonator (lower κ) implies lower final temperature, if there are two atoms in the cavity, decreasing κ can *increase* the temperature.

Comparison of the temperature plots in Figs. 2.7 and 2.8 with the plots of the correlation strength in Fig. 2.6 reveals strong similarities. Indeed one sees that the excess heating caused by the presence of the other atom coincides with the buildup of correlations in the motion. In other words, the correlation established between two atoms results in a loss of efficiency of cavity cooling, with final temperatures pushed up to the Doppler limit.

2.4.3 The origin of correlation: numerical tests

As we have seen above, the motion of the atoms becomes correlated due to the cavity-mediated cross-talk. This interaction occurs via the force, via the friction, and via the diffusion as well. We would like to know which of these interaction channels is responsible for the correlation. In our simulation we can conveniently answer this question if we artificially weaken only particular channels of interaction and measure the correlation.

The interaction can be eliminated from the deterministic force using the approximation (2.15). Friction and diffusion contain interaction at various levels. On the one hand, cross-friction and cross-diffusion are direct interactions between the atoms. On the other hand – through the determinant $\mathcal{D}'$ – the positions of both atoms influence the friction and diffusion constants for the other atoms. This parametric interaction was not analyzed, but does not seem to play a prominent role. Both cross-friction and cross-diffusion can be eliminated by simply suppressing the off-diagonal terms in the friction and diffusion matrices.

The elimination of the interaction can be made continuous with mixing parameters $0 \leq y_F, y_\beta, y_\mathcal{D} \leq 1$, giving the force, the friction, and the diffusion with the following formulae:

$$F' = y_F F + (1 - y_F) F_0, \tag{2.21}$$

$$\beta'_{km} = y_\beta \beta_{km} + \delta_{km}(1 - y_\beta)\beta_{km}; \tag{2.22}$$

$$\mathcal{D}'_{km} = y_\mathcal{D} \mathcal{D}_{km} + \delta_{km}(1 - y_\mathcal{D})\mathcal{D}_{km}. \tag{2.23}$$

We show an example of what this gives for detuning $\Delta_A = -5000\gamma$, decay rate $\kappa = 0.5\gamma$ and coupling $g_0 = 30\gamma$ in Fig. 2.9. The results of these investigations are quite unanimous. It can be seen that linearization of the potential has no systematic effect on correlation strength, and correlations are slightly enhanced if the noise is decorrelated. If cross-friction is eliminated, however, all correlations disappear. We can therefore conclude that the dominant effect leading to correlated motion is related to cross-friction.

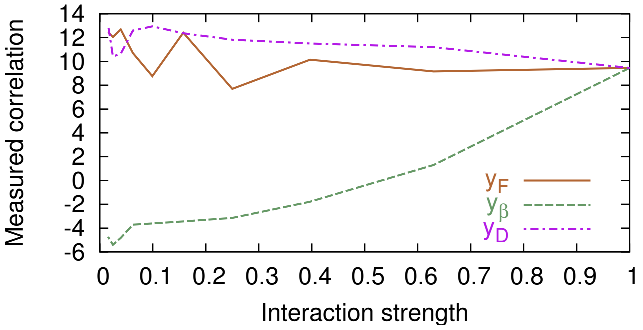

Figure 2.9: *Correlation for various interaction channel strengths.* The interaction via the conservative, the friction, and the diffusion forces is weakened by the mixing ratios y_F, y_β and $y_\mathcal{D}$, as described in the text. The correlation strength was then measured using our correlation parameter. Cross-friction is seen to play the dominant role in the establishment of correlation.

2.5 The origin of correlation: analytical expansion for deep trapping

The emergence of motional correlations between trapped atoms can be examined analytically using the formulas presented in Section 2.3. Both friction and diffusion matrices have an "isotropic" term proportional to δ_{km}, which acts on each atom separately, and an "interaction" term, containing cross-friction and cross-diffusion. The latter can be rewritten in the following form, using the notation $g_k = g(\mathbf{x}_k)$:

$$\frac{2\hbar\eta^2}{|\mathcal{D}'|^2} P(\{\mathbf{x}_l\}) \begin{pmatrix} \nabla_1 g_1^2 \\ \vdots \\ \nabla_N g_N^2 \end{pmatrix} \circ \begin{pmatrix} \nabla_1 g_1^2 & \cdots & \nabla_N g_N^2 \end{pmatrix}, \tag{2.24}$$

where the prefactor P depends on the positions of all atoms symmetrically.

For well-trapped atoms $x_k \ll \lambda$ (x_k denoting the distance of atom k from the nearest trapping site), the coupling constants can be approximated as

$$g_k = g(x_k) = g_0 \cos(k_C x_k) \approx g_0 \left(1 - \frac{1}{2} k_C^2 x_k^2\right). \tag{2.25}$$

Substituting these into the interaction parts of the matrices (2.24) yields:

$$\frac{8\hbar\eta^2}{|\mathcal{D}'|^2} P(\{\mathbf{x}_l\}) g_0^4 k_C^4 r^2 \begin{pmatrix} x_1/r \\ \vdots \\ x_N/r \end{pmatrix} \circ \begin{pmatrix} x_1/r & \cdots & x_N/r \end{pmatrix}, \tag{2.26}$$

where the "radius", $r = \left(\sum_l x_l^2\right)^{\frac{1}{2}}$, is the distance of the system from the origin in the coordinate space. This matrix is a projector to the vector $(x_1, \ldots, x_N)$, and hence the interaction terms affect only the "radial" motion.

In the well-trapped case we can write the friction and diffusion matrices to second order in the coordinates x_l as:

$$\boldsymbol{\beta}_{km} = \beta_0 \delta_{km} + \beta_1 x_k x_m, \tag{2.27}$$

$$\mathcal{D}_{km} = \mathcal{D}_0 \delta_{km} + \mathcal{D}_1 x_k x_m. \tag{2.28}$$

The following notation is used:

$$\beta_0 = 2\hbar \frac{\eta^2}{|\mathcal{D}_0'|^2}\gamma g_0^2 k_C^2 \frac{2\Delta_A}{\Delta_A^2+\gamma^2} k_C^2 x_k^2, \tag{2.29}$$

$$\mathcal{D}_0 = 2\hbar^2 \frac{\eta^2}{|\mathcal{D}_0'|^2}\gamma g_0^2 k_C^2 \left(\frac{2}{5}+\frac{3}{5}k_C^2 x_k^2\right), \tag{2.30}$$

$$\beta_1 = 2\hbar \frac{\eta^2}{|\mathcal{D}_0'|^2} g_0^4 k_C^4 \mathrm{Im}\left\{\frac{1}{\mathcal{D}_0'^2}\left[\mathcal{D}_0'(1-3\chi) + 2(1-\chi)\Big((i\Delta_A-\gamma)^2 - \sum_l g(\mathbf{x}_l)^2\Big)\right]\right\}, \tag{2.31}$$

$$\mathcal{D}_1 = 2\hbar^2 \frac{\eta^2}{|\mathcal{D}_0'|^2} g_0^4 k_C^4\, 4\frac{\kappa\Delta_A+\gamma\Delta_C}{|\mathcal{D}_0'|^2}, \tag{2.32}$$

where $\mathcal{D}_0'$ stands for the Bloch determinant $\mathcal{D}'$ defined in eq. (2.7), evaluated at the trapping site. Near the trapping site all x_k go to zero, and only $\mathcal{D}_0$ remains finite. This prevents the atoms from stopping completely: they are "heated out" from the trapping sites themselves. At some distance from the trapping sites the interaction terms become important as well, in the coordinate space this induces extra diffusion and friction in the radial direction. Provided g_0 is high enough, radial friction is enhanced much more than radial diffusion, leading to a "freezing out" of the radial mode, i.e. a motion at approximately constant distance from the origin.

2.6 Conclusions

As pointed out in several previous papers, the motion of particles in a cavity is coupled quite generally through the field mode. This implies the buildup of motional correlations, which we have investigated here in more detail. In general we found that in steady state these correlations are hard to see directly and it is difficult to find good qualitative measures to characterize them. Mostly they are strongly perturbed by various diffusion mechanisms. However, they still play an important role in the dynamics and thus can be observed indirectly. As one consequence they can lead to a significant change (increase) in the steady temperature, which directly relates to trapping times and localization properties. This poses limits to cavity induced cooling for large particle numbers.

From the various mechanisms at work, cross friction turns out to be the most important. It creates correlation and leads to a fast thermalization of two distant particles without direct interaction. Hence, this mechanism should prove vital for the implementation of sympathetic cooling of distant ensembles coupled by a far off-resonant cavity field. In order to get efficient coupling the two species should have comparable oscillation frequencies, so that correlation buildup and thermalization is fast. Also the finesse of the cavity should be large (long photon lifetime).

The second important coupling mechanism, which works via the joint steady state potentials, was suggested for use in the implementation of conditional phase shifts [59]. It can be viewed as a cavity-enhanced dipole–dipole coupling. Although this contribution will become more important for larger atom-field detunings, the conditions for this part to dominate the dissipative cross friction seem rather hard to achieve in practice. Finally we found that the noise forces acting on different atoms contain nonlocal correlations too. These are particularly important for large detunings and relatively low photon numbers, where spontaneous emission is strongly reduced. As a result they could seriously perturb bipartite quantum gates in cavities.

Chapter 3

Publication: Self-organization of atoms in a cavity field: Threshold, bistability, and scaling laws

3.1 Introduction

The manipulation of cold atoms and molecules by laser light is a rapidly growing field and has become a suitable ground for studying fundamental phenomena of physics both experimentally and theoretically [15]. In the last decade, the emphasis has partly been shifted towards many-body effects in the dynamics of weakly interacting atoms [73, 74]. The mechanical action of the electromagnetic radiation field on free atoms rarely manifests these effects. The refractive index of a cloud of atoms is simply composed of the product of the single atom polarizability and the optical density. Standard laser cooling methods were also conceived on the basis of single-atom processes. Only at densities as high as the ones achievable in a magneto-optical trap does the dipole-dipole interaction between atom pairs give rise to a Lorentz–Lorenz-type refractive index and present an appreciable nonlinearity in the optical density [75, 76]. The underlying process, the reabsorption of spontaneously scattered photons in the atomic cloud [77, 78], heats the atomic motion and hence limits the attainable minimum temperature. In addition, this effect also introduces spatial instability into the atomic cloud and thus hinders degeneracy in phase space by optical means [79].

The mechanical effect of light on atoms inside a high-finesse resonator is substantially modified with respect to free space, which is the source of a variety of interesting phenomena in optical cavity quantum electrodynamics [19, 20]. The basic reason is that a cavity photon makes many round-trips between the mirrors and thus the back action of the atom on the field, enhanced by the cavity finesse, cannot be neglected. As opposed to the external forces exerted by laser fields, the light forces in a cavity cannot be separated from the dynamics of the resonator mode, which is strongly influenced by that of the atom.

The coupled atom-field dynamics can yield an efficient damping of the atomic motion via the mirror loss dissipation channel [71, 25]. Such "cavity cooling" schemes have recently been demonstrated experimentally [53, 80]. The fact that cavity cooling allows for replacing the spontaneous emission, which is the dissipation channel in all laser cooling schemes, by irreversible photon loss from the cavity has important consequences. First, the internal structure of the atom is not important and the mechanism can be operated on a wide range of species. Second, the problem of the reabsorption of spontaneously scattered photons, the source of the instability of atomic clouds at high densities, can be suppressed.

The dynamics of atoms in a resonator is inherently a many-body problem even at a small density of the ensemble [49, 81]. As all atoms are coupled to the same cavity mode, the modification of the field by one atom is experienced by a remote atom as well as by itself. The cavity cooling mechanism may become inefficient since the delicate dynamical correlation between one atom and the field mode could be perturbed by the motion of another atom [64, 31]. Indeed, one of the cavity cooling schemes was found to slow down linearly with increasing number of atoms [63].

In a recent Letter we have predicted a cooperative behavior of the atoms driven by a laser in a direction perpendicular to the axis of a standing wave cavity [27]. At high pump laser intensities (above a threshold) the homogeneous atomic cloud self-organizes into one of two regular checkerboard patterns that maximize scattering into the cavity. The constructive interference of fields radiated by the individual atoms produces an intensity which depends quadratically on the number of atoms (superradiance). Corresponding to the two patterns, there are two possible phases of the output field with 180 degrees difference, which have been observed in an experiment by Black, Chan, and Vuletic [56].

The onset of self-organization is relatively fast, on the microsecond time scale. A basic property of the present system is that the field created by the atoms traps and simultaneously cools them so that the organized pattern remains stable on a long time scale (10's of ms). The cavity cooling mechanism now acts on many atoms without losing efficiency. There is no external finite-temperature heat bath to define the temperature which, instead, is set by the dynamical equilibrium of the dipole force fluctuations and the cavity cooling effect. This is a distinctive feature with respect to the recently demonstrated collective atomic recoil laser in a ring cavity (CARL) [50, 82, 83, 84], where a magneto-optical trap is necessary to stabilize the organized phase and the otherwise transient gain [85], and also to inject noise for obtaining the phase transition-like behavior [86, 87, 88].

In the present paper we discuss in detail the self-organization process, from the viewpoint of phase transitions. A mean-field approach leads to a well-defined threshold in the pumping strength. Comparison to numerical simulations reveals effects scaling unusually with the atom density, a characteristic feature of this cavity-coupled many-atom system.

The paper is organized as follows. In Sect. 3.2, the equations of a semiclassical model are recapitulated, where the atoms are represented as simple linearly polarizable particles. Thereby the theory applies to a much wider class of particles than alkali atoms. The main features of the self-organization process, such as time scales, superradiance, collective cooling, are surveyed using a numerical example in Sect. 3.3. Then, in Sect. 3.4, we introduce a one-dimensional mean-field model and determine the threshold and critical exponent. In Sect. 3.5, we present the results of detailed numerical simulations, which show effects beyond mean-field. The atom number enters the physics of the system in a form other than the density. Above a certain atom number, stable defects appear in the self-organized pattern and modify the system properties, which is accounted for in Sect. 3.6. In Sect. 3.7, the cooperative atomic behavior is discussed in detail by demonstrating the superradiance, and the ensuing improvement of localization by collectivity. We conclude in Sect. 3.8.

3.2 Semiclassical model

We consider N atoms in an open optical resonator (Fig. 3.1). The atoms are illuminated from the side by a "transverse" standing-wave laser pump with frequency ω. This geometry corresponds to various experimental setups realizing the controlled transport of atoms from the side into a cavity [57, 80] where the standing-wave pump amounts to a "conveyor belt" [89]. There is an efficient scattering of photons into the cavity mode quasi-resonant with the pump, $\omega_C \approx \omega$, due to the enhanced dipole coupling described by the single-photon Rabi frequency $g = \omega_C^{1/2}[2\epsilon_0\hbar V]^{-1/2}d_{eg}$, for a mode volume V and atomic transition dipole moment d_{eg} along the cavity mode polariza-

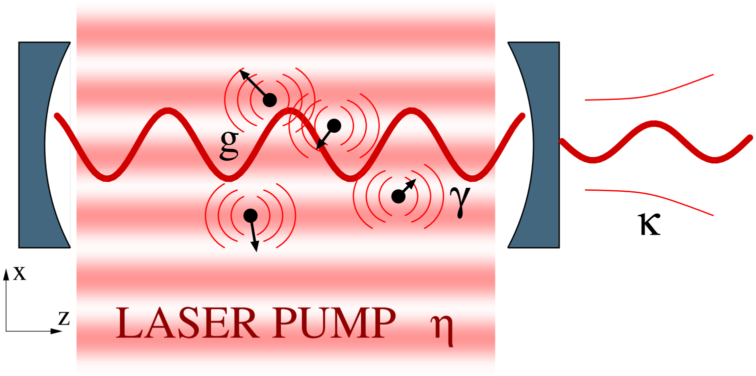

Figure 3.1: The setup: transversely driven atoms moving in a standing-wave cavity. The laser intensity is given by the maximum free-space Rabi frequency (pumping strength) η. The atoms couple to the cavity mode with 1-photon Rabi frequency g. The loss channels are: spontaneous emission (rate 2γ) and cavity loss (rate 2κ).

tion. Large detuning of the laser from the atomic transition $|\omega - \omega_A| \gg \gamma$, where 2γ is the full atomic linewidth at half maximum, ensures that the upper level of the atoms can be adiabatically eliminated. This model then describes a very general class of linearly polarizable particles—in the following, we continue to use “atoms” for convenience. For the sake of simplicity, we restrict the atomic motion to two dimensions, along the pump laser and the cavity axis, coordinates x and z, respectively, without losing any relevant physical effect. Motion in the third dimension could be taken into account in the same way as along x.

The quantum master equation for the density matrix reads

$$\dot{\rho} = -\frac{i}{\hbar}\left[H, \rho\right] + \mathcal{L}\rho \, . \tag{3.1}$$

Here the Hamiltonian is

$$H = \sum_{j=1}^{N} \frac{\mathbf{p}_j^2}{2M} - \hbar\Delta_C a^\dagger a + \hbar U_0 \sum_{j=1}^{N} E^\dagger(\mathbf{r}_j) E(\mathbf{r}_j) \, , \tag{3.2a}$$

where $a, a^\dagger$ are the boson operators of the cavity mode, $\mathbf{r}_j = (x_j, z_j)$ and $\mathbf{p}_j = (p_{xj}, p_{zj})$ are the position and momentum vectors of the jth atom. The Liouville operator describing the cavity photon losses with rate 2κ, and the spontaneous emission reads

$$\begin{aligned}\mathcal{L}\rho = {} & 2\kappa\left(a\rho a^\dagger - \frac{1}{2}a^\dagger a\rho - \frac{1}{2}\rho a^\dagger a\right) - \Gamma_0 \sum_{j=1}^{N}\Big(E^\dagger(\mathbf{r}_j)E(\mathbf{r}_j)\rho + \rho E^\dagger(\mathbf{r}_j)E(\mathbf{r}_j) \\ & - 2\int d^2\mathbf{u}\; N(\mathbf{u}) E(\mathbf{r}_j) e^{-ik_A \mathbf{u}\mathbf{r}_j} \rho e^{ik_A \mathbf{u}\mathbf{r}_j} E^\dagger(\mathbf{r}_j)\Big) \, .\end{aligned} \tag{3.2b}$$

In the above formulas, $E(\mathbf{r})$ is the dimensionless electric field,

$$E(\mathbf{r}) = f(\mathbf{r})a + \eta(\mathbf{r})/g \approx \cos(kz)a + \cos(kx)\eta/g \, . \tag{3.2c}$$

The Rabi frequency of the driving laser is $\eta(\mathbf{r})$, whose position dependence is given by a $\cos(kz)$ mode function for a standing-wave field. In the following, we are going to refer to the maximum value of the Rabi frequency η as “pumping strength”. The variation of the pump field along the cavity axis and that of the cavity mode function $f(\mathbf{r})$ along the transverse direction (Gaussian envelope) are neglected. The detunings are defined as $\Delta_C = \omega - \omega_C$ and $\Delta_A = \omega - \omega_A$. The parameters

$$U_0 = \frac{g^2 \Delta_A}{\Delta_A^2 + \gamma^2} \; , \; \Gamma_0 = \frac{g^2 \gamma}{\Delta_A^2 + \gamma^2} \; , \tag{3.3}$$

describe the dispersive and absorptive effects of the atoms, respectively, as they shift and broaden the resonance line of the cavity. In the last term of Eq. (3.2b), the integral represents the averaging over the angular distribution $N(\mathbf{u})$ of the random recoil due to spontaneous emission into the free-space modes.

Instead of directly using the density matrix, we consider the evolution of the corresponding joint atom-field Wigner function [72]. This can be systematically approximated by semiclassical equations for a set of classical stochastic variables, α, $\mathbf{p}_j$, $\mathbf{r}_j$, the index $j = 1, \ldots, N$ labeling the atoms,

$$\dot{\alpha} = i\Big[\Delta_C - U_0 \sum_j \cos^2(kz_j)\Big]\alpha - \Big[\kappa + \Gamma_0 \sum_j \cos^2(kz_j)\Big]\alpha - \eta_{\text{eff}} \sum_j \cos(kz_j)\cos(kx_j) + \xi_\alpha \; , \tag{3.4a}$$

$$\dot{p_{xj}} = -\hbar U_0 (\eta/g)^2 \frac{\partial}{\partial x_j} \cos^2(kx_j) - i\hbar(\eta_{\text{eff}}^* \alpha - \eta_{\text{eff}} \alpha^*) \frac{\partial}{\partial x_j} \cos(kx_j)\cos(kz_j) + \xi_{xj} \; , \tag{3.4b}$$

$$\dot{p_{zj}} = -\hbar U_0 |\alpha|^2 \frac{\partial}{\partial z_j} \cos^2(kz_j) - i\hbar(\eta_{\text{eff}}^* \alpha - \eta_{\text{eff}} \alpha^*) \frac{\partial}{\partial z_j} \cos(kx_j)\cos(kz_j) + \xi_{zj} \; , \tag{3.4c}$$

where the effective pumping strength for the cavity mode is

$$\eta_{\text{eff}} = \frac{\eta g}{-i\Delta_A + \gamma} \; . \tag{3.5}$$

These equations include Langevin noise terms ξ_α, ξ_{xj}, and ξ_{zj}, defined by the non-vanishing second-order correlations,

$$\langle \xi_\alpha^* \xi_\alpha \rangle = \kappa + \sum_{j=1}^{N} \Gamma_0 \cos^2(kz_j) \; , \tag{3.6a}$$

$$\langle \xi_n \xi_\alpha \rangle = i\hbar \Gamma_0 \partial_n \mathcal{E}(\mathbf{r}_j) \cos(kz_j) \; , \tag{3.6b}$$

$$\langle \xi_n \xi_m \rangle = 2\hbar^2 k^2 \Gamma_0 |\mathcal{E}(\mathbf{r}_j)|^2 \overline{u_n^2} \delta_{nm} + \hbar^2 \Gamma_0 \Big[\partial_n \mathcal{E}^*(\mathbf{r}_j)\, \partial_m \mathcal{E}(\mathbf{r}_j) + \partial_n \mathcal{E}(\mathbf{r}_j)\, \partial_m \mathcal{E}^*(\mathbf{r}_j)\Big] \; , \tag{3.6c}$$

where the indices $n, m = x_j, z_j$. The noise terms associated with different atoms are not correlated. The complex dimensionless electric field $\mathcal{E}(\mathbf{r})$ is derived from Eq. (3.2c), replacing the field operator a by the complex variable α. We iterate the coupled, stochastic Ito-type differential equations (3.4) by a Monte Carlo-type algorithm.

There are two types of force terms in the equations of the momentum components. The terms in the first lines derive from the usual one-dimensional "optical lattice" potentials, the laser pump keeps the atoms inside the resonator via this term. In the second lines, the force terms originate from the coherent redistribution of photons between the pump and the field mode. The potentials depending on the amplitude α, which itself is a variable, are not conservative (all but the optical lattice created by the transverse pump). The time-delayed correlations in the dynamics of the atomic motion and the field mode can result in a friction force on the atoms, known as cavity cooling [71, 90, 21, 47, 48, 72, 91, 92].

3.3 Self-organization

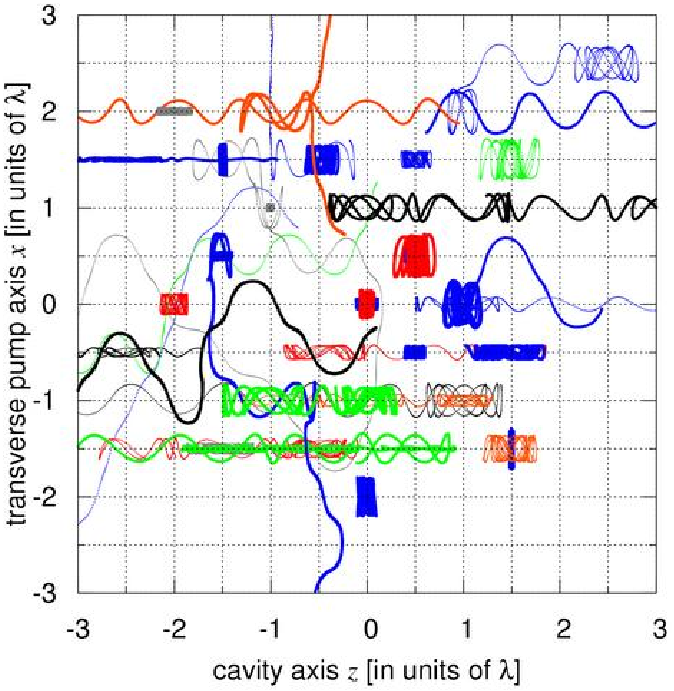

Figure 3.2: Two-dimensional trajectories of 40 rubidium atoms in a cavity, during the initial 50 μsec. A checkerboard pattern of trapped atoms emerges, untrapped atoms move mainly along the cavity axis. Parameters: $\gamma = 20/\mu$sec, $(g, \kappa) = (2.5, 0.5)\gamma$, atomic detuning $\Delta_A = -500\gamma$, cavity detuning $\Delta_C = -\kappa + NU_0$, and the pumping strength $\eta = 50\gamma$.

We study he motion of the atoms in the cavity by numerically integrating the set of stochastic ordinary differential equations (3.4). To be specific, ^{85}Rb were considered, with the $5^2\mathrm{S}_{1/2}, \mathrm{F} = 3 \leftrightarrow 5^2\mathrm{P}_{3/2}, \mathrm{F} = 4$ transition. Starting from a gas of thermal atoms (random positions from a uniform, and velocities from a thermal distribution) and no light in the cavity mode ($\alpha = 0$), with the right choice of parameters we observe a buildup of the cavity field accompanied by the appearance of an organized pattern in the spatial distribution of the atoms. This is illustrated in Fig. 3.2, where the trajectories of 40 atoms during the initial 50 μs of a run are shown. The grid lines denote points of maximum coupling to the standing-wave cavity or pump field. Trapped atoms are oscillating about intersections of grid lines, where a single atom can scatter pump photons into the cavity mode most efficiently. For many atoms, however, destructive interference can inhibit the scattering process: the source term in Eq. (3.4a) contains the factor $\sum_j \cos(kx_j)\cos(kz_j)$, which can be small even if all the atoms are maximally coupled due to the alternating signs of the summands. In contrast to this, in Fig. 3.2, only every second “maximally coupled” site—the black or the white fields of a checkerboard—is occupied, leading to an efficient Bragg scattering of pump photons into the cavity.

The emergence of a checkerboard pattern of atoms with every second point of maximum coupling empty happens only due to the good choice of the parameters ensuring positive feedback, as explained in the following. Initially, in the random position distribution some atoms scatter into the cavity in a given phase and some with an opposite phase, and thus most of the scattered field is canceled. The dipole force (first term of Eq. (3.4b)) attracts atoms towards antinodes of the pump (for red detuning, $\Delta_A < 0$), but almost no field in the cavity means no substantial modification of the uniform position distribution along the cavity axis. This can be seen in Fig. 3.2, where most atoms are well trapped along the transverse axis but some meander along the cavity axis. Due to statistical fluctuations either the in-phase or opposite-phase scatterers will be in tiny majority, and a small cavity field does build up. The dipole force due to the cavity field, first term of Eq. (3.4c), now attracts atoms towards antinodes of the cavity. The crucial point to consider is the interference of the cavity and pump fields, giving the second terms in Eqs. (3.4b,c). The product $\cos(kx_j)\cos(kz_j)$ alternates sign between the black and white fields of the checkerboard. For a right choice of detuning Δ_C, there is a positive feedback and the atoms are attracted towards the "majority" sites and are repelled from the "minority" sites, due to the interference.

The initial fast buildup continues over a longer timescale, with the kinetic energy of the oscillating and the free-flying untrapped atoms dissipated owing to the cavity cooling mechanism (for the transverse pumping case and for the chosen detuning Δ_C, it is the one described in Ref. [92]). This leads to an increase of the ratio of trapped atoms and to a stronger localization in the vicinity of the antinodes. Simultaneously, the coherent scattering into the cavity improves, giving a slow increase in the cavity field intensity. The time evolution of the photon number is plotted in Fig. 3.3 for this self-organization process of 40 and 160 atoms. In the latter case, the photon number scale was rescaled by a factor of 16. This way, the overlap of the two curves demonstrates the superradiance effect, i. e., the intensity is quadratically proportional to the atom number.

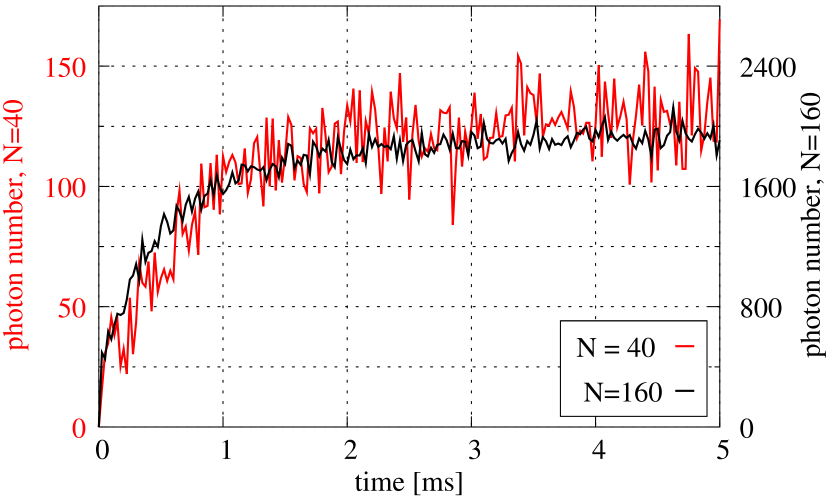

Figure 3.3: The time evolution of the photon number in the cavity on a long time scale, for $N = 40$ and $N = 160$ atoms (note the different vertical scaling). The parameters are the same as in Fig. 3.2

In this phase transition-like process, the reduction of the kinetic energy is not a good characterization of the cooling efficiency. For the motion along the cavity axis, the transition from vanishing photon number to the "superradiated" light field is accompanied by a change of the heat capacity of the atomic ensemble since the number of quadratic degrees of freedom changes from one (kinetic energy) to two (kinetic and potential energy). In deep harmonic traps, even a very low level of excitation can correspond to high kinetic energies. Thus even though the temperature can increase, cavity-induced dissipation increases the phase space density of the system by improving localization. An appropriate measure of this process is the effective phase space volume of the system (the inverse of the phase space density), measured by the Heisenberg uncertainty product $\Delta x\Delta p_x/\hbar$ and $\Delta z\Delta p_z/\hbar$ for each degree of freedom. Here $(\Delta x)^2$ and $(\Delta z)^2$ are the averages of the squared distance of the atom from the nearest antinode along the direction x and z, respectively. For a harmonic potential, the dimensionless effective phase space volume amounts precisely to the mean number of excitation quanta. For untrapped atoms with mean kinetic energy

$\langle p^2/m\rangle = k_B T$, the phase space volume is $\lambda\sqrt{mk_BT}/(4\sqrt{3}\hbar)$.

In Fig. 3.4, the time evolution of the Heisenberg uncertainty product is shown for three cases. When the pumping strength is below threshold ($N = 40$, $\eta = 10\gamma$), the uncertainty product is a constant. Here the spatial distribution of the atomic ensemble remains uniform—the transverse pump is too weak to induce any noticeable spatial modulation at temperatures $k_BT \approx \hbar\kappa$. Thus $\langle \Delta z\Delta p_z\rangle =$ const. and $\langle \Delta x\Delta p_x\rangle =$ const. reveal that the temperature itself does not change in either direction. At the cavity cooling limit $k_BT = \hbar\kappa$ the numerical value for the phase space volume from the last paragraph is $13.4\hbar$, in accordance with the value along the transverse x direction. Along the cavity axis z, however, the phase space volume is above this estimate, indicating a higher temperature. Above threshold, the phase space volume transiently jumps to high values for both directions, and then it is gradually decreased. Compression is apparently more efficient along the cavity axis, here the phase space goes considerably below the value corresponding to the uniform distribution. In both plots the two curves corresponding to $N = 40$ and $N = 160$ are very similar, which manifests that the cooling rate of the ensemble is independent of the atom number. This is a very important observation, being at variance with the expectation that the efficiency of cavity cooling mechanism is reduced for increasing number of atoms. This prediction was made for a setup where the external pump field is injected directly into the cavity. Apparently it does not apply to the transverse pumping case studied here.

With the help of these few examples, we surveyed three important properties appearing in the dynamics of a laser-driven atomic ensemble coupled to a cavity mode: (i) the system rapidly self-organizes into a checkerboard pattern in a trapping field, (ii) which is generated by a collective, superradiant scattering into the cavity, and finally, (iii) the energy of the atoms is dissipated at a rate independent of the number of atoms. This behaviour requires a sufficiently strong pumping strength, indicating the possibility of a well-defined threshold separating two different stability regions. This threshold is discussed in the next section within the framework of a mean field approximation.

3.4 Mean-field approximation

The essence of the self-organization process can be understood on the ground of conservative mean-field forces acting on the atoms. This amounts to treating the cavity field as if it responded immediately to the positions of the atoms. Cavity cooling, which is directly related to the time lag of the cavity field, is absent in this model. Moreover, the mean-field approach corresponds to the thermodynamic limit of the system: $N \to \infty$, $g \to 0$, $\kappa =$ const. with $Ng^2 =$ const. Physically, the limit can be thought of as taking larger cavities (cavity length $l_{\text{cav}} \to \infty$) filled with a gas of atoms of constant density (atom number $N \propto l_{\text{cav}}$). Due to the $V^{-1/2}$ dependence of the coupling constant g on the mode volume V, one then has $Ng^2 =$ const., neglecting the variation of the waist of the mode. Moreover, due to larger photon travel time between the mirrors, the reflectivity has to scale like $\propto l_{\text{cav}}^{-1}$ to keep $\kappa =$ const. For the sake of simplicity, we analyze one-dimensional motion along the cavity.

3.4.1 Potentials

Taking $x_j = 0, j = 1, \ldots, N$, according to Equation (3.4c) each atom moves in a potential

$$V(z) = U_2\cos^2(kz) + U_1\cos(kz) \tag{3.7}$$

composed of the sum of a $\lambda/2$ periodic potential stemming from the cavity field and a λ periodic one arising from the interference between cavity and pump fields. The potential depths are given

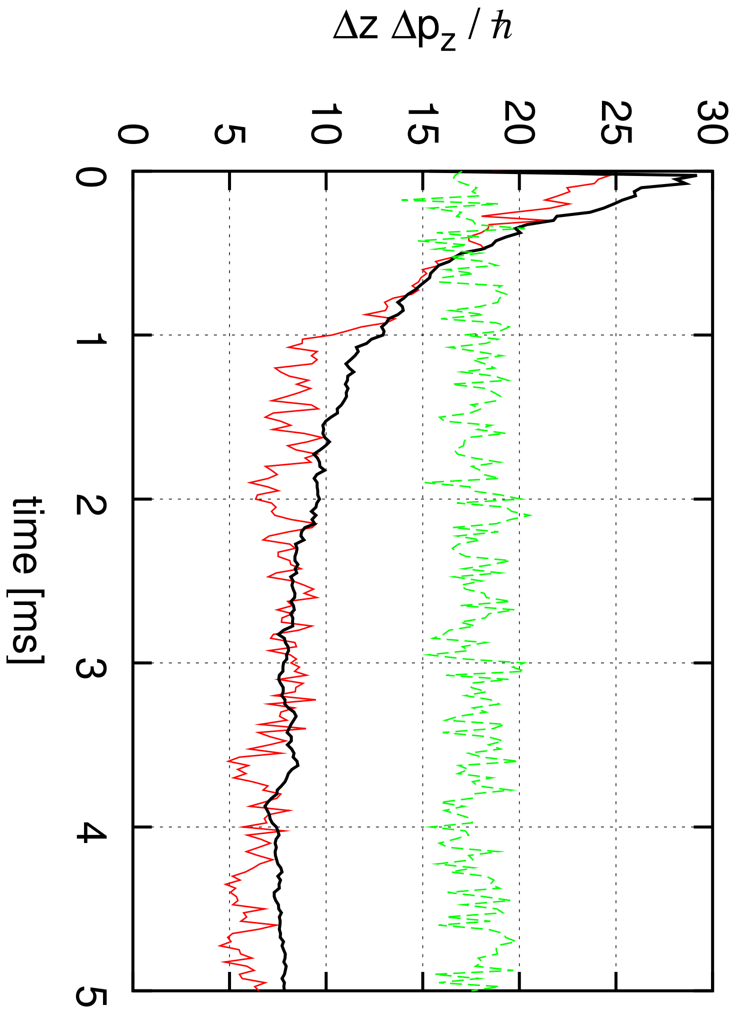
$\Delta z\ \Delta p_z / \hbar$
0
5
10
15
20
25
30
0
1
2
3
4
5
time [ms]

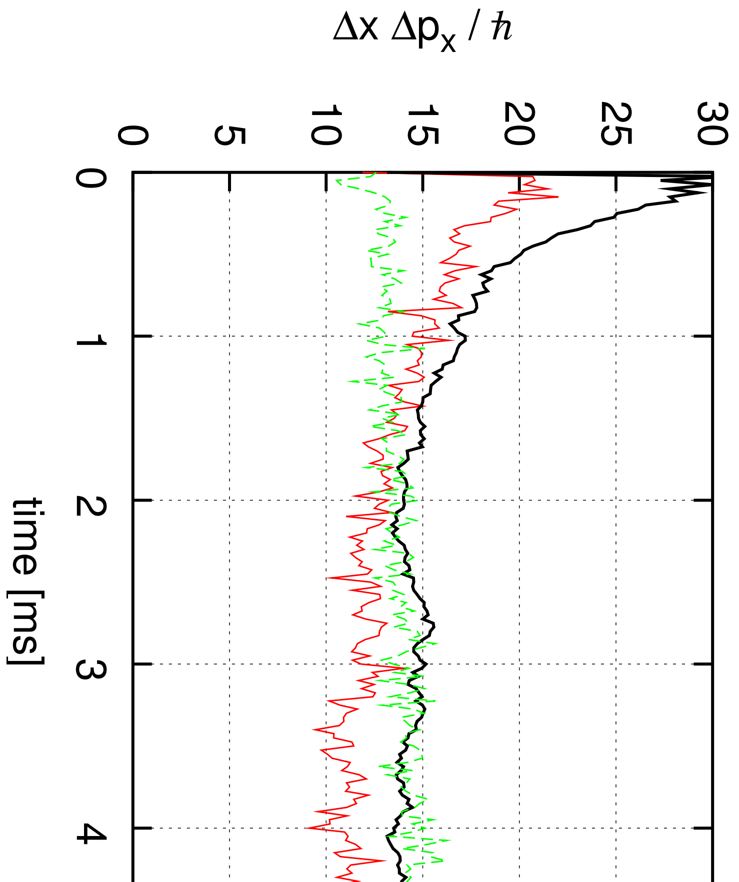
$\Delta x\ \Delta p_x / \hbar$
0
5
10
15
20
25
30
0
1
2
3
4
time [ms]

by

$$U_2 = N^2 \langle \cos(kz) \rangle^2 \, \hbar I_0 \, U_0 \tag{3.8a}$$

$$U_1 = 2N \langle \cos(kz) \rangle \, \hbar I_0 \left(\Delta_C - N U_0 \langle \cos^2(kz) \rangle \right) . \tag{3.8b}$$

These, in the mean-field approximation, depend on the position of the individual atoms only via the mean value

$$\Theta = \langle \cos(kz) \rangle = \frac{1}{N} \sum_{i=1}^{N} \cos(k z_i) \, , \tag{3.9}$$

which can be considered a spatial order parameter, and via the bunching parameter

$$\mathcal{B} = \langle \cos^2(kz) \rangle = \frac{1}{N} \sum_{i=1}^{N} \cos^2(k z_i) \, . \tag{3.10}$$

The order parameter Θ has characteristic values: (i) $\Theta \approx 0$ describes the uniform distribution, (ii) $\Theta \to \pm 1$ corresponds to a self-organized phase with atoms in the even or odd antinodes, respectively. Finally, I_0 represents the maximum number of photons each atom can scatter into the cavity:

$$I_0 = \frac{|\eta_{\text{eff}}|^2}{[\kappa + N\Gamma_0 \mathcal{B}]^2 + [\Delta_C - N U_0 \mathcal{B}]^2} \, . \tag{3.11}$$

In equilibrium the spatial distribution of the atoms and the above averages are time-independent, which makes it possible to attribute a physical meaning to the potential (3.7). Since the potential depends on the position distribution, however, the system is highly nonlinear.

For $U_0 < 0$, obviously $U_2 < 0$ and the cavity field gives a potential with "even" wells at $kz = 2n\pi$ and "odd" ones at $kz = (2n+1)\pi$. The interference term ($\propto \cos(kz)$) discriminates between the even and odd sites, raising the energy of one of them and lowering that of the other. If $2\,|U_2| < |U_1|$ this effect is so strong that $V(z)$ yields a potential with wells at the even and hills at the odd sites – or the other way around, depending on the sign of U_1.

The sign of U_1 is crucial. To simplify the dependence, let us require a cavity detuning $\Delta_C < -N\,|U_0|$ so that the second factor in U_1 is always negative regardless the momentary configuration of the atoms. To be specific, in the following we are going to use

$$\Delta_C = N U_0 - \kappa \, . \tag{3.12}$$

If the atoms accumulate around the even (odd) antinodes, then $\Theta \approx +1$ ($\Theta \approx -1$) and the $U_1 \cos kz$ potential is attractive at the even (odd), while repulsive at the odd (even) sites. Therefore Eq. (3.12) is the proper choice for positive feedback that makes the runaway solution of self-organization possible.

Two more parameters describing spatial order are used later in this work: (i) the "defect ratio", the ratio of atoms closer to minority sites than majority sites; (ii) the "localization parameter", the position variance (along the cavity axis and/or the transverse pump)

$$\mathcal{D}_z = \frac{1}{N} \sum_{i=1}^{N} \left(\frac{k z_i}{\pi} \right)^2 \, , \tag{3.13}$$

where z_i is measured from the nearest antinode of the cavity mode function. A uniform distribution of atoms gives a defect ratio close to 50 % and a localization parameter of $1/12$. For a self-organized pattern, both parameters approach 0.

3.4.2 Canonical distribution

We suppose that the phase-space distribution of the atoms factorizes to position and momentum dependence, the latter simply given by a thermal distribution with mean energy $k_B T$. There is no external finite-temperature heat bath to set $k_B T$, it is instead determined by the dynamics (3.4) through the equilibrium of the cavity cooling and the Langevin noise terms. This allows for a position- and time-dependent effective temperature, effects neglected in this model. For a far-detuned pump, cavity losses dominate spontaneous emission, and an estimate $k_B T \approx \hbar\kappa$ is provided by the Einstein relation. The spatial density of the atoms in the potential $V(z)$ is then given by a canonical distribution,

$$\rho(z) = \frac{1}{Z} \exp(-V(z)/(k_B T)) \, , \tag{3.14}$$

with the partition function $Z = \int \exp(-V(z)/(k_B T)) dz$ ensuring that $\rho(z)$ is normalized to unity. In our case the potential $V(z)$ is a function of the density $\rho(z)$, therefore this equation has to be solved in a self-consistent manner.

A direct approach to solving (3.14) is to use it iteratively to determine the $\rho(z)$ for given values of the physical parameters. We set the temperature to the cavity cooling limit $k_B T = \hbar\kappa$. Note that the temperature parameter T just rescales the pumping strength η, e.g., taking $k_B T = 2\hbar\kappa$ would correspond to increasing η by a factor of $\sqrt{2}$. The results thus obtained after 100 iterations of (3.14) for an experimentally realistic example are shown in Fig. 3.5 (empty diamonds). There we plot the percentage of atoms near odd sites, i.e., with $|(2m+1)\lambda/2 - z| < \lambda/4$ for any integer m, as a function of the pumping strength. Below a certain threshold in the pumping laser amplitude η^* (vertical dotted line) the atoms are distributed uniformly, for stronger pumping this symmetry is broken. Two examples of such self-organized position distributions obtained by the iterations are shown in the insets. Note also that the convergence of the iterations is slow near the critical η^*

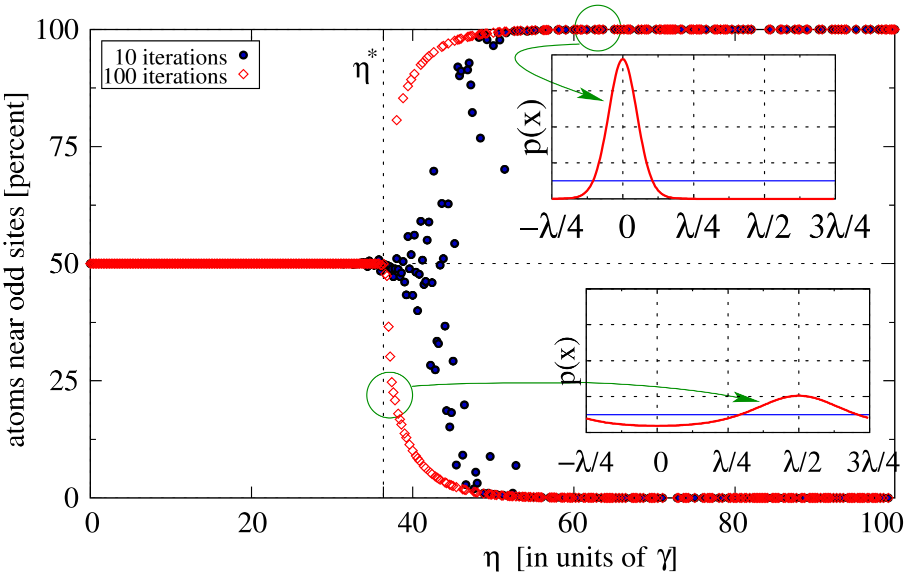

Figure 3.5: Numerical iterations of the mean-field approximation. The percentage of atoms near odd sites after 10 (full circles) and 100 (empty diamonds) iterations is shown varying the pumping strength η. The vertical line is at η^* of (3.19). The two insets show two steady-state position distribution functions at two different pumping strengths. Parameters: $\kappa = \gamma/2, \Delta_A = -500\gamma$, $Ng^2 = 200\gamma^2$ $\Delta_C = -\kappa - Ng^2/|\Delta_A|$, $k_B T = \hbar\kappa$.

(critical slowing down), this is evidenced by plotting the results after 10 iterations (full circles) as well.

The uniform distribution, $\rho(z) = 1/\lambda$ leads to $\Theta = 0$, $\mathcal{B} = 1/2$, which give $V(z) = 0$, thus the distribution fulfills (3.14) trivially for any values of the physical parameters. To investigate its stability, we add an infinitesimal perturbation to it:

$$\rho^{(0)}(z) = \frac{1}{\lambda} + \epsilon g(z) \frac{1}{\lambda} \,, \tag{3.15}$$

with ϵ infinitesimal, and the general λ-periodic perturbation function

$$g(z) = \sum_{m=1}^{\infty} \left(A_m \cos(mkz) + B_m \sin(mkz) \right) \,, \tag{3.16}$$

$$\sum_m A_m^2 + B_m^2 = 1 \,.$$

Since the spatial average of $g(z)$ disappears, $\rho^{(0)}(z)$ is normalized to 1. Iterating (3.14) once leads to the new density function

$$\rho^{(1)}(z) = \frac{1}{\lambda} - N\epsilon \frac{A_1}{\lambda} \frac{\hbar I_0}{k_B T} (\Delta_C - \frac{N}{2} U_0) \cos(kz) + o(\epsilon^2). \tag{3.17}$$

To lowest order in ϵ the only relevant perturbation is that proportional to $\cos kz$. Stability requires that the first-order correction in ϵ be self-contracting. Substituting (3.12) for the cavity detuning, we have the following instability threshold for the uniform distribution:

$$N I_0 \hbar \left(\frac{N}{2} |U_0| + \kappa \right) > k_B T \,. \tag{3.18}$$

For far-detuned atoms $|\Delta_A| \gg N g^2/\kappa$, i.e., when the total cavity mode shift by the atoms is much smaller than the cavity linewidth $N|U_0| \ll \kappa$, this translates to the following threshold on the pumping strength:

$$\eta > \eta^* = \sqrt{\frac{k_B T}{\hbar \kappa}} \frac{\kappa |\Delta_A|}{\sqrt{N} g} \sqrt{2} \,. \tag{3.19}$$

This approximation of the critical value η^* is in good agreement with the simulations shown on Fig. 3.5, giving $\eta^* = 35.4\gamma$, which differs by less than γ from the actual value. To make the physical content more transparent, this condition can be expressed in terms of the transverse pumping power density (energy/unit area/unit time) as

$$P_{\text{in}} > k_B T \left(\frac{\Delta_A}{\gamma} \right)^2 \kappa \frac{4k^3}{3N/V} \,. \tag{3.20}$$

As shown in the next Section, the condition (3.19) amounts to requiring that the potential depth along the cavity axis of a self-organized checkerboard pattern exceed significantly the energy scale of thermal fluctuations.

3.4.3 Critical exponent

The stability analysis of the uniform distribution of atoms $\rho(z) = 1/\lambda$ has revealed the critical value of the pumping strength η^*. Moreover, we have seen that for $\eta \approx \eta^*$, the relevant perturbation gives

$$\rho(z) = 1/\lambda + \epsilon \cos(kz)/\lambda. \tag{3.21}$$

Going beyond first-order perturbations, the above formula allows us to solve Eq. (3.14) self-consistently.

Pumping the atoms slightly above threshold, $\eta = \eta^*(1+\delta)$, with $\delta \ll 1$, we expect (3.21) to give a good approximation of $\rho(z)$, with ϵ depending nonlinearly on δ. Substituting it into (3.14) we need to expand the exponential to third order to obtain a solution to lowest order in the small parameters. This analytical calculation yields $\epsilon \propto \delta^{1/2}$, i.e., above the critical value ϵ increases from 0 as the square root of the dimensionless excess pumping strength. The order parameter $\theta = \epsilon/2$ and the percentage of majority atoms $(2\epsilon/\pi)$ both depend linearly on the small parameter ϵ. Therefore, the analytical result shows the critical exponent of this phase transition to be $\frac{1}{2}$.

3.5 Numerical simulations of the phase transition

In the mean-field description of the steady state, the number of atoms enters only in the form of the atomic density $N/V \propto Ng^2$. The approximation is expected to be valid in the thermodynamic limit, i.e., $N \to \infty$ with the atomic density and the cavity loss rate constant. Trying to approach this limit in simulations of Eq. (3.4) we are in for a surprise. In Fig. 3.6, we show the measured percentage of defect atoms after 4 ms of simulation time as a function of the pumping laser strength. The thermodynamic limit is approached in three steps, $N = 50, 200$, and 800. The parameters are the same as in Fig. 3.5, the atoms had random initial velocities from a thermal distribution with average kinetic energy $\hbar\kappa$. The initial positions were either uniformly distributed ("up") or at "odd" points of maximal coupling ("down"). In this controlled way we mimic the ramping of the laser power. Although the "down" curves show reasonable agreement with the mean field result, the "up" curves scale anomalously: a hysteresis is observed, whose breadth increases with the atom number.

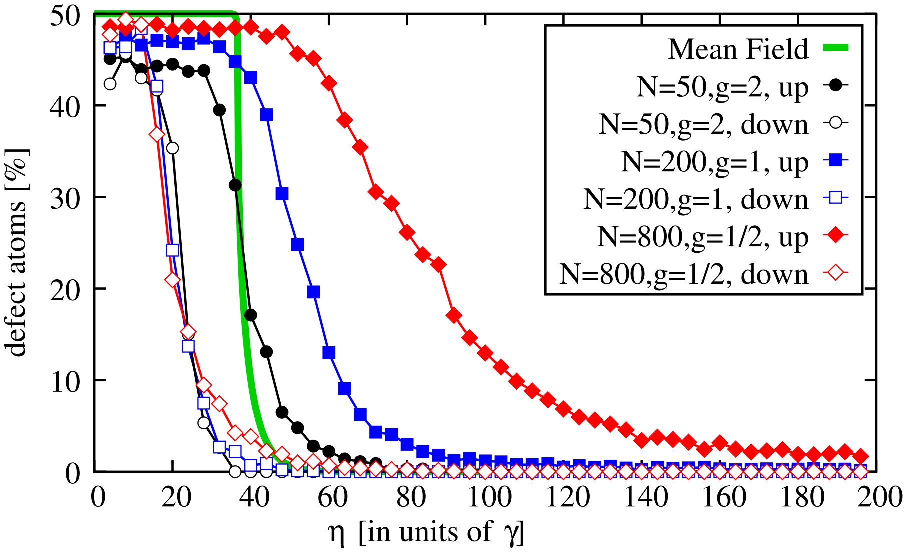

Figure 3.6: Ratio of defect atoms against pumping strength η, 4ms after the loading of the trap with a uniform ("up") or organized ("down") gas of atoms. The different curves show the approach towards the thermodynamic limit. The parameters are the same as in Fig. 3.5.

The hysteresis effect observed in Fig. 3.6 but absent from the mean-field prediction is due to the long timescales associated with reaching a steady state. In fact, thermal fluctuations do not only alter the equilibrium solution by smoothing out the concentration differences due to the dynamics (this is correctly rendered by the mean field approach), but they can also delay significantly the onset of that equilibrium. This slowing down is effective if the energy scale of thermal fluctuations is at least of the same order as the potential diffences due to the statistical fluctuations in the initial positions of the atoms.

The statistical fluctuations for a finite uniformly distributed atomic ensemble lead to $(N - \delta N)/2$ atoms around the $kz = 2n\pi$ and $(N + \delta N)/2$ atoms are around the $kz = (2n+1)\pi$ positions. Taking uniform distributions around the respective antinodes, we have $\sum \cos(kz_i) \approx 2\delta N/\pi$ and $\sum \cos^2(kz_i) \approx N/2$. The potential difference then reads

$$\Delta E = 2\,|U_1| = \hbar I_0 \frac{8\delta N}{\pi}(\kappa - N|U_0|/2) = \hbar \frac{4\delta N}{\pi}\frac{\eta^2 g^2}{\kappa \Delta_A^2}\,. \tag{3.22}$$

For the final expression in the second line, we considered the far-detuned regime, $|\Delta_A| \gg \gamma \sim \kappa \sim g$, and $N|U_0|, N\Gamma_0 \ll \kappa$.

The self-organization occurs "instantly" if the trap depth originating from the statistical fluctuations exceeds the average kinetic energy $k_B T$ of the atoms. Using the expectation value of the finite-size fluctuations, $\delta N \approx \sqrt{N}$, we obtain

$$\eta > \eta_\uparrow = \sqrt{\frac{k_B T}{\hbar\kappa}}\frac{\kappa\,|\Delta_A|}{N^{1/4} g}\frac{\sqrt{\pi}}{2}. \tag{3.23}$$

Comparison with (3.19) gives $\eta_\uparrow = \sqrt{\pi/8}\,N^{1/4}\,\eta^*$: the functional dependence of the two thresholds on the physical parameters are the same, except for the "anomalous" scaling of $\eta_\uparrow$ with N as the thermodynamic limit is approached.

To check the laboratory timescale threshold for self-organization (3.23), we performed simulations with the same physical parameters as in Figs. 3.5 and 3.6, starting from uniformly distributed atoms, but this time increasing the atom number with $Ng^4 = \text{const}$. In Fig. 3.7, the percentage of defect atoms is plotted as a function of the pumping η. These numerical results confirm that the threshold depends on Ng^4, moreover, the value $\eta_\uparrow = 83\gamma$ from (3.23) with $k_B T = \hbar\kappa$ is also consistent with the simulations. In the transition regime, there is a remarkable overlap of the curves corresponding to various number of atoms with keeping Ng^4 constant, indicating that the equilibration time also scales with Ng^4.

The "down" curves of Fig. 3.6 are invariant with respect to the thermodynamical limit, but the threshold they give is only 50–80 % of the mean-field prediction η^* of Eq. (3.19). Again, this can be explained with an argument based on the comparison of energy scales. Instead of the statistical fluctuations in the position distribution, we now have a well defined initial state: $\sum \cos kz_i = \sum \cos^2 kz_i = N$. The threshold $\Delta E > k_B T$ now gives the particularly simple result: $\eta > \eta_\downarrow = \eta^*/2$. This is slightly below the "down" curves of Fig. 3.6, the difference can be attributed to the nonoptimal coupling due to the position spread of the trapped atoms.

In the last curve of Fig. 3.7, $N = 3200$, the atom-cavity coupling g is the smallest parameter, and thus the system does not strictly realize the strong-coupling regime of cavity QED. In fact, self-organization does not depend on strong coupling: small g can be compensated by increasing the number of atoms. We remark that the experimental setup of [56] was also operated out of the strong coupling regime.

3.6 Stable defect atoms

The curve in Fig. 3.7 corresponding to $N = 3200$ deviates slightly from the other data and for large pumping strength it converges to a nonzero value of the defect atoms. In fact, for the parameters chosen there, defect atoms can be stably trapped at the minority sites of the checkerboard of maximally coupled points, which presents another important physical element of the system

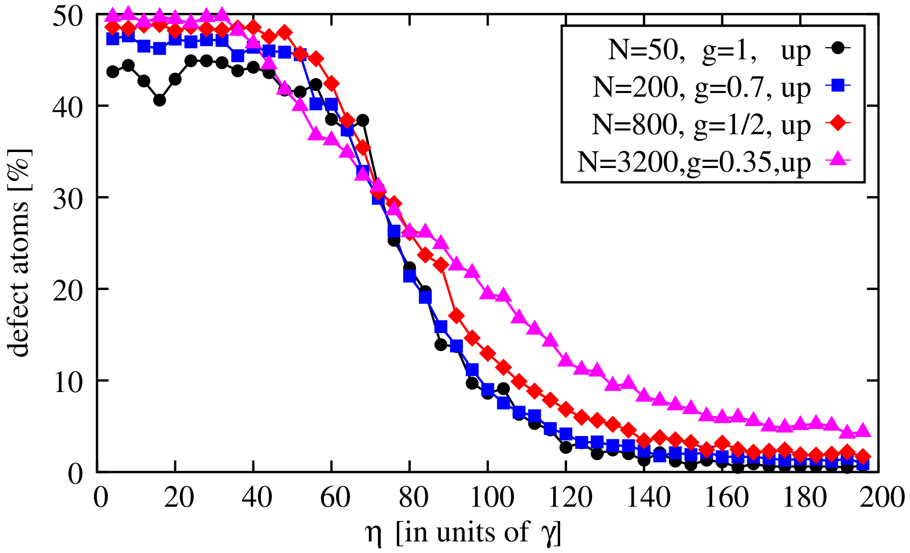

Figure 3.7: Ratio of defect atoms in the ensemble (measure of the spatial order) as a function of the control parameter η (given in units of γ). There is a clear threshold for self-organization which is independent of the atom number provided Ng^4 is kept constant. Parameters are the same as in Figs. 3.6 and 3.5.

beyond the capabilities of the simple mean-field theory. In the following we discuss the condition for the appearance of defects and the upper limit on their number.

For the analytical treatment of the defect atoms we use the 1D model of Section 3.4. If the atoms are perfectly self-organized, say, $kz_j = 2n_j\pi$ with integer n_j for every j, then the potential depths of Eqs. (3.8a) scale with the number of atoms as $U_2 = -N^2\, I_0\, |U_0|$, and $U_1 = -N\, 2I_0\kappa$. Thus, for large enough N, the $\lambda/2$-periodic potential is dominant and atoms can be trapped in the minority sites. These stable “defect” atoms reduce the superradiant scattering of the self-organized pattern.

How many defects can stably reside in the pattern? For simplicity, we take $N - M$ atoms exactly at $kz = 2n\pi$ and $M < N/2$ “defect” atoms at $kz = (2n+1)\pi$, neglecting the position spread. We then obviously have $\sum \cos(kz_i) = N - 2M$ and $\sum \cos^2(kz_i) = N$. Substituting this and the prescription (3.12) for the cavity detuning into (3.8a) we obtain

$$U_2 = -(N-2M)^2\, |U_0|\, \hbar I_0\ , \tag{3.24a}$$

$$U_1 = -2(N-2M)\hbar I_0 \kappa\ , \tag{3.24b}$$

$$I_0 = \frac{|\eta_{\text{eff}}|^2}{[\kappa + N\Gamma_0]^2 + \kappa^2}\ . \tag{3.24c}$$

Defect atoms can persist if at every $kz = n\pi$ there is a potential minimum:

$$0 < 2\,|U_2| - |U_1| = 2\hbar I_0 (N-2M)\,[(N-2M)\,|U_0| - \kappa]\ ,$$

which entails

$$\frac{N}{2} - \frac{\kappa}{2\,|U_0|} > M\ . \tag{3.25}$$

If some defect atoms appear, the rise in their number is limited by the above inequality. In particular, if the left-hand-side is negative, there can be no stable defects: the condition for the possibility of stable defects reads

$$N > N_{\text{thr}} = \frac{\kappa}{|U_0|}\ . \tag{3.26}$$

Note that this threshold is independent of the pumping strength. The maximum number of defects is limited by

$$M < M_{\mathrm{max}} = \frac{N - N_{\mathrm{thr}}}{2}. \tag{3.27}$$

Working at large atomic detuning, $|U_0| \approx g^2 / |\Delta_A|$, we find that defects can appear if the total mode frequency shift due to the atoms exceeds the cavity linewidth:

$$N g^2 > \kappa \, |\Delta_A| \, . \tag{3.28}$$

This inequality puts a lower bound on the atomic density. Equivalently, it amounts to an upper bound on the atomic detuning Δ_A: to avoid the occurrence of defects a large detuning can be chosen. This, $|\Delta_A| \gg N g^2/\kappa$, is exactly the "far-detuned" limit of the previous Sections, used to derive the thresholds η^*, $\eta_\uparrow$ and $\eta_\downarrow$. Likewise, none of the curves in Fig. 3.6 satisfy Eq. (3.28). On Fig. 3.7, however, the curve corresponding to $N = 3200$ is above the critical density (3.28).

For comparison to the full solution of the dynamics, we numerically simulated the equations (3.4) at fixed $\kappa = \gamma/2$, $g = 5\gamma/2$, $\Delta_A = -500\gamma$, and $\eta = 50\gamma$. The number of atoms was varied from 0 to 200, 25 runs with different random seeds were performed for each atom number for a duration of 5 ms. The conditions for self-organization derived in Sects. 3.4 and 3.5, give for this parameter setting a threshold atom number $N \gtrsim$ 10–40 (for $k_B T = \hbar\kappa$–$\hbar\gamma$).

The numerical results presented in Fig. 3.8 show that the ratio of defect atoms averaged over the 25 trajectories is well below 50%. For small atom numbers this is merely a "finite size" effect compatible with a balanced binomial distribution. For 15 atoms the defect ratio is still about half, for 18 atoms it is only a quarter of that expected from the uniform distribution. The ratio then drops down to the percent range, indicating stable self-organization, for 50 or more atoms. Concerning the appearance of defect atoms, Eq. (3.26) gives $N > N_{\mathrm{thr}} \approx 40$. Due to non-perfect bunching this threshold is shifted to somewhat higher values. The insert of Fig. 3.8 shows the absolute number of defect atoms after 5 ms, averaged over the runs: the minimum at $N \approx 60$ followed by a rise can be identified with the threshold, which is in accordance with the previous, simple estimate.

The transition from the perfectly ordered phase to the one where defect atoms can be present manifests itself in the statistical properties of the system. As discussed in Sect. 3.3, the appropriate measure of the thermal excitations is the phase space volume, given by the Heisenberg uncertainty product $\Delta z \Delta p_z/\hbar$. In Fig. 3.9, this is plotted as a function of the atom number: both the final phase space volume of individual runs after 5 ms (dots) and the average over these trajectories after 2, 3, 4 and 5 ms (continuous lines) are shown. For very few atoms, the phase space volume is scattered around the value of 13.4, corresponding to uniform spatial distribution and mean kinetic energy $k_B T = \hbar\kappa$. For $N \approx 50$, the decrease of the average phase space volume and the reducing variance around the mean show that the more stable the self-organized pattern, the less thermally excited the system is. At $N \approx 60$, a broad peak (due to the transition to a double well potential) heralds the appearance of stable defect atoms. This is followed by a slow but steady increase, which can be attributed to the rising percentage of defects.

To indicate some of the dynamics, Fig. 3.9 shows the Heisenberg product at earlier times as well: at 2, 3, and 4 milliseconds. The appearance of defect atoms slows down the equilibration process, but the respective curves converge uniformly to the one obtained at 5 ms. This demonstrates that the cooling time is closely independent of the atom number.

3.7 Collective effects in the self-organized phase

The most direct evidence of cooperative action is superradiance into the resonator mode that can be measured by detecting the power output from the cavity. In the self-organized checkerboard

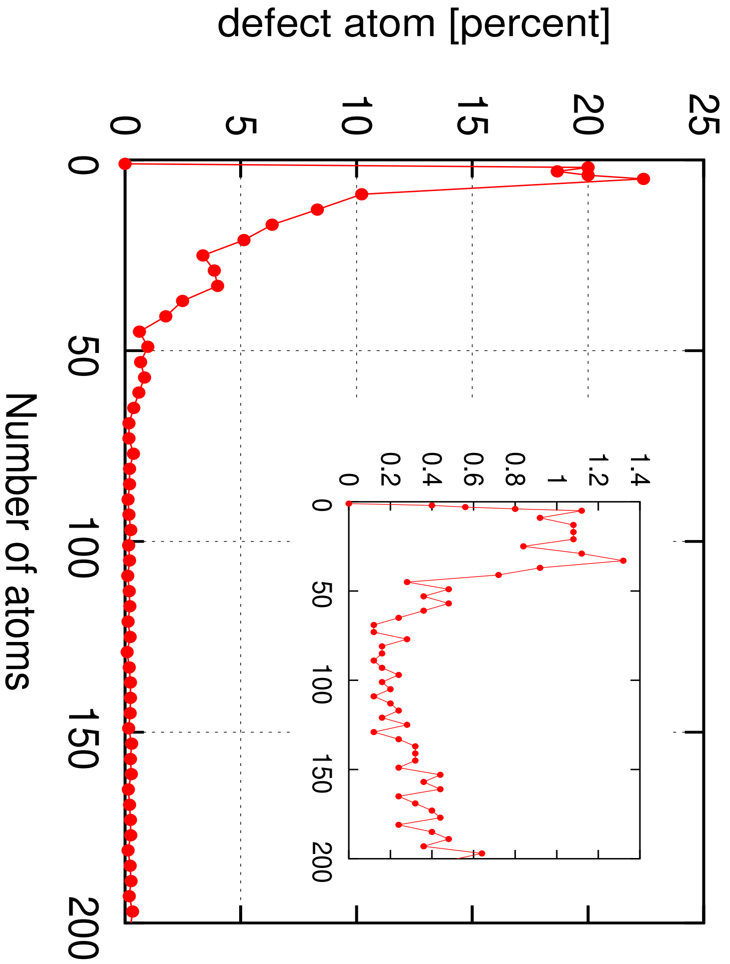

Figure 3.8: Defect atom ratio 5 ms after loading the trap as a function of the atom number. Each point is an average over 25 runs of the simulation. The inset shows the average number defects. The physical parameters are: $\kappa = \gamma/2$, $g = 2.5\gamma$, $\Delta_A = -500\gamma$, $\eta = 50\gamma$.

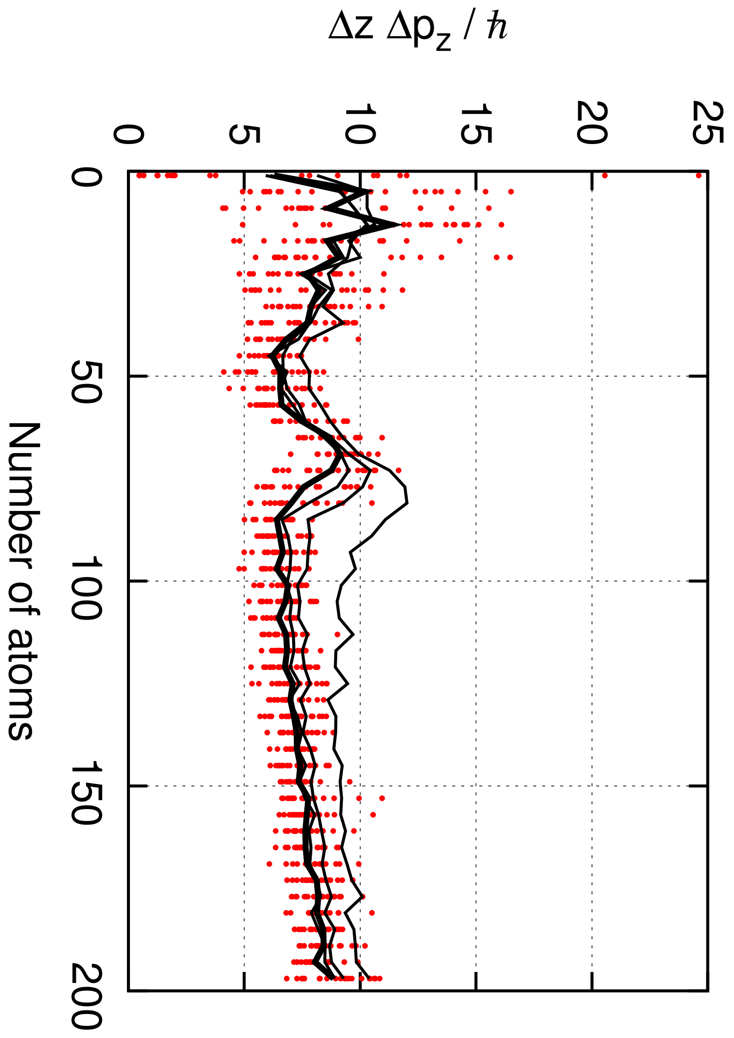

Figure 3.9: The normalized phase space volume of the system. Dots represent the values taken at individual trajectories at 5 ms, the thick solid line is their average. The thin lines correspond to the average over the trajectories at 2, 3, and 4 ms. The physical parameters are the same as in Fig. 3.8

pattern each atom radiates with the same phase, and so the cavity photon number $|\alpha|^2$ increases quadratically with the number of atoms. This can be observed in the numerical simulations of Eq.(3.4), gradually increasing the number of atoms as detailed in the previous Section. The cavity photon number is shown on a logarithmic scale in Fig. 3.10. For many atoms in the cavity ($N >$ 20) the intensity data are well approximated by the fitted quadratic function $|\alpha|^2 = 0.08N^2$. The steady-state solution of Eq. (3.4a) reads

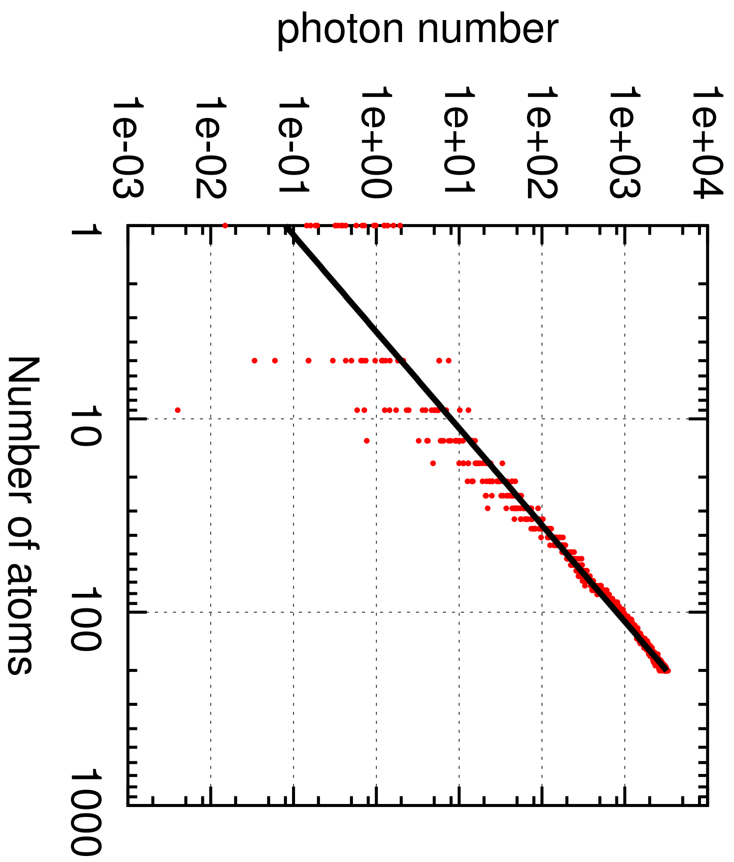

Figure 3.10: Photon number in the cavity 5ms after loading. At high atom numbers ($N > 20$) the simulation results (dots) are fitted well by a quadratic function (black line), indicating that the atoms scatter cooperatively. The physical parameters are the same as in Fig. 3.8

$$|\alpha|^2 = I_0 \left\langle \cos(kz_j) \cos(kx_j) \right\rangle^2 N^2 \; . \tag{3.29}$$

If all atoms are perfectly at the antinodes ($\left\langle \cos(kz_j) \cos(kx_j) \right\rangle^2 = \Theta = \mathcal{B} = 1$) this yields a coefficient of 0.125. The value from the simulations is 30% below this: the difference can be attributed to the position spread and to the defect atoms.

The superradiance has important effects on the spatial distribution of the atoms about their respective field antinodes. With increasing number of atoms the trap deepens so that the size of the atomic clouds about the antinodes is compressed, as shown in Fig. 3.11. We note again the

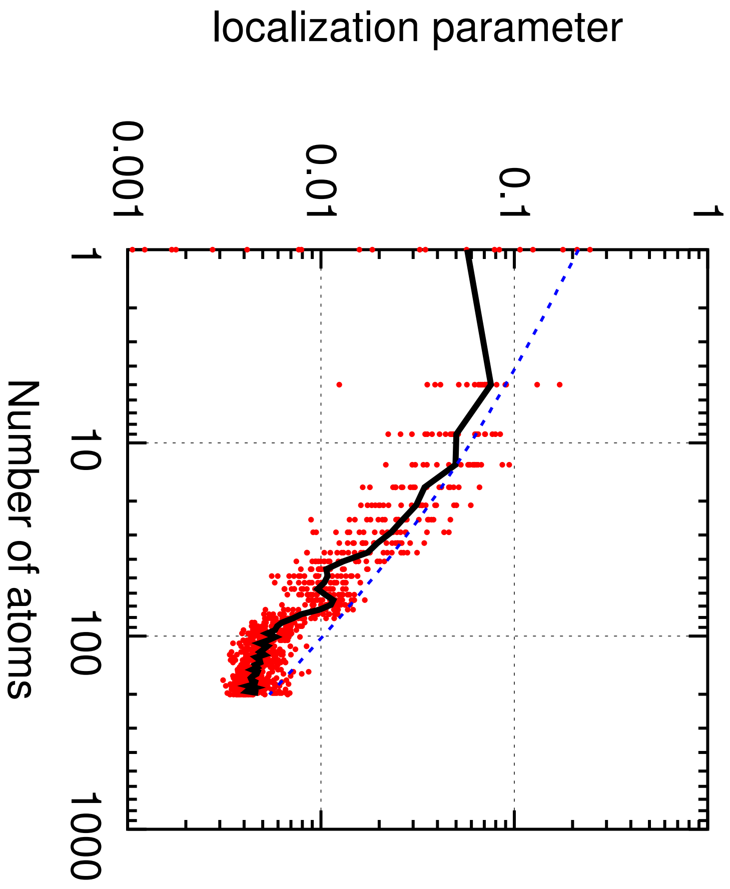

Figure 3.11: The localization parameter $\mathcal{D}_z = \sum_i (kz_i/\pi)^2/N$ measured by the simulation (dots) and averaged over runs (continuous black line) shows an overall $1/N$ dependence as a function of the atom number. The dashed line is the approximation of Eq. (3.31). The physical parameters are the same as in Fig. 3.8

appearance of the shoulder at $N \approx 60$ due to the transition into the double-well potential with stable defect atoms. Apart from this, the overall decrease of the localization parameter in the range $N = 10, \ldots, 200$ is proportional to $1/N$. As we show below, this scaling law can be derived by a careful examination of the self-generated trap potential.

We consider one-dimensional motion of the atoms in the limit where they are strongly localised in the vicinity of the antinodes. In this limit of harmonic oscillation the field amplitude in Eq. (3.4a) is coupled to the atomic positions only through the sum $\sum z_i^2$, i.e., through the localization parameter defined in Eq. (3.13). It is instructive to introduce new coordinates in the configuration space: the mean radius $r = \sqrt{\sum z_i^2/N}$, and a number of $N-1$ angular coordinates φ_j with canonically conjugate momenta $p_{\varphi j} = Nmr^2\dot{\varphi}_j$, these latter decoupled from the field dynamics. Only the radial motion is damped by the cavity cooling mechanism, the angular ones are not. For the coordinate r the potential is composed of the harmonic attraction $\propto r^2$ and a centrifugal repulsion $\propto 1/r^2$. There is a potential minimum and the radius is damped into it by cavity cooling. For large number of atoms the cloud size at an antinode can be simply estimated by the radius at the potential minimum. In this way we discard the role of fluctuations in this coordinate, assuming that the variance is much smaller than the mean.

For a quasi-stationary field amplitude, the harmonic potential is $m\nu^2 N r^2/2$ with vibration frequency

$$\nu = \sqrt{\frac{\hbar k^2}{m}\left(\frac{|U_0|\eta}{g}|\alpha| + 2|U_0||\alpha|^2\right)}\,. \tag{3.30}$$

The angular kinetic energies are of the form $p_{\varphi_j}^2/(2mNr^2)$, $j = 1, \ldots, (N-1)$. The momenta p_{φ_j} can be estimated by their initial value in the unorganized phase, when all degrees of freedom have the same energy $k_B T/2$ and the radius is $r = \lambda/\sqrt{48}$. The potential minimum is just at the radius where the harmonic potential energy equals the sum of the centrifugal energies. Simple algebra leads to the cloud size

$$r^2 \approx \frac{\lambda^2}{8\pi\sqrt{3}}\sqrt{\frac{k_B T}{\hbar|U_0|}}\left(\frac{\eta}{g}|\alpha| + 2|\alpha|^2\right)^{-\frac{1}{2}}\,, \tag{3.31}$$

and since $|\alpha|^2 \propto N^2$, the $1/N$ law for the localization parameter follows. Altogether, the increase in atom number results in a smaller cloud size in the vicinity of the antinodes, a very important virtue of the collective atomic action. This compression is limited by the dipole-dipole interaction of the atoms near the same antinode, which effect was not taken into account in the present model.

3.8 Conclusion

A dilute cloud of non-interacting cold atoms in a high-Q cavity can undergo a phase transition if driven from the side by a laser sufficiently red detuned from an atomic resonance. Increasing the laser power above a threshold the atoms self-organize into a lattice so as to scatter most effectively into the cavity mode. In this way the atoms minimize their energy in the optical potential generated from the interference pattern of the cavity and pump field. Under proper conditions the atoms are cooled in this process giving long term stability to the pattern.

The phenomenon has been previously seen in simulations and strong evidence was found in experiments [56], but threshold, scaling and efficiency of the effect with atom number, cavity parameters and system size remained unclear. Here we gave a thorough analytical discussion of the effect. A continuous density approach allowed us to derive analytical formulas for the critical pump power as a function of atom number and cavity volume and showed that the effect should persist if one scales up the volume at fixed atomic density, i.e., $Ng^2 = \text{const.}$ Numerical simulations of the evolution for finite durations revealed a hysteresis between the ordered and homogeneous density phase on varying the control parameter, i.e., the pumping strength. This shifts the observable threshold in the pumping strength, which then scales with Ng^4. We still have a cooling mechanism for large numbers of any type of optically polarizable particles.

The system is composed of non-interacting atoms that communicate via a commonly coupled, single cavity mode. The cavity component of the system plays a multiple role. First, the binding energy of the ordered phase is stored in the superradiantly enhanced field intensity of this single mode. Next, as an attractive feature of this system, the outcoupled field intensity directly serves as a possibility of time-resolved monitoring of the formation of the ordered phase. Note that in setups without resonator, the uncontrolled scattered field can lead to a binding of micrometer-sized particles in an ordered pattern in liquid [30, 93]. In the cavity scheme, finally, the viscous motion is provided by the dynamically coupled single-mode cavity field. Apart from the geometry, this is also a distinctive feature with respect to CARL.

From the laser cooling point of view, the picture is complicated by the phase transition. The appropriate measure of the cooling efficiency is the phase space volume occupied by the system. The self-organization process reduces this volume below that of a system at the cavity cooling limit with uniform spatial distribution. Moreover, the steady state is established within milliseconds, and this is closely independent of the number of atoms in the cloud (numerical simulations confirm this up to few hundreds of atoms). Collective cooling was previously known only for the stochastic cooling method [94] and has been predicted for common vibrational modes of trapped particles [95]. The collective behaviour strongly improves the localization, i.e., the size of the atom cloud pieces at the trapping sites is proportional to the inverse of the atom number.

This work could be extended to various directions. First of all, the numerical simulations should confirm some of the statements of the present paper on a larger range of the atom number, or on a longer time scale (e.g., the dependence of the hysteresis on the duration of the evolution). Our prescription for the pump-cavity detuning Δ_C in Eq. (3.12) is probably impractical in the limit of large atom numbers, as one has to go closer to the resonance in order to initiate the self-organization. Next, the maximum achiveable densities can not be determined in the present model as some of the limiting factors were omitted, e.g., vacum-mediated dipole-dipole interaction between the atoms, the eventual superradiant enhancement of the spontaneous scattering into lateral directions, etc. In extremely good cavities, quantum effects in the motion of the atoms begin to play an important role [96, 44], which was not studied here. Finally, the nature of the phase transition is strongly determined by the geometry of the cavity mode: the possible trapping sites are defined by the antinodes of the cavity mode and the transverse pumping field. This situation can be essentially modified in a cavities with different geometry, e.g., ring or confocal resonator.

Chapter 4

Publication: Self-organization of a laser-driven cold gas in a ring cavity

4.1 Self-organization in a Ring Cavity

The system is composed of a gas of N polarizable particles coupled to two degenerate optical modes of a ring resonator, described by the plane wave mode functions $f_1(x) = e^{ikx}$ and $f_2(x) = e^{-ikx}$, with coherent amplitudes α_1 and α_2. The particles are driven by a pump laser oriented perpendicular to the cavity axis. The electric field in the cavity is then given by $E(x) = f_1(x)\alpha_1 + f_2(x)\alpha_2 + E_{\text{pump}}$, where the last pumping field term is assumed to be constant along the resonator axis 'x'. For simplicity, we consider the system only along this spatial dimension: the atoms are supposed to be confined near the resonator axis by e.g. a strong dipole trap. The interaction is in the dispersive regime, i.e. the pump laser is very far detuned with respect to the resonance frequencies of the gas particles: no real excitations need take place. The gas can then in principle even be composed of molecules, but we refer to the gas particles as "atoms". The atoms redistribute photons by coherent scattering between the two modes and the pump field. This process feeds the cavity modes with an effective amplitude η. The dynamics of the cavity modes with the scatterers at x_j, $j = 1...N$ is given by the following differential equations [25]:

$$\frac{d}{dt}\begin{pmatrix}\alpha_1\\ \alpha_2\end{pmatrix} = \mathbf{A}\begin{pmatrix}\alpha_1\\ \alpha_2\end{pmatrix} - i\eta\sum_{j=1}^{N}\begin{pmatrix}f_1^*(x_j)\\ f_2^*(x_j)\end{pmatrix}, \tag{4.1}$$

using a formal vector notation, with the coupling matrix

$$\mathbf{A} = \begin{pmatrix} i(\Delta_C - NU_0) - \kappa & -iNU_0\sigma \\ -iNU_0\sigma^* & i(\Delta_C - NU_0) - \kappa \end{pmatrix}. \tag{4.2}$$

The diagonal terms include the detuning between the pump laser and the cavity modes, $\Delta_C = \omega - \omega_C$, the cavity decay rate κ, and the shift of the cavity resonance with an amount of U_0 per atom. This shift is due to forward scattering and is related to the atomic properties by $U_0 = -\omega_C\chi'/\mathcal{V}$, where χ' is the real part of the linear polarizability and $\mathcal{V}$ is the mode volume. The total frequency shift due to the polarized gas, expressed in terms of a dimensionless collective coupling parameter $\zeta = NU_0/\kappa$, will later be used to describe the density of the atom cloud (neglecting a filling factor). The off-diagonal terms, i.e. the coupling between the cavity modes stems from the stimulated back reflection off the gas. This process is heavily dependent on the positions of the atoms, through the complex parameter $\sigma = \frac{1}{N}\sum_j e^{-2ikx_j}$ describing spatial order. Similar to the Debye-Waller factor, $|\sigma|$ is 1 if the gas forms a perfect lattice with period of an integer multiple of $\lambda/2$, and less than 1 for a non-perfect lattice; for a homogeneous gas, it is $|\sigma| \propto 1/\sqrt{N}$. The phase of σ gives x_0, the "position of the lattice" modulo $\lambda/2$, with the definition $\sigma = |\sigma|\, e^{-2ikx_0}$.

Interaction between the gas and the cavity field lifts the degeneracy of the cavity modes. The eigenmodes of the cavity are

$$h_-(x) = \sin k(x - x_0)\ , \quad h_+(x) = \cos k(x - x_0)\ , \tag{4.3}$$

these have nodes ($h_-(x)$), or antinodes ($h_+(x)$) at $x_0 + n\lambda/2$, respectively. The corresponding amplitudes,

$$\beta_- = ie^{ikx_0}\alpha_1 - ie^{-ikx_0}\alpha_2\ , \quad \beta_+ = e^{ikx_0}\alpha_1 + e^{-ikx_0}\alpha_2\ , \tag{4.4}$$

are not coupled by the interaction with the atom gas. The frequencies of the eigenmodes h_- and h_+ are shifted with respect to the empty cavity, giving the effective detunings

$$\Delta_- = \Delta_C - (1 - |\sigma|)NU_0\ , \quad \Delta_+ = \Delta_C - (1 + |\sigma|)NU_0\ . \tag{4.5}$$

With the atoms at fixed positions x_j, the mode amplitudes take on the stationary values

$$\beta_- = \frac{2\eta}{\Delta_- + i\kappa} \sum_j \sin k(x_j - x_0)\ , \quad \beta_+ = \frac{2\eta}{\Delta_+ + i\kappa} \sum_j \cos k(x_j - x_0)\ . \tag{4.6}$$

If the atoms are uniformly distributed, both amplitudes vanish by destructive interference of the components scattered by different atoms (kx_0 is an arbitrary phase in this case). If the polarized gas roughly forms a lattice with period λ (x_0 giving the position of the lattice modulo $\lambda/2$), mode h_- will only be weakly coupled to the pump laser, since it has nodes at the lattice points. On the contrary, mode h_+ has antinodes at the atomic positions and thus is driven via stimulated Bragg scattering off the gas [84, 56].

The possibility of optical trapping of high field seekers with negligible spontaneous emission loss requires large red detuning, whereby the resonance shift U_0 is negative. It is known from cavity cooling theory that the pump field has to be detuned below the cavity frequency to ensure damped motional dynamics [25]. For large enough density ζ, however, if the polarized gas forms a more and more periodic structure, $|\sigma|$ increases from 0 to 1, and the frequency of mode h_+ may drop below the pump frequency, i.e. Δ_+ may become positive. This yields heating and instability of the gas. The effect is all the more prominent since at $\Delta_+ \approx 0$ the population of mode h_+ is resonantly enhanced. We will discuss ways to avoid this problem and the effect of the detuning Δ_C and the density ζ on the dynamics below.

4.2 The dynamics of the atoms

Up to this point, the polarized gas was considered as inert background against which the dynamics of the cavity field takes place. Now we relax this assumption, and treat the distribution of the gas particles as a dynamic quantity. As the gas particles move little on the characteristic timescale of the buildup of the cavity field, κ^{-1}, the atomic and cavity dynamics can be separated adiabatically, in a way reminiscent of the Born-Oppenheimer approximation for molecules. The motion of the gas particles is governed by the forces from the light field that depends on their positions. Since the field is far detuned from the atomic resonance, scattering into other than the cavity modes is negligible so that the motion of the particles is solely determined by the dipole force [65]. This can be decomposed into two terms: $F(x) = F_c(x) + F_p(x)$, with

$$F_c(x) = 4\hbar k U_0 \mathrm{Im}[e^{2ikx}\alpha_1\alpha_2^*]\ , \tag{4.7a}$$

$$F_p(x) = 2\hbar k \mathrm{Im}[\eta(e^{ikx}\alpha_1 - e^{-ikx}\alpha_2)]. \tag{4.7b}$$

The first term arises from stimulated transfer of photons between the counterpropagating plane-wave modes of the cavity, and the second term from stimulated transfer of pump and cavity photons. In the limit of high particle number N, the back-action of a single particle on the cavity field is negligible, and we can integrate the forces to arrive at the potential governing the dynamics. Using the eigenmodes $h_-(x)$ and $h_+(x)$ we have

$$\begin{aligned} V(x) = 2\hbar\eta\Big(\mathrm{Re}\beta_- \sin k(x-x_0) + \mathrm{Re}\beta_+ \cos k(x-x_0)\Big) + \\ + \frac{1}{2}\hbar U_0\Big((|\beta_+|^2 - |\beta_-|^2)\cos 2k(x-x_0) + 2\mathrm{Re}[\beta_+^*\beta_-]\sin 2k(x-x_0)\Big)\ . \end{aligned} \tag{4.8}$$

The first line corresponds to scattering from the pump into the cavity: if the gas forms a λ-periodic grating, this describes a potential with attractive points at the lattice sites, i.e. the gas density maxima. The second line originates from multiple scattering between the running wave modes. This latter has a strong dependence on the density and causes deviations from a medium with linear refractive index: it attracts particles to maxima of the cavity field, and can create defects in the lattice, as explained later on.

4.3 Mean field approximation

For a large number of atoms but each of them weakly coupled to the cavity modes, the cloud can be treated by a mean field approach using a continuous position distribution $p(x)$. In the present model we phenomenologically add that the cloud has a finite temperature, microscopic calculations reveal that it is on the order of $k_BT = \hbar\kappa$. The thermodynamic limit then corresponds to taking a large cavity with mirrors whose reflectivity is scaled down with cavity length, homogeneously filled with the gas. The cavity length is limited by the requirement of large longitudinal mode spacing (as mentioned in the introduction). In this limit, we can apply the canonical distribution to the gas, giving

$$p(x) = \frac{1}{Z}\exp\left(-\frac{V(x)}{k_BT}\right), \tag{4.9}$$

with the partition function Z ensuring normalization $\int p(x)dx = 1$. Now since $V(x)$ depends on the mode amplitudes β_- and β_+, and these latter depend on the distribution $p(x)$ of the scatterers, eq. (4.9) has to be solved self-consistently.

Numerical solutions to the implicit equation (4.9) can be found by iterating the following steps. (i) Start from a random distribution $p^{(0)}(x) = \lambda^{-1} + \xi(x)$, where $\xi(x)$ is white noise: $\langle\xi(x)\xi(x')\rangle = \epsilon\delta(x-x')$, with amplitude $\epsilon \ll \lambda^{-2}$. (ii) Obtain from (4.6) the steady-state mode amplitudes $\beta_{1,2}$ for the given distribution $p^{(0)}(x)$. (iii) Calculate the dipole potential $V(x)$ by substituting $\beta_{1,2}$ into (4.8). (iv) The canonical distribution eq. (4.9) furnishes the new distribution $p^{(1)}(x)$ with which the procedure can be restarted. If the iterations converge, we obtain a self-consistent solution of (4.9), $p(x) = p^{(\infty)}(x)$. For weak pump amplitude η, this solution is the uniform distribution of the gas, $p(x) = \lambda^{-1}$. Above a certain threshold η_c, the uniform distribution is no longer stable and a nontrivial $p(x-x_0)$ builds up, with x_0 depending on the initial fluctuations. Fig. 4.1(a) shows this transition with a plot of the spatial order $|\sigma|^2$ as a function of the pumping strength. The narrowing of the "self-organized" density distributions is shown in fig. 4.1(b) using two specific values for the pump η above threshold.

The critical pump amplitude η_c can be determined analytically by a stability analysis of the uniform distribution. The only relevant Fourier components of a perturbation are those with period λ, as only these affect the amplitudes $\beta_\pm$: we can therefore take $p^{(0)}(x) = \lambda^{-1}[1 + \epsilon A\cos k(x - x_0) + \epsilon B\sin k(x-x_0)]$, with arbitrary x_0. The condition of stability then becomes that the

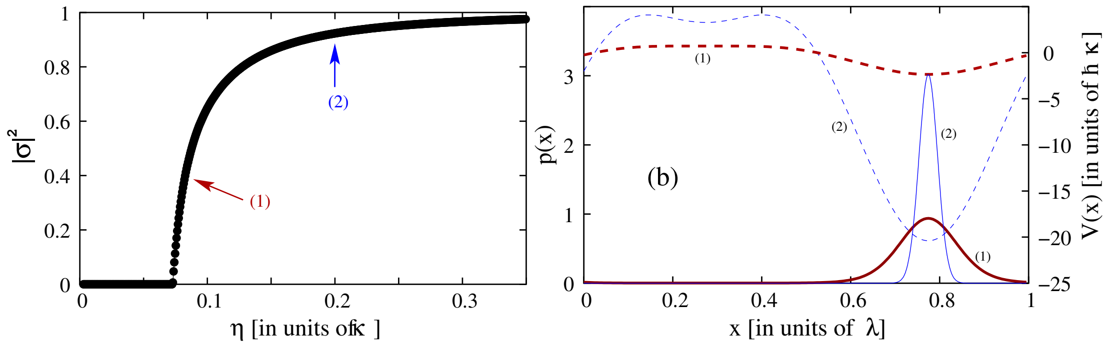

Figure 4.1: (a) Square of the order parameter $|\sigma|^2$ as a function of the effective pumping strength η. (b) Two typical atomic position distributions (solid lines) and the corresponding adiabatic potentials (dashed lines) for the specific pump strengths indicated by the arrows in (a), $\eta = 0.08\kappa$ (thick, marked by (1)) and $\eta = 0.2\kappa$ (thin, marked by (2)). Parameters: $\Delta_C = -4\kappa$, $\zeta = 1.2$, $U_0 = -0.004\kappa$.

magnitudes of A and B decrease during a single iteration of eq. (4.9) to first order in ϵ. For both A and B this translates to the condition $\eta < \eta_c$, with the critical pump amplitude

$$\eta_c = \sqrt{\frac{k_B T}{\hbar\kappa}}\sqrt{\frac{\kappa\,|U_0|}{\zeta}}\sqrt{\frac{\delta^2+1}{2\,|\delta|}}\,. \tag{4.10}$$

$P_L \geq c\kappa\frac{k_BT}{\hbar\omega}\left(\frac{N}{V}\chi'^2\right)^{-1}\frac{\delta^2+1}{2\delta}$ Here we use $\delta = (\Delta_C - NU_0)/\kappa$. The lowest pump power allowing for self-organization to happen is at the detuning $\delta = -1$, i.e. $\Delta_C = NU_0 - \kappa$.

As hinted in the introduction, this light-matter system is of particular interest because of the highly nonlinear dependence of the dynamics on the density of atoms. The order $|\sigma|^2$ as a function of the density parameter ζ at fixed pumping strength $\eta = 0.1\kappa$ is plotted in fig. 4.2(a). In accordance with eq. (4.10), below a critical density ζ_c the uniform distribution is stable. At densities $\zeta > \zeta_c$, where the pump is above threshold, a rough but surprisingly good approximation is that the atoms form a perfect lattice of period λ, which from eq. (4.8) gives for the potential:

$$V(x) \approx -\hbar\frac{2N\kappa\eta^2}{\Delta_+^2+\kappa^2}\Big(\frac{-2\Delta_+}{\kappa}\cos k(x-x_0) + \zeta\cos 2k(x-x_0)\Big)\,. \tag{4.11}$$

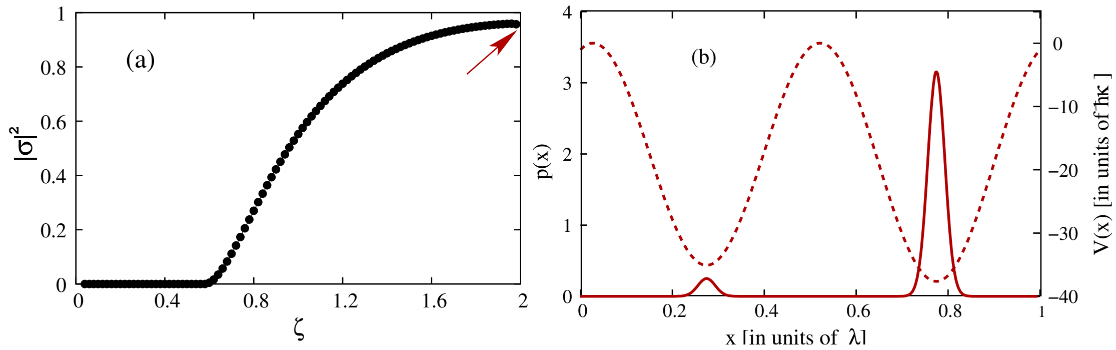

Figure 4.2: (a) Square of the order parameter as a function of the density of cloud (expressed by the collective coupling ζ) at a fixed pumping strength, $\eta = 0.1\kappa$, and detuning $\Delta_C = -4\kappa$, atomic light shift $U_0 = -0.004\kappa$. (b) The position distribution $p(x)$ showing "defect" atoms (solid line) and the self-consistent mean-field potential $V(x)$ (dashed line) for $\zeta = 2$, as indicated by the arrow on (a).

The lattice is defined by the first term having attractive minima at $kx = kx_0 + 2n\pi$. Due to the second, density-dependent term, a secondary peak can build up in the atomic density at $kx = kx_0 + (2n+1)\pi$, roughly for $\zeta > -\Delta_C/(4\kappa)$. "Defect" atoms can then appear in the lattice which radiate into the cavity mode h_+ in opposite phase with the atoms being at x_0, thus decreasing the photon number. However, in a thermal distribution these sites are hardly occupied such that the order parameter does not indicate this transition, which is at $\zeta = 1$ in the numerical example of fig. 4.2(a). The distribution $p(x)$ shows the presence of defects but is still dominated by a single peak around x_0 whose width decreases with increasing pump power.

At even higher optical densities, pumping above the threshold results in an instability of the atom cloud – this is the reason why the curve in fig. 4.2(a) is only plotted up to $\zeta = 2$. The iterations of eq. (4.9) no longer converge, but enter a loop of flipping between two localized distributions which differ in a shift by $\lambda/2$. This indicates a frustration of the system: when more atoms happen to be, say, close to the positions $x = x_0 + n\lambda$, for $\Delta_+ > 0$ they create a potential favoring the sites at $x = x_0 + (n + \frac{1}{2})\lambda$. The detuning Δ_+ becomes positive at large pump power when $\zeta > -\Delta_C/(2\kappa)$, which in fig. 4.2(a) corresponds to $\zeta > 2$. Note that in fig. 4.2(b), presenting a still stable, but markedly two-peaked distribution, the potential depths at the two possible sites become very close to each other.

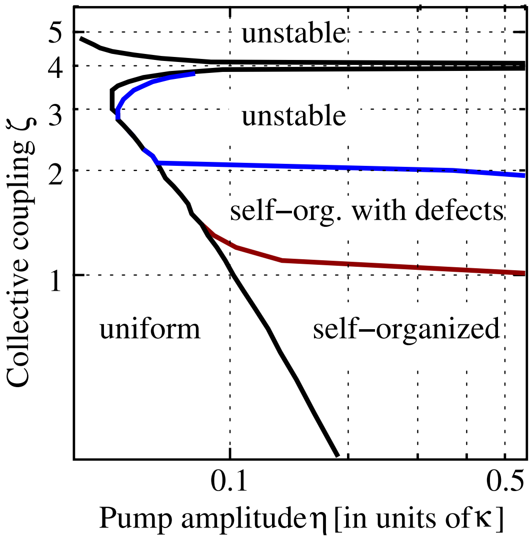

Figure 4.3: Phase diagram for fixed $\Delta_C = -4\kappa$ and $U_0 = -0.004\kappa$. The four regimes are indicated on the log-log plane of the dimensionless pumping strength η/κ and the optical density expressed in terms of the collective coupling parameter ζ.

We summarize the numerical results on a phase diagram in fig. 4.3. Choosing a fixed pump-cavity detuning, $\Delta_C = -4\kappa$, two parameters, namely the dimensionless optical density ζ and the pumping strength η/κ determine the equilibrium distribution. A complete map of sharply separated regimes, "uniform distribution", "self-organized lattice", "lattice with defects" (i.e. where the potential in the steady state has secondary minima, allowing the existence of defect atoms), and "no convergence", are presented. The overall $\eta_c \propto \zeta^{-1/2}$ dependence of the stability limit of the uniform distribution, see eq. (4.10), shows up clearly in this log-log plot. The unstable region is cut by a sharp resonance at $\zeta = 4$, which corresponds to the density where the detuning $\Delta_C = NU_0$. In accordance with eq. (4.10), this density leads to $\delta = 0$ and yields a divergence of the critical pump amplitude. For this setting the uniform distribution is stable against infinitesimal perturbations, no matter how strong the laser pump is. Finite fluctuations can, however, be amplified and for strong pumping the uniform distribution does become unstable. The other region boundaries are in good agreement with the analytical results for large η ($\zeta \approx 1$ and $\zeta \approx 2$), and are parallel with the η axis in the large η limit. This is due to the fact that in this limit the density distribution is sharply peaked, and then practically all η does is to set the potential depth, but not change the shape.

4.4 Conclusion

By mean-field analysis we revealed the various phases of an ensemble of cold atoms which are strongly coupled to the radiation modes of a lossy ring cavity and off-resonantly driven by a transverse laser. The interaction of linearly polarized particles with light is demonstrated to be strongly nonlinear in the large intensity and large density limit. In the proposed system of homogeneously pumped atoms moving along the axis of a ring resonator, both dependences are well resolved and the role of the density-dependent multiple photon scattering which is the source of nonlinearity is well displayed. A complete phase diagram has been obtained where the phase boundaries are interpreted by simple physical arguments.

The work was supported by the National Scientific Fund of Hungary (Contract Nos. T043079, T049234) and the Bolyai Program of the Hungarian Academy of Sciences. We acknowledge funding from the Austrian Science Foundation (P17709 and S1512).

Part II

Optomechanical coupling in the super-strong coupling regime

Chapter 5

Background

In the second Part of this Thesis we explore the interaction due to optomechanical coupling in systems where the theoretical approach of the first Part cannot be applied. Again, the Chapters contain their own introductions, however, it is useful to provide the background and the basic ideas here.

Quite generally, optical manipulation of the motional state of objects relies on the modification of the propagation of light by matter. As seen in the first Part, it is the deflection of photons that gives rise to the forces acting on the object. However, to talk of *photons*, one first needs to define the *modes* of light, whose excitations can be quantized. In the context of atomic physics, the choice of modes is usually straightforward: in free space, the modes are given by the type of laser used, whereas in a high-Q optical cavity, they are defined by the boundary conditions due to the cavity mirrors. In the case of the resonator modes, the back-action of the atoms on the light manifests itself by a shift of the eigenfrequency of these modes that varies according to the position of the atoms.

We must be conscious of the fact that taking a *fixed mode function*, independent of the density distribution of the atoms, is always an approximation. In many cases, this approximation can work very well. However, if the number of trapped atoms is very large, and if their effective scattering cross-section is substantial, this is no longer the case. For the case of atoms in cavities, the approximation can be said to break down when the frequency shift due to the presence of all the trapped atoms together is comparable to the free spectral range. Equivalently, it breaks down if by reconfiguring the positions of the trapped atoms, one can shift the atoms+cavity coupled system from one resonance to the next. Clearly, in this case the forces on the atoms cannot be described by assuming a fixed mode function. In a recent article by Meiser and Meystre [97], this situation is referred to as the “super-strong coupling” regime.

As recent experiments are approaching the “super-strong coupling” regime [83, 98, 29], setting up the proper theoretical framework for such systems is a pressing task.

Assessing the possibilities for the appearance of band gaps in 1-dimensional optical lattices, in 1995 Deutsch et al. have proposed a model [36], where the back-action of atoms on the light is taken into account. They treated the trapped atoms as Dirac-delta concentrations of polarizability, and calculated the propagation of light solving the Helmholtz equation to all orders in multiple scattering, via the transfer matrix method. The lattice constant was then found self-consistently, claiming that “Since this configuration is self-consistent, with zero net force on the atoms, it must represent a state of minimum potential energy”.

In a pair of recent articles [99, 97], Meiser and Meystre have applied this model to atoms trapped in a high-Q standing-wave cavity in the super-strong coupling limit. Based on the minimization of the dipole energy, they have predicted a bistability of the atoms+cavity system. However, we believe that this approach is flawed. In a Comment to their papers, which is reproduced in Chapter 6, we have shown that this system is not expected to minimize the dipole Hamiltonian in steady state, and this invalidates the prediction for bistability.

How should one model the dynamics of the trapped atoms in the "super-strong coupling" regime? Instead of searching for an "energy funtion" to be minimized, one should compute the optical *forces*, as done for atoms in cavities. There, the conservation of momentum was used when the force was calculated based on "photon counting", and this should form the basis for the force calculations here as well. Following a well-established approach, we can find the force on the trapped particles by examining the rate of momentum extraction from the electromagnetic field. This can be calculated using the Maxwell Stress Tensor [100],

$$T_{ij} = \epsilon E_i E_j + \mu H_i H_j - \frac{1}{2}\delta_{ij}\left(\epsilon E^2 \mu H^2\right), \tag{5.1}$$

where i, j denote Cartesian coordinates. To find the force, we need to integrate the Stress Tensor on an arbitrary surface enclosing the trapped particle. This approach has been used, e.g., to find the stationary configuration of arrays of microspheres in 3 dimensions [101] and of rods in 2 dimensions [102]. We note here that although the momentum of the electromagnetic field in dielectric media has been the subject of a long debate, there are clear reasons to write this formula for the stress tensor, as summed up in [103].

To obtain the Maxwell Stress Tensor, one needs to calculate the electromagnetic fields around an object, which can be a very involved task. A hallmark of the "super-strong coupling" regime is that multiple scattering plays an important role, and thus the field has to be calculated self-consistently. In 2 or 3 dimensions, this is a highly nontrivial task [104, 105], but in the simple 1-dimensional model systems studied here the transfer matrix method as used in [36] is perfectly adequate. For further discussion, see Chapter 7.

One could expect that once having mapped out the forces as functions of the positions of the scatterers, we can "reverse engineer" a potential by integrating these forces, as done in Chapter 2 for two atoms in a cavity. However, this is not always possible, as there is no guarantee that the value of the potential does not depend on the path of integration. Already in the simple case of Chapter 2, if the laser is shone at the atoms "transversely" instead of feeding the cavity directly, no such potential can be produced. Curiously, we find in Chapter 7, that for 1-dimensional optical lattices, the existence of a potential depends on the relative power of the laser beams used to form the trap.

Chapter 6

Publication: Comment on ”Coupled dynamics of atoms and radiation-pressure-driven interferometers” and ”Superstrong coupling regime of cavity quantum electrodynamics”

In two recent articles [99, 97], Meiser and Meystre describe the coupled dynamics of movable atoms, mirrors and light in a pumped optical cavity. They take the effect of the atoms on the light field into account using a 1-dimensional non-perturbative model introduced by Deutsch et al. [36]. The mechanical effects of the off-resonant light on the atoms are described by a dipole Hamiltonian. They claim that the atoms trapped in the cavity field self-organize to form a regular lattice of atom clouds which behaves as a beam splitter (BS). This BS effectively splits the single cavity into two coupled resonators (“left” and “right”). An important prediction of [99, 97] is a bistability effect: optical forces will push this “atom BS” to a position where it is approximately an integer multiple of the half-wavelength away from the left (right) cavity mirror. Thus for a certain parameter regime the “left” (“right”) cavity is on resonance with the pump laser, and has intense light, while the other cavity has weak field.

We argue that the model used by Meiser and Meystre contains contradictions and errors involving the way the dynamics of the atoms (taking place on a much shorter timescale than that of the movable cavity mirror in [99]) is treated. The model hinges on two key assumptions. The first is a claim based on [36]: (i) *the gas of atoms forms a regular lattice of pancake-shaped clouds with lattice constant* $d_0 = \lambda/2(1 + 2\,\tan^{-1}\Lambda/\pi)$*, and can thus be replaced by a fictitious “atom BS”.* Here $\Lambda = k\eta\alpha/(2\epsilon_0)$ is the dimensionless polarizability density of a cloud of surface density η composed of atoms of polarizability $\alpha < 0$, with $k = 2\pi/\lambda$ denoting the free-space wavenumber of the pump laser. The second assumption is used to find the steady state position of the atom BS: (ii) *the atoms strive to minimize the total dipole potential* H_{int} *(eq. (2) of [99], or eq. (3) of [97]).* In this Comment we show that these assumptions are inconsistent, and that (ii) has to be replaced by a formula for the *force* on the atoms. We present the required expression for the force which allows us to determine the steady state of this system. This does not exhibit the bistability phenomenon of [99, 97].

The setup considered in [99, 97] is an open system: laser light enters the cavity through the

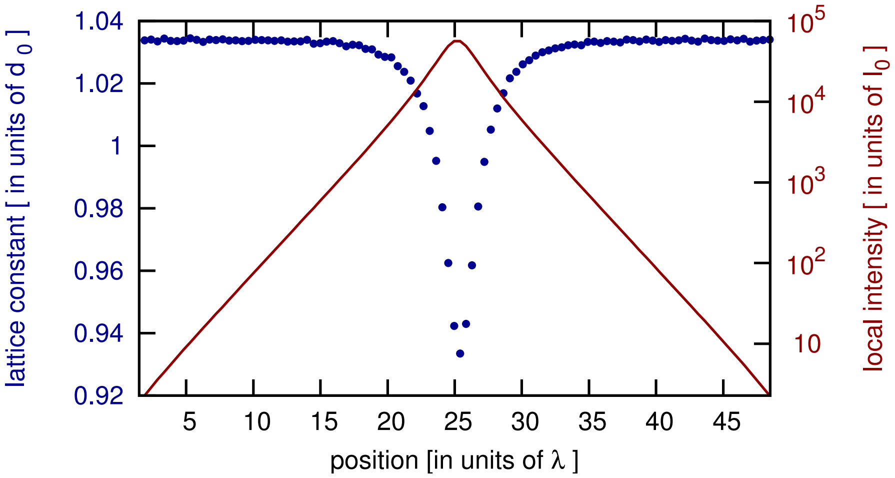

Figure 6.1: (color online) A configuration found by Monte-Carlo type minimization of the dipole potential, for $N = 100$ atom clouds with polarizability $\Lambda = 0.1$, symmetrically pumped in free space (no cavity). The local lattice constant (blue dots, in units of the original $d_0 = 0.468\lambda$) and the electric field intensity at the atomic positions (red line, exponential scale, in units of the pump intensity I_0) are plotted. The total dipole energy is some 1000 times lower than that of the regular optical lattice of assumption (i). The atoms form two slabs with lattice constant exceeding d_0, impervious to the pump laser (pump frequency deep in the band gap, see [36]). These two self-organized atom mirrors constitute a high-Q cavity, trapping light in the middle. There the intensity is some 10^4 times that of the pump lasers. Inside the "atom mirrors" the intensity falls off exponentially.

mirrors, carrying momentum and energy, and is coupled out of the cavity at the mirrors. It is not at all clear what function of the system parameters is minimized in a steady state. Minimizing the dipole energy certainly does not lead to steady state configurations. To illustrate this point, it is worthwhile to consider a conceptually simpler situation, namely atoms trapped in a standing wave laser field without any cavities involved. As illustrated in Fig. 6.1, using the model of Meiser and Meystre but allowing all of the atom clouds to move independently, a Monte Carlo algorithm to minimize the dipole energy leads to configurations differing from a simple lattice. Starting from the regular lattice configuration, the atoms decrease the dipole energy by forming a *self-organized cavity* resonant with the pump beam. The intensity inside this cavity is thus enhanced by the resonance, and a few atoms coupled to this intense field contribute to the total dipole potential by such a large amount, that its absolute value exceeds that of the original energy by orders of magnitude (see the figure caption for details). The mirrors of this self-organized cavity are slabs of an atomic lattice with lattice constant exceeding d_0 such that the pump field is in the band gap [36] of these slabs and decays exponentially inside them. The complicated spatial structure of this solution clearly shows that assumption (ii) cannot lead to (i), one of them has to be dropped. The configuration represented in Fig. 6.1 is not a steady state at all: as we discuss below, radiation pressure would push the two slabs apart. Thus, assumption (ii) has to be revisited. We remark that inside an optical cavity, dipole energy minimization leads to similar artifacts, in the "superstrong coupling" limit as well.

The reason why dipole energy minimization does not supply the steady states is that the atomic positions are coupled parametrically to the light field. This problem is met, and is tackled in a very neat way, when the motion of atoms coupled to a *single-mode high-Q* optical resonator is to be described in a classical approximation (Ehrenfest theorem). In the standard approach (e.g., [31]), the starting point is the quantum Hamiltonian $\hat{H} = \sum_{j=1}^{N} \hat{H}_{\text{atom}}(\hat{p}_j, \hat{\sigma}_j, \hat{\sigma}_j^\dagger) + \hat{H}_{\text{field}}(\hat{a}, \hat{a}^\dagger) + \hbar \sum_{j=1}^{N} g(\hat{z}_j)(\hat{\sigma}_j^\dagger \hat{a} + \hat{\sigma}_j \hat{a}^\dagger)$, with $\hat{z}_j$, $\hat{p}_j$, and $\hat{\sigma}_j$ denoting the position, momentum, and deexcitation operator of the j-th atom, $g(z)$ the mode function of the cavity, and $\hat{a}$ the cavity photon annihilation operator. The coupling between atoms and the cavity field is of the celebrated Jaynes–Cummings type. The classical approximation should furnish equations of motion for $z_j = \langle \hat{z}_j \rangle$ and $p_j = \langle \hat{p}_j \rangle$. In order to derive these, for slowly moving atoms, the separation of the timescales is invoked. The internal variables $\hat{a}$ and $\hat{\sigma}_j$, which equilibrate fast on the timescale of atomic motion, are replaced by their adiabatic steady state expectation values, which depend on all of the atom coordinates $\hat{z}_l$ (as well as the intensities and phases of the pumping lasers). One could be tempted to use the "effective" Hamiltonian $\hat{H}_{\text{eff}}(\hat{z}_j, \hat{p}_j)$ obtained from $\hat{H}$ in this way, and derive the atomic dynamics from it via the Heisenberg equations of motion, i.e., $dp_j/dt = \left\langle -d\hat{H}_{\text{eff}}/d\hat{z}_j \right\rangle = -d \left\langle \hat{H}_{\text{eff}} \right\rangle /dz_j = -d \left\langle \hat{H} \right\rangle /dz_j$. The correct procedure, however, is to apply the adiabatic approximation to the original Heisenberg equations

$$\frac{d}{dt}\hat{p}_j = \frac{1}{i\hbar}[\hat{p}_j, \hat{H}] = -\frac{d}{d\hat{z}_j}\hat{H} = \hat{F}_j, \tag{6.1}$$

where the force operator is $\hat{F}_j = -\hbar(\hat{\sigma}_j^\dagger \hat{a} + \hat{\sigma}_j \hat{a}^\dagger)\, dg(\hat{z}_j)/d\hat{z}_j$, and use $dp_j/dt = \left\langle \hat{F}_j \right\rangle$. In other words, the differentiation should only be applied w.r.t. *explicit* z_j-dependence of $\left\langle \hat{H} \right\rangle$, since $\left\langle d\hat{H}/d\hat{z}_j \right\rangle$ is not the same as $d \left\langle \hat{H} \right\rangle /dz_j$. Using $d \left\langle \hat{H} \right\rangle /dz_j$ to define the dynamics supplies steady states where the "dipole potential" $\left\langle \hat{H} \right\rangle = \left\langle \hat{H}_{\text{eff}} \right\rangle$ is minimized, but these are not the true steady states of the system: in these states the force on the atom $\left\langle \hat{F}_j \right\rangle$ does not vanish.

We now turn to the setup considered by Meiser and Meystre, where the back-action of the atoms on light is so substantial that the cavity no longer has a fixed mode function. To be self-contained, and to fix notation, we briefly summarize the model, detailed in [99, 97, 36].

Assuming that the atoms are fixed on the timescale of the field dynamics, the light field is calculated by solving the Helmholtz equation in a one-dimensional approximation,

$$\partial_z^2 E(z) + k^2 E(z) = -2k\Lambda E(z) \sum_j \delta(z - z_j). \tag{6.2}$$

The right-hand-side embodies the polarizability of the trapped atoms, which are assumed to form pancake-shaped clouds of axial size much smaller than a wavelength. The solution of this equation is trivial: between two atom clouds, the electric field is a superposition

$$\begin{aligned} E(z_{j-1} < z < z_j) &= A_j e^{ik(z-z_j)} + B_j e^{-ik(z-z_j)} \\ &= C_{j-1} e^{ik(z-z_{j-1})} + D_{j-1} e^{-ik(z-z_{j-1})}. \end{aligned} \tag{6.3}$$

The field has to fulfil boundary conditions:

$$E(z = z_j - 0) = E(z = z_j + 0); \tag{6.4a}$$

$$\partial_z E(z = z_j - 0) = \partial_z E(z = z_j + 0) + 2k\Lambda E(z_j). \tag{6.4b}$$

These conditions are equivalent to representing the atom clouds by BS's, i.e., $A_j = tC_j + rB_j$, $D_j = tB_j + rC_j$ with complex reflection and transmission coefficients $r = i\Lambda/(1 - i\Lambda)$, $t = 1/(1 - i\Lambda)$ [36].

The dynamics of the atoms is given by the *dipole force* acting on them. Instead of minimizing a dipole potential, the true *steady state* of the system is then specified by the positions of all the atom clouds $z_j, j = 1, \ldots, N$ such that the optical field of the cavity – the solution of (6.2) – exerts no net force on any of the clouds. In the following we show two ways to calculate this force acting on an infinitely thin atom cloud (BS).

The force on an atom cloud is can be obtained by integrating the the force on a single atom over the whole cloud. A microscopic model of light-matter interaction leads to two types of force: the dispersive *dipole force* and the dissipative *scattering force* [10]. This latter is often referred to as "radiation pressure", but following Meiser and Meystre we use this term to denote the mechanical effects of light in general. In [99, 97] the atom-pump detuning is assumed to be so large that the scattering force can be neglected, tantamount to assuming $\Lambda \in \mathbb{R}$. For linearly polarizable particles the dipole force time-averaged over an optical period is given [10] $F = \frac{1}{4}\alpha\nabla\left|E(\mathbf{x})\right|^2$. Calculating this force for an infinitely thin disk-shaped atom cloud poses a problem, as the electric field $E(z)$ is not differentiable at the atomic positions z_j. One must calculate the force on a disk of finite extent $z_j - w \ldots z_j + w$, and only then take the limit $w \to 0$. Since the electric field is polarized in the plane of the disk, there is no surface contribution [106], and the integral in the limit of vanishing width gives

$$F_j = \frac{\eta\alpha}{8}\left(\partial_z\left|E\right|^2(z_j - 0) + \partial_z\left|E\right|^2(z_j + 0)\right) \tag{6.5}$$

for the force on a unit surface ("radiation pressure"). This result is independent of the way in which the limit is approached, i.e. of the axial density distribution of the cloud. Substituting the modal decomposition of Eq. (6.3), using the BS relations, and the fact that as $\Lambda \in \mathbb{R}$, we have $|A_j|^2 + |D_j|^2 = |B_j|^2 + |C_j|^2$, some algebra leads to the simple formula

$$F_j = \frac{\epsilon_0}{2}\left(|A_j|^2 + |B_j|^2 - |C_j|^2 - |D_j|^2\right). \tag{6.6}$$

There is another, macroscopic way to arrive at the light-induced force on a scatterer. This consists of calculating the Maxwell stress tensor and integrating it on an arbitrary fictitious surface enclosing the body (see, e.g., Ref. [101]). In the 1D model of [36, 99], this is very easily done. For a selected atom cloud, we take the surface around it to consist of two planes orthogonal to the cavity axis, between the atom cloud and the two neighbouring clouds. As the electromagnetic wave inside the cavity is transverse, both the $\mathbf{E}$ and $\mathbf{B}$ vectors lie in the planes, and the only part of the stress tensor contributing to the integral is the term with the energy density. For the plane waves of (6.3) this results in (6.6). We remark that this line of thought is also alluded to by Meiser and Meystre, and although is not applied to the atoms, it is used to derive the force on the movable cavity mirror in Eq. (10) of [99].

The difference between (a) minimizing the dipole potential, and (b) requiring the dipole force to vanish is illustrated in Fig. 6.2. Here we put a weakly reflective BS ($\Lambda = 0.1$) in a high-Q cavity composed of two Dirac-δ distributions of polarizability with $\Lambda = 10$, corresponding to transmission probability $T \approx 0.01$, as in [99, 97]. To a good approximation the cavity only supports a single $\sin(z)$-mode, and since the BS is weakly reflective, we are not in the "superstrong coupling" limit: the Hamiltonian approach would constitute a reasonable approximation. Note however, that in Fig. 6.2(a), the intensities to the right of the trapped atom are slightly higher than to its left, indicating the corrections to the single-mode approximation, and also the bistability of [99]. When minimizing the dipole energy (a), the BS occupies a position where it is not coupled strongly to the cavity, far from an antinode of the mode function. Thus the system is near-resonant with the driving field, and the intracavity intensity is enhanced by the resonance, some 500 times the intensity outside. Extremely high intensity means large negative dipole energy for the trapped atom – however, note that at the position of the atom, the derivative of the intensity is nonvanishing, and thus the force F is nonzero. Requiring this *force* to vanish brings the atom to a mode function antinode (b), where the coupling is stronger, hence the frequency shift is larger, than in (a). For this specific example, this is already enough to shift the system out of resonance and to decrease the intracavity intensity below the free-space value.

The BS used to model the atom cloud in the cavity considered by [99, 97], has an effective $\Lambda \approx 1$, and thus the system is in the "superstrong coupling limit". We plot the force exerted by the cavity field on such a BS as a function of its position and of the detuning (equivalently, cavity size) in Fig. 6.3. The boundaries between the gray shaded and white areas correspond to equilibrium. Note however, that for a fixed drive detuning, of the two equlibrium solutions per half wavelength only one is stable, the one where $\partial/\partial z_a\, F < 0$. Thus there is no bistability of the kind predicted in [99]. The areas enclosed by the solid contour lines, where the force on the BS becomes very large, indicate that the system is on resonance and the field gradient at the BS position is high. These correspond to the black structures on Fig. 2. of [97], where the determinant D (Eq. (12) of [97]) becomes small, which there are falsely interpreted as equilibrium positions.

In the example shown in Fig. 6.2, the maxima of the intensity to the left and to the right of the trapped BS are equal. In fact, an analogous statement holds for the steady state of any one-dimensional system composed of N consecutive beam splitters, held together by the dipole force, regardless of the BS parameters of the system components. This follows from formula (6.6) for the dipole force, whereby for every $j = 1, \ldots, N$: $|A_j|^2 + |B_j|^2 = |C_j|^2 + |D_j|^2$. Furthermore, since there is no absorption, $|A_j|^2 + |D_j|^2 = |B_j|^2 + |C_j|^2$ at every BS. These relations imply that $|A_1| = |A_2| =, \ldots, = |A_N| = |C_1| = |C_2| =, \ldots, = |C_N|$; $|B_1| = |B_2| =, \ldots, = |B_N| = |D_1| = |D_2| =, \ldots, = |D_N|$, i.e., the plane waves pass the atom clouds unattenuated, suffering only phase shifts. Thus, the envelope of the intensity oscillations of the electric field is constant throughout the sample. This is in line with the intuitive picture of "radiation pressure" caused by the collisions of photons with the atom clouds. However, these results are in direct contradiction to those obtained by Meiser and Meystre: the nonconstant field envelopes in the "bistability regime" are explicitly plotted in Fig. 3 of [97].

We now revisit assumption (i). Assuming that there exists a steady state of N identical disk-

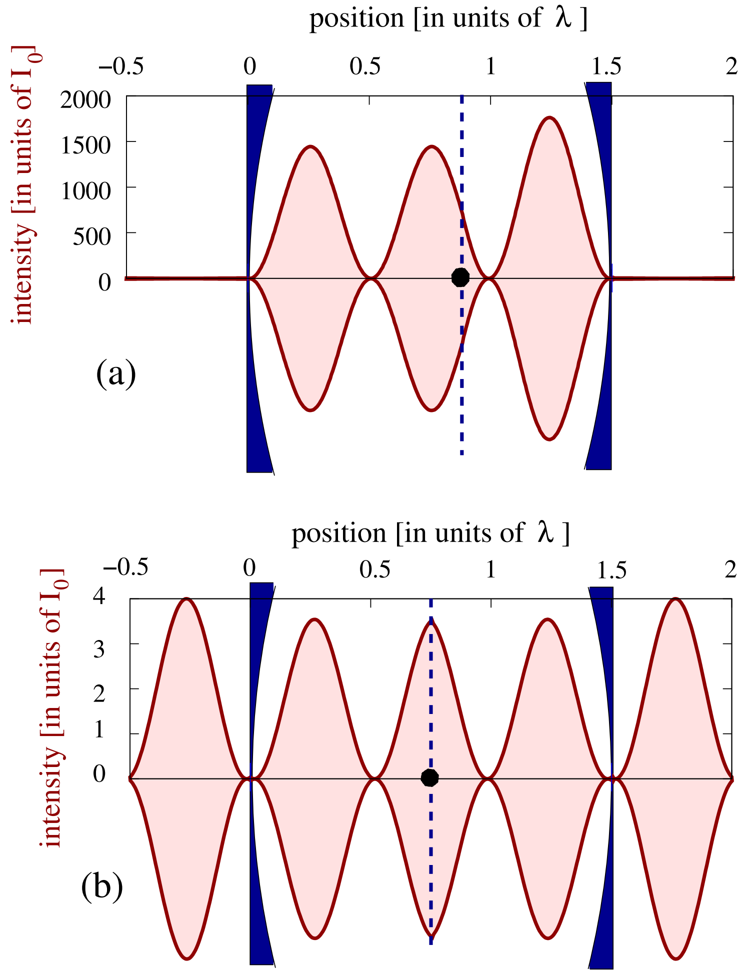

Figure 6.2: (color online) Steady states of a single atom (atom cloud) of polarizability $\Lambda = 0.1$ in a symmetrically pumped cavity, according to (a) minimization of the dipole energy; and (b) vanishing dipole force. The cavity is formed by two highly reflective mirrors ($\Lambda = 10$) at $z = 0$ and $z = 1.501\lambda$. The position of the atom (black dot and vertical dotted line) induces no substantial change of the *mode function* of the cavity. However, it influences the *intensity* of the cavity mode (filled red curve, in units of the free-space intensity I_0, mirrored for better visibility). In (a), the system is on resonance, the intracavity intensity is so high (some $500 I_0$) that the intensity outside the cavity is hardly seen on this range; in (b), the atom is maximally coupled to the cavity, shifts it out of resonance and reduces the intensity below the free-space value.

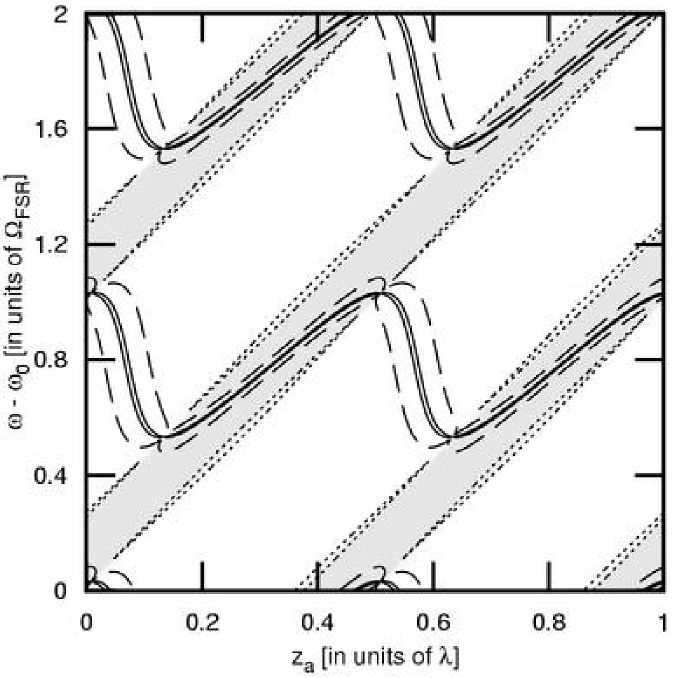

Figure 6.3: Force on a single beam splitter with $\Lambda = 1$ in a standing-wave cavity with parameters as in [99, 97] (mirror transmission probability $T \approx 0$) pumped by a laser via one of the end mirrors. Contour lines are: solid, $|F| = 10F_0$; dashed, $|F| = F_0/10$; dotted, $|F| = F_0/1000$, where F_0 is the radiation pressure force that would act on the beam splitter in the absence of the cavity. Gray background indicates positive (rightward) forces, white background negative (leftward) forces. Extremely high forces ($|F| > 10F_0$, the small areas enclosed by the solid contour lines) occur whenever a part of the cavity is on resonance with the drive. The boundaries between the gray and white areas, where $F \approx 0$, are the (stable or unstable) equilibrium positions.

shaped atom clouds trapped by the light field in a cavity, we find that these clouds have to form a perfect lattice. This is true because in the steady state the light permeates the stack of clouds unattenuated. Thus $|E(x)|^2 = |E_0|^2 + |E_1|^2 + 2\,|E_0 E_1| \cos(2kx - \Phi(x))$ everywhere in the sample, the clouds only contribute to the phase: $\Phi(x_j < x < x_{j+1}) = \sum_{l=1}^{j} \chi_l$. The phase slip at the l'th cloud χ_l depends not only on the polarizability density Λ of the clouds, but also on the pump asymmetry, i.e., the ratio of the intensities of the left- and rightwards propagating waves, see [35] for details. Since the clouds are identical, and the light fills the structure unattenuated, both these parameters are equal for all clouds. Thus, $\chi_l = \chi$ for every $l = 1, \ldots, N$, therefore the atom clouds form a perfect lattice (possibly with gaps of an integer multiple of $\lambda/2$) with lattice constant $d = \frac{\lambda}{2\pi}(\pi - \chi)$. However, the value of the phase slip χ, and thus of the lattice constant d, is not trivial to determine, due to the dependence on the pump asymmetry. For the atoms trapped inside the asymmetrically pumped cavity considered by Meiser and Meystre, this asymmetry varies with the pump detuning: on resonance, it is negligible, while far from resonance, it is substantial. Thus Eqs. (24) and (25) of [99] (taken from [36] for symmetric pumping) *cannot be applied* to this system. Even more crucially, whether or not the equilibrium sets in depends on the *dynamics*. We have found [35] that for large lattices, even a small pump asymmetry can lead to a dynamical instability of the equilibrium configuration.

Common wisdom holds that “dipole force is conservative”. Even in the strong coupling regime of cavity QED it is often possible to construct a “potential” by integrating the dipole force (e.g., [31]). For many particles trapped in the same cavity, this potential should also include the field-mediated (parametric) interaction between those particles. We have found [35], that in the generic case even this approach breaks down. For asymmetric pumping (as in [99, 97]), $\partial F_j(z_1, \ldots, z_N)/\partial z_l \neq \partial F_l(z_1, \ldots, z_N)/\partial z_j$, and thus no potential function $V(z_1, \ldots, z_N)$ can be constructed that obeys the Young theorem about the commutativity of partial derivatives.

Chapter 7

Publication: Optomechanical coupling in a one-dimensional optical lattice

Optical lattices (OL) are perfectly periodic arrays of particles trapped by the standing wave interference pattern of several laser beams [107, 18]. OL's are created in 1,2, or 3 dimensions, in various shapes and sizes. Whereas in the 90's occupancies of about 1% were realistic, OL's can now be loaded from Bose-Einstein condensates and filling factors of up to 5 can be achieved [108]. OL's have important applications as model systems for solid state physics [109], for quantum information science [110], or metrology [111].

Optical Lattices are generally produced using extremely far detuned lasers: detunings of about 10^7 times the atomic transition linewidth are not uncommon. On the one hand, this ensures that the dipole force dominates the scattering force, and the particles are only slightly heated by the light used to trap them. On the other hand, in this regime the particles do not affect the propagation of light very much, and thus optical back-action is avoided. The advantage is that this way light is a tool to produce an inert potential. However, in related systems, it is the optical back-action that gives rise to useful or interesting phenomena such as cavity-induced cooling of atoms [25, 53], or cooling of micromirrors [22, 23, 24].

So far, the only back-action effect seen in Optical Lattices is a tiny but observable reduction of the lattice constant with respect to the naive expectation (in a one-dimensional OL, this would be half of the wavelength of the trap laser, $d = \frac{\lambda}{2}$). This has been predicted [36] , and subsequently demonstrated [112], by I. Deutsch *et al.*, and unambiguously observed in an experiment of Weidemüller *et al.* [37]. This phenomenon can be simply understood as a consequence of the fact that the effective wavelength of light is reduced as it has to pass through the thin cloud of trapped particles [36].

A generic physical effect due to the back-action is that the trap light mediates an *interaction* between the particles, which can affect the equilibrium configuration and open the possibility of collective motion. In many experimental setups this interaction is negligible, and therefore it has largely been overlooked to this day. An exception is when the trap light is spatially confined in a high-Q optical resonator [83, 98], where this interaction creates correlations between the motion of trapped atoms [31], and can lead to the formation of ordered structures in real space (self-organization, [27, 32, 56]) or in momentum space (correlated atomic recoil laser, [86, 88, 113, 114]). Another important exception is the phenomenon of "optical binding", discovered in 1989 by Burns, Fournier and Golovchenko [30], which has very recently attracted the attention of several groups [93, 115, 116, 117, 102]. The description of this phenomenon is rather involved, including the solution of multiple scattering in a 2- or 3-dimensional situation, and thus, analytical results are rarely found (an exception is [118]).

In this paper we study the radiative atom-atom interaction due to opto-mechanical coupling in the simplest possible case, a one-dimensional optical lattice in free space. Using the framework of Deutsch et al. [36] as a starting point, the trapped clouds of atoms will be identified with single scattering centers, i.e., beam splitters in one dimension. We derive the optical force on such a beam splitter and generalize the standard "radiation pressure" and "dipole force" [10]. These latter can be considered as perturbative approximations to our exact result, in which the back-action of the scatterer on the optical field is neglected. The exact result accounting for back-action can be interpreted by means of a simple physical picture, in terms of multiple reflection within the beam splitter.

The modification of the optical force, due to back action, on a single atom cloud is small. However, we have found that tuning a hitherto neglected parameter of an optical lattice its consequences can become striking. This parameter, the "asymmetry", is the relative power of the pump beams constituting the trap. For symmetric OL's — created by two counterpropagating beams with the same intensity — the back-action induced interaction leads to the reduction of the lattice constant d mentioned above, and we predict that it also causes the center-of-mass oscillations to soften. In asymmetric lattices, the reduction of the lattice constant d is enhanced (in some cases by several orders of magnitude), and arises even for blue detuning, where the first intuition would suggest that d increases. However, this equilibrium phenomenon is masked by dynamic effects. The interaction induced by back-action leads to a dynamic instability of optical lattices, which happens already at moderate pump asymmetries. Small lattice fluctuations give rise to an exponentially increasing density wave propagating along the direction of the weaker beam, which ultimately leads to a destruction of the lattice: the particles will all be pushed away by the stronger beam. Viscous friction can prevent this instability, but even with an arbitrary amount of friction (overdamped limit) there is a critical asymmetry beyond which the OL becomes unstable. Curiously, the propagating density waves arise in the overdamped limit as well, in spite of the fact that the dynamics is first-order. We study these effects numerically and analytically, providing an analytical characterization of the density waves and closed formulas for the critical asymmetries.

This Article is organized as follows. We first introduce the model of Deutsch et al. [36] we use to compute the back-action of trapped particles on the trapping field, in Section 7.1. Then we derive simple closed formulas for the optical forces on trapped atom clouds, using the Maxwell Stress Tensor, in Section 7.2. We calculate the equilibrium optical lattice configuration revealing that the lattice constant is reduced if the pump asymmetry is increased in Section 7.3. This effect, however, is masked by the dynamics of the lattice, which we explore using numerical simulation in Section 7.4. We characterize the vibrational modes of the lattice by a full analytical solution of the dynamics close to equilibrium in Section 7.5. Although the analytical calculations are for a perfect lattice, the main features of the dynamics persist even in the presence of noise, as we illustrate in Section 7.6. We address some of the experimental issues and give estimations for the real-life values of the physical quantities involved in Section 7.7. Finally, we give an outlook and show how some of the features of dynamics arise in related systems in Section 7.8.

7.1 The light in an optical lattice

We consider a one-dimensional dipole trap constituted by two counter-propagating laser beams of equal polarization and frequency, coming from the same "master laser", and thus phase stabilized with respect to each other. The transverse profile (y and z dependence) of the electric fields is assumed to be Gaussian, with beam diameter much larger than the wavelength, $w \gg \lambda$. Thus the intensity maxima and minima are both thin disks. Suppressing the vector indices, in the usual complex notation we write the electric field incident from the left as $E(x,t) = E_0 e^{ikx-i\omega t}$, and from the right $E(x,t) = E_1 e^{-ikx-i\omega t}$. In the following, for brevity we drop the trivial phase factors $e^{-i\omega t}$. Although the two incident plane waves have the same frequency, their intensities

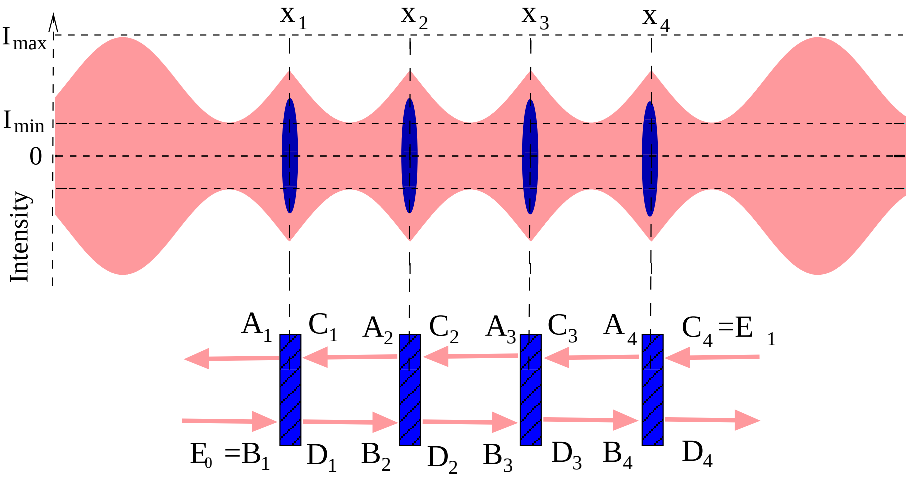

Figure 7.1: A dipole trap created by two lasers of equal frequency but unequal power. The intensity (in light red), mirrored for better visibility, ranges between $I_{\text{min}} = \frac{1}{2}\epsilon_0\, c\, (|E_0| - |E_1|)^2$ and $I_{\text{max}} = \frac{1}{2}\epsilon_0\, c\, (|E_0| + |E_1|)^2$. Trapped particles form disk-shaped clouds (in dark blue), and are modeled as beam splitters. Due to the pump asymmetry, the electric field has no nodes. Back-action of trapped particles distorts the field and reduces the lattice constant.

$I_j(x) = \frac{1}{2}\epsilon_0 c\, |E_j(x)|^2$, for $j = 1, 2$, can be different — for definiteness, we choose $I_1 > I_0$. We quantify this intensity imbalance using two alternative dimensionless quantities, the normalized difference of the intensities, the *pump asymmetry*

$$\mathcal{A} = \frac{I_1 - I_0}{\sqrt{I_0 I_1}} > 0\,; \tag{7.1}$$

and the *pump power ratio*

$$\mathcal{P} = \frac{I_1}{I_0} = \frac{|E_1|^2}{|E_0|^2} = \frac{1}{4}\left(\mathcal{A} + \sqrt{4 + \mathcal{A}^2}\right)^2 > 1\,. \tag{7.2}$$

For almost symmetric pumping ($\mathcal{A} \ll 1$), the two are related by $\mathcal{P} = 1 + \mathcal{A}$, whereas for highly asymmetric pumping ($\mathcal{A} \gg 1$), roughly $\mathcal{P} = \mathcal{A}^2$.

The trap is used to hold particles, which can be (ultra-)cold atoms or sub-micron size plastic beads, with diameter much smaller than the wavelength. For simplicity we assume linear polarizability of these particles (the dipole transitions are not saturated). The particles can be “high-field seekers”: cold atoms, with the trapping light red detuned with respect to the characteristic frequency ω_A of the atomic resonance, or sub-micron plastic beads, where the index of refraction of the surrounding medium is lower than that of the trapped particles. In this case, the particles accumulate around the intensity antinodes. Alternatively, they can be “low-field seekers”: for cold atoms, this corresponds to blue detuning of the lattice lasers, $\omega < \omega_A$, for microscopic particles it means that they are surrounded by a medium with an index of refraction exceeding their own. In that case, the particles are expelled from regions where the intensity is high: if some external trap mechanism prevents their escaping the beam in the transverse y and z directions, they will gather around the nodes of the trapping field. In either case, we assume that the particles are cold enough and the laser beams intensive enough so that they are deeply trapped, and thus form a stack of pancake-shaped clouds. Within a single cloud, we average over transverse motion of particles, thus each cloud is represented by an infinitely thin plane of linearly polarizable material. The limits of validity of these simplifying assumptions are discussed briefly in Section 7.7.

The strength of interaction of a cloud of trapped particles with the laser depends on the linear polarizability α of the particles (a complex quantity), and on their areal density

$$\eta = \frac{N_\lambda}{\lambda^2} = \frac{\text{(number of particles in a cloud)}}{\text{(cloud cross-section)}}, \tag{7.3}$$

with N_λ denoting the number of atoms in a part of the cloud with area λ^2. Together these give the dimensionless complex coupling constant ζ, the (areal density of the) polarizability of a cloud :

$$\zeta = k\eta\frac{\alpha}{2\epsilon_0}. \tag{7.4}$$

The real part, $\mathrm{Re}\,\zeta$, describes dispersive atom-light interactions. It is positive for red detuning (of the trap laser with respect to the atomic resonance), negative for blue detuning. The imaginary part, $\mathrm{Im}\,\zeta$, which is always positive, corresponds to dissipation. For a detailed discussion of how ζ is related to the parameters of the trapped atoms or microbeads and the laser, see Section 7.7.

As is well known, the polarizability ζ is proportional to the optical forces that trap the particles in the lattice, which we are going to discuss in the next Section. However, it also gives the magnitude of the back-action of the cloud on the trapping light. Following Deutsch et al. [36], we take this effect into account by calculating the propagation of the trap light via the scalar Helmholtz equation, with the N clouds represented by Dirac-δ distributions of linearly polarizable material:

$$(\partial_x^2 + k^2)E(x) = -2kE(x)\sum_{j=1}^{N}\zeta\delta(x - x_j). \tag{7.5}$$

If the dissipative part of the light-matter interaction (spontaneous emission) can be neglected, $\zeta \in \mathbb{R}$, the Helmholtz equation (7.5) for propagation of light is identical to the Kronig-Penney model in solid state physics for the propagation of electrons. Even with dissipation, for general $\zeta \in \mathbb{C}$, the solution of Eq. (7.5) between two clouds is a superposition of plane waves,

$$\begin{aligned} E(x_{j-1} < x < x_j) &= A_j e^{-ik(x-x_j)} + B_j e^{ik(x-x_j)} \\ &= C_{j-1} e^{-ik(x-x_{j-1})} + D_{j-1} e^{ik(x-x_{j-1})}. \end{aligned} \tag{7.6}$$

Integrating Eq. (7.5) over x_j, for $j = 1, \ldots, N$, reveals that the scatterers constitute boundary conditions for the field:

$$E(x = x_j - 0) = E(x = x_j + 0); \tag{7.7a}$$

$$\partial_x E(x = x_j - 0) = \partial_x E(x = x_j + 0) + 2k\zeta E(x_j). \tag{7.7b}$$

Substituting the modal decomposition (7.6), the boundary conditions give simple algebraic relations between the mode amplitudes to the left and to the right of each atom cloud. These have the form of Beam Splitter (BS) relations:

$$A_j = \mathfrak{r}B_j + \mathfrak{t}C_j; \tag{7.8a}$$

$$D_j = \mathfrak{t}B_j + \mathfrak{r}C_j, \tag{7.8b}$$

with reflection and transmission coefficients [36]

$$\mathfrak{r} = \frac{i\zeta}{1 - i\zeta}, \quad \mathfrak{t} = \frac{1}{1 - i\zeta}, \quad \text{whereby} \quad \zeta = -i\frac{\mathfrak{r}}{\mathfrak{t}}. \tag{7.9}$$

We note that a general linear optics four-port can be described by 4 independent real parameters, whereas here we have only 2: the real and imaginary parts of ζ. The reason is that we require that the electric field be continuous at the position of the BS (infinitely thin beam splitter):

$$A + B = C + D, \tag{7.10}$$

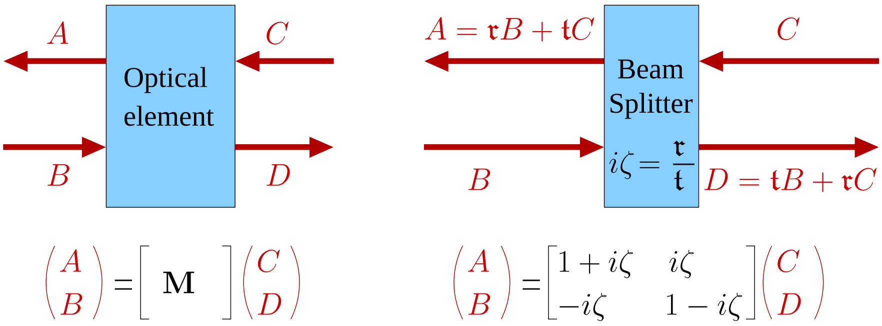

Figure 7.2: The Transfer Matrix relates the mode amplitudes to the left of an optical element to the mode amplitudes to the right of it. As an illustration, we give the Transfer Matrix of a Beam Splitter.

which leads directly to $\mathfrak{r} + 1 = \mathfrak{t}$. As a result of interference the electric field is reduced at the position of the BS with respect to its expected value based on the incoming amplitudes B and C: $A + B = C + D = \mathfrak{t}(B + C)$. As discussed in the following Section, this leads to a reduction of the "dipole force" and "radiation pressure". The imaginary part of ζ describes dissipation,

$$|A|^2 + |D|^2 = |B|^2 + |C|^2 - 2\mathrm{Im}\,\zeta\,|\mathfrak{t}(B + C)|^2\,, \tag{7.11}$$

and

$$|\mathfrak{r}|^2 + |\mathfrak{t}|^2 = 1 - 2\,|\mathfrak{t}|^2\,\mathrm{Im}\,\zeta \tag{7.12}$$

For purely dispersive interaction, $\zeta \in \mathbb{R}$, photon number is conserved, $|\mathfrak{r}|^2 + |\mathfrak{t}|^2 = 1$, and time inversion invariance is expressed by $\mathfrak{r}^*\mathfrak{t} + \mathfrak{t}^*\mathfrak{r} = 0$. In that case, the reflection and transmission coefficients are $\mathfrak{r} = i\sin\chi_0 e^{i\chi_0}$ and $\mathfrak{t} = \cos\chi_0 e^{i\chi_0}$, with $\chi_0 = \tan^{-1}\zeta$.

7.1.1 The Transfer Matrix Method

Since a single atom cloud is modeled as a beam splitter, an optical lattice consisting of several (hundreds of) such clouds can be represented by cascaded BS's, as illustrated in Figure 7.1. The beam splitter relations and those for free propagation of light give $4N$ linear equations for the $4N$ mode amplitudes $A_j, B_j, C_j, D_j, j = 1, \ldots, N$, where $E_0 = B_1$ and $E_1 = C_N$ are the incident electric fields. The most straightforward way to obtain the simultaneous solution of all of these equations is via the transfer matrix (TM) method, as used, e.g., in [36].

The essence of the Transfer Matrix method, as illustrated in Fig. 7.2, is that instead of relating the outgoing modes to the incoming ones, we relate the modes to the left of an optical element to the modes to the right of it. For a linear system the relationship will be linear, and thus is given by a matrix; in our case, its size is 2 × 2. The advantage of the approach is that it is very easy to scale up a system: the TM of a composite (cascaded) system is just the matrix product of the TM's of its components.

For a single atom cloud, the BS relations (7.8) give

$$\mathbf{M}_{BS} = \frac{1}{\mathfrak{t}}\begin{pmatrix} \mathfrak{t}^2 - \mathfrak{r}^2 & \mathfrak{r} \\ -\mathfrak{r} & 1 \end{pmatrix} = \begin{pmatrix} 1+i\zeta & i\zeta \\ -i\zeta & 1-i\zeta \end{pmatrix} = \mathbf{1} + i\zeta\begin{pmatrix} 1 & 1 \\ -1 & -1 \end{pmatrix} = \mathbf{1} + i\zeta\mathbf{B}, \tag{7.13}$$

with the parametrization (7.9) for $\mathfrak{r}$ and $\mathfrak{t}$, and the matrix $\mathbf{B}$ defined by the last equality. This can be contrasted with the TM for the corresponding incoherent scattering process, where for the *intensities* A, B, C, and D we have $A = RB+TC$, and $D = RC+TB$, with $R, T > 0, R+T = 1$:

$$\mathbf{M}_{SC} = \frac{1}{T}\begin{pmatrix} T^2 - R^2 & R \\ -R & 1 \end{pmatrix} = \begin{pmatrix} 1-\rho & \rho \\ -\rho & 1+\rho \end{pmatrix} = \mathbf{1} - \rho\mathbf{B}^\dagger \tag{7.14}$$

where $\rho = R/T$. Now $\mathbf{B} = (1;-1)^\dagger \circ (1;1)$ is the dyadic product of two orthogonal vectors, and thus $\mathbf{B}^2 = \mathbf{B}^{\dagger 2} = 0$. It follows directly that $\mathbf{M}_{SC}(\rho)\mathbf{M}_{SC}(\rho') = \mathbf{M}_{SC}(\rho+\rho')$ and $\mathbf{M}_{BS}(\zeta)\mathbf{M}_{BS}(\zeta') = \mathbf{M}_{BS}(\zeta+\zeta')$: two subsequent scattering processes can be represented by a single process, and the parameters ρ, respectively, ζ, are additive. For incoherent scattering processes this relation is used to show that ρ is proportional to the resistivity. For coherent scattering, however, no simple conclusions involving the "reflectivity" of a cascade of BS's can be drawn. The complication is that whereas the intensities do not change during free propagation, the amplitudes acquire phases, and in coherent processes these phases play a role. Thus it is vitally important to include the propagation of light with wavevector k between BS's over length d into the transfer matrix of a unit of an optical lattice:

$$\mathbf{M} = \mathbf{M}_{BS}\mathbf{P}(d) = \mathbf{M}_{BS}\begin{pmatrix} e^{ikd} & 0 \\ 0 & e^{-ikd} \end{pmatrix} = \begin{pmatrix} (1+i\zeta)e^{ikd} & i\zeta e^{-ikd} \\ -i\zeta e^{ikd} & (1-i\zeta)e^{-ikd} \end{pmatrix}. \tag{7.15}$$

Due to the nontrivial propagation there is now no simple additive parameter.

We can rewrite the transfer matrix $\mathbf{M}$ into a form useful for analytical calculations, and giving the TM of a regular optical lattice instantly. For this, first note an important property of the TM of a beam splitter: reflection symmetry along x. By "reflection" we here refer to the exchange of the amplitudes of the left- and right-propagating components, which for the formal vector composed of the field amplitudes can be realized by multiplication by a matrix:

$$\begin{pmatrix} D \\ C \end{pmatrix} = \boldsymbol{\sigma}\begin{pmatrix} C \\ D \end{pmatrix}; \qquad \boldsymbol{\sigma} = \begin{pmatrix} 0 & 1 \\ 1 & 0 \end{pmatrix} \qquad \text{(reflection along } x\text{)}. \tag{7.16}$$

As this is a reflection, $\boldsymbol{\sigma}^{-1} = \boldsymbol{\sigma}$. For a beam splitter, reflection along x corresponds to the simultaneous swapping of the amplitudes $A \leftrightarrow D$ and $B \leftrightarrow C$. By Eq. (7.8), this is a symmetry of the BS relations,

$$\begin{pmatrix} A \\ B \end{pmatrix} = \mathbf{M}_{\mathrm{BS}}\begin{pmatrix} C \\ D \end{pmatrix} \quad \Leftrightarrow \quad \begin{pmatrix} D \\ C \end{pmatrix} = \mathbf{M}_{\mathrm{BS}}\begin{pmatrix} B \\ A \end{pmatrix}, \tag{7.17}$$

regardless of whether the BS is purely dispersive, $\zeta \in \mathbb{R}$, or there is some dissipation, $\zeta \in \mathbb{C}$. Using the more concise formalism introduced above, we have:

$$\boldsymbol{\sigma}\mathbf{M}_{\mathrm{BS}}\boldsymbol{\sigma} = \mathbf{M}_{\mathrm{BS}}^{-1}. \qquad \text{(reflection symmetry of a BS).} \tag{7.18}$$

Reflection symmetry also holds for free propagation, $\boldsymbol{\sigma}\mathbf{P}(d)\boldsymbol{\sigma} = \mathbf{P}(-d)$, and therefore also for $\mathbf{P}(d/2)\mathbf{M}_{\mathrm{BS}}\mathbf{P}(d/2)$. Due to reflection symmetry then, the product of the eigenvalues of $\mathbf{P}(d/2)\mathbf{M}_{\mathrm{BS}}\mathbf{P}(d/2)$ has to be 1. Since this TM has the same spectrum as $\mathbf{M} = \mathbf{M}_{\mathrm{BS}}\mathbf{P}(d)$, the same holds for $\mathbf{M}$: $\det\mathbf{M} = 1$, and its eigenvalues can be written as $m_\pm = e^{\pm i\Theta}$, where Θ is a complex number[1]. The characteristic equation of $\mathbf{M}$ is $m_\pm^2 - \operatorname{tr}\mathbf{M}m_\pm + 1 = 0$, whose solution supplies us with the formula for Θ:

$$\cos\Theta = \frac{1}{2}\operatorname{tr}\mathbf{M} = \cos kd - \zeta\sin kd. \tag{7.19}$$

---

[1] For $\operatorname{Im}\Theta \neq 0$, we have $|m_-| < 1 < |m_+|$ or $|m_+| < 1 < |m_-|$. Multiplication of many transfer matrices is therefore numerically ill conditioned: Important variables can take on different orders of magnitude and are then added together. In numerical calculations in mesoscopic physics it can therefore be advisable to fall back to the scattering matrix. For the transfer matrices in our case, usually $|\operatorname{Im}\Theta|$ is of the order of $\operatorname{Im}\zeta$, and as normally $|N\operatorname{Im}\zeta| < 1$ (required so that absorption does not alter the asymmetry too much throughout the sample), these numerical issues do not concern us.

We can use this result to rewrite the transfer matrix $\mathbf{M}$:

$$\mathbf{M} = \cos\Theta + i\begin{pmatrix} \zeta\cos kd + \sin kd & \zeta e^{-ikd} \\ -\zeta e^{ikd} & -\zeta\cos kd - \sin kd \end{pmatrix} = \cos\Theta + i\mathbf{A}\sin\Theta \qquad (7.20)$$

where the last equation defines the matrix $\mathbf{A}$. Now obviously tr $\mathbf{A} = 0$, and its eigenvectors $\mathbf{u}$ and $\mathbf{w}$ are the same as those of $\mathbf{M}$, the corresponding eigenvalues have to be ± 1 (to have $m_\pm = e^{\pm i\Theta}$). Therefore $\mathbf{A}^2 = 1$, and thus, as noted in [36], $\mathbf{M} = e^{i\Theta\mathbf{A}}$. For the TM of equidistant lattices, we then simply have $\mathbf{M}^N = e^{iN\Theta\mathbf{A}} = \cos(N\Theta) + i\mathbf{A}\sin(N\Theta)$. Thus, Θ/d is analogous to the Bloch quasimomentum, and (7.19) is the transcendental equation giving the dispersion relation of Bloch states.

7.2 Dipole force

We have described how to calculate the amplitudes of the modes inside a 1D system of optical scatterers. We now address the question of how to specify the equilibrium positions of these scatterers, more generally, what the optical forces on them are. The first issue is important since in standard textbooks the optical forces are usually derived from the dipole coupling Hamiltonian, and therefore it is tempting to identify the zero-temperature equilibrium configuration of a system with the one minimizing the dipole potential (e.g., [119, 99, 97]). However, as discussed in [34], this approach is flawed, and in the regime where the atomic back-action is substantial, it can lead to nonphysical results. Instead of deriving the *potential*, we have to derive the *force* on the trapped particles.

The optical force on a body is the rate of the extraction of momentum from the electromagnetic field due to the presence of the body. To quantify this, we can enclose the body in a fictitious "box", and integrate the momentum flux (the Maxwell Stress Tensor) on the boundary of this box, as, e.g., in [101]. For the planar atom clouds in our 1D model this is very easily done. For a selected atom cloud, we take the surface around it to consist of two planes orthogonal to the x axis, between the atom cloud and the two neighbouring clouds. As the electromagnetic wave is transverse, both the $\mathbf{E}$ and $\mathbf{B}$ vectors lie in the planes, and the only part of the stress tensor contributing to the integral is the term with the energy density. For the plane waves of (7.6) this results in a simple formula for the areal density F of the optical force (the force divided by the transverse area, with dimensions of pressure) on a cloud:

$$F = \frac{\epsilon_0}{2}\left(|A|^2 + |B|^2 - |C|^2 - |D|^2\right). \qquad (7.21)$$

Although the simple formula (7.21) for the force is very practical for both numerical and analytical work, we can gain more insight into the physics it represents by rewriting it to show its position dependence explicitly. Taking incident field amplitudes $B(x) = E_0 e^{ikx}$ and $C(x) = E_1 e^{-ikx}$, the BS relations of Sect. 7.1 supply us with the outgoing amplitudes $A(x)$ and $D(x)$, which can be substituted into Eq. (7.21) to give

$$F(x) = 2\frac{I_0 - I_1}{c}\frac{\operatorname{Im}\zeta}{|1 - i\zeta|^2} - 4\frac{\sqrt{I_0 I_1}}{c}\frac{\operatorname{Re}\zeta}{|1 - i\zeta|^2}\sin(2kx + \varphi) + 2\frac{I_0 - I_1}{c}\frac{|\zeta|^2}{|1 - i\zeta|^2}, \qquad (7.22)$$

where $\varphi = \arg B(x=0) - \arg C(x=0)$ is the relative phase of the two incident trapping beams at $x = 0$. For low density or weak polarizability $|\zeta| \ll 1$, the force is typically dominated by the first two terms. To first order in ζ, these arise from the standard microscopic light-induced forces [10] acting on each scatterer independently. To apply the model of [10], we assume large detuning from the atomic resonances and low saturation of the dipoles (linear regime). Then if we neglect the back-action of the particles on the light, each of them experiences the electric field $E(x) = E_0 e^{ikx} + E_1 e^{-ikx}$, and we can directly apply the formulas from [10] giving the "dissipative" and "reactive" part of the mechanical effects of light. This reproduces the first two terms of Eq. (7.22), apart from the factors of $|1 - i\zeta|^{-2}$. Thus the formula (7.22) for the force can be seen as a generalization of the standard theory for light-induced forces to the regime where it is not enough to account for the effect of the dipoles on the electric field only perturbatively. Alternatively, if the individual dipoles interact weakly with the field — which is the standard case for trapped ultracold atoms — Eq. (7.22) can be derived from the microscopic forces, and thus embodies the effects of multiple scattering within the cloud, similarly to the Lorentz-Lorenz formula. We present this derivation in Appendix 7.9.

The first term of Eq. (7.22) embodies a part of "radiation pressure" arising due to *absorption of light* in the cloud. It is proportional to the difference of the incident photon fluxes, and always gives a force pointing towards the weaker source.[2] The second term, using the terminology of [10], is up to the factor of $|1 - i\zeta|^{-2}$ the density of the reactive or "dipole" force, also referred to as "gradient force". It arises due to the *interference of reflected and transmitted light*, i.e., absorption of photons from one trap beam and stimulated emission into the other one. As expected, for $\mathrm{Re}\,\zeta > 0$, the gradient force attracts particle clouds towards areas of high intensity, for $\mathrm{Re}\,\zeta < 0$, it expels the clouds from such regions. The third term can be rewritten as $c^{-1}(2\,|\mathfrak{r}|^2\, I_0 - 2\,|\mathfrak{r}|^2\, I_1)$, revealing that it is due to the *incoherent reflection* of the photons off the atom cloud, i.e., taking reflection into account without the effects of interference (which are supplied by the second term). This third term is proportional to the square of the polarizability, $|\zeta|^2$, and thus is usually negligible for single atoms. However, in dense atom clouds, it can be of the order of, or much larger than, the first two terms.

For a *single* trapped cloud, we can always construct a potential by simply integrating the force (7.22): $V(x) = -\int_0^x F(x')dx'$. As this can be useful to understand the possibilities of trapping with two beams of different intensities, we plot it, along with some of its naïve approximations, for a specific example in Fig.7.3. However, as soon as *two or more* clouds are trapped by the same field, their back-action on the field creates an effective interaction between them, and this potential cannot directly be applied. One might expect that a potential can be constructed that takes the interaction into account as well (as for atoms trapped in a high-Q cavity [31]), but, as we find later, in Sect. 7.5, this turns out not to be the case. In an asymmetric dipole trap, no potential can be constructed that supplies the dynamics of several trapped clouds.

Clearly the force (7.22) describes a sequence of (asymmetric) potential wells in one dimension if the intensity difference of the beams is so small that the dipole force (second term) dominates the scattering forces (first and last terms). A cloud can be trapped at the origin, $x = 0$, if

$$\sin\varphi = -\frac{1}{2}\mathcal{A}\frac{|\zeta|^2 + \mathrm{Im}\,\zeta}{\mathrm{Re}\,\zeta}; \qquad \cos\varphi = \pm\sqrt{1 - \frac{\mathcal{A}}{\mathcal{A}_{\max}}}, \tag{7.23}$$

where ± is "+" for red detuning, $\zeta > 0$, and "$-$" for blue detuning, $\zeta < 0$, and

$$\mathcal{A}_{\max} = 2\left|\frac{\mathrm{Re}\,\zeta}{|\zeta|^2 + \mathrm{Im}\zeta}\right| \tag{7.24}$$

is the maximum of the asymmetry for trapping along x; for $\mathcal{A} > \mathcal{A}_{\max}$ there are no traps. Thus a BS which is illuminated by mutually coherent laser beams from the two sides can be at equilibrium even if the lasers have unequal intensities, but only if $\mathcal{A} < \mathcal{A}_{\max}$ (see [120] for a similar analysis of the gradient force counteracting the dissipative force). In the purely dispersive case, i.e., if the imaginary part of ζ can be neglected ($\mathrm{Im}\,\zeta \ll (\mathrm{Re}\,\zeta)^2$), the relation (7.24) assumes the simple

---

[2] Note that the fluctuations of this force, arising from the spontaneous emission accompanying absorption, lead to a heating of the cloud, which limits the timescale of experiments. We come back to this issue in Sect. 7.7.

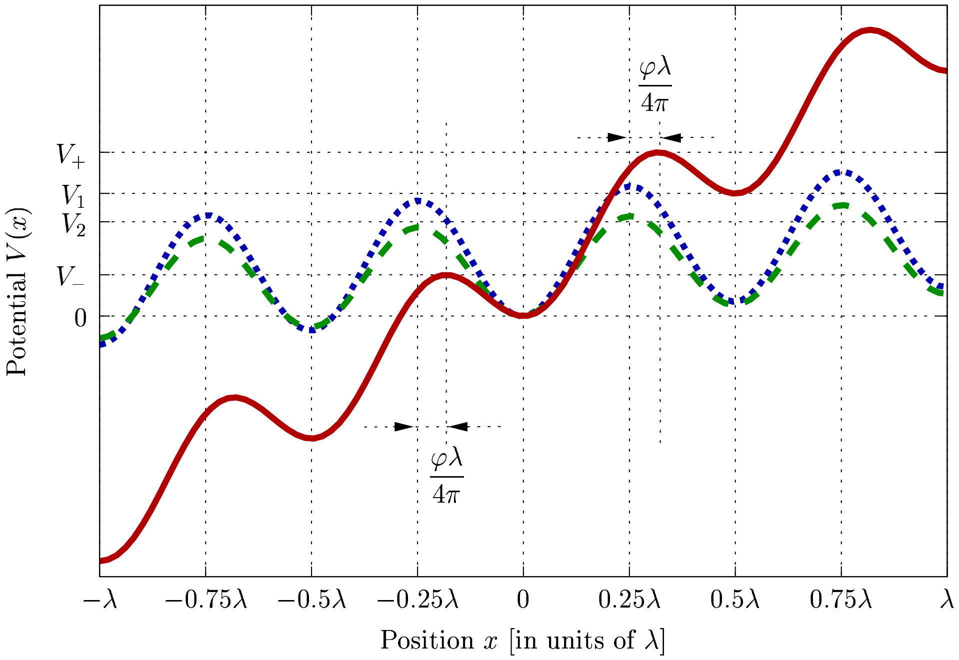

Figure 7.3: Potential of the force for a *single* trapped cloud, with polarizability $\zeta = 0.5 + 0.025i$, incident intensities $I_1 = 4I_0$. Dotted (blue) line: potential obtained by integrating the sum of the microscopic forces, the "dipole force" and the "radiation pressure" [10] on the particles in the cloud, neglecting the change of the mode amplitudes due to the atoms. The depth of the resulting sinusoidal potential is $V_1 = 4\mathrm{Re}\,\zeta\sqrt{I_0 I_1}/\omega$, slightly decreased (increased) to the left (right) by $\pi\mathrm{Im}\,\zeta(I_1 - I_0)/\omega$. Slashed (green) line: potential obtained by including the factors of $|1 - i\zeta|^2$, accounting for the decrease of the intensity inside the clouds (similarly to the Lorentz-Lorenz formula). For these parameters this amounts to a reduction of the potential depth by 20%. Continuous (red) line: the correct potential, defined as $V(x) = -\int_0^x F(x')dx'$ with the force calculated via the Maxwell Stress Tensor, Eq. (7.22). Besides the decrease of the potential depth, this correctly accounts for the mechanical effects of reflected light, including the third term of Eq. (7.22). This decreases (increases) the potential height to the left (right) by approximately $\pi\left|\mathfrak{r}\right|^2(I_1 - I_0)/\omega$.

form

$$\zeta\mathcal{A} < 2; \quad \mathcal{A}_{\max} = 2/\zeta; \quad \zeta_{\max} = 2/\mathcal{A}. \tag{7.25}$$

This criterion can be intuitively understood in the following way. If $|E_0|^2 < |E_1|^2$, more photons are incident on the right of the BS than the left, giving a force on it. If enough light is transmitted ($|\mathfrak{t}| > \frac{1}{2}|\mathfrak{r}|\mathcal{A}$), and the interference is favourable (depending on the position of the BS), the imbalance in the outgoing number of photons is enough to counteract this force, leading to a steady state.

7.2.1 Equilibrium of a single cloud

The simple and very sugggestive formula (7.21) for the mechanical effects of light can be used to make statements about objects which are only acted on by optical forces and are at equilibrium. Since the force (7.21) has to vanish,

$$|A|^2 + |B|^2 = |C|^2 + |D|^2 \qquad \text{(force vanishes)}, \tag{7.26}$$

Furthermore, due to the possibility of dissipation inside the object, we have

$$|A|^2 + |D|^2 \leq |B|^2 + |C|^2, \qquad \text{(dissipation)} \tag{7.27}$$

Together, these relations give

$$|A| \leq |C| \qquad \text{and} \qquad |B| \leq |D|, \tag{7.28}$$

with equality if $\operatorname{Im}\zeta = 0$. When passing through the object, both beams lose in intensity, this loss is proportional to $\operatorname{Im}\zeta$. For purely dispersive interaction ($\zeta \in \mathbb{R}$), the intensities of the beams are unchanged.

Although in this one-dimensional setting the presence of an optically trapped purely dispersive BS cannot be inferred by observing the *intensities* of the transmitted light, the BS does alter the *phases* of the fields. Consider a single trapped pancake-shape atom cloud modeled as infinitely thin sheet of nondissipative polarizable material. At equilibrium, $\arg(A+B) = \arg(C+D)$ leads via (7.28) to $\arg A + \arg C = \arg B + \arg D$. For the two relative phases $\chi = \arg D - \arg C$ and $\varphi = \arg B - \arg C$ we then find, using $|A+B| = |C+D|$:

$$\sin\varphi_\pm = -\frac{1}{2}\zeta\mathcal{A};, \qquad \cos\varphi_\pm = \pm\frac{1}{2}\sqrt{4-\zeta^2\mathcal{A}^2}; \tag{7.29}$$

$$\sin\chi_\pm = \frac{\zeta\sqrt{4+\mathcal{A}^2} \pm \zeta\sqrt{4-\zeta^2\mathcal{A}^2}}{2(1+\zeta^2)}; \qquad \cos\chi_\pm = \frac{-\zeta^2\sqrt{4+\mathcal{A}^2} \pm \sqrt{4-\zeta^2\mathcal{A}^2}}{2(1+\zeta^2)}. \tag{7.30}$$

Here, the "$\pm$" refers to "$+$" ("$-$") being stable, and "$-$" ("$+$") being unstable equilibrium for red (blue) detuning. Clearly, Eq. (7.29) is just Eq. (7.23) rewritten for $\zeta \in \mathbb{R}$. The angle φ shows the effect of the "back-action" force directly: for symmetric pumping and red (blue) detuning, it is zero ($-\pi$), and if I_1 is increased with respect to I_0, it increases too, showing that the atom cloud has been pushed by the "back-action" force. Since both the trap depth and this "push" are independent of the sign of ζ, we have $\varphi(\zeta,\mathcal{A}) - \varphi(\zeta,\mathcal{A}=0) = \varphi(-\zeta,\mathcal{A}) - \varphi(-\zeta,\mathcal{A}=0)$. It is not so intuitive, but follows directly from (7.30), that the change in χ due to asymmetry is also insensitive to the sign of the detuning: $\chi(\zeta,\mathcal{A}) - \chi(\zeta,\mathcal{A}=0) = \chi(-\zeta,\mathcal{A}) - \chi(-\zeta,\mathcal{A}=0)$.

Finally we can calculate the phase slip $\Delta\phi$ of the intensity function at the position of the BS:

$$2/(\epsilon_0 c)\cdot I_{\text{left}}(x) = |A(x)+B(x)|^2 = |C|^2 + |B|^2 + 2|BC|\cos(2kx-\chi); \tag{7.31}$$

$$2/(\epsilon_0 c)\cdot I_{\text{right}}(x) = |C(x)+D(x)|^2 = |C|^2 + |B|^2 + 2|BC|\cos(2kx+\chi). \tag{7.32}$$

We can read off $\Delta\phi = 2\chi$.

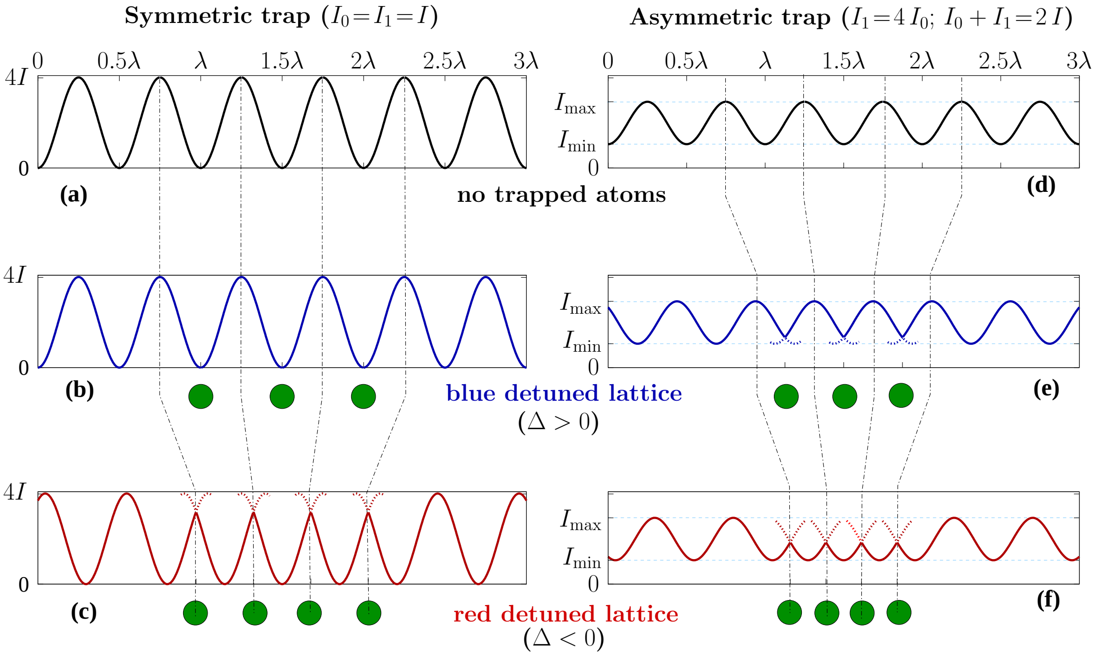

Figure 7.4: Back-action of trapped particles (e.g., atoms) on the intensity of light constituting an optical dipole trap. Top line: the empty trap, created by two counter-propagating beams with equal (a) or unequal (d) intensity. In the asymmetric trap, the intensity ranges between $I_{\min} = (\sqrt{I_1}-\sqrt{I_0})^2$ and $I_{\max} = (\sqrt{I_1}+\sqrt{I_0})^2$. The total power is the same for both traps ($I_0+I_1 = 2I$). Middle line: blue detuning. For symmetric pumping (b), the trapped atoms sit in the dark and have no effect on the lattice. For asymmetric pumping (e), destructive interference between the trap beams cannot be perfect, and thus the atoms are polarized. As a result, the trap *contracts*. Bottom line: red detuning. The lattice constant is reduced in both symmetric (c) and asymmetric (f) trap, but this reduction is enhanced by the asymmetry.

7.3 Self-consistent lattice constant

The result of Eq. (7.28) obtained in the previous Section implies that *in any 1-dimensional structure held together by monochromatic light, with no other types of (external or interaction) forces present except for those from the purely dispersive dipole interaction with the trap light, the light permeates the structure unattanuated.* This is a generalization of the finding of Deutsch et al. [36], who have shown that light permeates a *regular lattice* unattanuated. In formulas, at equilibrium

$$|A_1| \leq |A_2| \ \leq \ldots \leq |A_N| \leq |C_N| = |C|, \tag{7.33}$$

$$|B| = |B_1| \geq |B_2| \geq \ldots \ \ \geq |B_N| \geq |D_N|, \tag{7.34}$$

with equality if and only if $\zeta_1, \ldots, \zeta_N \in \mathbb{R}$. Although one might expect that due to disorder, light would be localized in a 1D lattice, this is not so if it is the light which creates the lattice itself is considered. The random variation of the coupling constants ζ causes a random variation of the lattice constant, the two types of disorder are obviously correlated. For the propagation of the light creating the lattice, either of these noises alone would localize light, but they combine to ensure that the trap light is not localized at all.

Now consider the steady state of $N > 1$ identical, purely dispersive trapped clouds, with $\zeta_1 =, \ldots, = \zeta_N = \zeta < 2/\mathcal{A}$. Since at every cloud $|C_j/B_j| - |B_j/C_j| = \mathcal{A}$, the phase slips are all equal: $\chi_1 =, \ldots, = \chi_N = \chi$. Thus the equilibrium configuration is an equidistant lattice, $x_j = x_j^{(0)} = x_1^{(0)} + (j-1)d$. The lattice constant d is clearly independent of N, and from $\Delta\phi = 2\chi$, we find explicitly

$$\text{red detuning, } \zeta > 0: \quad d(\zeta, \mathcal{A}) = \frac{\lambda}{2}\left(1 - \frac{\chi(\zeta,\mathcal{A})}{\pi}\right); \quad kd = \pi - \chi; \tag{7.35a}$$

$$\text{blue detuning, } \zeta < 0: \quad d(\zeta, \mathcal{A}) = \frac{\lambda}{2}\left|\frac{\chi(\zeta,\mathcal{A})}{\pi}\right| \qquad kd = -\chi; \tag{7.35b}$$

For symmetric pumping, $\mathcal{A} = 0$, we recover the results of Deutsch et al. [36]: for blue detuning $d(\zeta < 0, \mathcal{A} = 0) = \lambda/2$, whereas for red detuning we have $d(\zeta > 0, \mathcal{A} = 0) = d_{\rm symm}(\zeta) = \frac{\lambda}{2}(1 - 2\tan^{-1}(\zeta)/\pi)$. For a given ζ, increasing the pump asymmetry $\mathcal{A}$ causes the phase shift χ to increase, and d to be reduced; this extra reduction turns out to be exactly the same for both red and blue detuning. Contraction of a blue detuned lattice is somewhat counter-intuitive. Naively one could expect the wavelength of the trap light to be *increased* due to the trapped particles as it happens if the particle positions are random. For symmetric pumping, as noted in [36], the equilibrium positions of the particles are exactly at the antinodes, where they do not interact with the field, and thus do not affect the wavelength. For asymmetric pumping, we find that near the intensity minima the atoms *decrease* the effective wavelength, as illustrated in Fig. 7.4. Near the intensity maxima however, their effect is to increase the wavelength by such a large amount that for randomly positioned atoms the expected effective increase of the light passing through the gas is recovered.

The reduction of the lattice constant resulting from the pump asymmetry is shown in Fig.7.5 (thick red lines). For $\mathcal{A} > 2/\zeta$, the inequality (7.25) is violated, the stronger beam pushes all the particles away: thus the thick (red) lines in the Figure all terminate at some at $\mathcal{A} = 2/\zeta$. For red detuning, the lattice constant at this critical asymmetry is, remarkably, exactly half of its value at symmetric pumping: $d(\zeta{>}0,\, \mathcal{A}{=}2/\zeta) = \frac{1}{2}d_{\rm symm}(\zeta)$, a decreasing function of ζ. For blue detuning, the critical lattice constant $d(\zeta{<}0,\, \mathcal{A}{=}2/\zeta)$ *increases* with increasing ζ.

7.4 Dynamics of the lattice

We have found the interesting phenomenon that back-action related effects can be enhanced by using an optical lattice where the trapping beams have unequal intensities. The next step is to investigate this situation in a computer simulation.

7.4.1 Numerical simulation, overdamped dynamics

Numerical simulation of the dynamics of the optical lattice is quite straightforward. Given the positions and velocities of the N atom clouds, the electric fields to the right and to the left of any cloud can be computed by the Transfer Matrix Method, as outlined in Section 7.1.1. Having obtained the mode amplitudes, the optical force on all clouds is given by (7.21). The dynamics of the lattice is then given by a set of second-order ordinary differential equations:

$$m\ddot{x}_j = -\mu\dot{x}_j + F_j(x_1, \ldots, x_N), \quad \text{for} \quad j = 1, \ldots, N. \tag{7.36}$$

In addition to the optical forces, we have also included viscous friction with coefficient μ (related to the single-particle friction coefficient μ_A by $\mu = \eta\mu_A$) to the system: this should stabilize the optical lattice. In experiments with cold atoms in vacuum, this can correspond to some laser cooling mechanism, whereas for plastic beads immersed in water, μ follows from the Stokes law.

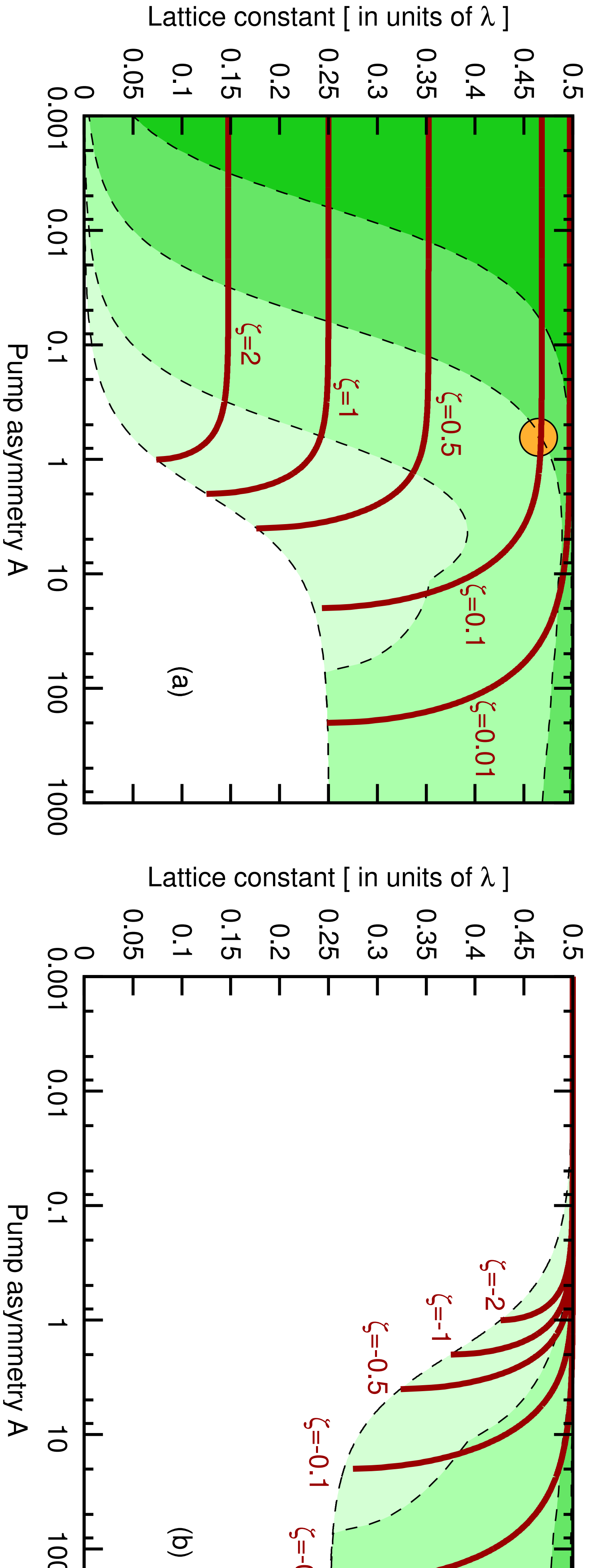
Lattice constant [in units of λ]
0
0.05
0.1
0.15
0.2
0.25
0.3
0.35
0.4
0.45
0.5
0.001
0.01
0.1
1
10
100
1000
Pump asymmetry A
ζ=2
ζ=1
ζ=0.5
ζ=0.1
ζ=0.01
(a)
Lattice constant [in units of λ]
0
0.05
0.1
0.15
0.2
0.25
0.3
0.35
0.4
0.45
0.5
0.001
0.01
0.1
1
10
Pump asymmetry A
ζ=-2
ζ=-1
ζ=-0.5
ζ=-0.1
(b)

Before discussing the simulation results, we digress on the timescales in this dynamical system and introduce the overdamped limit. Without damping, the characteristic timescale of the cloud dynamics is given by the oscillation period of deeply trapped clouds. From formula (7.22) for the force, it can be seen that for small displacements, $|x| \ll \lambda$, trapped clouds experience a harmonic restoring force $F = z_{\text{single}} x$, where

$$z_{\text{single}} = -\beta \frac{|\cos\varphi|}{|1 - i\zeta|^2}, \quad \text{with} \quad \beta = 8\frac{k}{c} |\text{Re}\,\zeta| \sqrt{I_0 I_1}, \tag{7.37}$$

and $\cos\varphi$ is given by Eq. (7.29). Thus the oscillation frequency of a single trapped cloud is

$$\omega_{\text{single}} = \omega_{\text{osc}} \frac{\sqrt{|\cos\varphi|}}{|1 - i\zeta|}, \quad \text{with} \quad \omega_{\text{osc}} = \sqrt{\frac{\beta}{m}}. \tag{7.38}$$

For low asymmetries, $\mathcal{A} \ll \mathcal{A}_{\max}$, where $|\cos\varphi| \approx 1$, and weak coupling, $|\zeta| \ll 1$, whereby $|\mathsf{t}|^2 \approx 1$, we have $\omega_{\text{single}} \approx \omega_{\text{osc}}$, and the characteristic timescale of undamped cloud motion is the oscillation period of a single trapped cloud:

$$\tau_{\text{osc}} = 2\pi \sqrt{\frac{m}{\beta}}. \tag{7.39}$$

Due to the viscous friction, the velocity relaxes towards the value F/μ exponentially in timescale

$$\tau_{\text{vel}} = \frac{m}{\mu}, \tag{7.40}$$

as can be seen by setting F to a constant in (7.36). For small damping, this timescale exceeds τ_{osc} by far ($\tau_{\text{vel}} \gg \tau_{\text{osc}}$), and we expect the system to perform many oscillations before the mechanical energy is totally dissipated. On the other hand, if $\tau_{\text{vel}} \ll \tau_{\text{osc}}$, the system is overdamped: the clouds reach the velocity F/μ in the short timescale of τ_{vel}, and then, on longer timescales, their motion can be described by the first-order equation obtained by dropping the inertial term of (7.36):

$$\mu \dot{x}_j = +F_j(x_1, \ldots, x_N), \quad \text{for} \quad j = 1, \ldots, N. \tag{7.41}$$

For harmonically trapped clouds, using (7.22), (7.37), and (7.41), we can expect them to relax to the equilibrium positions at the bottom of their respective traps exponentially during time

$$\tau_{\text{d}} = \frac{\mu}{\beta}. \tag{7.42}$$

For consistency, we can check if during time τ_{vel} the variation of the force, $dF = v\tau_{\text{vel}}(dF/dx)$ is really small for $v = F/\mu$ and $F = -\beta x$. From $dF = F\beta m/\mu^2 \ll F$ we obtain the condition that we are in the overdamped limit if

$$\beta m \ll \mu^2; \quad \text{equivalently} \quad \tau_{\text{vel}} \ll \tau_{\text{d}}; \quad \text{or} \quad \tau_{\text{osc}} \ll \tau_{\text{d}}. \tag{7.43}$$

The last condition is equivalent to the first two because $\tau_{\text{osc}} = 2\pi\sqrt{\tau_{\text{vel}}\tau_{\text{d}}}$. In fact, for plastic beads trapped in water, the experiments are typically in this overdamped regime (see Section 7.7 for more details).

For the moment, we consider the dynamics of perfectly identical and purely dispersive clouds ($\zeta_1 = \zeta_2 =, \ldots, = \zeta_N \in \mathbb{R}$) with no dynamical noise. This first step towards understanding the dynamics of real optical lattices already provides important surprises. In any realistic simulation, absorption and noise also have to be considered. Inclusion of absorption amounts to setting $\text{Im}\,\zeta > 0$. To include dynamical noise, Langevin terms need to be added to to (7.36) or (7.41). To account for the uncertainty in the number of particles per cloud, we have to have $\zeta_1 \neq \zeta_2 \neq \ldots, \neq \zeta_N$. We address these questions later, in Section 7.6.

We explore the dynamics of optical lattices by slightly perturbing the equilibrium and using numerical simulation to find how the system reacts. Specifically, we fix the cloud polarizabilities ζ, the pump asymmetry $\mathcal{A}$, and set up a lattice configuration,

$$x_j^{(0)} = x_1^{(0)} + (j-1)d, \quad \text{such that} \quad F_j(x_1^{(0)}, \ldots, x_N^{(0)}) = 0, \quad \text{for every } j = 1, \ldots, N. \tag{7.44}$$

The lattice constant d depends on the choice of parameters ζ and $\mathcal{A}$ according to Eq. (7.35), and the position $x_1^{(0)}$ is fixed by the relative phases of the pump beams. Next we add a small perturbation to this lattice, in the form of a random configurational noise. We denote the position of each cloud with respect to its equilibrium position by ξ_j, such that

$$x_j(t) = x_j^{(0)} + \xi_j(t), \tag{7.45}$$

and the initial displacement $\xi_j(t=0)$ is a uniformly distributed random varible between $-\xi_{\text{initial}}$ and $+\xi_{\text{initial}}$, with specifically $\xi_{\text{initial}} = 5 \cdot 10^{-4}\lambda$. We also start the clouds with random velocities uniformly distributed between $-\omega_{\text{osc}}\,\xi_{\text{initial}}$ and $\omega_{\text{osc}}\,\xi_{\text{initial}}$.

In optical lattices with symmetric pumping (an example shown in Fig. 7.6), the atom clouds oscillate almost independently, and roughly with the expected timescale of τ_{osc} (as seen on Fig. 7.6a). However, instead of centering on $\xi = 0$, these oscillations are uniformly displaced, and this displacement itself varies with time in an oscillating fashion. Thus, the center-of-mass oscillations of the whole lattice have a longer timescale, in the example shown in Fig. 7.6, this is roughly $10\omega_{\text{osc}}$. The total intensity inside the structure is not homogeneous: the random displacements create some "cavities" where some extra light is trapped, or from where extra light can be expelled. As the atom clouds oscillate, so does the intensity, around the average value of $I_0 + I_1$ roughly with the frequency ω_{osc}. The local pump power ratio, the ratio of left– to right–propagating intensities, however, is roughly independent of position in the lattice, and oscillates at the same rate as the center-of-mass, at ω_{osc}. This produces a signal — the variation of the transmitted intensities — that could be used for detection of the "slow" center-of-mass oscillations. This is the signal that would be expected for a single beam splitter oscillating at the slow frequency $10\,\omega_{\text{osc}}$, resulting from the change of the phases acquired by the beams until they reach the beam splitter.

Friction damps the oscillations of the atom clouds, and in the overdamped limit — an example shown in Fig. 7.7 — as expected, instead of oscillations we only see the damping of the initial noise. The center of mass relaxes on a longer timescale here too, but much longer: in Fig. 7.7, this timescale is roughly $100\tau_{\text{d}}$.

This picture is drastically changed in the presence of pump asymmetry. In the example shown in Fig. 7.8, we set $I_1 = 1.42 I_0$. Initially, in the first $10\tau_{\text{osc}}$, the qualitative features familiar from the symmetric pumping case can be observed, the only difference being that the local pump power ratio now depends on x, as seen in Fig.7.8c. Thereafter, however, the oscillations of neighboring atom clouds appear to phase lock, and thus a *density wave* appears in the system, propagating in the direction opposite to the stronger laser beam, crossing the whole lattice once every τ_{osc}. This wave determines all of the three plotted properties, and is amplified in time. In fact, this amplification is exponential, and after roughly another $10\tau_{\text{osc}}$ the amplitudes of the cloud oscillations are so large that some clouds merge, and, eventually, the whole lattice is pushed away by the stronger beam.

The overdamped limit of the dynamics in an asymmetric trap reveals even more surprises. Starting the simulation with the same realization of noise as in Fig. 7.7, but a larger pump asymmetry, $I_1 = 1.87 I_0$, we observe (see Fig. 7.9) that most of the initial excitation is damped out as before. However, the same phase-locked oscillations as seen for the undamped case appear here, and the clouds *oscillate in spite of overdamping*. The amplitude of oscillations is larger for larger

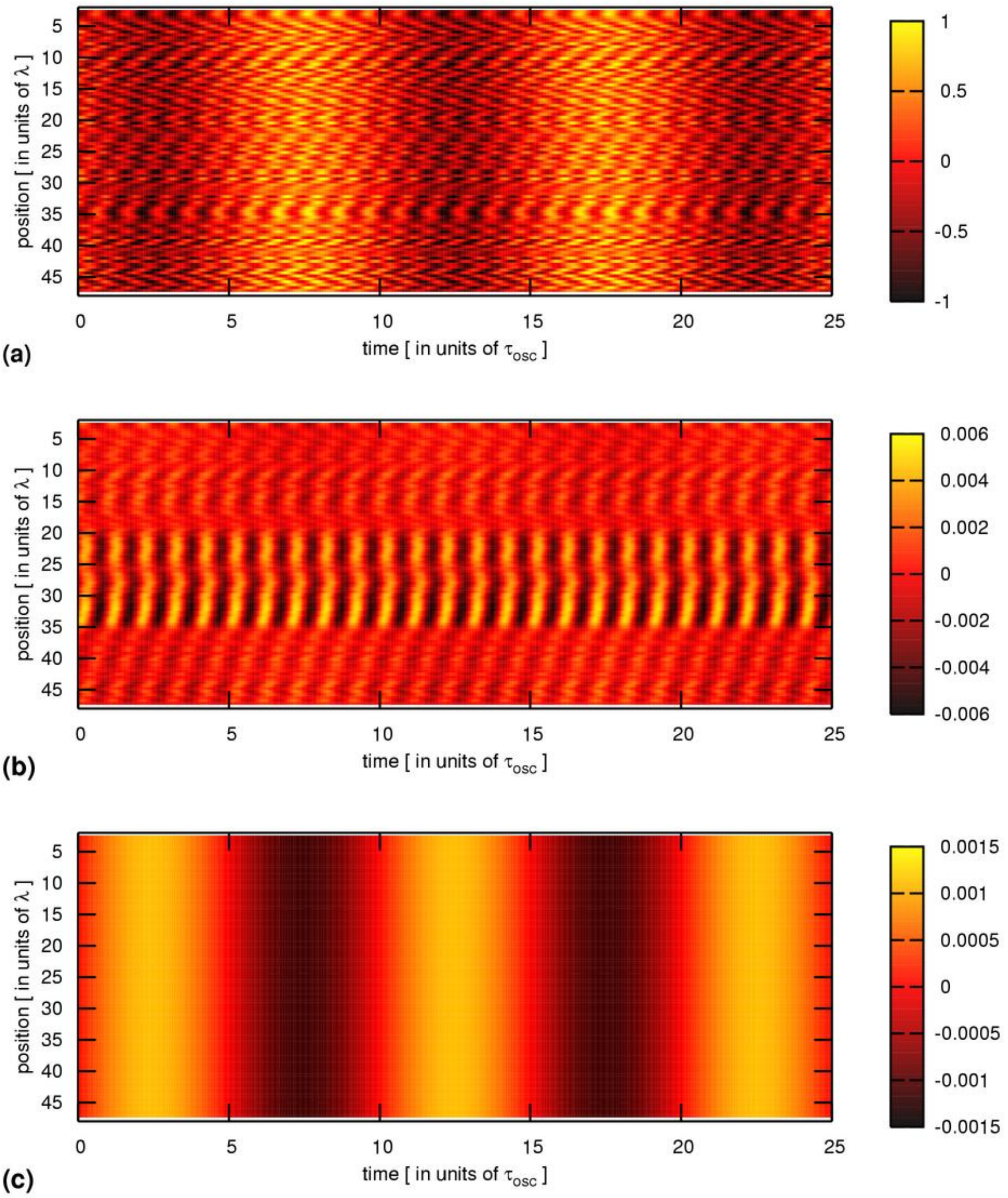

Figure 7.6: Numerical simulation of the dynamics of an optical lattice of $N = 100$ clouds with polarizability $\zeta = 0.1$ each, with symmetric pumping $I_0 = I_1$, after initial excitation (random displacement from the equilibrium with maximum magnitude $\xi_{\text{initial}} = 5 \cdot 10^{-4}\lambda$ and random velocity of maximum magnitude $\omega_{\text{osc}}\xi_{\text{initial}}$). No friction forces are assumed ($\mu = 0$). Color coding stands for position distortions ξ in (a), excess intensity $I(x) - (I_0 + I_1)$ in (b), and excess pump asymmetry $I_{\text{left}}(x)/I_{\text{right}}(x) - I_1/I_0$ in (c).

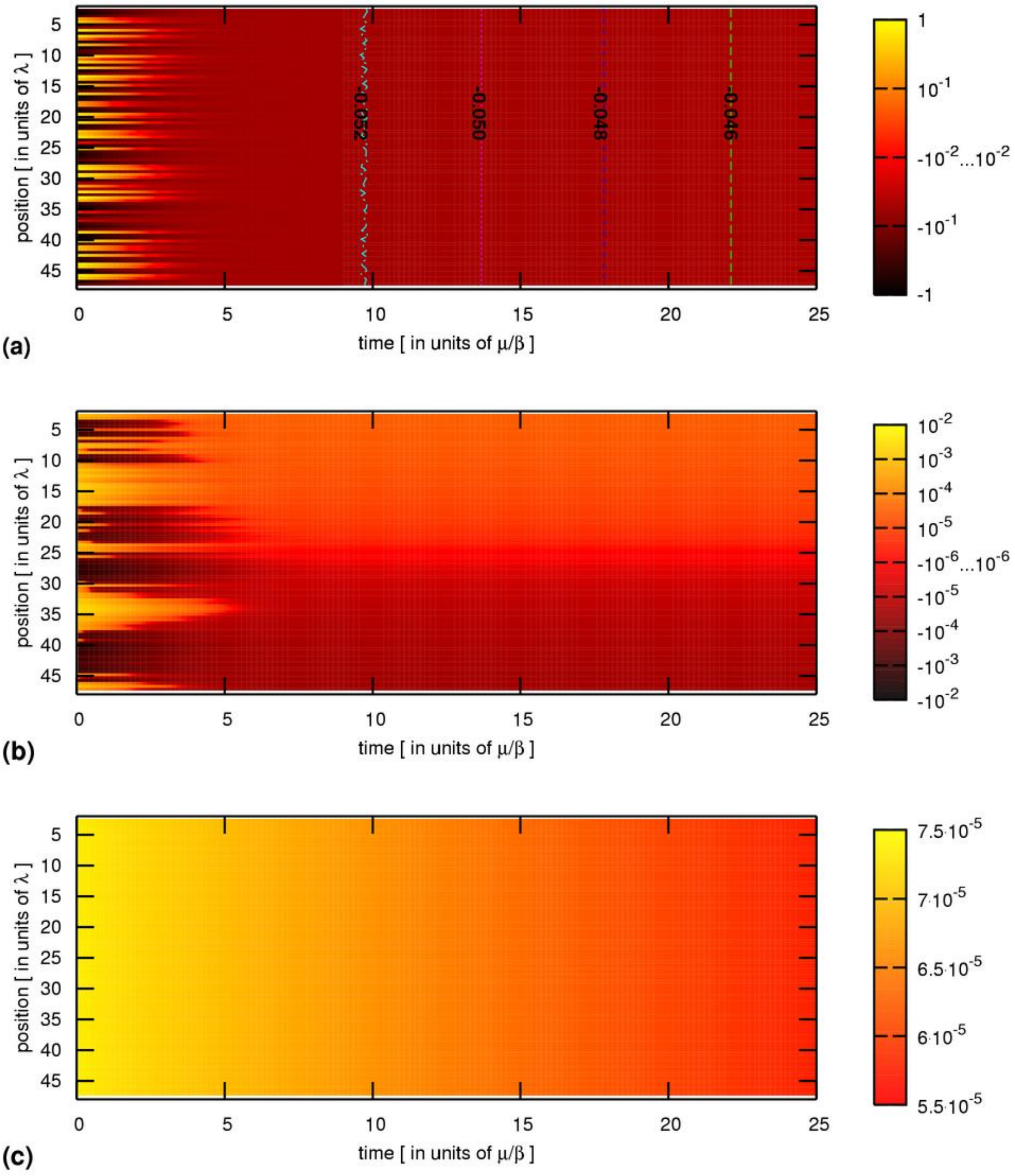

Figure 7.7: Numerical simulation of the dynamics of an optical lattice of $N = 100$ clouds with polarizability $\zeta = 0.1$ each, with symmetric pumping $I_0 = I_1$, after initial excitation (random displacement from the equilibrium with maximum magnitude $\xi_{\text{initial}} = 5 \cdot 10^{-4}\lambda$). The overdamped limit is assumed ($\mu^2 \gg \beta m$). Color coding stands for position distortions ξ in (a), excess intensity $(I(x) - (I_0 + I_1)$ in (b), and excess pump asymmetry $(I_{\text{left}}(x)/I_{\text{right}}(x) - I_1/I_0)$ in (c).

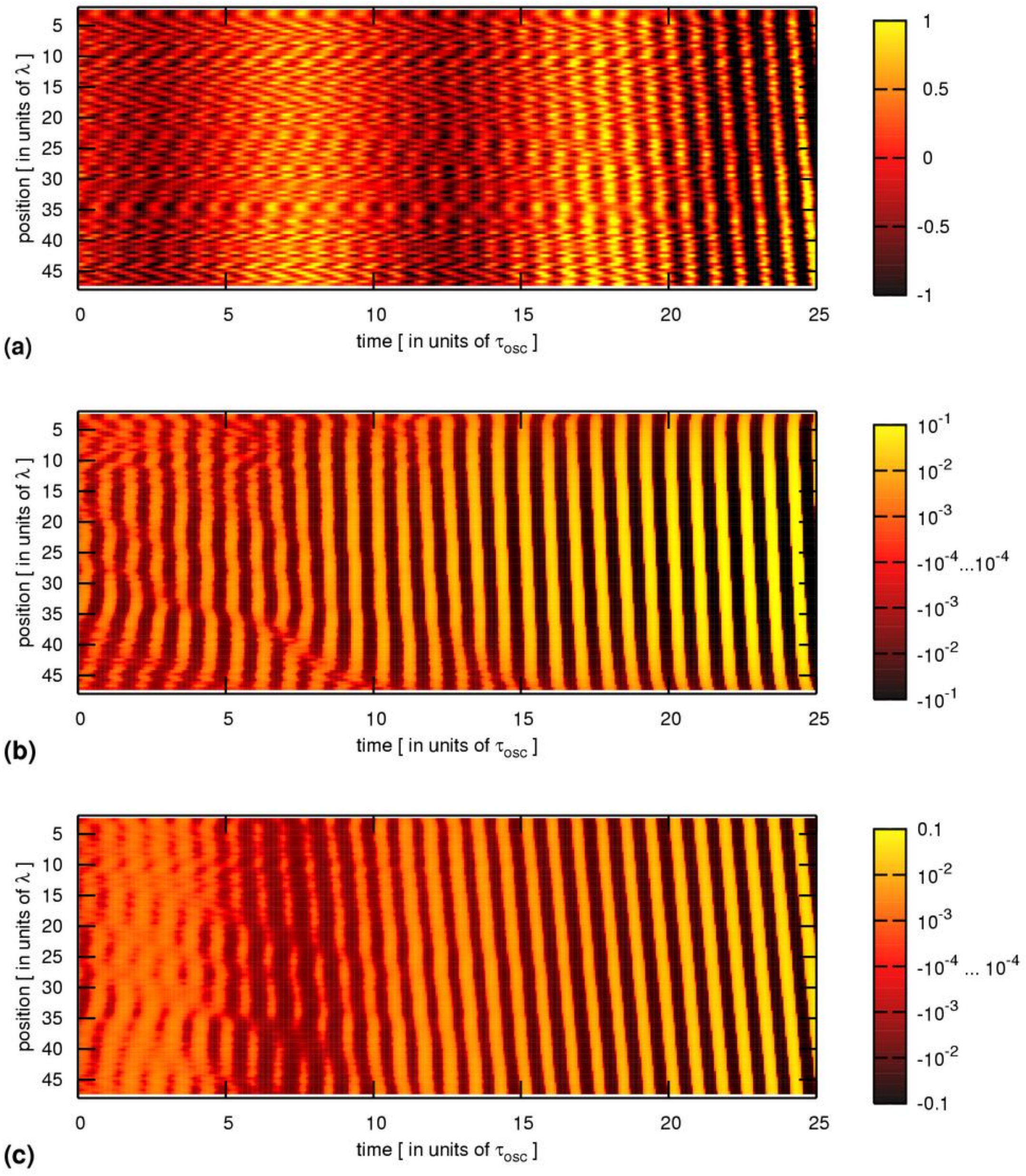

Figure 7.8: Numerical simulation of the dynamics of an optical lattice of $N = 100$ clouds with polarizability $\zeta = 0.1$ each, with asymmetric pumping, $I_1 = 1.42 I_0$, after initial excitation (random displacement from the equilibrium with maximum magnitude $\xi_{\mathrm{initial}} = 5 \cdot 10^{-4}\lambda$ and random velocity of maximum magnitude $\omega_{\mathrm{osc}}\xi_{\mathrm{initial}}$). No friction forces are assumed ($\mu = 0$). Color coding stands for position distortions ξ in (a), excess intensity $(I(x) - (I_0 + I_1)$ in (b), and excess pump asymmetry $(I_{\mathrm{left}}(x)/I_{\mathrm{right}}(x) - I_1/I_0)$ in (c).

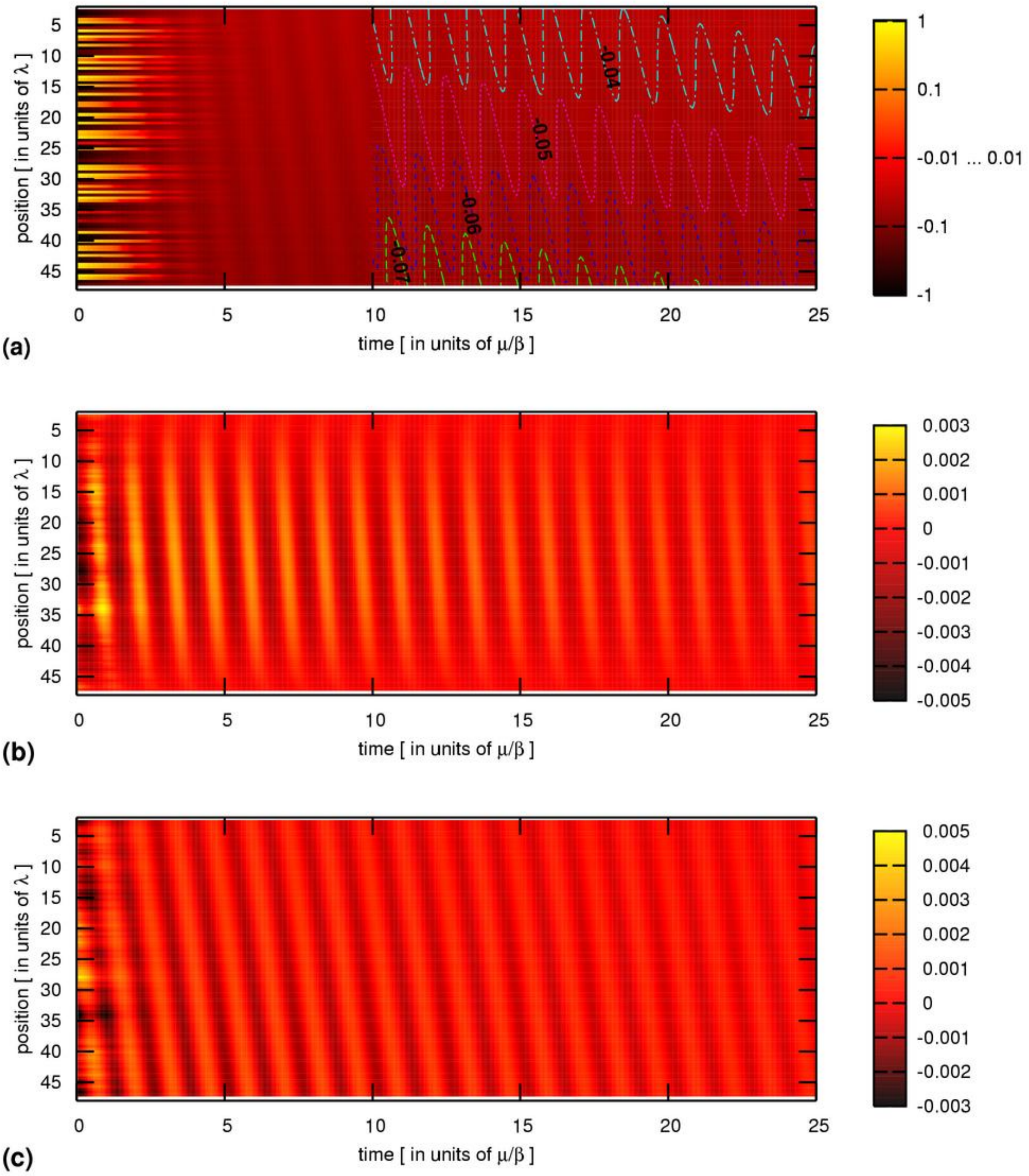

Figure 7.9: Numerical simulation of the dynamics of an optical lattice of $N = 100$ clouds with polarizability $\zeta = 0.1$ each, with asymmetric pumping $I_1 = 1.87 I_0$, after initial excitation (random displacement from the equilibrium with maximum magnitude $\xi_{\text{initial}} = 5 \cdot 10^{-4} \lambda$). The overdamped limit is assumed ($\mu^2 \gg \beta m$). Color coding stands for position distortions ξ in (a), excess intensity $(I(x) - (I_0 + I_1)$ in (b), and excess pump asymmetry $(I_{\text{left}}(x)/I_{\text{right}}(x) - I_1/I_0)$ in (c). In (a), for better readability, for $t > 10\mu/\beta$ some contour lines are shown, from top to bottom: $\xi = -0.04\,\xi_{\text{initial}}$ (dash-dotted), $\xi = -0.05\,\xi_{\text{initial}}$ (dash-dot-dotted), $\xi = -0.06\,\xi_{\text{initial}}$ (short dashed), and $\xi = -0.06\,\xi_{\text{initial}}$ (long dashed).

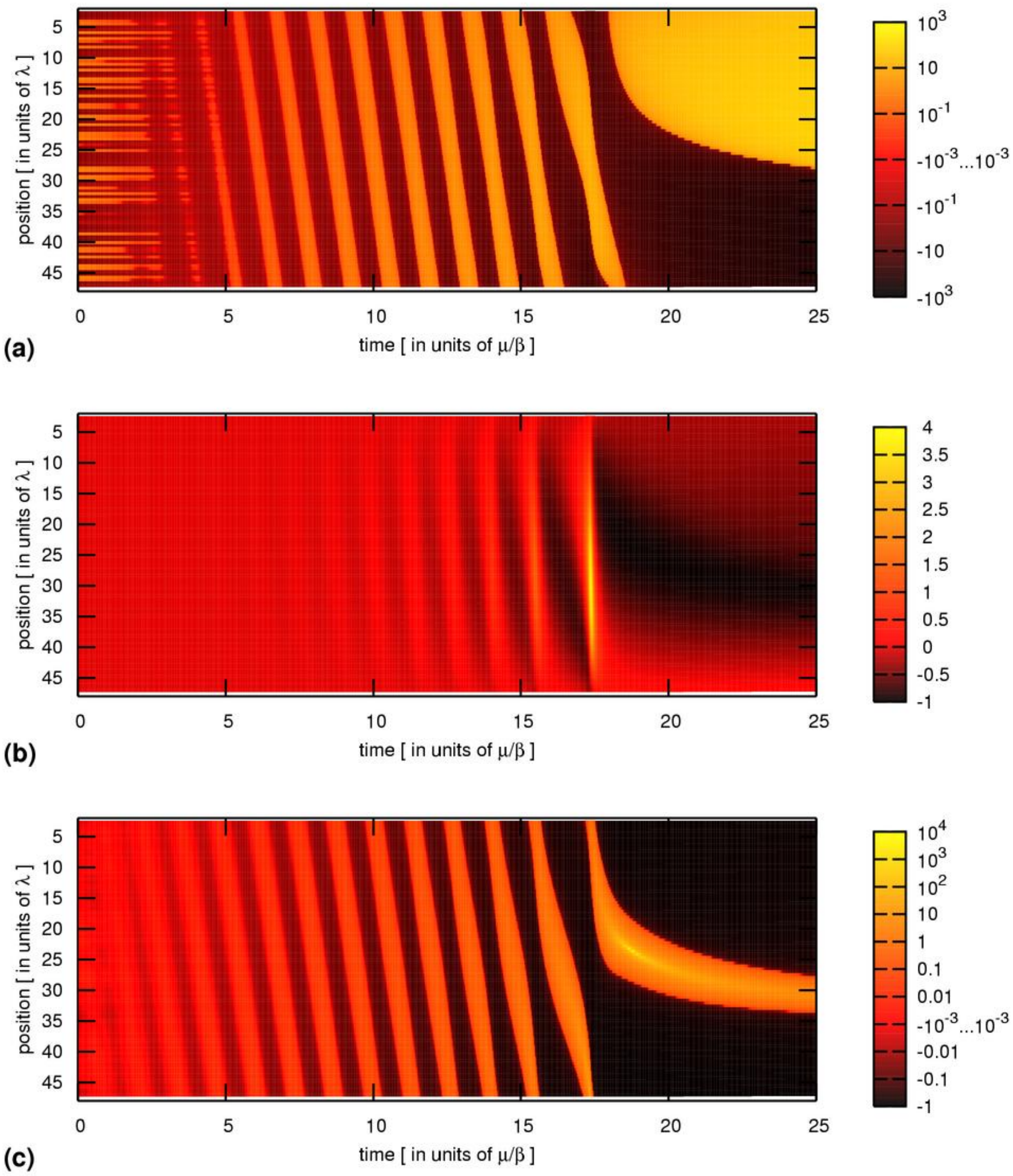

Figure 7.10: Numerical simulation of the dynamics of an optical lattice of $N = 100$ clouds with polarizability $\zeta = 0.1$ each, with asymmetric pumping $I_1 = 1.88 I_0$, after initial excitation (random displacement from the equilibrium with maximum magnitude $\xi_{\text{initial}} = 5 \cdot 10^{-4}\lambda$). The overdamped limit is assumed ($\mu^2 \gg \beta m$). Color coding stands for position distortions ξ in (a), excess intensity $(I(x) - (I_0 + I_1)$ in (b), and excess pump asymmetry $(I_{\text{left}}(x)/I_{\text{right}}(x) - I_1/I_0)$ in (c).

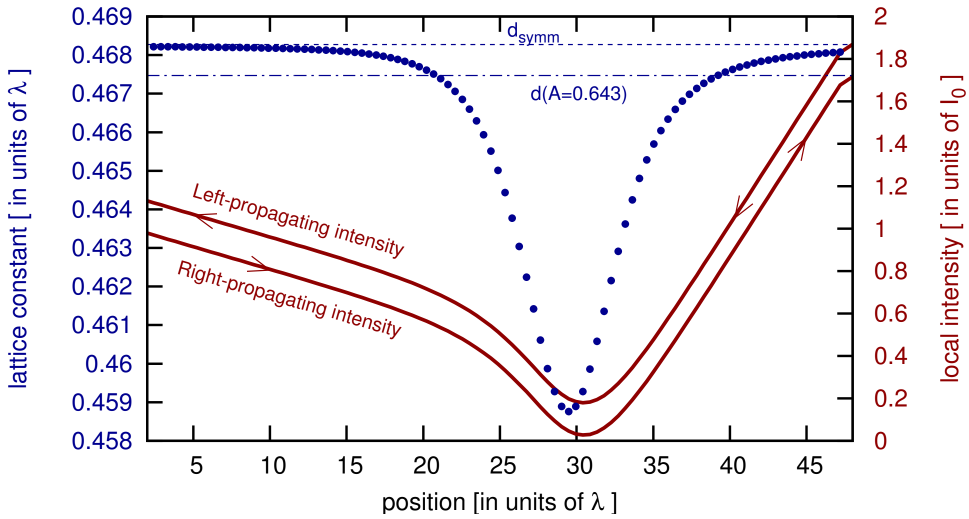

Figure 7.11: Snapshot of the simulation plotted in Fig. 7.10 at time $t = 25\mu/\beta$. The local lattice constant is shown in blue points, with the lattice constant d_{symm} corresponding to symmetric pumping, and the equilibrium lattice constant d with the asymmetry used here $\mathcal{A} = 0.643$ also displayed for reference. The continuous (red) lines show the variation of the intensities in the left- and rightwards propagating modes inside the structure (their sum is the total intensity).

x, i.e., it increases towards the source of the stronger pump. The oscillations are all damped with the same timescale of – for these parameters – roughly 22 τ_{d}, and on a longer timescale of roughly $100\tau_{\mathrm{d}}$ the center-of-mass relaxes as well. Increasing the asymmetry further, to $I_1 = 1.88 I_0$, leads to an instability very similar to that occurring in the undamped case. As seen in Fig. 7.10a, after a few τ_{d} most of the initial excitation dies out, except for the displacement of the center-of-mass and for the density wave with wavelength equal to the system size. Now, however, this wave is amplified, and between 15 and 20 τ_{d} the dynamics of the lattice is changed. The lattice breaks into two blocks, each of them with roughly the original lattice constant d, the one to the left is displaced towards the right, the one to the right displaced towards the left. As shown in Fig. 7.11, in both slabs the average lattice constant is slightly above the expected value based on Eq. 7.35. At their boundary, which in this run happens to be around $x = 30\lambda$, the lattice constant is reduced, and, as shown in Fig. 7.10b, the intensity is reduced as well. Thus optical forces push the two blocks towards each other. Later, at about $t \approx 45\tau_{\mathrm{d}}$, the blocks meet, and at their boundary two atom clouds merge (this is not shown in the Figure). Subsequently, other clouds merge as well and eventually (after thousands of μ/β) the whole structure will be pushed away by the stronger beam. Note that $I_1/I_0 \approx 1.87$ corresponds to $\mathcal{A} \approx 0.64$ and therefore the Figs. 7.9 and 7.10 are both in the parameter regime denoted by the (orange) circle in Fig. 7.5.

After giving a taste of the dynamics in the undamped and overdamped limit, we now summarize some of the qualitative observations based on the simulations of the full equations of motion (7.36).

- For symmetric lattices, both the oscillation and the damping timescales of the center of mass of the structure are longer than those of the motion of the individual clouds.
- At small asymmetries, due to damping, the system still settles down to an equlibrium, which can be a regular optical lattice.
- For asymmetries exceeding a critical value $\mathcal{A} > \mathcal{A}_{\mathrm{crit}}$, but easily satisfying $\mathcal{A} < 2/\zeta$,

however, the steady state optical lattice configuration is never attained. Clouds merge, and, in typical runs, eventually the whole structure is pushed away by the stronger beam.

- Increasing the friction μ can help to stabilize the system, i.e., increase $\mathcal{A}_{\text{crit}}$. However, friction only helps up to a limit: there is a value of the asymmetry $\mathcal{A}_*$, such that if $\mathcal{A} > \mathcal{A}_*$, even the overdamped dynamics fails to converge to the optical lattice – and, typically, for this second limit we also have $\mathcal{A}_* \ll 2/\zeta$.
- Curiously, although oscillations die out faster and faster if the damping coefficient μ is increased, they do not disappear as $\mu \to \infty$. We have *oscillations even in the overdamped limit.*
- As intuitively expected, both $\mathcal{A}_{\text{crit}}$ and $\mathcal{A}_*$ are smaller if the clouds have larger polarizability ζ.
- Quite surprisingly, however, $\mathcal{A}_{\text{crit}}$ and $\mathcal{A}_*$ depend on the number of clouds N in the structure: both $\mathcal{A}_{\text{crit}}(\zeta, \mu, N)$ and $\mathcal{A}_*(\zeta, N)$ decrease with increasing N. Thus, an asymmetric trap can only support a finite number of atom clouds with polarizability ζ: even though an equlibrium optical lattice configuration with any N exists, this configuration is unstable for $N > N_{\text{crit}}(\zeta, \mu, \mathcal{A})$.

Due to the above listed curious effects, the asymmetry-induced contraction of the optical lattice given by (7.35) and plotted in Fig. 7.5 would not occur in a real experiment with extremely asymmetric dipole trap. Even with an arbitrary amount of viscous friction, if $\mathcal{A} > \mathcal{A}_*(\zeta, N)$, the lattice would become unstable and be destroyed. This is already illustrated on Fig. 7.5, where the (green) shaded areas limited by dashed lines are the parameter regimes where optical lattices of specific sizes can be created (i.e., stabilized by viscous friction), for various values of N. The boundary between the darkest and second darkest areas (which is hardly resolved in Fig. 7.5 (b)) corresponds to the onset of the instability for $N = 1000$; the two subsequent boundaries are for $N = 100$ and $N = 10$. The last dashed line, the one that separates the white area from the one with the lightest shade, corresponds to $\zeta = 2/\mathcal{A}$, and is in fact the limit of stability for an OL consisting of 2 clouds as well as for a single cloud. These limits of stability are also plotted directly as functions of ζ and $\mathcal{A}$ in Fig. 7.12, where the color coding is the same as in Fig. 7.5, but data for larger lattice sizes is also included.[3]

7.5 Dynamics near equilibrium: analytical results

We can gain an analytical understanding of the phenomena listed above by studying the dynamics infinitesimally close to an equilibrium configuration. There we can develop the optical force on all of the clouds into a Taylor series, and from the nonlinear equation (7.36) we obtain, using the notations introduced in Eqs. (7.45) and (7.44), the linearized form

$$m\ddot{\xi}_j = -\mu\dot{\xi}_j + \sum_{l=1}^{N} D_{jl}\xi_l, \tag{7.46}$$

---

[3] The color coding and slashed lines denoting the regimes of stability come in fact from the analytical calculations detailed in Section 7.5, and not directly from simulations themselves (the computational cost is only linear with N, but simulations with $N = 10^6$ are still impractical). Therefore they correspond to stability with respect to infinitesimal perturbations. As such, they have been checked via simulation and seen to be correct several times, as illustrated in the examples in Figs. 7.9 and 7.10.

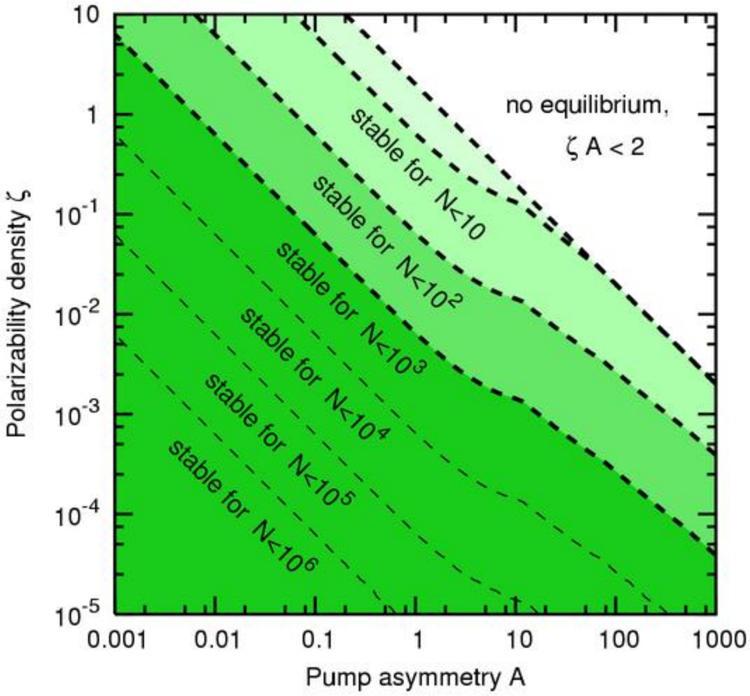

Figure 7.12: Parameter regimes where an optical lattice can be stabilized by viscous friction. White area is unstable, see Eq. (7.25). Thick slashed lines correspond to the slashed lines on Fig. 7.5

where the matrix $\mathbf{D}$ is defined by

$$D_{jl} = \frac{\partial}{\partial x_l} F_j(x_1 = x_1^{(0)}, \ldots, x_N = x_N^{(0)}), \tag{7.47}$$

or, in a more suggestive way,

$$D_{jl} = \lim_{\xi \to 0} \frac{1}{\xi} F_j(x_n = x_n^{(0)} + \delta_{ln}\, \xi, \quad n = 1, \ldots, N). \tag{7.48}$$

In (7.46) we have a set of N coupled linear differential equations. The diagonal part of $\mathbf{D}$ describes the oscillations of the clouds around their equilibrium positions. The off-diagonal terms are responsible for coupling these oscillations: they contain the interaction mediated by the trapping laser field. To understand the dynamics we need to find the eigenvectors and eigenvalues of $\mathbf{D}$. These will provide us with the noninteracting vibrational modes: their spatial structure, their frequencies and their damping coefficients. We detail the calculations below, broken down into several steps. For these calculations, for simplicity we assume purely dispersive interaction, $\zeta \in \mathbb{R}$.

7.5.1 Eigenmodes of light in the lattice

To find the force on the j'th cloud, given by Eq. (7.21), we have to obtain A_j, B_j, C_j and D_j. The first step to their calculation is to find the eigenvectors of the transfer matrix of one unit of the lattice, $\mathbf{M}(k, d)$ (see Section 7.1.1). We fix the pump power ratio $\mathcal{P}$, which gives the lattice constant d via Eq. (7.35), and set set $k = 2\pi/\lambda$, i.e., we calculate the transmission of the light constituting the periodic dipole trap. The periodicity of the optical lattice suggests that one of the eigenvectors is

$$\mathbf{u} = e^{ikd}\mathbf{P}(-d)\begin{pmatrix}\sqrt{\mathcal{P}}\\ e^{i\chi}\end{pmatrix} = \begin{pmatrix}\sqrt{\mathcal{P}}\\ e^{-i\chi}\end{pmatrix}; \quad \text{eigenvector of } \mathbf{M}\text{, eigenvalue } e^{+i\Theta} \tag{7.49}$$

where the factor e^{ikd} was introduced for convenience, and we used Eq. (7.35). We find that indeed $e^{i\Theta}\mathbf{u} = \mathbf{M}_{\text{BS}}\mathbf{P}(d)\mathbf{u}$, if $\Theta = \varphi + \chi + kd$, whereby, using Eq. (7.29) and Eq. (7.35) we have for both red and blue detuning,

$$\sin\Theta = \frac{1}{2}\left|\zeta\right|\mathcal{A};, \qquad \cos\Theta = -\frac{1}{2}\sqrt{4-\zeta^2\mathcal{A}^2}. \tag{7.50}$$

The other eigenvector can be found using Eq. (7.17), the reflection symmetry of the BS: $\boldsymbol{\sigma}\mathbf{P}(d)\mathbf{u} = \mathbf{M}_{\text{BS}}\boldsymbol{\sigma}e^{i\Theta}\mathbf{u} = e^{i\Theta}\mathbf{M}_{\text{BS}}\mathbf{P}(d)(\mathbf{P}(-d)\boldsymbol{\sigma}\mathbf{u}$, and by the reflection symmetry of free propagation $\boldsymbol{\sigma}\mathbf{P}(d) = \mathbf{P}(-d)\boldsymbol{\sigma}$ we have

$$\mathbf{w} = e^{-ikd}\mathbf{P}(-d)\boldsymbol{\sigma}\mathbf{u} = \begin{pmatrix}e^{i\chi}\\ \sqrt{\mathcal{P}}\end{pmatrix}; \quad \text{eigenvector of } \mathbf{M}\text{, eigenvalue } e^{-i\Theta}\ , \tag{7.51}$$

corresponding to asymmetric pumping with $I_0 > I_1$. As expected, for propagation of the trap beams we have $\Theta \in \mathbb{R}$, ensuring that these beams do indeed permeate the lattice unattanuated. Note that as $\mathbf{M}$ is not Hermitian, $\mathbf{u}$ and $\mathbf{w}$ do not form an orthonormal basis: $\mathbf{u}^\dagger\mathbf{u} = \mathbf{w}^\dagger\mathbf{w} = 1+\mathcal{P}$, and $\mathbf{u}^\dagger\mathbf{w} = 2\sqrt{\mathcal{P}}e^{i\chi}$.

7.5.2 Propagation of light in the perturbed lattice

We now compute the mode amplitudes A_j, B_j, C_j, D_j inside an optical lattice composed of purely dispersively scattering identical clouds. At equilibrium, with $\left|E_1\right|^2 = \mathcal{P}\left|E_0\right|^2$, we have an equidistant lattice with lattice constant given by Eq. (7.35), and, as seen above,

$$\begin{pmatrix}A_j\\ B_j\end{pmatrix} = \mathbf{M}^{N-j+1}\begin{pmatrix}C_N\\ D_N\end{pmatrix} = \mathbf{M}^{N-j+1}\mathcal{E}_0\mathbf{u} = \mathcal{E}_0 e^{i(N-j+1)\Theta}\mathbf{u}, \tag{7.52}$$

with the complex factor $\mathcal{E}_0 = E_1 e^{-ik(x_N+d)}\mathcal{P}^{-1/2}$, note that $|\mathcal{E}_0| = |E_0|$.

Now if we perturb the optical lattice by displacing the l'th element by ξ, as in Eq. (7.48), the transfer matrix of the whole structure is changed, and this affects the outgoing modes. We can then write the fields at the far left end of the structure in terms of the fields at the far right end in the following way:

$$e^{iN\Theta}\mathbf{u} + \frac{\xi}{k}\begin{pmatrix}a^{(l)}\\ 0\end{pmatrix} = \mathbf{M}^{l-1}\mathbf{P}(\xi)\mathbf{M}_{\text{BS}}\mathbf{P}(-\xi)\mathbf{P}(d)\mathbf{M}^{N-l}\left[\mathbf{u} + \frac{\xi}{k}\begin{pmatrix}0\\ b^{(l)}\end{pmatrix}\right]. \tag{7.53}$$

The perturbations can be expanded in the basis given by the eigenvectors $\mathbf{u}$ and $\mathbf{w}$:

$$\begin{pmatrix}a^{(l)}\\ 0\end{pmatrix} = a_u^{(l)}\mathbf{u} + a_w^{(l)}\mathbf{w}; \qquad a_u^{(l)} = -\sqrt{\mathcal{P}}e^{i\chi}a_w^{(l)}; \qquad a^{(l)} = -(\mathcal{P}-1)e^{i\chi}a_w^{(l)} \tag{7.54a}$$

$$\begin{pmatrix}0\\ b\end{pmatrix} = b_u^{(l)}\mathbf{u} + b_w^{(l)}\mathbf{w}; \qquad b_w^{(l)} = -\sqrt{\mathcal{P}}e^{-i\chi}b_u^{(l)}; \qquad b^{(l)} = -(\mathcal{P}-1)e^{-i\chi}b_u^{(l)}. \tag{7.54b}$$

Note that to first order in $\varepsilon = \xi/k$,

$$\mathbf{P}(\varepsilon/k)\mathbf{M}_{\text{BS}}\mathbf{P}(-\varepsilon/k) = \mathbf{M}_{\text{BS}} - 2\varepsilon\zeta\boldsymbol{\sigma}, \tag{7.55}$$

with the matrix $\boldsymbol{\sigma}$ corresponding to reflection about x as defined in (7.16). We can now gather the first-order terms from (7.53), and have

$$\begin{aligned} a_u^{(l)}\mathbf{u} + a_w^{(l)}\mathbf{w} &= \mathbf{M}^N(b_u^{(l)}\mathbf{u} + b_w^{(l)}\mathbf{w}) - 2\varepsilon\zeta\,\mathbf{M}^{l-1}\boldsymbol{\sigma}\mathbf{P}(d)\mathbf{M}^{N-l}\mathbf{u} \\ &= b_u^{(l)}e^{iN\Theta}\,\mathbf{u} + b_w^{(l)}e^{-iN\Theta}\,\mathbf{w} \;+\; 2\,|\zeta|\,e^{-i\chi}e^{i(N-2l+1)\Theta}\,\mathbf{w}. \end{aligned} \tag{7.56}$$

The $\mathbf{u}$ and $\mathbf{w}$ components of this equation, together with the relations (7.54) give

$$a_w^{(l)} = -2\,|\zeta|\,e^{-i\chi}e^{i(2N-2l+1)\Theta}\frac{1}{\mathcal{P}e^{-iN\Theta} - e^{iN\Theta}} \tag{7.57a}$$

$$b_u^{(l)} = 2\,|\zeta|\,\sqrt{\mathcal{P}}e^{i(N-2l+1)\Theta}\frac{1}{\mathcal{P}e^{-iN\Theta} - e^{iN\Theta}} \tag{7.57b}$$

Note that each of these expressions contains the denominator $\mathcal{P}e^{-iN\Theta} - e^{iN\Theta}$, which can give a resonant enhancement for certain values of the asymmetry.

We can now proceed to calculate the mode amplitudes inside the perturbed optical lattice using the transfer matrices.

For $j > l$, i.e., light to the right of the displaced cloud (the stronger beam is the one incident from the right), we have

$$\begin{aligned} j > l: \quad \begin{pmatrix} A_j \\ B_j \end{pmatrix} &= \mathcal{E}_0\mathbf{M}^{N-j+1}\left[\mathbf{u} + \varepsilon b_u^{(l)}\left(\mathbf{u} - \sqrt{\mathcal{P}}e^{-i\chi}\mathbf{w}\right)\right] \\ &= \mathcal{E}_0 e^{i(N-j+1)\Theta}\mathbf{u} + \varepsilon\mathcal{E}_0 b_u^{(l)}\left[e^{i(N-j+1)\Theta}\mathbf{u} - e^{-i(N-j+1)\Theta}\sqrt{\mathcal{P}}e^{-i\chi}\mathbf{w}\right]. \end{aligned} \tag{7.58}$$

To first order in ε we then have

$$\frac{|A_j|^2 + |B_j|^2}{|E_0|^2} \;=\; \mathcal{P} \;+\; 1 \;+\; 2\varepsilon(\mathcal{P} \;+\; 1)\mathrm{Re}\,b_u^{(l)} \;-\; 4\mathcal{P}\varepsilon\mathrm{Re}\left[b_u^{(l)}e^{-2i(N-j+1)\Theta}\right]. \tag{7.59}$$

For $j < l$, the transfer matrix of the displaced l'th cloud also enters the calculation:

$$\begin{aligned} \begin{pmatrix} A_j \\ B_j \end{pmatrix} &= \mathcal{E}_0\left[\mathbf{M}^{N-j+1} - 2\varepsilon\zeta\,\mathbf{M}^{l-j}\boldsymbol{\sigma}\mathbf{P}(d)\mathbf{M}^{N-l}\right]\left[\mathbf{u} + \varepsilon b_u^{(l)}\left(\mathbf{u} - \sqrt{\mathcal{P}}e^{-i\chi}\mathbf{w}\right)\right] \\ &= \mathcal{E}_0 e^{i(N-j+1)\Theta}\mathbf{u} + \varepsilon\mathcal{E}_0\left[b_u^{(l)}e^{i(N-j+1)\Theta}\mathbf{u} - b_u^{(l)}e^{-i(N-j+1)\Theta}\sqrt{\mathcal{P}}e^{-i\chi}\mathbf{w}\right. \\ &\qquad\qquad\qquad\qquad\qquad\qquad\qquad\qquad \left. -2\zeta e^{i(N-2l+j)\Theta}e^{ikd}\mathbf{w}\right]. \end{aligned} \tag{7.60}$$

In this case, to first order in ε the sum of the intensities gives

$$\begin{aligned} \frac{|A_j|^2 + |B_j|^2}{|E_0|^2} &= \mathcal{P} + 1 + 2\varepsilon(\mathcal{P} + 1)\mathrm{Re}\,b_u^{(l)} - 4\mathcal{P}\varepsilon\mathrm{Re}\left[b_u^{(l)}e^{-2i(N-j+1)\Theta}\right] \\ &\qquad + 8\,|\zeta|\,\sqrt{\mathcal{P}}\varepsilon\mathrm{Re}\,e^{i(2j-2l-1)\Theta}. \end{aligned} \tag{7.61}$$

7.5.3 Explicit form of D

Using the above formulas (7.59) and (7.61), we can read off the forces, and obtain

$$D_{jl} = \begin{cases} -2\beta\sin\Theta\,\mathrm{Im}\,\dfrac{\mathcal{P}e^{2i(j-l)\Theta}}{\mathcal{P} - e^{i2N\Theta}}, & j > l \\ -2\beta\sin\Theta\,\mathrm{Im}\,\dfrac{\mathcal{P}}{\mathcal{P} - e^{i2N\Theta}} + \beta\cos\Theta, & j = l \\ -2\beta\sin\Theta\,\mathrm{Im}\,\dfrac{e^{2iN\Theta}e^{2i(j-l)\Theta}}{\mathcal{P} - e^{i2N\Theta}}, & j < l \end{cases} \tag{7.62}$$

where β is given by Eq. (7.37), and ω_{osc} by Eq. (7.38).

For symmetric pumping we can take the limit $|E_1| \to |E_0|$ of (7.62), and find quite simply[4]

$$D_{jl} = -\beta\delta_{jl} + \beta\frac{N\zeta^2}{1+N^2\zeta^2}. \tag{7.63}$$

7.5.4 Lattice vibration eigenmodes

For symmetric pumping, close to equilibrium, substitution of Eq. (7.63) into Eq. (7.46) gives

$$F_j = -\beta\frac{1}{1+N^2\zeta^2}\,\xi_j + \beta\frac{N\zeta^2}{1+N^2\zeta^2}\sum_{l\neq j}(\xi_l - \xi_j). \tag{7.64}$$

The clouds behave as uniformly coupled oscillators. The coupling of the oscillators is independent of the distance $j-l$ of the sites, but does depend on the size N of the whole structure. This coupling can be enhanced by increasing the system size N, however, it reaches a maximum of $\beta\,|\zeta|\,/2$ when $N\,|\zeta| = 1$, and further increase of N results in a *decrease* of the coupling roughly as $1/N$. It is quite clear that the coupling does not affect the common mode (or center-of-mass motion) of the lattice, i.e., when all of the clouds oscillate with the same phase. As seen from (7.64), the "spring constant" and the oscillation frequency, of this mode are

$$z_0 = -\beta\frac{1}{1+N^2\zeta^2}, \qquad \omega_0 = \frac{\omega_{\text{osc}}}{\sqrt{1+N^2\zeta^2}}. \tag{7.65}$$

The spring constant z_0 is lower in magnitude than the naive expectation of $z_{\text{single}} = -\beta/(1+\zeta^2)$ from Eq. (7.37), whereby the oscillations of the center-of-mass are slower than naively expected. For all other modes of vibration, orthogonal to the center-of-mass mode, however, the coupling increases the frequencies. Using (7.63) it is directly seen that they are degenerate, and have the spring constant and oscillation frequency

$$z_1 = z_2 =, \ldots, = z_N = -\beta; \qquad \omega_1 = \omega_2 =, \ldots, = \omega_N = \omega_{\text{osc}}. \tag{7.66}$$

slightly larger in magnitude than the naive expectations z_{single} and ω_{single}. For the examples plotted in Figs. 7.6 and 7.7, $N\zeta = 10$ resulted in the approximately tenfold slower oscillations and 100 times slower damping of the center-of-mass, than of the other modes.

For asymmetric pumping ($|E_1| > |E_0|$), the analysis of the dynamics is considerably more involved. The main problem is that the matrix $\mathbf{D}$ itself is not symmetric any more. Thereby, the force F_j is *not conservative*, not even in the infinitesimal neighbourhood of the equilibrium configuration: If it were, $F_j = -\partial/\partial x_j\, V(x_1...x_N)$ would imply that $\mathbf{D}$ is a Hessian matrix, symmetric by Young's theorem. We remark that asymmetric force matrices have been found in studies of the stability of the 2-dimensional equilibrium configurations of optically trapped microspheres in a single plane transverse to the standing wave [116].

Although for asymmetric pumping $\mathbf{D}$ is not symmetric, we can still look for the eigenmodes of lattice vibrations, given by the eigenvectors of $\mathbf{D}$. This task is involved, since the eigenvalues and eigenvectors of a nonsymmetric real matrix can be complex, not orthogonal to each other, and are in general complicated to find. Note, however, an important symmetry of the system close to equilibrium, revealed by (7.62): $\mathbf{D}$ is a Toeplitz matrix (i.e., $D_{j+1,l+1} = D_{j,l}$ for every $j, l = 1, \ldots, N-1$), and thus the coupling between two clouds only depends on their distance $l-j$. If $\mathbf{D}$ was a circulant matrix, i.e., it had the additional property that $D_{j,N} = D_{j+1,1}$ for

---

[4] In fact, the derivation of (7.62) is not valid for symmetric pumping, and therefore one must use a different approach. However, as we show in Appendix 7.10, a mathematically sound procedure also leads to (7.63).

every $j = 1, \ldots, N-1$, its eigenvectors would be the Fourier vectors $[v_b]_j = e^{ibj2\pi/N}$, for $b = 0, \ldots, N-1$. Although $\mathbf{D}$ does not have this property, a similar statement does hold for it: $D_{j,N} = \mathcal{P} D_{j+1,1}$ for every $j = 1, \ldots, N-1$. Thus we can look for its eigenvectors in the following form:

$$[v_b]_j = (\mathcal{P} e^{2\pi i b})^{j/N}, \tag{7.67}$$

corresponding to density waves with complex wavenumbers, the imaginary part the wavenumbers given by $\alpha = \log(\mathcal{P})/(Nd)$. Direct application of (7.62) shows that these $\mathbf{v}_b$ are indeed eigenvectors, and after some algebra the corresponding eigenvalues z_b of $\mathbf{D}$, with $b = 0, \ldots, N-1$, are found to be

$$z_b = \beta \cos\Theta \left[1 + \frac{\zeta^2 \sqrt[N]{\mathcal{P}} \mathcal{A}^2}{(\sqrt[N]{\mathcal{P}} e^{i\pi b/N} - e^{-i\pi b/N})^2} \right]^{-1}. \tag{7.68}$$

This can be contrasted with the naively expected $z_{\text{single}} = \beta \cos\Theta [1 + \zeta^2]^{-1}$, based on Eq.(7.38).

As expected, the eigenmodes (7.67) of the lattice vibrations are complex, except for $b = 0$, which corresponds to a distorted center-of-mass mode and, if N is even, $b = N/2$, the density wave of highest wavenumber possible (π/d). Both of these modes are stable, as $z_{N/2} < z_0 < 0$, and damped if $\mu > 0$. Since $\mathbf{D}$ is real, all other modes form conjugate pairs: $z_b = z^*_{N-b}$ and $\mathbf{v}_b = \mathbf{v}^*_{N-b}$.

We now discuss the physical meaning of complex eigenmodes and eigenfrequencies. Consider a pair of complex eigenvalues $z_b = z^*_{N-b}$ with $0 < b < N/2$, and the corresponding eigenvectors $\mathbf{v}_b = \mathbf{v}^*_b$. Both $\operatorname{Re} \mathbf{v}_b$ and $\operatorname{Im} \mathbf{v}_b$ describe density waves of wavenumber $k_b = 2\pi b/(Nd)$, modulated so their amplitude increases exponentially with rate $\alpha = (\log \mathcal{P})/(Nd)$ towards the source of the more intensive beam. Now since $\mathbf{D}\mathrm{Re}(\mathbf{v}_b) = \operatorname{Re}(\mathbf{D}\mathbf{v}_b) = \operatorname{Re}(z_b \mathbf{v}_b) = \mathrm{Re} z_b \mathrm{Re} \mathbf{v}_b - \mathrm{Im} z_b \mathrm{Im} \mathbf{v}_b$, and $\mathbf{D}\mathrm{Im}(\mathbf{v}_b) = \operatorname{Im}(\mathbf{D}\mathbf{v}_b) = \operatorname{Im}(z_b \mathbf{v}_b) = \mathrm{Im} z_b \mathrm{Re} \mathbf{v}_b + \mathrm{Re} z_b \mathrm{Im} \mathbf{v}_b$, time evolution by Eq. (7.46) does not lead out of the subspace of $\mathbb{R}^N$ spanned by the modes $\mathrm{Re}\mathbf{v}_b$ and $\mathrm{Im}\mathbf{v}_b$. For any superposition

$$\boldsymbol{\xi}(t) = p(t)\mathrm{Re}(\mathbf{v}_b) + q(t)\mathrm{Im}(\mathbf{v}_b) = \mathrm{Re}\Big\{ \big[p(t) - iq(t)\big] \, \mathbf{v}_b \Big\}, \tag{7.69}$$

with $p(t), q(t) \in \mathbb{R}$, Eq.(7.46) can be rewritten as

$$m\ddot{p} = -\mu \dot{p} + (\mathrm{Re} z_b)\, p + (\mathrm{Im} z_b)\, q \tag{7.70}$$

$$m\ddot{q} = -\mu \dot{q} - (\mathrm{Im} z_b)\, p + (\mathrm{Re} z_b)\, q. \tag{7.71}$$

A linear combination of these two differential equations gives $m(p-iq)^{\cdot\cdot} = -\mu(p-iq)^{\cdot} + z_b(p-iq)$, a single complex homogeneous second-order linear differential equation, whose general solution can be written down straight away:

$$p(t) - iq(t) = c_+ e^{(\kappa_b^+ - i\omega_b^+)t} + c_- e^{(\kappa_b^- - i\omega_b^-)t}. \tag{7.72}$$

Here $c_\pm = p_\pm - iq_\pm$ are arbitrary constants, and

$$(\kappa_b^\pm - i\omega_b^\pm) = \frac{-\mu \pm \sqrt{\mu^2 + 4mz_b}}{2m}, \tag{7.73}$$

with $\kappa_b^- < \kappa_b^+$ to fix notation, which also means $\omega_b^- < 0$ and $\omega_b^+ > 0$. Substituting the solution (7.72) together with Eq. (7.67) into Eq. (7.69), we have $\xi_j(t) = \xi(x = jd, t)$ for every $j = 1, \ldots, N$, with

$$\xi(x,t) = \mathrm{Re}\, \left(c_+ e^{\kappa_b^+ t} e^{\alpha x} e^{i(k_b x - \omega_b^+ t)} \right) + \mathrm{Re}\, \left(c_- e^{\kappa_b^- t} e^{\alpha x} e^{i(k_b x - \omega_b^- t)} \right). \tag{7.74}$$

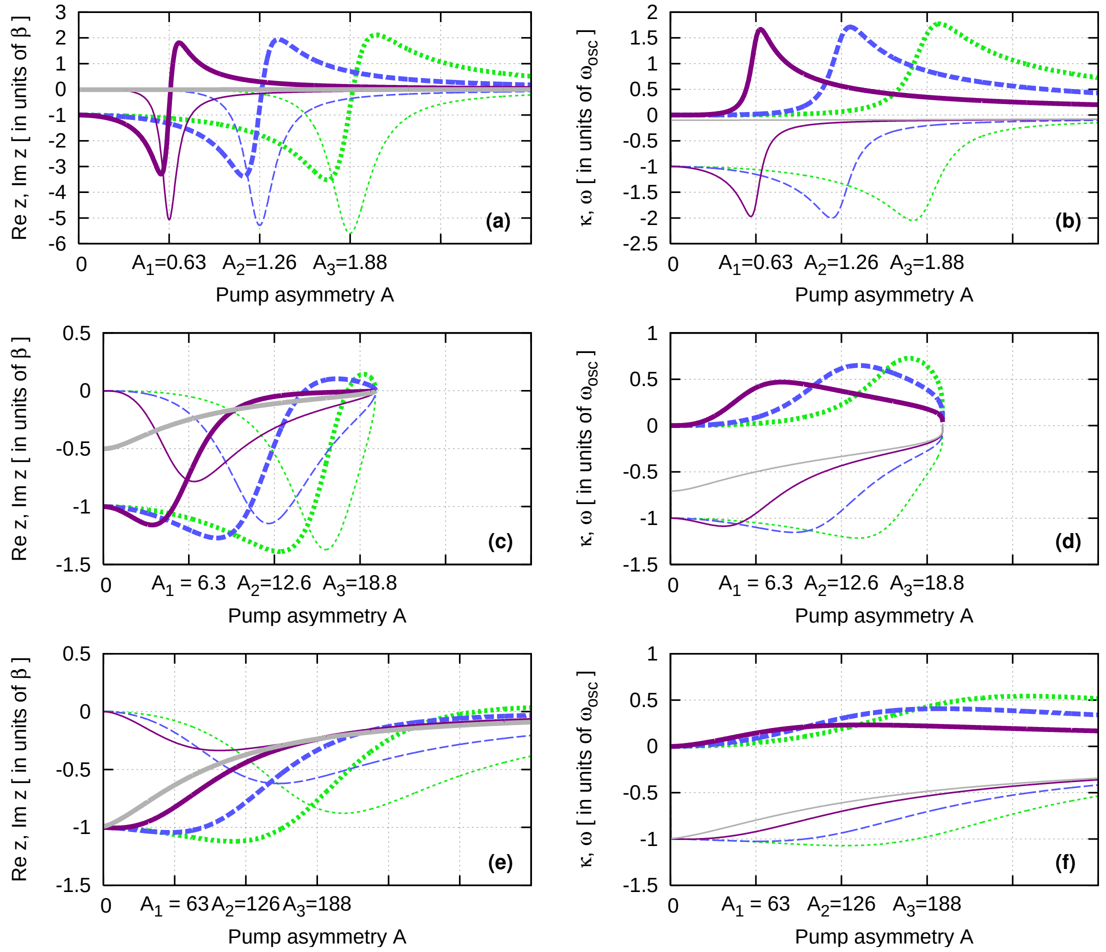

Figure 7.13: Damping rate κ_b^+ (thick) and frequency ω_b^+ (thin) of the first few eigenmodes $b = 0$ (continuous light grey), $b = 1$ (continuous purple), $b = 2$ (slashed blue), $b = 3$ (dotted green) of optical lattices in the overdamped (left column) and undamped (right column) limit. In the overdamped case, these are directly given by the real and imaginary parts of the eigenvalues of the force matrix $\mathbf{D}$: $\kappa_b^+ \tau_\mathrm{d} = \mathrm{Re} z_b/\beta$, and $\omega_b^+ \tau_\mathrm{d} = \mathrm{Im} z_b/\beta$, whereas in the undamped case, by the square root of z_b: $\kappa_b^+/\omega_\mathrm{osc} = \mathrm{Re}\sqrt{z_b/\beta}$, and $\omega_b^+/\omega_\mathrm{osc} = \mathrm{Im}\sqrt{z_b/\beta}$. In (a) and (b), a lattice of $N = 100$ clouds of polarizability $\zeta = 0.1$ is taken, the same choice of parameters as used for the illustrations of the dynamics in Figs.7.6 – 7.10. As $N\zeta = 10$, this is in the strong collective coupling regime, clearly separated resonances are seen at the predicted positions. In (c) and (d), $N = 10$ and $\zeta = 0.1$, and thus the collective coupling is weaker, the resonances overlap strongly. As $\mathcal{A}$ approaches $2/\zeta = 20$, the trap depth decreases sharply, and for $\mathcal{A} > 20$ the curves do not continue as the dipole force is no longer able to hold the clouds against the scattering force. In (e) and (f), $N = 1000$, and $\zeta = 10^{-4}$ means that the collective coupling is weak, $N\zeta \ll 1$. Although the resonances can still be distinguished, they overlap almost completely, and the instability rate κ, the maximum of the κ_b, is a smoothly increasing function of the asymmetry.

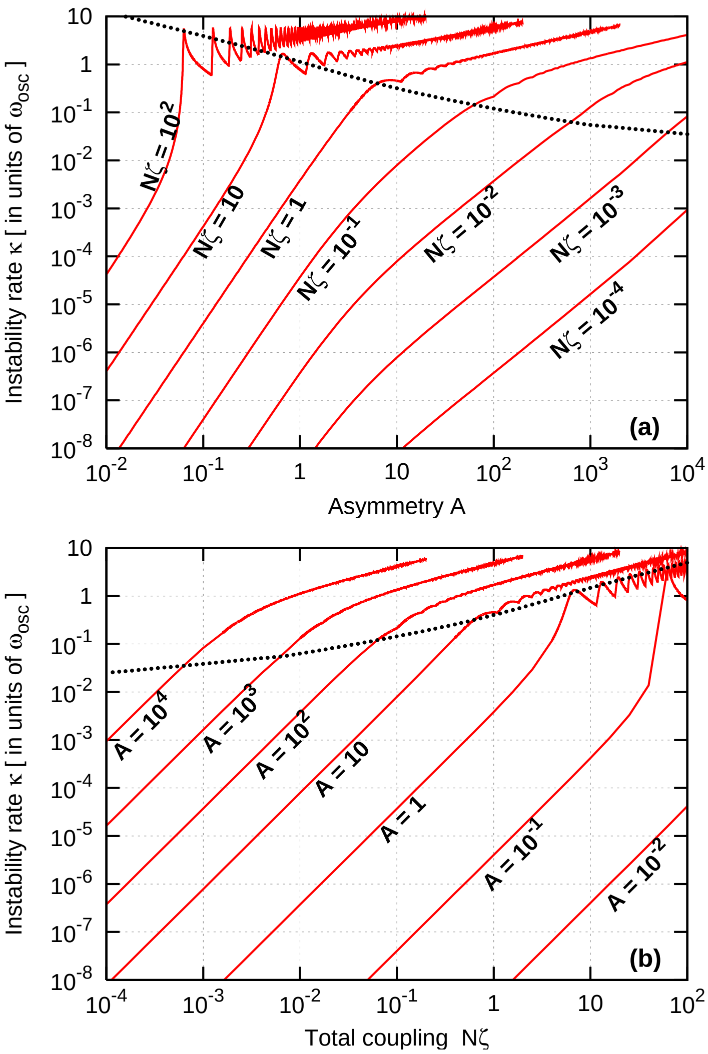

Figure 7.14: Exponential rate κ of instability (the largest of the κ_b) for an undamped optical lattice, for various settings of the collective coupling as function of the asymmetry (a), and for various settings of the asymmetry $\mathcal{A}$ as functions of the collective coupling $N\zeta$ (b). For these plots we set $N = 1000$, but for $N \gg 1$, a change in N does not affect the curves except for the termination point of the lines (which is at $\zeta\mathcal{A} = 2$). Note that ω_{osc} itself depends on both the asymmetry $\mathcal{A}$ and the coupling constant ζ (but *not* on the total number of occupied sites N) in a nontrivial way. On both plots, the dotted line shows the growth rate if the asymmetry is set near the first resonance, i.e., $\mathcal{A} = 2\pi/(N\zeta)$. The ripples on the plots at large instability rates $\kappa > 1$ are caused by the resonances illustrated in Fig. 7.13. For low instability rates $\kappa < 0.1$, and weak total coupling $N\zeta < 1$, we find that for κ varies smoothly with $N\zeta$ and $\mathcal{A}$. Under these conditions at low asymmetries $\mathcal{A} < 1$, $\kappa \approx \omega_{\text{osc}}(N\zeta)^2\mathcal{A}^3/(2\pi)^3$ (analytical estimate), whereas for large asymmetries $\mathcal{A} > 10$, the data can be well fitted with $\kappa \approx 0.015\,\omega_{\text{osc}}(N\zeta)^2\mathcal{A}^{1.7}$.

Thus a general solution of the dynamics (infinitesimally close to equilibrium) in this subspace corresponds to two superimposed density waves of wavelength Nd/b, one copropagating with the stronger beam ($\omega_b^- < 0$), and one counterpropagating ($\omega_b^+ > 0$). Their phase velocities are given by $Nd\left|\omega_b^\pm\right|/(2\pi b)$. As $\kappa_b^- < 0$ for any values of the variables, the copropagating wave is exponentially damped with characteristic timescale $1/\left|\kappa_b^-\right|$, but the counterpropagating wave can be either damped or amplified. Thus, this pair of modes is stable if $\kappa_b^+ < 0$, which corresponds to

$$m(\mathrm{Im}\, z_b)^2 < -\mu^2 \mathrm{Re}\, z_b. \tag{7.75}$$

An analogous criterion of stability has been derived for the distorsions of the equilibrium patterns of optically trapped microspheres in a single plane transverse to the trap axis, in [116].

For symmetric pumping $\mathcal{A} = 0$, the matrix $\mathbf{D}$ is symmetric, the eigenmodes (7.67) are the Fourier components, and the eigenvalues (7.68) are all real and negative, thus the lattice is stable. As discussed a few paragraphs earlier, almost all modes have the same frequency as a single trapped cloud, $z_1 = z_2 =, \ldots, = z_N = -\beta$, except the center-of-mass mode, with $z_0 = -\beta/(1 + N^2\zeta^2)$. With the introduction of a pump asymmetry $\mathcal{A} > 0$, the eigenmodes and eigenvalues (apart from $b = 0$, and $b = N/2$, if N is even) acquire imaginary parts, and as $\mathcal{A}$ is further increased, the real parts of the eigenvalues turn positive one by one. The first few eigenvalues are shown as functions of $\mathcal{A}$ for two examples in Fig. 7.13. In the "strong collective coupling", $N\zeta \gg 1$ limit (Fig. 7.13 a), we observe clearly separated resonances. In this limit, whenever $\pi - \Theta \lesssim \pi/N$, we have $\sqrt[N]{\mathcal{P}} \approx 1$, and the denominator of Eq. (7.68) is approximately $1 - \sin^2\Theta/\sin^2(\pi b/N)$, which, with Eq.(7.50), places the resonance for mode b at $\mathcal{A} \approx \mathcal{A}_b$, where

$$\mathcal{A}_b = b\frac{2\pi}{N\zeta}. \tag{7.76}$$

The simple relation $\mathcal{A} = 2\pi/(N\zeta)$ indeed fits the boundaries between the shaded green areas of Fig. 7.5 and Fig. 7.12 almost perfectly for $\mathcal{A} < 1$. Outside of the strong collective coupling regime (Fig. 7.13 b), the resonances are not well resolved. It may even happen (as in the plotted example) that mode $b = 2$ becomes absolutely unstable ($\mathrm{Re}\, z_2 > 0$) at lower $\mathcal{A}$ than mode $b = 1$. This causes the "shoulder" in the $N = 10$ instability limit on Fig. 7.5, and on all of the slashed lines at around $\mathcal{A} \approx 10$ on Fig. 7.12. In Fig. 7.13 (c) and (d), the critical asymmetry is $\mathcal{A} = 2/\zeta = 20$, there we have $\Theta = \pi/2$ and all eigenvalues are 0; for $\mathcal{A} > 20$ all modes are unstable. The instability rate, i.e., the largest of the κ_b, is plotted for a wider range of parameters in Fig. 7.14.

In the absence of damping, $\mu = 0$, Eq. (7.73) gives $\omega_b^\pm = \pm\mathrm{Im}\sqrt{z_b/m}$ and $\kappa_b^\pm = \pm\mathrm{Re}\sqrt{z_b/m}$. With asymmetric pumping the eigenvalues z_b of all modes with $b \neq 0, N/2$ are complex, and thus an instability always ensues, but might be very slow on the experimental timescale (discussed in Section 7.7). As shown by Eq.(7.75), damping can restore the stability of the modes as long as the real parts of the eigenvalues are negative. The bth mode is overdamped if $\mu^2 \gg |z_b|\, m$, its dynamics is then effectively first-order (cf. Subsection 7.4.1), and the copropagating mode disappears (is damped out on a very short timescale). For the counterpropagating mode we then have $\omega_b^+ = -\mathrm{Im}\, z_b/\mu$, and $\kappa_b^+ = \mathrm{Re}\, z_b/\mu$. Even with arbitrarily strong damping, the OL becomes unstable if $\mathrm{Re}\, z_b > 0$, as then $\kappa_b^+ > 0$ (and the right hand side of Eq. (7.75) is negative). This "absolute instability" is used to define the shaded areas in Figs. 7.5 and 7.12. The overdamped dynamics close to this absolute instability limit is illustrated in Figs. 7.9 and 7.10, which show the results of numerical integration of Eq. (7.41) near this limit.

7.6 Stability with respect to noise

For the simulation reported in Section 7.4 as well as for the analytical calculations we considered a perfectly regular lattice made of purely dispersive and infinitely thin clouds with deterministic dynamics. However, the phenomena we found are fairly robust: these approximations can be somewhat relaxed without altering the qualitative picture. We do not go into the details very much here but illustrate this statement with examples from "noisy" simulations in Fig. 7.15. We simulate clouds of finite thickness by placing many (on average 10) infinitely thin sheets at a single site, the only interaction between them being that mediated by the trap light. To simulate the density inhomogeneity of an optical lattice, the sheets are distributed randomly (Poissonian distribution), in a way as to model a parabolic external confinement: $p(x) \propto \exp\left([x - 20\lambda]^2/[2 \times (15\lambda)^2]\right)$. 1000 sheets of $\zeta = 0.01 + 2i \times 10^{-5}$ are distributed this way over 100 lattice sites, and so an optical lattice of roughly 30 sites with $\zeta \approx 0.3 + 6 \times 10^{-4}i$ is formed, the polarizability decreasing smoothly towards the edges. Furthermore, Dirac-δ correlated noise terms are added to the equations of motion, which, using the reduced units (length in λ, time in τ_{osc} (7.39), electric field in E_0), read:

$$\dot{x}_j(t + \Delta t) = \dot{x}_j(t) + f_{CU}\frac{\eta_1}{\eta_j}\left(|A_j|^2 + |B_j|^2 - |C_j|^2 - |D_j|^2\right) - \mu_{CU}\dot{x}_j(t)\mathcal{D}\sqrt{\Delta t}\,\Xi, \quad (7.77)$$

with dimensionless constants $f_{CU} = \pi/\left[4\,|\mathrm{Re}\,\zeta_1|\,\sqrt{\mathcal{P}}\right]$, $\mu_{CU} = \mu_A\,[\pi\eta_1\lambda c]^{1/2}/\left[4m_A\,|\mathrm{Re}\zeta_1|\,\sqrt{\mathcal{P}}I_0\right]^{1/2}$, and a choice of $D_0 = 0.01$, where Ξ is a random noise variable of average zero and variance of 1. Similarly, in the overdamped limit, where the time unit is τ_{d} of Eq. (7.42), we add the noise terms to obtain

$$x_j(t + \Delta t) = x_j(t) + f'_{CU}\frac{\eta_1}{\eta_j}\left(|A_j|^2 + |B_j|^2 - |C_j|^2 - |D_j|^2\right) + \mathcal{D}\sqrt{\Delta t}\,\Xi, \quad (7.78)$$

where now $f'_{CU} = \left[16\pi\,|\mathrm{Re}\,\zeta_1|\,\sqrt{\mathcal{P}}\right]^{-1}$, and $D_0 = 0.01$ as above.

As seen in the Fig. 7.15, in the regime of large collective coupling $\sum_j \zeta_j = 10$ the same qualitative features as observed on Figs. 7.8-7.10 appear. In the undamped case (a), the center of mass oscillations are 10 times slower, and the other oscillations synchronize so that a density wave propagating towards the source of the stronger laser beam arises, which crosses the whole system in τ_{osc}. In the overdamped case, we also find the same qualitative feature of synchronization of the oscillations, and a sharp instability limit, although this occurs at slightly higher pump asymmetry, and the propagation of the wave is slower, than in the noiseless case (oscillation timescale is roughly $2\tau_{\mathrm{d}}$). Due to the inhomogeneous density distribution the shape of the propagating density wave is altered, but is still quite smooth as the long-range interaction averages out the local noise.

7.7 Experimental issues

7.7.1 Cold atoms

For optical lattices consisting of ultracold atoms trapped in vacuum it is cumbersome to produce viscous friction forces. In the absence of friction our model predicts that any asymmetry in the intensities of the trap beams should give rise to a dynamic instability of the lattice. However, observation of this instability can be hampered by noise. Even if all experimental precautions are made, one source of noise cannot be canceled: absorption and spontaneous emission of photons from the trapping lasers by the atoms. In the following, we discuss what experimental parameters are necessary for the dynamic instability to be substantially faster than the heating due to absorption.

Most optical lattice experiments use alkali atoms, since they have simple electronic level structure, with the trap lasers tuned near the D line. We use the notation of [10], the fields are assumed to be polarized along z, the quantization axis for the atoms. The dipole transition matrix element

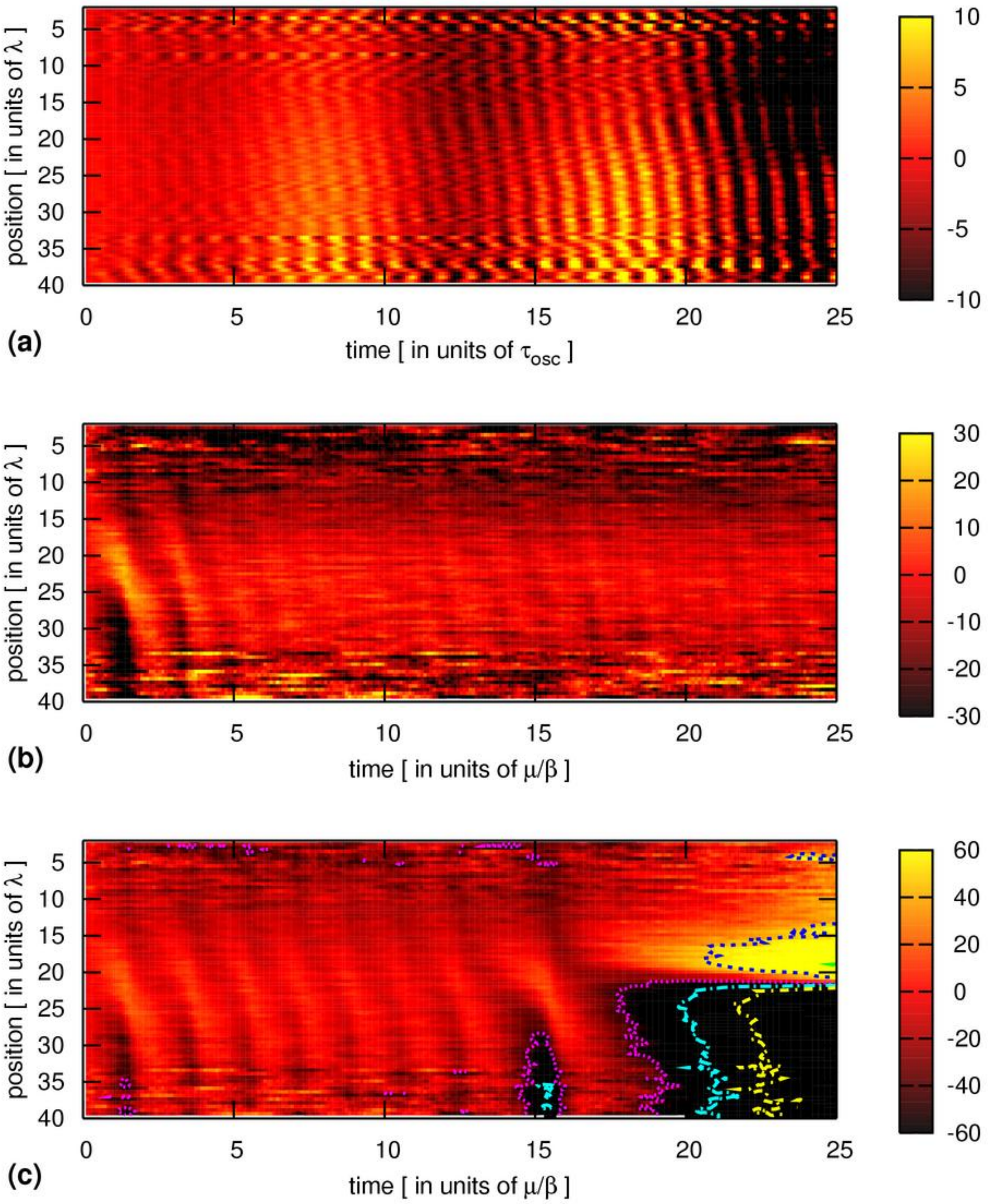

Figure 7.15: Numerical simulation of the dynamics of an optical lattice with noise. 1000 sheets of $\zeta = 0.01$ are distributed over 100 lattice sites according to a Gaussian centered on $x = 20\lambda$ of width 15λ. Thus $\zeta \approx 0.3$ in the center of the structure, and decreases to $\zeta \approx 0$ near the edges, with Poissonian distribution of ζ. At each site, $\mathrm{Im}\zeta = 2 \times 10^{-3}\mathrm{Re}\zeta$. Color coding stands for the average displacement ξ of the sheets at each site is after initial excitation (random independent displacement of each sheet from equilibrium with maximum magnitude $\xi_{\mathrm{initial}} = 5 \cdot 10^{-4}\lambda$ and random velocity of maximum magnitude $\omega_{\mathrm{osc}}\xi_{\mathrm{initial}}$). In (a), no friction forces are assumed ($\mu = 0$), and $I_1 = 1.39 I_0$. In (b) and (c) the overdamped limit is taken, with $I_1 = 1.902 I_0$ and $I_1 = 1.904 I_0$ respectively.

	$^{87}\mathrm{Rb}$	$^{23}\mathrm{Na}$
m_A	$1.44 \cdot 10^{-25}\mathrm{kg}$	$3.82 \cdot 10^{-26}\mathrm{kg}$
λ	$\lambda = 0.78\mu\mathrm{m}$	$\lambda = 0.59\mu\mathrm{m}$
$m_A c^2$	$1.30 \times 10^{-8}\mathrm{J}$	$3.43 \times 10^{-9}\mathrm{J}$
$\hbar\omega$	$2.5 \times 10^{-19}\mathrm{J}$	$3.37 \times 10^{-19}\mathrm{J}$
$\hbar\Gamma$	$4.02 \times 10^{-27}\mathrm{J}$	$6.49 \times 10^{-27}\mathrm{J}$
E_{rec}	$5.00 \times 10^{-30}\mathrm{J}$	$3.32 \times 10^{-29}\mathrm{J}$
$\hbar\omega/(m_A c^2)$	1.963×10^{-11}	9.83×10^{-11}

Table 7.1: Some physical constants for the D lines of $^{87}\mathrm{Rb}$ and $^{23}\mathrm{Na}$

d_{eg} is related to the linewidth Γ and frequency ω_0 by

$$\Gamma = \frac{\omega_0^3}{3\pi\epsilon_0\hbar c^3} d_{eg}^2. \tag{7.79}$$

The Rabi frequency Ω gives the characteristic energy of the dipole coupling:

$$\hbar\Omega(\mathbf{r}) = -d_{eg}\left|E(\mathbf{r})\right|. \tag{7.80}$$

Note that the value of the Rabi frequency depends on the position $\mathbf{r}$ of the atom. For red detuning, atoms will be near antinodes, and we can take $|E(\mathbf{r})| \approx |E_1| + |E_0|$. For blue detuning, cold atoms will initially be near the nodes, $|E(\mathbf{r}) \approx ||E_1| - |E_0|||$, however, if they are heated, the latter expression underestimates the electric field, for atoms with high kinetic energies $|E(\mathbf{r})| \approx |E_1| + |E_0|$ is more appropriate. Linear polarizability is only a good approximation if the atomic transition is not saturated. This can be ensured by choosing $|Delta| \gg |\Omega|$: the upper-state population σ_{ee} then reads

$$\sigma_{ee} = \frac{\Omega^2/4}{\Delta^2 + (\Gamma/2)^2} \approx \frac{\Gamma/2}{|\Delta|} \frac{3\lambda^2(I_0 + I_1)}{4\pi\hbar\,|\Delta|\,\omega} Q, \tag{7.81}$$

where the Q is a dimensionless correction factor accounting for the effects of localization in the asymmetric trap:

$$\text{red detuning:} \quad Q = 1 + \frac{2\sqrt{\mathcal{P}}}{\mathcal{P}+1}; \tag{7.82a}$$

$$\text{blue detuning, well trapped atoms:} \quad Q = 1 - \frac{2\sqrt{\mathcal{P}}}{\mathcal{P}+1}; \tag{7.82b}$$

$$\text{not well trapped atoms:} \quad Q = 1. \tag{7.82c}$$

We require $\sigma_{ee} < 10^{-2}$, say. In the large detuning ($|\Delta| \gg \Gamma$) and low saturation ($|\Omega| \ll |\Delta|$) limit the complex polarizability α of a single atom can be expressed as

$$\alpha = -\frac{d_{eg}^2}{\hbar}\frac{1}{\Delta}\left(1 + i\frac{\Gamma/2}{(-\Delta)}\right) = \frac{\Gamma/2}{(-\Delta)}\frac{3}{4\pi^2}\epsilon_0\lambda^3\left(1 + i\frac{\Gamma/2}{(-\Delta)}\right). \tag{7.83}$$

Thus the polarizability (divided by the transverse area) of an atom cloud reads simply

$$\zeta = \frac{k\eta\alpha}{2\epsilon_0} = \frac{\Gamma/2}{(-\Delta)}\frac{3N_\lambda}{4\pi}\left(1 + i\frac{\Gamma/2}{(-\Delta)}\right). \tag{7.84}$$

By virtue of Eq. (7.84), the back-action of the atom clouds on the field, i.e., ζ, can be enhanced by working at only moderately large detuning (as opposed to the $\Delta \approx -10^7\Gamma$ of many optical lattice experiments).

The trap depth U_{dip} of the dipole trap, for single atoms moving independently, can be estimated by neglecting any feedback effects on the field. The trap then has a $U(x) \propto \cos^2 kx$ form, with the trap depth given by:

$$U_{\text{dip}} = \frac{1}{4}|\alpha|\left((|E_0|+|E_1|)^2 - (|E_0|-|E_1|)^2\right) = |\alpha E_0 E_1| = 2\hbar|\Delta|\,\sigma_{ee}\frac{2\sqrt{\mathcal{P}}}{Q(\mathcal{P}+1)}. \tag{7.85}$$

The trapped atoms absorb part of the trapping laser beams, and most of this absorbed power is reemitted as radiation with frequency close to ω, corresponding to spontaneous emission, but some of it heats the motion of the atom. On average, each absorbed and spontaneously emitted photon increases the kinetic energy of the atom by an amount known as the *recoil energy*,

$$E_{\text{rec}} = k_B T_{\text{rec}} = \frac{\hbar^2 k^2}{m_A}. \tag{7.86}$$

Since the rate of spontaneous emission of photons is $dN/dt = \Gamma\sigma_{ee}$, the *heating rate*, or the rate of increase of kinetic energy of the atoms, can be expressed as

$$P_{\text{heat}} = \Gamma\sigma_{ee}E_{\text{rec}} = \Gamma\sigma_{ee}\frac{\hbar^2 k^2}{m_A}. \tag{7.87}$$

Heating due to absorption leads first to a breakdown of the Dirac-δ approximation used in our model (7.5), and, more crucially, on a longer timescale of t_{heat}, the atoms eventually "evaporate" from the optical lattice. We can estimate the timescale for heating of the atoms out from the trap by:

$$t_{\text{heat}} = \frac{U_{\text{dip}}}{P_{\text{heat}}} = \frac{1}{\omega}\frac{|\Delta|}{\Gamma/2}\frac{m_A c^2}{\hbar\omega}\frac{2\sqrt{\mathcal{P}}}{Q(\mathcal{P}+1)} \tag{7.88}$$

For ^{87}Rb and ^{23}Na, this is roughly $t_{\text{heat}} \approx 10^{-5}\ |\Delta|/(\Gamma/2)$s, and $t_{\text{heat}} \approx 1.6\cdot 10^{-6}\ |\Delta|/(\Gamma/2)$s, respectively.

The back-action induced dynamic instabilities can only be observed in an experiment if they are much faster than the evaporation:

$$\kappa\, t_{\text{heat}} \gg 1. \tag{7.89}$$

As seen from Eqs.(7.73), (7.37), (7.68), both $\kappa_b^{\pm}$ and $\omega_b^{\pm}$ are proportional to the oscillation frequency ω_{osc} of a single atom cloud (which is the same as the oscillation frequency of a single atom) in the trap is, which is

$$\omega_{\text{osc}} = \sqrt{\frac{8k|\zeta|}{c\eta m_A}}\sqrt[4]{I_0 I_1} = \sqrt{\frac{2U_{\text{dip}}k^2}{m_A}} = \sqrt{\frac{2\hbar\Gamma}{m_A c^2}}\sqrt{\frac{|\Delta|}{\Gamma/2}}\sqrt{\sigma_{ee}}\omega\sqrt{\frac{2\sqrt{\mathcal{P}}}{Q(\mathcal{P}+1)}}. \tag{7.90}$$

As shown in Fig. 7.14, the constant of proportionality depends sensitively on the choice of asymmetry. Using the estimates of the caption of Fig. 7.14, we find that the instability is faster than dipole heating at low asymmetries $\mathcal{A} < 1$ if

$$1 \ll \kappa t_{\text{heat}} = 0.008\sqrt{\sigma_{ee}}\sqrt{\frac{\Gamma/2}{|\Delta|}}N^2\left(\frac{3N_\lambda}{4\pi}\right)^2\sqrt{\frac{\Gamma/2}{\omega}}\sqrt{\frac{m_A c^2}{\hbar\omega}}Q^{-3/2}\mathcal{A}^3, \tag{7.91}$$

	$^{87}\mathrm{Rb}$		$^{23}\mathrm{Na}$	
$\Delta/(\Gamma/2)$	-10^4	-10^5	-10^4	-10^5
$I_0 + I_1$	$0.21\,\mathrm{kW/cm^2}$	$21\,\mathrm{kW/cm^2}$	$0.79\,\mathrm{kW/cm^2}$	$79\,\mathrm{kW/cm^2}$
ζ	2.39×10^{-4}	2.39×10^{-5}	2.39×10^{-4}	2.39×10^{-5}
t_{heat}	$77\,\mathrm{ms}$	$770\,\mathrm{ms}$	$11\,\mathrm{ms}$	$116\,\mathrm{ms}$
τ_{osc}	$1.73\,\mu\mathrm{s}$	$0.547\,\mu\mathrm{s}$	$0.53\,\mu\mathrm{s}$	$0.17\,\mu\mathrm{s}$
$t_{\mathrm{inst}} = \kappa^{-1}$	$0.33\,\mathrm{ms}$	$10\,\mathrm{ms}$	$0.10\,\mathrm{ms}$	$3.2\,\mathrm{ms}$

Table 7.2: Some experimental requirements and the relevant timescales for the instability, for an optical lattice of $N = 500$ disk-shaped clouds of areal density $\eta = 10/\lambda^2$ each (corresponding to a 3D lattice with filling factor of 2.5). The pump asymmetry is set at $\mathcal{P} = 10$, and laser power is chosen so that the population of the upper level is $\sigma = 10^{-3}$.

whereas for large asymmetries $\mathcal{A} > 10$ we have

$$1 \ll \kappa t_{\mathrm{heat}} = 0.085\sqrt{\sigma_{ee}}\sqrt{\frac{\Gamma/2}{|\Delta|}}N^2\left(\frac{3N_\lambda}{4\pi}\right)^2\sqrt{\frac{\Gamma/2}{\omega}}\sqrt{\frac{m_A c^2}{\hbar\omega}}\mathcal{A}^{-1.3}. \tag{7.92}$$

Roughly for $^{87}\mathrm{Rb}$, $\omega_{\mathrm{osc}}t_{\mathrm{heat}} \approx 0.14\,[|\Delta|/(\Gamma/2)]^{3/2}$, whereas for $^{23}\mathrm{Na}$, $\omega_{\mathrm{osc}}t_{\mathrm{heat}} \approx 0.070\,[|\Delta|/(\Gamma/2)]^{3/2}$. Some concrete examples are given in Table 7.2.

7.7.2 Plastic beads

Although the largest optical lattices to date consist of trapped atoms, optical forces can be used to trap much bigger objects as well. Since the earliest days of optical trapping [120] a large amount of work has gone into trapping plastic microspheres (or "beads") of diameter comparable to, or even larger than, the wavelength of the trap laser. It has been realized as early as 1989 [30], that the interference between the incident and the scattered fields gives rise to an effective interaction between microscopic beads, which later has been shown to modify the structure of 1-dimensional arrays of trapped beads significantly [93, 115, 119]. Recently, research has focused on the *transverse* motion of particles which are in the same plane, trapped at an antinode of the standing-wave interference pattern of two opposing laser beams; note that this is the degree of freedom averaged out in our model. It has been found in [116] that the beads can "crystallize" into intricate periodic or quasiperiodic structures, and with the addition of new beads some modes of motion of these structures can become unstable.

In most experiments with trapped microspheres, the size of the beads is of the same order of magnitude as the wavelength of the lasers. It is usually assumed that much smaller beads, which are Rayleigh scatterers, do not have interesting dynamics [116]. However, the type of instability explored in this Article could be studied with optically trapped beads of very small size instead of cold atoms. The radius of the beads should be small enough so that they can be taken as pointlike scatterers. Such experiments could be hard to perform as stronger Brownian motion makes trapping of very small beads more difficult. However, due to the overdamped dynamics of these beads, the experimental signatures of optomechanical coupling would be more straightforward to detect.

7.8 Conclusions

We have considered the dynamics of a 1-dimensional optical lattice due to the nonlinearities caused by multiple reflections of photons within the lattice. We adopted the simple model where the trap beams are approximated as plane waves, and all transverse dynamics is neglected [36]. Here the atom clouds affect the fields as beam splitters with dimensionless coupling constant $\zeta = -i\mathfrak{r}/\mathfrak{t}$. We supplemented this model by a derivation of the force on the trapped atom clouds, based on the Maxwell Stress Tensor. We have shown the corrections this force brings to the standard "radiation pressure" and "dipole force". These corrections are substantial in the regime of strong coupling (dense atom clouds, $\zeta > 1$), and impose a limit on the asymmetry between the trap beam intensities even for purely dispersive atom-light interaction. We then analyzed the dynamics of large lattices, including the mechanical interaction between the trapped atom clouds that is mediated by the trap light. Since the system is 1-dimensional, the interaction does not decay with the distance of the atom clouds, and thus alters the dynamics more and more substantially as the system size (number N of clouds) is increased. For symmetric pumping, this leads to a softening of the center-of-mass oscillations, and a slight identical shift of all other modes of oscillation. For asymmetric pumping, it gives rise to an instability of the lattice which has the form of a density wave copropagating with the weaker beam. In the limit of strong collective coupling ($N\zeta \gg 1$) the propagation velocity and growth rate of these waves can be resonantly enhanced at certain values of the pump asymmetry $\mathcal{A}$. Although viscous friction can restore the stability of the optical lattice, there is a critical asymmetry (depending nontrivially on both N and ζ), above which the density waves arise and eventually destroy the lattice even in the overdamped limit.

The interaction due to multiple scattering is important for microscopic particles, trapped by light, whose size is comparable to the wavelength. In such systems effects similar to those we describe here (nonconservative forces, oscillating and unstable modes even in the overdamped limit) have already been predicted for the 2-dimensional motion of "photonic clusters" in a plane transverse to the trap beams [116]. There, however, the situation is much more complex due to the higher dimensionality and to the more complicated scattering. In the Mie regime, multiple reflections *within* a single bead lead to nontrivial modifications with respect to the pointlike (Rayleigh) scatterer, and this is thought to be essential: in [116], it is stated that vibration frequencies of photonic clusters of Rayleigh particles are always real.

In the 1-dimensional OL studied in this paper, the asymmetric pumping drives a net energy and momentum flow through the system, relating it to crystals driven far from equilibrium. Indeed, traveling density waves have been predicted to arise in arrays of vortices in a type-II superconductor [121], and have been experimentally observed and analyzed in a chain of water drops dragged by oil [122, 123]. These systems, and the one we study in this Article, share the common trait that the interaction between the components (arising from the Lorentz force in the first case, and from the hydrodynamic interaction in the second) is not symmetric in the sense of Newton's third law. However, for the vortices and the water droplets, this interaction has finite range, and therefore leads to a well-defined dispersion relation in the thermodynamic limit. In our 1-dimensional system, however, as the interaction is infinite range, the thermodynamic limit does not make sense. Thus there is no dispersion relation and we cannot speak of "phonons".

In this paper we have revealed that tuning the pump asymmetry opens the possibilities of using optical lattices as a model system for driven crystals far from equilibrium, a largely uncharted topic of physics. Although some of the intriguing features of the dynamics, in particular, the resonant enhancement of the instability, are specific to the optical lattice, some of them are generic (traveling density waves, complex wave vectors, etc.). This shows a novel way, based on optomechanical coupling, of using optical lattices to explore a subject traditionally belonging to condensed matter physics.

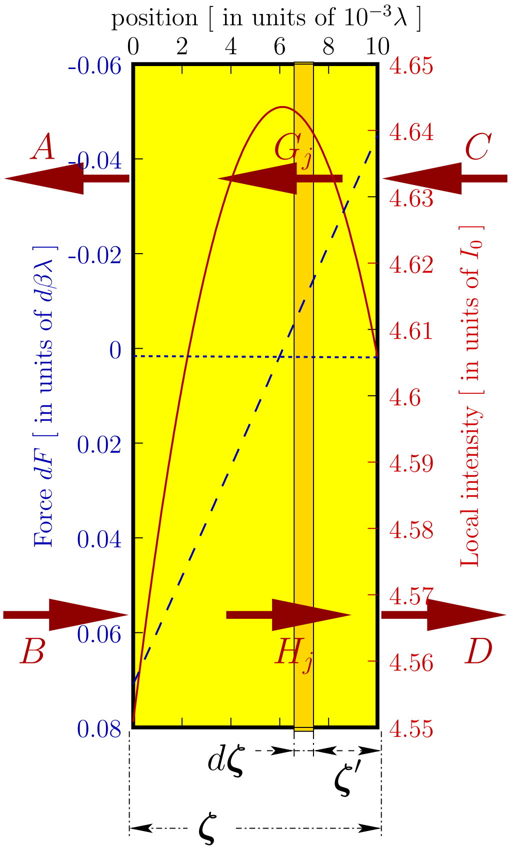

Figure 7.16: A single atom cloud, with $\zeta = 0.5 + 0.025i$, and a slice (dark background). The intensity of the electric field (continuous red line) varies inside the atom cloud, and so does the the "radiation pressure" (dotted blue line) and "dipole force" (slashed blue line), the 1st and 2nd terms of the force (7.93) on a single slice. The forces are plotted in units of $\lambda d\beta = 8\pi\epsilon_0 \mathrm{Re}\, d\zeta\, |BC|$, where $n = 200$ slices were taken with coupling constant $d\zeta_1 = d\zeta_2 =, \dots, = d\zeta_{200} = d\zeta = \zeta/200$. The dipole trap is asymmetric, with $|C| = 1.5\,|B|$.

We acknowledge funding from the Austrian Science Foundation (Contract Nos. P17709 and S1512) and from the National Scientific Fund of Hungary (NF68736 and T049234).

7.9 Appendix: Derivation of the force based on multiple scattering

In Section 7.2 we have derived the optical force on an atom cloud in an asymmetric dipole trap. We have shown that to first order in the polarizability ζ of the cloud, the force can be explained in terms of the standard theory of the mechanical effects of light on atoms: it is the sum of the "radiation pressure" and the "dipole force" on each particle due the incident fields. However, the force depends *nonlinearly* on the polarizability ζ. Inasmuch as this nonlinearity is due to the large polarizability of the individual particles, our formula (7.22) provides an *extension of* the standard formulas for the optical forces. If, however, the polarizability of each particle is small, the force on the atom cloud can be *derived from* the standard optical force. We provide this derivation below.

According to the standard theory of optical forces on atoms [10], in the regime of linear polarizability the force an atom in a superposition of two counterpropagating standing waves,

$E(x) = He^{ikx} + Ge^{-ikx}$, reads

$$\mathcal{F} = \frac{k}{2}\left(|H|^2 - |G|^2\right)\operatorname{Im}\alpha - k\operatorname{Im}GH^*\operatorname{Re}\alpha \tag{7.93}$$

$$= -\frac{k}{2}\mathrm{Re}\left\{\left[2\left(\operatorname{Im}GH^*\right) + i\left(|H|^2 - |G|^2\right)\right]\alpha\right\}. \tag{7.94}$$

Here we have united the first term, the “radiation pressure”, and the second term, the “dipole force”, in a complex quantity. We would like to use this formula to find the total force on a pancake-shaped thin atom cloud, with width $l \ll \lambda$, transverse area $w \gg \lambda^2$, and total polarizability ζ, in a trap with electric field incident from the left, Be^{ikx}, and from the right, $Ce^{-ik(x-l)}$. For $\zeta \ll 1$, the back-action of the atoms on the light field can be neglected in a zeroth approximation, and the formula (7.93) can be applied directly. This is equivalent to calculating the optical force based on the Maxwell Stress Tensor and taking into account the modification of the light field due to the cloud only to first order in ζ. For ζ of the order of 1 (or for very asymmetric pumping and $\mathrm{Im}\zeta < \zeta^2$), this approach constitutes a bad approximation: we need to go on.

To proceed, we divide the atom cloud into a sequence of slices such that the polarizability of each size is infinitesimal,

$$\zeta = \sum_{i=1}^{n} d\zeta_j, \quad \text{with} \quad |d\zeta_j| \ll 1 \quad \text{for every } j = 1, \ldots, n. \tag{7.95}$$

This is illustrated in Fig. 7.16. Since the whole cloud is assumed to be much thinner than λ, we neglect the phases picked up be the light during propagation between the slices. As shown in Sect. 7.1, for such infinitesimally closely spaced beam splitters the polarizability parameter ζ is additive, hence the requirement (7.95). Now each slice only effects the electric field perturbatively ($|\mathfrak{r}_j| = |d\zeta_j| \,/\, |1 - id\zeta_j| \ll 1$), and thus the field at the jth slice is to a good approximation the superposition of just two plane waves: $E(x-x_j) = G_j e^{ik(x-x_j)} + H_j e^{-ik(x-x_j)}$, with x_j denoting the position of the slice. We can find the amplitudes G_j and H_j simply using the additivity of ζ:

$$\begin{pmatrix} H_j \\ G_j \end{pmatrix} = \begin{pmatrix} (1+i\zeta') & i\zeta' \\ -i\zeta' & (1-i\zeta') \end{pmatrix} \begin{pmatrix} C \\ D \end{pmatrix}, \quad \text{with} \quad \zeta' = \sum_{l=j+1}^{n} d\zeta_l. \tag{7.96}$$

Multiplying this force by the areal atom density of the jth slice, $\eta_j = (d\zeta_j/\zeta)(N_\lambda/\lambda^2)$, we obtain the areal density of the force on the jth slice:

$$dF_j = -\epsilon_0 \mathrm{Re}\left\{\left[2\left(\operatorname{Im}G_j H_j^*\right) + i\left(|H_j|^2 - |G_j|^2\right)\right] d\zeta_j\right\}. \tag{7.97}$$

The force on the whole cloud is the sum of the forces on the individual slices, which in the limit of infinitesimal slices becomes a complex integral:

$$F = \sum_j dF_j = \int dF = \epsilon_0 \mathrm{Re}\int_0^{\zeta}\left\{-2\mathrm{Im}\,DC^* - i(|D|^2 - |C|^2) + 2\,|D+C|^2\,\zeta'^*\right\} d\zeta', \tag{7.98}$$

using Eq. (7.96) to express G_j and H_j. Since the integrand is linear in ζ', the integral is easily evaluated to give

$$F = \epsilon_0(|D|^2 - |C|^2)\mathrm{Im}\,\zeta - 2\epsilon_0(\mathrm{Im}\,DC^*)\mathrm{Re}\,\zeta + \epsilon_0\,|D+C|^2\,|\zeta|^2. \tag{7.99}$$

Here, formally, the first term is exactly the “radiation pressure”, the second, the “dipole force”, summed over all the particles due to an electric field $De^{ikx} + C^{-ikx}$, and all the nonlinear “multiple scattering” corrections are in the third term. Bear in mind, however, that some of the nonlinearity is “hidden” in D, which is related to the incident amplitude B nonlinearly in ζ:

$$D = \frac{1}{1 - i\zeta}(i\zeta C + B). \tag{7.100}$$

Substitution of this relation into (7.99) yields

$$F = 2\frac{I_0 - I_1}{c}\frac{\operatorname{Im}\zeta}{|1 - i\zeta|^2} - 4\frac{\sqrt{I_0 I_1}}{c}\frac{\operatorname{Re}\zeta}{|1 - i\zeta|^2}\sin(2kx + \varphi) + 2\frac{I_0 - I_1}{c}\frac{|\zeta|^2}{|1 - i\zeta|^2}, \tag{7.101}$$

with the incident intensities $I_0 = \frac{1}{2}\epsilon_0 c\,|B|^2$ and $I_1 = \frac{1}{2}\epsilon_0 c\,|C|^2$, and the relative phase $\varphi = \arg B - \arg C$. This is identical to the formula (7.22) derived via the Maxwell Stress Tensor in Sect. 7.2.

7.10 Appendix: Symmetrically pumped lattice

We have derived the analytical form of the force matrix $\mathbf{D}$ in Section 7.5, and we could describe the dynamics of a symmetrically pumped lattice simply by taking the limit $\mathcal{A} \to 0$ of the formulas. This seems to make perfect sense, as the final formulas, i.e., the force matrix $\mathbf{D}$ (7.62), eigenmodes of vibration $\mathbf{v}_b$ (7.67), and the corresponding eigenvalues z_b (7.68) have well defined limiting values for $I_1 \to I_0$. However, it is quite disturbing that the *derivation* of these formulas does not work for $I_0 = I_1$. If $\mathcal{P} = 1$, the two vectors $\mathbf{u}$ (7.49) and $\mathbf{w}$ (7.51) are parallel and thus they do not subtend a basis (not even a nonorthogonal one). We therefore fill a gap in this Section by deriving the formulas for symmetric pumping. Reassuringly, the same results are found as by directly taking the limit.

In the symmetric pumping case the 2×2 transfer matrix $\mathbf{M}$ only has one eigenvector $\mathbf{u}$ ($= e^{-i\chi}\mathbf{w}$). This awkward situation arises because for symmetric pumping $\Theta = \pi$, thus $\operatorname{tr}\mathbf{M} = 2$ (see Eq. (7.19)), and then the characteristic equation has a the single eigenvalue 1 with a multiplicity of 2. Although such matrices are not diagonalizable, their functions can still be computed efficiently using the Jordan form. Instead of just referring the reader this general recipe, we here give the detailed calculation.

Since we have a single eigenvector $\mathbf{u}$, it is useful to take a second vector $\mathbf{z}$ orthogonal to it:

$$\mathbf{u} = \frac{1}{\sqrt{2}}\begin{pmatrix} 1 \\ e^{-i\chi} \end{pmatrix}; \qquad \mathbf{z} = \frac{1}{\sqrt{2}}\begin{pmatrix} 1 \\ -e^{-i\chi} \end{pmatrix}. \tag{7.102}$$

Note that with these definitions $\mathbf{u}$ and $\mathbf{z}$ provide an orthonormal basis. Substitution of χ leads to:

$$\text{red detuning, } \zeta > 0: \quad \mathbf{u} = \frac{e^{-i\tan^{-1}\zeta}}{\sqrt{2}\sqrt{1+\zeta^2}}\begin{pmatrix} 1 + i\zeta \\ 1 - i\zeta \end{pmatrix}; \quad \mathbf{z} = \frac{e^{-i\tan^{-1}\zeta}}{\sqrt{2}\sqrt{1+\zeta^2}}\begin{pmatrix} 1 + i\zeta \\ -1 + i\zeta \end{pmatrix}; \tag{7.103a}$$

$$\text{blue detuning, } \zeta < 0: \quad \mathbf{u} = \frac{1}{\sqrt{2}}\begin{pmatrix} 1 \\ -1 \end{pmatrix}; \qquad \mathbf{z} = \frac{1}{\sqrt{2}}\begin{pmatrix} 1 \\ 1 \end{pmatrix}. \tag{7.103b}$$

It can easily be checked by direct calculation that a decomposition analogous to Eq. (7.20) can be given:

$$\mathbf{M} = -1 + 2i\,|\zeta|\,\mathbf{u} \circ \mathbf{z}^\dagger, \tag{7.104}$$

and this can be used directly to show that for any $n \in \mathbb{N}$,

$$\mathbf{M}^n \mathbf{u} = (-1)^n \mathbf{u}; \tag{7.105a}$$

$$\mathbf{M}^n \mathbf{z} = (-1)^n \mathbf{z} + n(-1)^{n-1} 2i \, |\zeta| \, \mathbf{u}. \tag{7.105b}$$

Mirror reflection of $\mathbf{u}$ along x is now simpler then for the asymmetric pumping case. We have

$$\zeta \boldsymbol{\sigma} \mathbf{P}(d) \mathbf{u} = - \, |\zeta| \, \mathbf{u}. \tag{7.106}$$

Perturbation of the optical lattice (infinitesimal displacement of the l^{th} cloud by $\xi \to 0$) given in Eq. (7.53) still only affects the outgoing modes, but now for $a^{(l)}$ and $b^{(l)}$ of Eq. (7.53) we have

$$\begin{pmatrix} a^{(l)} \\ 0 \end{pmatrix} = a_u^{(l)} \mathbf{u} + a_z^{(l)} \mathbf{z}; \qquad a_u^{(l)} = a_z^{(l)} = \frac{a}{\sqrt{2}}; \tag{7.107a}$$

$$\begin{pmatrix} 0 \\ b \end{pmatrix} = b_u^{(l)} \mathbf{u} + b_z^{(l)} \mathbf{z}; \qquad b_u^{(l)} = -b_z^{(l)} = \frac{b e^{i\chi}}{\sqrt{2}}. \tag{7.107b}$$

$$\tag{7.107c}$$

Using these decompositions, to first order in the small parameter $\varepsilon = k\xi$, Eq. (7.53) can be written as

$$\frac{1}{\sqrt{2}} a^{(l)} (\mathbf{u} + \mathbf{z}) = \frac{b^{(l)} e^{i\chi}}{\sqrt{2}} (-1)^N \big[(1 + 2N \, |\zeta| \, i) \, \mathbf{u} - \mathbf{z} \big] \; - \; 2(-1)^N \, |\zeta| \, \mathbf{u}. \tag{7.108}$$

The $\mathbf{u}$ and $\mathbf{z}$ components of this equation together give

$$b^{(l)} = \frac{\sqrt{2} \, |\zeta| \, e^{-i\chi}}{1 + N \, |\zeta| \, i} \tag{7.109}$$

Having obtained b, we can use the transfer matrices to find the mode amplitudes A_j and B_j inside the structure, from right to left successively.

$$\begin{aligned} j > l: \quad \begin{pmatrix} A_j \\ B_j \end{pmatrix} &= \mathcal{E}_0 \mathbf{M}^{N-j+1} \left[\mathbf{u} + \varepsilon \frac{b e^{i\chi}}{\sqrt{2}} \left(\mathbf{u} - \mathbf{z} \right) \right] \\ &= (-1)^{(N-j+1)} \mathcal{E}_0 \left\{ \mathbf{u} + \varepsilon \frac{b e^{i\chi}}{\sqrt{2}} \Big[(1 + (N - j + 1) 2 \, |\zeta| \, i) \, \mathbf{u} - \mathbf{z} \Big] \right\}. \end{aligned} \tag{7.110}$$

Now due to $\mathbf{u}^\dagger \cdot \mathbf{z} = 0$, it is easier to compute the sum of the mode intensities to first order in ε:

$$\frac{|A_j|^2 + |B_j|^2}{|E_0|^2} = 1 \; + \; 2 \, \varepsilon \, \mathrm{Re} \frac{b e^{i\chi}}{\sqrt{2}} \big[1 + (N - j + 1) 2 \, |\zeta| \, i \big]. \tag{7.111}$$

$$\begin{aligned} j \le l: \quad \begin{pmatrix} A_j \\ B_j \end{pmatrix} &= \mathcal{E}_0 \left[\mathbf{M}^{N-j+1} - 2\varepsilon \zeta \mathbf{M}^{l-j} \boldsymbol{\sigma} \mathbf{P}(d) \mathbf{M}^{N-l} \right] \left[\mathbf{u} + \varepsilon \frac{b e^{i\chi}}{\sqrt{2}} \left(\mathbf{u} - \mathbf{z} \right) \right] \\ &= (-1)^{(N-j+1)} \mathcal{E}_0 \left\{ \mathbf{u} + \varepsilon \frac{b e^{i\chi}}{\sqrt{2}} \Big[(1 + (N - j + 1) 2 \, |\zeta| \, i) \, \mathbf{u} - \mathbf{z} \Big] - 2 \, \varepsilon \, |\zeta| \, \mathbf{u} \right\}. \end{aligned} \tag{7.112}$$

To first order in ε we now have:

$$\frac{|A_j|^2+|B_j|^2}{|E_0|^2} = 1\,+\,2\,\varepsilon\,\mathrm{Re}\,\frac{be^{i\chi}}{\sqrt{2}}\left[1+(N-j+1)2\,|\zeta|\,i\right]-4\varepsilon\,|\zeta|\,. \tag{7.113}$$

Having found the intensities, we now only need to subtract them to find the force (7.21):

$$D_{jl}=\frac{k}{\varepsilon}F_j=\frac{\epsilon_0}{2}\left[2\mathrm{Re}\left(\frac{be^{i\chi}}{\sqrt{2}}2\,|\zeta|\,i\right)-\delta_{lj}4\,|\zeta|\right]2k\,|E_0|^2=\beta\left(\frac{N\zeta^2}{1+N^2\zeta^2}-\delta_{lj}\right) \tag{7.114}$$

with $\beta = 8k\,|\zeta|\,I_0/c = 4k\,|\zeta|\,\epsilon_0\,|E_0|^2$ as in Eq. (7.37). This is identical to Eq. (7.63), found in Section 7.5 as the limit of the full result Eq. (7.62) as $|E_1|\to|E_0|$.

Part III

Additional research done during the PhD

Chapter 8

Publication: A computable measure of nonclassicality for light

Quantum mechanics, and in particular quantum electrodynamics, enjoys impeccable internal consistency and shows unmatched agreement with experimental observations. Something remaining unresolved is determining its borderline to the classical world, where quantum rules are not observed. A first step towards understanding the quantum to classical transition is to find a description of classical states within quantum theory. One can then ask how much *non-classicality* any given state possesses.

Coherent states [124] are generally accepted to be the most classical of the quantum states of a harmonic oscillator. They reflect the wave-like nature of fields, are generated by classical currents, and are pointer states in realistic environments. Adopting this notion, we call a state *classical* if it is a coherent state, or a mixture thereof (cf. [125]). All other quantum states are *nonclassical*.

With recent progress in quantum optics an increasing wealth of light fields are created deviating more and more from coherent states [126, 127, 128, 129, 130]. Such nonclassical states are distinguished by e.g. sub-Poissonian photon statistics, squeezing, photon number oscillations or negative values of the Wigner function. Most of these signatures can be quantified defining degrees of nonclassicality.

As a central problem, however, none of the above properties detects nonclassicality infallibly [131]: e.g. a so-called Schrödinger cat state $|\alpha\rangle + |-\alpha\rangle$, with $\alpha \gg 1$ has Poissonian photon statistics, negligible squeezing, and yet is highly nonclassical. It is therefore desirable to have a general measure of nonclassicality. This could quantify a resource for a variety of applications that are brought about by the quantum features of light.

A clear-cut "universal" approach to quantifying nonclassicality has been formulated by Hillery [132]. He defined the trace distance of a state σ from the set of classical states as a measure of its nonclassicality. This gives 0 for coherent-state mixtures and nonzero for any other state. However, its computation involves minimization over an infinite number of variables. Consequently Hillery's nonclassical distance has not yet been evaluated exactly for any nonclassical state (for alternative 'distance–based' measures and approximations see [133, 134, 135, 136]). Another universal measure, proposed by Lee [137], is the amount of Gaussian smoothing required to transform the Glauber P–function into a positive distribution and quantifies the noise necessary to wash out nonclassicality. This measure, however, lacks continuity: it lies between 0 and $1/2$ for Gaussian states, but is 1 for any non-Gaussian pure state, no matter how close it is to a Gaussian [138].

In this Letter we propose a universal measure of nonclassicality, the *Entanglement Potential* (EP), that can be computed efficiently for single-mode states of light. It is based on the observation that coherent states are the only pure states that produce uncorrelated outputs when split by a linear optical device [139, 140, 141]. We define the EP of a state σ as the amount of two-mode

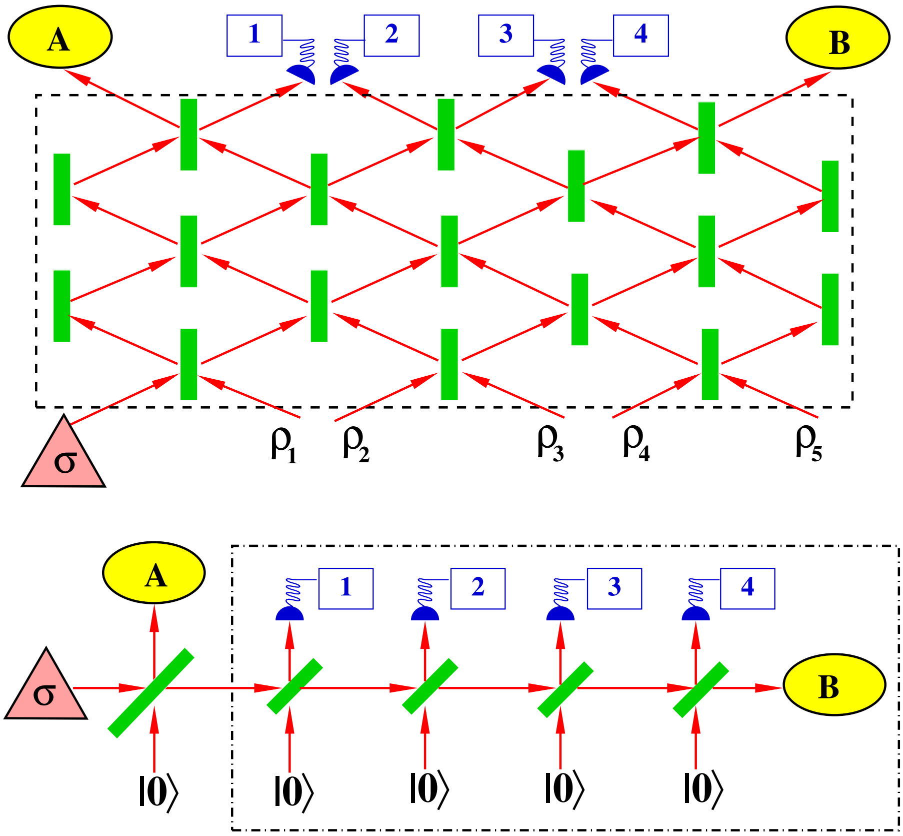

Figure 8.1: (top) A linear optics "black box" (dashed line) creating entanglement between A and B from a nonclassical input state σ. Classical states enter via auxiliary input ports. Photon number measurements are made at the extra output ports. (bottom) An equivalent form of the black box for empty auxiliary ports. The dash-dotted box is local to B.

entanglement (quantum correlations) that can be produced from σ and auxiliary classical states with linear optics and photodetectors. A precise definition follows below.

Entanglement is a genuine quantum feature that gives rise to the most striking "nonclassical" effects [142, 143]. With the advent of Quantum Information Technology (QIT) it has become a crucial resource for many applications. The leading role of quantum optics in the study of the foundations of quantum mechanics [144, 145] and in the implementation of many QIT protocols has recently triggered a lot of interest in the characterization, generation, and distillation of entanglement between optical fields [146, 147, 148, 149, 150, 151, 152]. This provides EP with a direct physical meaning: single-mode nonclassicality as an entanglement resource. Moreover, it supplies a pool of results and methods from QIT for the study of nonclassicality.

At first glance, computation of EP seems prohibitively complicated. For any nonclassical state σ one has to find the optimal linear optical transformation and auxiliary states to create the most two-mode entanglement. However, as we show below, the optimal linear optics entangler is the same for any state, and consists of a single beamsplitter (BS) and an additional vacuum input.

A representation of the transformations that we allow in the definition of the EP is shown in Fig. 8.1 (top). A passive linear optical transformation can be modeled by a circuit of BS's (including phase-shifters) [153]. This transforms input and auxiliary states according to a linear unitary map $a_i' = \sum_i U_{ij} a_j$ between input and output mode operators. At the output two modes are sent to A(lice) and B(ob), all others are measured by ideal photodetectors. Linear operations conditioned on a measurement outcome (e.g. [154]) are excluded, since they can increase the amount of existing nonclassicality.

The displacement of one input mode with $D(\alpha) = \exp(\alpha a^\dagger - \alpha^* a)$ amounts to (local) displacement of all output modes by amounts depending on the circuit of BS's. Mixing the displaced input modes translates to local mixing of the output modes with additional classical communication. As these operations cannot increase entanglement, vacuum ancillas are optimal for entangling the modes of Alice and Bob.

With vacuum ancillas, the circuit of BS's inside the box can be simplified to a standard form. As shown in Fig. 8.1 (bottom), this consists of a single BS splitting the input in two modes going to Alice and Bob, and a series of additional BS's further splitting the signal in Bob's side. Now all measurements can be carried out in Bob's auxiliary modes, and since local operations do not increase entanglement on average, Bob can expect no advantage from splitting off and measuring a part of his beam. The optimal entangling device is therefore a single BS. Although we currently lack of a general proof, all examples we checked analytically and numerically indicate that the transmissivity of the optimal BS is $1/2$ independent of the input state. We denote by U_{BS} this 50:50 BS transformation, which induces the mapping $a = 2^{-\frac{1}{2}}(a_A + a_B)$ on the input mode annihilation operator.

Clearly, the EP is zero for classical states. Moreover, any decomposition of a given output two-mode mixed state in terms of pure states $\rho = \sum_i p_i \left|\Psi_i\right\rangle\left\langle\Psi_i\right|$ must be consistent term-by-term with a pure input $\left|\psi_i\right\rangle\left|0\right\rangle = U_{BS}^{-1}\left|\Psi_i\right\rangle$: this is necessary for the corresponding input mixed state to have a vacuum auxiliary mode. Thus any separable output state must correspond to a convex combination of input states $\left|\alpha_i\right\rangle\left|0\right\rangle$, whereby all nonclassical input states, pure or mixed, will generate entanglement, and have a positive EP. This can be seen as an extension of the results of [140, 141]. Since coherent displacement and phase shifting can be realized on a single BS with an additional strong coherent beam, the EP is invariant with respect to "classical" operations, as defined in [136].

To obtain a specific measure of nonclassicality an entanglement measure has to be chosen. The value of the EP of a state depends on this measure, and different choices may give rise to different orderings between states. Here we consider two alternatives.

A computable measure of nonclassicality for pure as well as for mixed single-mode states is obtained by taking the logarithmic negativity $E_\mathcal{N}$ [155] leading to the following *definition* for the *Entanglement Potential*,

$$EP(\sigma) \equiv E_\mathcal{N}(\rho_\sigma) = \log_2 ||\rho_\sigma^{T_A}||_1. \tag{8.1}$$

Here $\rho_\sigma = U_{BS}(\sigma \otimes |0\rangle\langle 0|)U_{BS}^\dagger$, ρ^{T_A} denotes the partial transpose of ρ, and $||\cdot||_1$ is the trace norm. A nonzero value of $E_\mathcal{N}$ reveals nonseparability, however, the converse is not true in general [156]. The so-called bound entangled states are not detected by the partial transposition criterion. Although examples of such non-Gaussian states exist [157], it remains an open question whether bound entanglement can arise in our setup, i.e. whether or not EP detects all nonclassical states.

An entanglement measure that does detect all entangled states is the relative entropy of entanglement E_{RE} [158]. We will call the induced nonclassicality measure *Entropic Entanglement Potential* (EEP), defined as

$$EEP(\sigma) \equiv \min_{\rho \in \mathcal{D}} \operatorname{tr} \rho_\sigma(\log_2 \rho_\sigma - \log_2 \rho) \tag{8.2}$$

where minimization is carried out over the set $\mathcal{D}$ of all two-mode separable states. EEP detects all nonclassical states, and can be calculated for important classes of states. For finite dimensional mixed states, it can be numerically computed by an iterative procedure [159]. For pure states, it reduces to the von Neumann entropy in one of the output arms. Moreover, EEP gives a lower bound to the nonclassical relative entropy distance.

In the remainder of this Letter we calculate the EP and EEP for a variety of nonclassical states.

The EP and the EEP of a Fock state $|n\rangle$ are

$$EP(n) = -n + 2\log_2 \sum_{k=0}^{n} \sqrt{\binom{n}{k}}, \tag{8.3}$$

$$EEP(n) = n - 2^{-n} \sum_{k=0}^{n} \binom{n}{k} \log_2 \binom{n}{k}. \tag{8.4}$$

In the large-n limit, the two diverge logarithmically and differ only in a constant: $EP(n) \approx \frac{1}{2}\log_2(2\pi n)$; $EEP(n) \approx EP(n) - (1 - 1/\ln 4)$. The entanglement potential can thus detect the nonclassicality of Fock states, and shows that it increases with the photon number.

For any finite superposition of coherent states $|\Psi\rangle = \sum_k c_k |\alpha_k\rangle$ both EP and EEP can be calculated exactly using the "metric tensor" of [160]. This yields complicated formulas, a notable exception being the "odd coherent state" $|\alpha\rangle - |-\alpha\rangle$, for which both EP and EEP are 1, independent of α. If the coherent states constituting $|\Psi\rangle$ are truly distinct $|\alpha_i - \alpha_k| \gg 1$, the nonclassicality is determined by the probability amplitudes c_k, and the coherent amplitudes α_k bring only an exponentially small correction. Such "Schrödinger cat" (SC) superpositions are typical examples of nonclassical states. Neglecting the correction arising from the overlaps, we obtain for the EP and the EEP of a SC state:

$$EP(\Psi) \approx 2\log_2 \sum_k |c_k| \tag{8.5}$$

$$EEP(\Psi) \approx -\sum_k |c_k|^2 \log_2 |c_k|^2 . \tag{8.6}$$

The most nonclassical superposition of N coherent states is that where the probability amplitudes are of equal magnitude: in that case $EP = EEP = \log_2 N$.

Gaussian states are displaced squeezed thermal states: $\rho(\alpha, r, \phi, \bar{n}) = D(\alpha)S(r,\phi)\rho_{\bar{n}}S(r,\phi)^\dagger D(\alpha)^\dagger$. Here $\rho_{\bar{n}}$ is a thermal state of average photon number $\bar{n}$, and $S(r,\phi) = \exp(\frac{1}{2}r[e^{i\phi}(a^\dagger)^2 - e^{-i\phi}a^2])$ is the squeezing operator. It is well known [161] that Gaussian states are classical for $r \leq r_c$, where the nonclassicality threshold is $r_c = \ln(2\bar{n}+1)/2$. Using the results of Wolf et al.[152], it immediately follows that the EP of a general Gaussian state is given by the nonclassical part of the squeezing,

$$EP(\rho(\alpha, r, \phi, \bar{n})) = \frac{r - r_c}{\ln 2}, \tag{8.7}$$

if $r > r_c$ and 0 otherwise. For Gaussian states EP detects nonclassicality (cf. [162]), and is a monotonous function of Lee's nonclassical depth [137]. The EEP of a pure Gaussian state is found by noting that for a BS, displacement in the input is mapped to (local) displacements at the output, and squeezing is mapped to two-mode squeezing followed by local squeezing in each mode. Hence, the EEP is the entropy in a single mode of the corresponding two-mode squeezed vacuum,

$$EEP(\rho(\alpha, r, \phi, 0)) \;=\; \cosh^2(r/2)\log_2\cosh^2(r/2) \;-\; \sinh^2(r/2)\log_2\sinh^2(r/2). \tag{8.8}$$

For strong squeezing ($r \gg 1$) we again find approximate equality with EP up to a constant: $EEP(\rho_{\alpha,r,\phi,0}) \approx r/\ln 2 - (2 - 1/\ln 2)$. For weak $r \ll 1$ squeezing, however, EEP increases more slowly with r: $EEP(\rho_{\alpha,r,\phi,0}) \approx \log_2(r\, e^{-1/2}/2)\, r^2/2$.

A quantitative measure allows us to investigate how much nonclassicality is lost in a physical process. As an example we study photon dissipation, the dominant decoherence process for states propagating in an optical fiber. The corresponding interaction picture master equation is $\dot{\rho} = \frac{1}{2}\gamma(2a\rho a^\dagger - a^\dagger a\rho - \rho a^\dagger a)$. For coherent states this results in an exponential damping of the amplitude, thus the Glauber P function of any state changes as $P(\alpha) \to \xi^{-1} P(\xi^{-1/2}\alpha)$ with $\xi = \exp(-\gamma t)$.

For a SC undergoing photon loss the EP can be calculated exactly using the metric tensor [160]. For weak dissipation, decoherence dominates power loss, and the constituent coherent states $\left|\xi^{1/2}\alpha_i\right\rangle$ can still be considered approximately orthogonal. The whole state, however, becomes more and more entangled with the environment, resulting in a deterioration of its purity. This also reduces the EP: we obtain explicitly

$$EP(t) \approx \log_2\left(1 + 2\sum_{i<k} |\langle\alpha_i|\, \alpha_k\rangle|^{1-\xi(t)}\, |c_i|\, |c_k|\right). \tag{8.9}$$

Although the EP or EEP of SC states is independent of the phase-space distance of the constituent coherent states, this distance determines the decoherence behaviour. For a two-component cat, at intermediate times $|\alpha_1 - \alpha_2|^{-2} < \gamma t \ll 1$ the EP is given by $EP(t) \approx \exp(-t/T_D)2\,|c_1c_2|\,/\ln 2$, with the well-known decoherence timescale $T_D = 2\,|\alpha_1 - \alpha_2|^{-2}\,\gamma^{-1}$.

Formula (8.7) can be used to study the nonclassicality of Gaussian states in Gaussian channels. In particular, for a nonclassical Gaussian state ($r > r_c$) linearly coupled to a heat bath of mean photon number n_T we find

$$EP(t) = -\frac{1}{2}\log_2\left[e^{-\gamma t}e^{-2(r-r_c)} + (1-e^{-\gamma t})(2n_T+1)\right].$$

For $n_T > 0$ this formula is valid up to a finite time $t_c = \gamma^{-1}\log[1 + (1-e^{-2(r-r_c)})/(2n_T)]$: thereafter the state is classical ($EP(t \geq t_c) = 0$). We now concentrate on photon dissipation, i.e. $n_T = 0$, where the state remains nonclassical at any time. For weak squeezing, $0 < r - r_c \ll 1$, the above formula reduces to an exponential decay, $EP(t) \approx (\ln 2)^{-1}(r - r_c)e^{-\gamma t}$. For strong squeezing, $r - r_c \gg 1$, we find a different decoherence behaviour. Initially, EP decreases linearly with time,

$$\gamma t \ll e^{-2(r-r_c)} \quad : \quad EP(t) \approx \frac{r-r_c}{\ln 2} - \frac{e^{2(r-r_c)}}{2\ln 2}\gamma t. \tag{8.10}$$

The loss rate of EP is exponentially large in the initial squeezing. After a short time $\tau = \gamma^{-1}e^{-2(r-r_c)}$ the EP of the highly squeezed state follows a general curve:

$$\gamma t > e^{-2(r-r_c)} \quad : \quad EP(t) \approx -\frac{1}{2}\log_2\left(1 - e^{-\gamma t}\right). \tag{8.11}$$

The initial squeezing now only adds a minor correction, exponentially small in $r - r_c$, to the EP. On longer timescales, $\gamma t \gg 1$, the EP of strongly squeezed states also decreases exponentially, $EP(t) = (2\ln 2)^{-1}\left(1 - e^{-2(r-r_c)}\right)e^{-\gamma t}$. Here we explicitly included the small correction in r, which is the only memory of the initial parameters.

Fig. 8.2 shows the time dependence of EP during photon loss for various states. Squeezed states retain EP better than other nonclassical states: although the weakly squeezed state ($r - r_c = 0.1$) initially has less EP than either the single-photon Fock state or the two examples of SC states, after $t > 2\gamma$ it is more valuable than these for entanglement generation. The most fragile states are the SC's, which lose EP on short timescales given by the T_D mentioned above. Notice that (8.9) gives an excellent approximation of the EP for SC's.

The definition of EP in (8.1) has brought up the still open question of whether bound entanglement can be obtained from single-mode nonclassical light, auxiliary classical states, linear

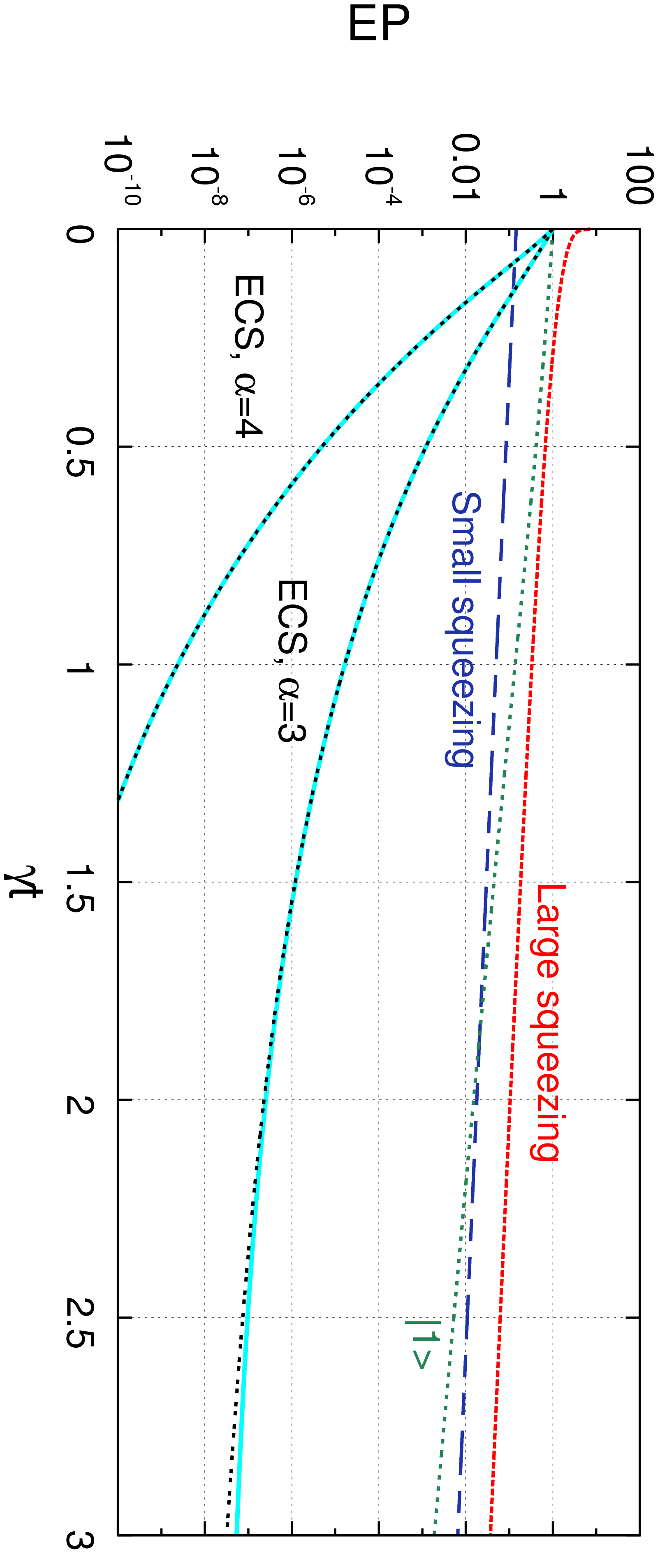
EP
100
1
0.01
10^{-4}
10^{-6}
10^{-8}
10^{-10}
0
0.5
1
1.5
2
2.5
3
γt
Large squeezing
Small squeezing
|1>
ECS, α=3
ECS, α=4

optics and photodetectors. The study of the additivity properties of the Entanglement Potential—some examples show that it is super-additive—and the extension of the concept to multi-mode nonclassical fields are subjects of further research.

This work was supported by the Austrian Science Fund (S 1512), the DFG, the European Union (IST-2001-38877, MERG-500783), and by the National Scientific Fund of Hungary (T043079).

Bibliography

[1] P. LEBEDEV, Untersuchungen über die Druckkräfte des Lichtes, *Annalen der Physik* **6**, 433 (1901).

[2] E. F. NICHOLS and G. F. HULL, A preliminary communication on the pressure of heat and light radiation, *Phys. Rev.* **13**, 307 (1901).

[3] E. F. NICHOLS and G. F. HULL, The pressure due to radiation, *Phys. Rev.* **17**, 26 (1903).

[4] A. ASHKIN, Acceleration and trapping of particles by radiation pressure, *PRL* **24**, 156 (1970).

[5] A. ASHKIN and J. M. DZIEDZIC, Optical trapping and manipulation of viruses and bacteria, *Science* **235**, 1517 (1987).

[6] D. G. GRIER, A revolution in optical manipulation, *Nature* **424**, 810 (2003).

[7] R. FRISCH, Experimenteller Nachweis des Einsteinschen Strahlungsrückstosses, *Zeitschrift für Physik A* **86**, 42 (1933).

[8] T. W. HÄNSCH and A. L. SCHAWLOW, Cooling of gases by laser radiation, *Optics Communications* **13**, 68 (1975).

[9] J. P. GORDON and A. ASHKIN, Motion of atoms in a radiation trap, *Phys. Rev. A* **21**, 1606 (1980).

[10] C. COHEN-TANNOUDJI, Atomic motion in laser light, in *Fundamental Systems in Quantum Optics, Proceedings of the Les Houches Summer School, Session LIII*, edited by J. DALIBARD, J.-M. RAIMOND, and J. ZINN-JUSTIN, pp. 1–164, North-Holland, Amsterdam, 1992.

[11] A. L. MIGDALL, J. V. PRODAN, W. D. PHILLIPS, T. H. BERGEMAN, and H. J. METCALF, First observation of magnetically trapped neutral atoms, *Phys. Rev. Lett.* **54**, 2596 (1985).

[12] S. CHU, Nobel lecture: The manipulation of neutral particles, *Rev. Mod. Phys.* **70**, 685 (1998).

[13] C. COHEN-TANNOUDJI, Nobel lecture: Manipulating atoms with photons, *Rev. Mod. Phys.* **70**, 707 (1998).

[14] W. D. PHILLIPS, Nobel lecture: Laser cooling and trapping of neutral atoms, *Rev. Mod. Phys.* **70**, 721 (1998).

[15] H. J. METCALF and P. VAN DER STRATEN, *Laser cooling and trapping*, Springer, 1999.

[16] E. A. CORNELL and C. E. WIEMAN, Nobel lecture: Bose-Einstein condensation in a dilute gas, the first 70 years and some recent experiments, *Rev. Mod. Phys.* **74**, 875 (2002).

[17] W. KETTERLE, Nobel lecture: When atoms behave as waves: Bose-Einstein condensation and the atom laser, *Rev. Mod. Phys.* **74**, 1131 (2002).

[18] I. BLOCH, Ultracold quantum gases in optical lattices, *Nature Physics* **1**, 23 (2005).

[19] C. J. HOOD, T. W. LYNN, A. C. DOHERTY, A. S. PARKINS, and H. J. KIMBLE, The atom-cavity microscope: Single atoms bound in orbit by single photons, *Science* **287**, 1447 (2000).

[20] P. W. H. PINKSE, T. FISCHER, P. MAUNZ, and G. REMPE, Trapping an atom with single photons, *Nature* **404**, 365 (2000).

[21] A. C. DOHERTY, T. W. LYNN, C. J. HOOD, and H. J. KIMBLE, Trapping of single atoms with single photons in cavity QED, *Phys. Rev. A* **63**, 013401 (2000).

[22] S. GIGAN, H. R. BÖHM, M. PATERNOSTRO, F. BLASER, G. LANGER, J. B. HERTZBERG, K. C. SCHWAB, D. BÄUERLE, M. ASPELMEYER, and A. ZEILINGER, Self-cooling of a micromirror by radiation pressure, *Nature* **444**, 67 (2006).

[23] O. ARCIZET, P.-F. COHADON, T. BRIANT, M. PINARD, and A. HEIDMANN, Radiation-pressure cooling and optomechanical instability of a micromirror, *Nature* **444**, 71 (2006).

[24] D. KLECKNER and D. BOUWMEESTER, Sub-kelvin optical cooling of a micromechanical resonator, *Nature* **444**, 75 (2006).

[25] P. DOMOKOS and H. RITSCH, Mechanical effects of light in optical resonators, *J. Opt. Soc. Am. B* **20**, 1098 (2003).

[26] C. GARDINER and P. ZOLLER, *Quantum Noise: A Handbook of Markovian and Non-Markovian Quantum Stochastic Methods with Applications to Quantum Optics*, Springer, 2004.

[27] P. DOMOKOS and H. RITSCH, Collective cooling and self-organization of atoms in a cavity, *Phys. Rev. Lett.* **89**, 253003 (2002).

[28] H. W. CHAN, A. T. BLACK, and V. VULETIĆ, Observation of collective-emission-induced cooling of atoms in an optical cavity, *Phys. Rev. Lett.* **90**, 063003 (2003).

[29] F. BRENNECKE, T. DONNER, S. RITTER, T. BOURDEL, M. KÖHL, and T. ESSLINGER, Cavity QED with a Bose–Einstein condensate, *Nature* **450**, 268 (2007).

[30] M. M. BURNS, J.-M. FOURNIER, and J. A. GOLOVCHENKO, Optical binding, *Phys. Rev. Lett.* **63**, 1233 (1989).

[31] J. K. ASBOTH, P. DOMOKOS, and H. RITSCH, Correlated motion of two atoms trapped in a single-mode cavity field, *Phys. Rev. A* **70**, 013414 (2004).

[32] J. K. ASBOTH, P. DOMOKOS, H. RITSCH, and A. VUKICS, Self-organization of atoms in a cavity field: Threshold, bistability, and scaling laws, *Phys. Rev. A* **72**, 053417 (2005).

[33] D. NAGY, J. K. ASBOTH, P. DOMOKOS, and H. RITSCH, Self-organization of a laser-driven cold gas in a ring cavity, *Europhys. Lett.* **74**, 254 (2006).

[34] J. K. ASBOTH and P. DOMOKOS, Comment on "Coupled dynamics of atoms and radiation-pressure-driven interferometers" and "Superstrong coupling regime of cavity quantum electrodynamics", *Phys. Rev. A* **76**, 057801 (2007).

[35] J. K. ASBOTH, H. RITSCH, and P. DOMOKOS, Collective excitations and instability of an optical lattice due to unbalanced pumping, *Phys. Rev. Lett.* **98**, 203008 (2007).

[36] I. H. DEUTSCH, R. J. C. SPREEUW, S. L. ROLSTON, and W. D. PHILLIPS, Photonic band gaps in optical lattices, *Phys. Rev. A* **52**, 1394 (1995).

[37] M. WEIDEMÜLLER, A. GÖRLITZ, T. W. HÄNSCH, and A. HEMMERICH, Local and global properties of light-bound atomic lattices investigated by Bragg diffraction, *Phys. Rev. A* **58**, 4647 (1998).

[38] J. K. ASBOTH, J. CALSAMIGLIA, and H. RITSCH, Computable measure of nonclassicality for light, *Phys. Rev. Lett.* **94**, 173602 (2005).

[39] A. YARIV, *Quantum Electronics*, John Wiley and sons, 1989.

[40] S. M. BARNETT and P. M. RADMORE, *Methods in Theoretical Quantum Optics*, Oxford University Press, USA, 2003.

[41] J. M. RAIMOND, M. BRUNE, and S. HAROCHE, Manipulating quantum entanglement with atoms and photons in a cavity, *Rev. Mod. Phys.* **73**, 565 (2001).

[42] P. HORAK, S. M. BARNETT, and H. RITSCH, Coherent dynamics of Bose-Einstein condensates in high-finesse optical cavities, *Phys. Rev. A* **61**, 033609 (2000).

[43] S. ZIPPILLI and G. MORIGI, Mechanical effects of optical resonators on driven trapped atoms: Ground-state cooling in a high-finesse cavity, *Phys. Rev. A* **72**, 053408 (2005).

[44] A. VUKICS, J. JANSZKY, and P. DOMOKOS, Cavity cooling of atoms: a quantum statistical treatment, *J. Phys. B* **38**, 1453 (2005).

[45] A. VUKICS, *Mobile atoms in a cavity field: Statistical and quantum aspects*, PhD thesis, University of Szeged, 2006.

[46] J. DALIBARD and C. COHEN-TANNOUDJI, Atomic motion in laser light: connection between semiclassical and quantum descriptions, *J. Phy. B: At. Mol. Opt. Phys.* **18**, 1661 (1985).

[47] V. VULETIĆ, H. W. CHAN, and A. T. BLACK, Three-dimensional cavity Doppler cooling and cavity sideband cooling by coherent scattering, *Phys. Rev. A* **64**, 033405 (2001).

[48] S. J. VAN ENK, J. MCKEEVER, H. J. KIMBLE, and J. YE, Cooling of a single atom in an optical trap inside a resonator, *Phys. Rev. A* **64**, 013407 (2001).

[49] P. MÜNSTERMANN, T. FISCHER, P. MAUNZ, P. W. H. PINKSE, and G. REMPE, Observation of cavity-mediated long-range light forces between strongly coupled atoms, *Phys. Rev. Lett.* **84**, 4068 (2000).

[50] D. KRUSE, M. RUDER, J. BENHELM, C. VON CUBE, C. ZIMMERMANN, P. W. COURTEILLE, T. ELSÄSSER, B. NAGORNY, and A. HEMMERICH, Cold atoms in a high-Q ring cavity, *Phys. Rev. A* **67**, 051802 (2003).

[51] A. C. DOHERTY, A. S. PARKINS, S. M. TAN, and D. F. WALLS, Motion of a two-level atom in an optical cavity, *Phys. Rev. A* **56**, 833 (1997).

[52] T. W. MOSSBERG, M. LEWENSTEIN, and D. J. GAUTHIER, Trapping and cooling of atoms in a vacuum perturbed in a frequency-dependent manner, *Phys. Rev. Lett.* **67**, 1723 (1991).

[53] P. MAUNZ, T. PUPPE, I. SCHUSTER, N. SYASSEN, P. W. H. PINKSE, and G. REMPE, Cavity cooling of a single atom, *Nature* **428**, 50 (2004).

[54] A. B. MUNDT, A. KREUTER, C. BECHER, D. LEIBFRIED, J. ESCHNER, F. SCHMIDT-KALER, and R. BLATT, Coupling a single atomic quantum bit to a high finesse optical cavity, *Phys. Rev. Lett.* **89**, 103001 (2002).

[55] G. R. GUTHÖHRLEIN, M. KELLER, K. HAYASAKA, W. LANGE, and H. WALTHER, A single ion as a nanoscopic probe of an optical field, *Nature* **414**, 49 (2002).

[56] A. T. BLACK, H. W. CHAN, and V. VULETIĆ, Observation of collective friction forces due to spatial self-organization of atoms: From Rayleigh to Bragg scattering, *Phys. Rev. Lett.* **91**, 203001 (2003).

[57] J. A. SAUER, K. M. FORTIER, M. S. CHANG, C. D. HAMLEY, and M. S. CHAPMAN, Cavity QED with optically transported atoms, *Phys. Rev. A* **69**, 051804 (2004).

[58] D. KRUSE, C. VON CUBE, C. ZIMMERMANN, and P. W. COURTEILLE, Observation of lasing mediated by collective atomic recoil, *Phys. Rev. Lett.* **91**, 183601 (2003).

[59] A. HEMMERICH, Quantum entanglement in dilute optical lattices, *Phys. Rev. A* **60**, 943 (1999).

[60] D. J. A GRIESSNER and P. ZOLLER, Cavity-assisted nondestructive laser cooling of atomic qubits, *J. Phy. B: At. Mol. Opt. Phys.* **37**, 1419 (2004).

[61] J. MCKEEVER, A. BOCA, A. D. BOOZER, J. R. BUCK, and H. J. KIMBLE, Experimental realization of a one-atom laser in the regime of strong coupling, *Nature* **425**, 268 (2003).

[62] A. KUHN, M. HENNRICH, and G. REMPE, Deterministic single-photon source for distributed quantum networking, *Phys. Rev. Lett.* **89**, 067901 (2002).

[63] P. HORAK and H. RITSCH, Scaling properties of cavity-enhanced atom cooling, *Phys. Rev. A* **64**, 033422 (2001).

[64] T. FISCHER, P. MAUNZ, T. PUPPE, P. W. H. PINKSE, and G. REMPE, Collective light forces on atoms in a high-finesse cavity, *New J. of Phys.* **3**, 11.1 (2001).

[65] M. GANGL and H. RITSCH, Cold atoms in a high-Q ring cavity, *Phys. Rev. A* **61**, 043405 (2000).

[66] R. BONIFACIO, G. ROBB, and B. M. NEIL, Propagation, cavity, and Doppler-broadening effects in the collective atomic recoil laser, *Phys. Rev. A* **56**, 912 (1997).

[67] D. JAKSCH, S. GARDINER, K. SCHULZE, J. CIRAC, and P. ZOLLER, Uniting Bose-Einstein condensates in optical resonators, *Phys. Rev. Lett.* **86**, 4773 (2001).

[68] M. GANGL and H. RITSCH, Collective dynamical cooling of neutral particles in a high-Q optical cavity, *Phys. Rev. A* **61**, 011402 (1999).

[69] P. DOMOKOS, T. SALZBURGER, and H. RITSCH, Dissipative motion of an atom with transverse coherent driving in a cavity with many degenerate modes, *Phys. Rev. A* **66**, 043406 (2002).

[70] T. FISCHER, P. MAUNZ, P. W. H. PINKSE, T. PUPPE, and G. REMPE, Feedback on the motion of a single atom in an optical cavity, *Phys. Rev. Lett.* **88**, 163002 (2002).

[71] P. HORAK, G. HECHENBLAIKNER, K. M. GHERI, H. STECHER, and H. RITSCH, Cavity-induced atom cooling in the strong coupling regime, *Phys. Rev. Lett.* **79**, 4974 (1997).

[72] P. DOMOKOS, P. HORAK, and H. RITSCH, Semiclassical theory of cavity-assisted atom cooling, *J. Phy. B: At. Mol. Opt. Phys.* **34**, 187 (2001).

[73] P. MEYSTRE, *Atom optics*, Springer, New York, 2001.

[74] Y. CASTIN, Coherent atomic matter waves, in *Proceedings of the Les Houches Summer School*, edited by R. KAISER, C. WESTBROOK, and F. DAVID, pp. 1–136, EDP Sciences and Springer-Verlag, 2001.

[75] O. MORICE, Y. CASTIN, and J. DALIBARD, Refractive index of a dilute Bose gas, *Phys. Rev. A* **51**, 3896 (1995).

[76] A. LAGENDIJK, B. NIENHUIS, B. A. VAN TIGGELEN, and P. DE VRIES, Microscopic approach to the Lorentz cavity in dielectrics, *Phys. Rev. Lett.* **79**, 657 (1997).

[77] G. LABEYRIE, E. VAUJOUR, C. A. MÜLLER, D. DELANDE, C. MINIATURA, D. WILKOWSKI, and R. KAISER, Slow diffusion of light in a cold atomic cloud, *Phys. Rev. Lett.* **91**, 223904 (2003).

[78] G. LABEYRIE, D. DELANDE, C. A. MÜLLER, C. MINIATURA, and R. KAISER, Coherent backscattering of light by an inhomogeneous cloud of cold atoms, *Phys. Rev. A* **67**, 033814 (2003).

[79] D. W. SESKO, T. G. WALKER, and C. E. WIEMAN, Behavior of neutral atoms in a spontaneous force trap, *J. Opt. Soc. Am. B* **8**, 946 (1991).

[80] S. NUSSMANN, K. MURR, M. HIJLKEMA, B. WEBER, A. KUHN, and G. REMPE, Vacuum-stimulated cooling of single atoms in three dimensions, *Nature Physics* **1**, 122 (2005).

[81] A. T. BLACK, J. K. THOMPSON, and V. VULETIĆ, Collective light forces on atoms in resonators, *J. Phy. B: At. Mol. Opt. Phys.* **38**, S605 (2005).

[82] B. NAGORNY, T. ELSÄSSER, and A. HEMMERICH, Collective atomic motion in an optical lattice formed inside a high finesse cavity, *Phys. Rev. Lett.* **91**, 153003 (2003).

[83] T. ELSASSER, B. NAGORNY, and A. HEMMERICH, Optical bistability and collective behavior of atoms trapped in a high-Q ring cavity, *Phys. Rev. A* **69**, 033403 (2004).

[84] S. SLAMA, C. VON CUBE, B. DEH, A. LUDEWIG, C. ZIMMERMANN, and P. W. COURTEILLE, Phase-sensitive detection of Bragg scattering at 1D optical lattices, *Phys. Rev. Lett.* **94**, 193901 (2005).

[85] R. BONIFACIO, L. D. SALVO, L. M. NARDUCCI, and E. J. D'ANGELO, Exponential gain and self-bunching in a collective atomic recoil laser, *Phys. Rev. A* **50**, 1716 (1994).

[86] J. JAVALOYES, M. PERRIN, G. L. LIPPI, and A. POLITI, Self-generated cooperative light emission induced by atomic recoil, *Phys. Rev. A* **70**, 023405 (2004).

[87] C. VON CUBE, S. SLAMA, D. KRUSE, C. ZIMMERMANN, P. W. COURTEILLE, G. R. M. ROBB, N. PIOVELLA, , and R. BONIFACIO, Self-synchronization and dissipation-induced threshold in collective atomic recoil lasing, *Phys. Rev. Lett.* **93**, 083601 (2004).

[88] G. R. M. ROBB, N. PIOVELLA, A. FERRARO, R. BONIFACIO, P. W. COURTEILLE, and C. ZIMMERMANN, Collective atomic recoil lasing including friction and diffusion effects, *Phys. Rev. A* **69**, 041403 (2004).

[89] D. SCHRADER, S. KUHR, W. ALT, M. MLLER, V. GOMER, and D. MESCHEDE, An optical conveyor belt for single neutral atoms, *Appl. Phys. B: Lasers and Optics* **73**, 819 (2001).

[90] G. HECHENBLAIKNER, M. GANGL, P. HORAK, and H. RITSCH, Cooling an atom in a weakly driven high-Q cavity, *Phys. Rev. A* **58**, 3030 (1998).

[91] K. MURR, On the suppression of the diffusion and the quantum nature of a cavity mode. Optical bistability: forces and friction in driven cavities, *J. Phys. B* **36**, 2515 (2003).

[92] P. DOMOKOS, A. VUKICS, and H. RITSCH, Anomalous Doppler-effect and polariton-mediated cooling of two-level atoms, *Phys. Rev. Lett.* **92**, 103601 (2004).

[93] W. SINGER, M. FRICK, S. BERNET, and M. RITSCH-MARTE, Self-organized array of regularly spaced microbeads in a fiber-optical trap, *J. Opt. Soc. Am. B* **20**, 1568 (2003).

[94] M. G. RAIZEN, J. KOGA, B. SUNDARAM, Y. KISHIMOTO, H. TAKUMA, and T. TAJIMA, Stochastic cooling of atoms using lasers, *Phys. Rev. A* **58**, 4757 (1998).

[95] P. L. K. ALMUT BEIGE and G. VITIELLO, Cooling many particles at once, *New J. of Phys.* **7**, 96 (2005).

[96] S. ZIPPILLI and G. MORIGI, Cooling trapped atoms in optical resonators, *Phys. Rev. Lett.* **95**, 143001 (2005).

[97] D. MEISER and P. MEYSTRE, Superstrong coupling regime of cavity quantum electrodynamics, *Phys. Rev. A* **74**, 065801 (2006).

[98] J. KLINNER, M. LINDHOLDT, B. NAGORNY, and A. HEMMERICH, Normal mode splitting and mechanical effects of an optical lattice in a ring cavity, *Phys. Rev. Lett.* **96**, 023002 (2006).

[99] D. MEISER and P. MEYSTRE, Coupled dynamics of atoms and radiation-pressure-driven interferometers, *Phys. Rev. A* **73**, 033417 (2006).

[100] J. D. JACKSON, *Classical Electrodynamics*, Wiley, 1998.

[101] M. I. ANTONOYIANNAKIS and J. B. PENDRY, Electromagnetic forces in photonic crystals, *Phys. Rev. B* **60**, 2363 (1999).

[102] T. M. GRZEGORCZYK, B. A. KEMP, and J. A. KONG, Stable optical trapping based on optical binding forces, *Phys. Rev. Lett.* **96**, 113903 (2006).

[103] E. I. ANTONOYIANNAKIS, *Electromangetic Fields and Forces in Nanostructures*, PhD thesis, University of London, 1998.

[104] P. DE VRIES, D. V. VAN COEVORDEN, and A. LAGENDIJK, Point scatterers for classical waves, *Rev. Mod. Phys.* **70**, 447 (1998).

[105] J. B. PENDRY and A. MACKINNON, Calculation of photon dispersion relations, *Phys. Rev. Lett.* **69**, 2772 (1992).

[106] S. M. BARNETT and R. LOUDON, On the electromagnetic force on a dielectric medium, *J. Phy. B: At. Mol. Opt. Phys.* **39**, S671 (2006).

[107] P. JESSEN and I. DEUTSCH, Optical lattices, 1996.

[108] G. CAMPBELL, J. MUN, M. BOYD, P. MEDLEY, A. LEANHARDT, L. MARCASSA, D. PRITCHARD, and W. KETTERLE, Imaging mott insulator shells, *Science* **313**, 649 (2006).

[109] W. HOFSTETTER, J. I. CIRAC, P. ZOLLER, E. DEMLER, and M. D. LUKIN, High-temperature superfluidity of fermionic atoms in optical lattices, *Phys. Rev. Lett.* **89**, 220407 (2002).

[110] G. K. BRENNEN, C. M. CAVES, P. S. JESSEN, and I. H. DEUTSCH, Quantum logic gates in optical lattices, *Phys. Rev. Lett.* **82**, 1060 (1999).

[111] M. TAKAMOTO, F.-L. HONG, R. HIGASHI, and H. KATORI, An optical lattice clock, *Nature* **435**, 321 (2005).

[112] G. BIRKL, M. GATZKE, I. H. DEUTSCH, S. L. ROLSTON, and W. D. PHILLIPS, Bragg scattering from atoms in optical lattices, *Phys. Rev. Lett.* **75**, 2823 (1995).

[113] S. SLAMA, S. BUX, G. KRENZ, C. ZIMMERMANN, and P. W. COURTEILLE, Superradiant Rayleigh scattering and collective atomic recoil lasing in a ring cavity, *Phys. Rev. Lett.* **98**, 053603 (2007).

[114] G. R. M. ROBB and W. J. FIRTH, Collective atomic recoil lasing with a partially coherent pump, *Phys. Rev. Lett.* **99**, 253601 (2007).

[115] S. A. TATARKOVA, A. E. CARRUTHERS, and K. DHOLAKIA, One-dimensional optically bound arrays of microscopic particles, *Phys. Rev. Lett.* **89**, 283901 (2002).

[116] J. NG, Z. F. LIN, C. T. CHAN, and P. SHENG, Photonic clusters formed by dielectric microspheres: Numerical simulations, *Phys. Rev. B* **72**, 085130 (2005).

[117] D. MAYSTRE and P. VINCENT, Making photonic crystals using trapping and binding optical forces on particles, *J. Opt. A: Pure Appl. Opt.* **8**, 1059 (2006).

[118] V. KARÁSEK and P. ZEMÁNEK, Analytical description of longitudinal optical binding of two spherical nanoparticles, *J. Opt. A: Pure Appl. Opt.* **9**, S215 (2007).

[119] D. MCGLOIN, A. E. CARRUTHERS, K. DHOLAKIA, and E. M. WRIGHT, Optically bound microscopic particles in one dimension, *Phys. Rev. E* **69**, 021403 (2004).

[120] A. ASHKIN, Acceleration and trapping of particles by radiation pressure, *Phys. Rev. Lett.* **24**, 156 (1970).

[121] R. A. SIMHA and S. RAMASWAMY, Traveling waves in a drifting flux lattice, *Phys. Rev. Lett.* **83**, 3285 (1999).

[122] T. BEATUS, T. TLUSTY, and R. BAR-ZIV, Phonons in a one-dimensional microfluidic crystal, *Nature Physics* **2**, 743 (2006).

[123] T. BEATUS, R. BAR-ZIV, and T. TLUSTY, Anomalous microfluidic phonons induced by the interplay of hydrodynamic screening and incompressibility, *Phys. Rev. Lett.* **99**, 124502 (2007).

[124] R. J. GLAUBER, Coherent and incoherent states of the radiation field, *Phys. Rev.* **131**, 2766 (1963).

[125] L. M. JOHANSEN, Nonclassical properties of coherent states, *Phys. Lett. A* **329**, 184 (2004).

[126] Q. A. TURCHETTE, N. P. GEORGIADES, C. J. HOOD, H. J. KIMBLE, and A. S. PARKINS, Squeezed excitation in cavity QED: Experiment and theory, *Phys. Rev. A* **58**, 4056 (1998).

[127] A. I. LVOVSKY and J. MLYNEK, Quantum-optical catalysis: Generating nonclassical states of light by means of linear optics, *Phys. Rev. Lett.* **88**, 250401 (2002).

[128] N. TREPS, U. ANDERSEN, B. BUCHLER, P. K. LAM, A. MAÎTRE, H.-A. BACHOR, and C. FABRE, Surpassing the standard quantum limit for optical imaging using nonclassical multimode light, *Phys. Rev. Lett.* **88**, 203601 (2002).

[129] K. MCKENZIE, N. GROSSE, W. P. BOWEN, S. E. WHITCOMB, M. B. GRAY, D. E. MCCLELLAND, and P. K. LAM, Squeezing in the audio gravitational-wave detection band, *Phys. Rev. Lett.* **93**, 161105 (2004).

[130] A. ZAVATTA, S. VICIANI, and M. BELLINI, Quantum-to-classical transition with single-photon-added coherent states of light, *Science* **306**, 660 (2004).

[131] T. RICHTER and W. VOGEL, Nonclassicality of quantum states: A hierarchy of observable conditions, *Phys. Rev. Lett.* **89**, 283601 (2002).

[132] M. HILLERY, Nonclassical distance in quantum optics, *Phys. Rev. A* **35**, 725 (1987).

[133] A. WÜNSCHE, V. V. DODONOV, O. V. MAN'KO, and V. I. MAN'KO, Nonclassicality of states in quantum optics, *Fortschr. Phys.* **49**, 1117 (2001).

[134] V. V. DODONOV, O. V. MAN'KO, V. I. MAN'KO, and A. WÜNSCHE, Hilbert–Schmidt distance and non-classicality of states in quantum optics, *J. Mod. Opt.* **47**, 633 (2000).

[135] P. MARIAN, T. A. MARIAN, and H. SCUTARU, Distinguishability and nonclassicality of one-mode Gaussian states, *Phys. Rev. A* **69**, 022104 (2004).

[136] T. A. M. PAULINA MARIAN and H. SCUTARU, Quantifying nonclassicality of one-mode Gaussian states of the radiation field, *Phys. Rev. Lett.* **88**, 153601 (2002).

[137] C. T. LEE, Measure of nonclassicality of nonclassical states, *Phys. Rev. A* **44**, R2775 (1991).

[138] N. LÜTKENHAUS and S. M. BARNETT, Nonclassical effects in phase space, *Phys. Rev. A* **51**, 3340 (1995).

[139] Y. AHARONOV, D. FALKOFF, E. LERNER, and H. PENDLETON, A quantum characterization of classical radiation, *Ann. Phys.* **39**, 498 (1966).

[140] M. S. KIM, W. SON, V. BUŽEK, and P. L. KNIGHT, Entanglement by a beam splitter: Nonclassicality as a prerequisite for entanglement, *Phys. Rev. A* **65**, 032323 (2002).

[141] W. XIANG-BIN, Theorem for the beam-splitter entangler, *Phys. Rev. A* **66**, 024303 (2002).

[142] J. A. WHEELER and W. H. ZUREK, *Quantum Theory and Measurement*, Princeton University Press, 1984.

[143] J. S. BELL, On the Einstein-Podolsky-Rosen paradox, *Physics* **1**, 195 (1964).

[144] A. ASPECT, J. DALIBARD, and G. ROGER, Experimental test of Bell's inequalities using time- varying analyzers, *Phys. Rev. Lett.* **49**, 1804 (1982).

[145] G. WEIHS, T. JENNEWEIN, C. SIMON, H. WEINFURTER, and A. ZEILINGER, Violation of Bell's inequality under strict Einstein locality conditions, *Phys. Rev. Lett.* **81**, 5039 (1982).

[146] G. GIEDKE, B. KRAUS, M. LEWENSTEIN, and J. I. CIRAC, Entanglement criteria for all bipartite Gaussian states, *Phys. Rev. Lett.* **87**, 167904 (2001).

[147] S. J. VAN ENK, Entanglement capabilities in infinite dimensions: Multidimensional entangled coherent states, *Phys. Rev. Lett.* **91**, 017902 (2003).

[148] V. GIOVANNETTI, S. LLOYD, L. MACCONE, and P. W. SHOR, Entanglement assisted capacity of the broadband lossy channel, *Phys. Rev. Lett.* **91**, 047901 (2003).

[149] G. ADESSO, A. SERAFINI, and F. ILLUMINATI, Determination of continuous variable entanglement by purity measurements, *Phys. Rev. Lett.* **92**, 087901 (2004).

[150] J. FIURASEK and N. J. CERF, How to measure squeezing and entanglement of Gaussian states without homodyning, *Phys. Rev. Lett.* **93**, 063601 (2004).

[151] S. L. BRAUNSTEIN and A. K. PATI, *Quantum Information with Continuous Variables*, Springer, 2003.

[152] M. M. WOLF, J. EISERT, and M. B. PLENIO, Entangling power of passive optical elements, *Phys. Rev. Lett.* **90**, 047904 (2003).

[153] M. RECK, A. ZEILINGER, H. J. BERNSTEIN, and P. BERTANI, Experimental realization of any discrete unitary operator, *Phys. Rev. Lett.* **73**, 58 (1994).

[154] J. CALSAMIGLIA, S. M. BARNETT, N. LÜTKENHAUS, and K.-A. SUOMINEN, Removal of a single photon by adaptive absorption, *Phys. Rev. A* **64**, 043814 (2001).

[155] G. VIDAL and R. F. WERNER, Computable measure of entanglement, *Phys. Rev. A* **65**, 032314 (2002).

[156] M. HORODECKI, P. HORODECKI, and R. HORODECKI, Mixed state entanglement and distillation: Is there a "bound" entanglement in nature?, *Phys. Rev. Lett.* **80**, 2539 (1998).

[157] P. HORODECKI and M. LEWENSTEIN, Bound entanglement and continuous variables, *Phys. Rev. Lett.* **85**, 2657 (2000).

[158] V. VEDRAL, M. B. PLENIO, M. A. RIPPIN, and P. L. KNIGHT, Quantifying entanglement, *Phys. Rev. Lett.* **78**, 2275 (1997).

[159] J. REHACEK and Z. HRADIL, Quantification of entanglement by means of convergent iteration, *Phys. Rev. Lett.* **90**, 127904 (2003).

[160] J. JANSZKY, J. ASBÓTH, A. GÁBRIS, A. VUKICS, M. KONIORCZYK, and T. KOBAYASHI, Two-mode Schrödinger cats, entanglement and teleportation, *Fortschr. Phys.* **51**, 157 (2003).

[161] P. MARIAN and T. A. MARIAN, Squeezed states with thermal noise. II. Damping and photon counting, *Phys. Rev. A* **47**, 4487 (1993).

[162] R. SIMON, Peres-Horodecki separability criterion for continuous variable systems, *Phys. Rev. Lett.* **84**, 2726 (2000).

Chapter 9

List of publications

9.1 Publications during the PhD

1 J. K. ASBÓTH, P. DOMOKOS: Comment on "Coupled dynamics of atoms and radiation-pressure-driven interferometers" and "Superstrong coupling regime of cavity quantum electrodynamics". *Phys. Rev. A* **76**, 057801 (2007), preprint arXiv:0705.4174v1[quant-ph]

2 J. K. ASBÓTH, H. RITSCH, P. DOMOKOS: Collective excitations and instability of an optical lattice due to unbalanced pumping. *Phys. Rev. Lett.* **98**, 203008 (2007) preprint cond-mat/0611690

3 C. MAES, J. K. ASBÓTH, H. RITSCH: Self ordering threshold and superradiant backscattering to slow a fast gas beam in a ring cavity with counter propagating pump. *Optics Express* **15**, 10, 6019-6035 (2007)

4 DÁVID NAGY, JÁNOS K. ASBÓTH, PETER DOMOKOS: Collective Cooling of Atoms in a Ring Cavity. *Acta Physica Hungarica B* **26** (1-2), 141-148 (2006),

5 NAGY D, ASBOTH J K, DOMOKOS P, RITSCH H: Self-organization of a laser-driven cold gas in a ring cavity. *Europhysics Letters* **74** (2), 254-260 (2006),

6 J. K. ASBÓTH, P. DOMOKOS, H. RITSCH, A. VUKICS: Self-organization of atoms in a cavity field: Threshold, bistability, and scaling laws. *Phys. Rev. A* **72**, 053417 (2005), preprint quant-ph/0508074

7 J. ASBOTH, J. CALSAMIGLIA, H. RITSCH: A computable measure of nonclassicality for light. *Phys. Rev. Lett.* **94**, 173602 (2005), preprint quant-ph/0411164

8 S. ZIPPILLI, J. ASBOTH, G. MORIGI, H. RITSCH: Forces and spatial ordering of driven atoms in a resonator in the regime of fluorescence suppression. *Appl. Phys. B: Lasers and Optics* **79**, No. 8, pp. 969 - 978 (2004)

9 J. K. ASBOTH, P. DOMOKOS, H. RITSCH: Correlated motion of two atoms trapped in a single-mode cavity field. *Phys. Rev. A* **70**, 013414 (2004) , preprint quant-ph/0312129

10 J. K. ASBOTH, P. ADAM, M. KONIORCZYK AND J. JANSZKY: Coherent-state qubits: entanglement and decoherence. *Eur. J. Phys. D* **30**, No. 3, pp. 403-410 (2004)

9.2 Publications before starting the PhD

11 A. VUKICS, J. ASBÓTH, G. MESZÉNA: Speciation in multidimensional evolutionary space. *Phys. Rev. E* **68**, 041903 (2003)

12 J. JANSZKY, J. ASBOTH, A. GABRIS, A. VUKICS, M. KONIORCZYK AND T. KOBAYASHI: Two-mode Schrödinger cats, entanglement and teleportation. *Fortschr. Phys.* **51**, No. 2-3, pp. 157-171 (2003)

13 J. JANSZKY, A. GABRIS, M. KONIORCZYK, A. VUKICS, J. ASBOTH: One-complex-plane representation: a coherent state description of entanglement and teleportation. *J. Optics B* **4**, S213-S217 (2002)